Sónia Cristina Alexandre Gouveia

Contributions to the analysis of short-term cardiovascular coupling

FACULDADE DE CIÊNCIAS
UNIVERSIDADE DO PORTO

Departamento de Matemática Aplicada
Faculdade de Ciências da Universidade do Porto
June 2009

Sónia Cristina Alexandre Gouveia

Contributions to the analysis of short-term cardiovascular coupling

U.PORTO

FACULDADE DE CIÊNCIAS
UNIVERSIDADE DO PORTO

PhD thesis submitted to
Faculdade de Ciências da Universidade do Porto
(para obtenção do grau de Doutor em Matemática Aplicada)

Advisers:
Ana Paula de Frias Viegas Proença Rocha
Pablo Laguna Lasaosa

Departamento de Matemática Aplicada
Faculdade de Ciências da Universidade do Porto
June 2009

There is no greater impediment to progress in the sciences
than the desire to see it take place too quickly.

Georg Christoph Lichtenberg (1742-99)
Mathematician, physicist and compulsive scribbler.

Acknowledgments

Because “It takes a village to raise a child”, I would like to express my thankfulness to some of its inhabitants.

I am very grateful to my advisors Doutora *Ana Paula Rocha* (DMA-FCUP) and Professor *Pablo Laguna* (CTG) for the scientific guidance, for the useful comments and for the criticisms during the research period. To Professor *Pedro Lago* (DMA-FCUP), my gratitude for the stimulating discussions and inciting ideas. Finally, I cannot help making reference to Professor *António Falcão de Freitas* (Hospital de São João, Portugal) for his legacies: the discussions held back then, make more sense now than ever.

This work would not have been possible without the dedicated experimental data provided by Professor *Philippe Van de Borne* (Erasme Hospital, Brussels, Belgium). I am also truly grateful for his time explaining me “secrets” about sympathetic activity and cardiovascular interactions. My thanks go also to *Sofia Beloka* (Erasme Hospital, Brussels, Belgium) for the helpful scientific collaboration, and for making me feel welcome during the “multi-culti” stayings in Brussels. To *Chris Janssen* (Erasme Hospital, Brussels, Belgium) and Professor *Margarida Brito* (DMA-FCUP) a warm thank you for the revision of the french thesis abstract.

This study was mostly carried out in the Departamento de Matemática Aplicada da Faculdade de Ciências da Universidade do Porto, Portugal (DMA-FCUP).
For creating a pleasant working atmosphere, I want to thank all that I have met during my staying: including *Argentina Leite*, *Hugo Magalhães*, *Isabel Silva*, *Ana Castro*, *Nadja Bressan*, *Susana Brás*, and more recently, *Margarida Silva* and *Conceição Rocha*. A special thank to *Rute Almeida*, for the useful discussions we had and her inputs during this work. Finally, I would like to acknowledge the former undergraduate FCUP students that I have worked with in the research projects I have participated during the PhD period, for their inspiring enthusiasm: *António Vela*, *Bruno Ferreira*, *Hugo Araújo*, *Lara Lacerda* and *Luís Barros*.

During the PhD period and, in particular during the development of the research projects I have participated, I felt rewarded by the contact with other researchers and other ways of being in research. Particularly, I would like to acknowledge the important discussions with Professor Ovídio Costa and Dr. Patrícia Costa (Centro de Medicina Desportiva do Porto), Doutor José Aparício (Pediatric Intensive Care Unit, Hospital de São João, Porto) and Professor João Winck (Serviço de Pneumologia, Hospital de São João, Porto).

The development of the work also demanded staying in the Communications Technology Group, Aragon Institute of Eng Research, University of Zaragoza, Spain (CTG).
To all of those related with the *spanish connection*, my entire gratefulness for being considered “as part of the group”. Special gratitude goes to the very missed *Aurora*, to *Juan Bolea* and to *Fernando Simón* for trying to make me feel like *at home* during my stayings in Zaragoza. Finally, to Professor *Leif Sörnmo*, a Spanish person living in a Nordic country, a warm thank you for the suggestions and the words of encouragement when I most needed them: they were *Anything But Grey.*

At last, the first ones... I would like to express tremendous gratitude and appreciation to my family and my friends for their constant support. The most special and warmest thank goes to my daughter Juliana and my son Nunito, for all the smiles and for all the tears of happiness, and to my husband Nuno, for the unlimited love and understanding. You three are the outcome of the farthermost successful research project I will ever be involved with. You are one in a million and a million in one.

Finally, I acknowledge the individual grant SFRH/BD/18894/2004 supported by FCT and ESF (III CSF). This work was also partially supported by funding from Centro de Matemática da Universidade do Porto (financed by FCT, Portugal through the programmes POCTI and POSI 2010, with national and ESF funds), and by funding from projects TEC2004-05263-C02-02 and TEC2007-68076-C02-02 (financed by CICYT/FEDER, Spain).

Porto, June 2009

Sónia Gouveia

Abstract

The joint analysis of vital signs is presently used for risk stratification and as an aid to clinical diagnosis of the related organs and systems. In particular, the joint study of the arterial blood pressure (ABP) and the electrocardiogram (ECG) allows to assess the baroreceptor reflex sensitivity (BRS), as a measure of the activity and the integrity of the autonomic nervous system (ANS). BRS quantification has been shown useful in the study of cardiac-pathological states, with lower BRS values being associated with increased morbidity and mortality. Also, BRS has been shown to have a prognostic value independent of better recognized measures of cardiovascular outcome. The BRS prognostic value has been assessed with the *gold standard* and invasive "Oxford" protocol, involving intravenous bolus of phenylephrine. Nowadays, the generally accepted possibility of studying the ANS function with spontaneous methods (without induced BRS-stimulation), turns the BRS into a non-invasive and more widely applicable analysis. Previous comparisons between drug-induced and spontaneous estimates evidence that they are different although correlated and, therefore, spontaneous BRS estimates can potentially have similar predictive power as the invasive ones.

The BRS is quantified from the joint analysis of the beat-to-beat series of systolic blood pressure (SBP) values and RR intervals, extracted respectively from the ABP and the ECG signals. The **sequences technique** is a popular method for time domain BRS estimation in spontaneous conditions, thanks to its ease of interpretation and implementation: the BRS estimate is the average of the slopes obtained from the SBP and RR values in each identified baroreflex sequence (BS). However, this technique fails to provide an estimate for low BRS patients, depending of the thresholds used. As a result, this analysis is considered to have limited value in ANS dysfunction cases, which are the crucial cases to identify. Furthermore, BSs have typically 3-beat length even for the normal ANS function cases, which questions the validity of a regression analysis over each BS.

The first step for BRS quantification is the detection of ABP and ECG reference points used to compute the SBP and RR series. For that purpose, a multimodal beat detector is presented in this thesis. This system is based on independent ABP and ECG analysis with subsequent fusion of the results, and makes use of a wavelet based ECG beat detector. The performance of the system is illustrated with real data.

The main contribution of this thesis is on time domain methods for spontaneous BRS assessment. The **events technique** is proposed to improve BRS analysis: the BRS estimate is the global slope obtained from the SBP and RR values in all identified baroreflex events (BEs). On one hand, the use of global slope estimators increases robustness and decreases dispersion in slope estimation. On the other hand, the number of beats in BEs is higher than in BSs and, thus, the use of BEs increases the probability of obtaining an estimate. Also, the increased number of beats in BEs further improves robustness and dispersion, because the influence of one beat in slope estimation is reduced. If BSs are identified, BRS estimates from BEs and BSs are highly correlated; for the cases of BSs absence, BRS estimates from BEs are the lowest and exhibit similar reproducibility and dispersion to those of the remaining cases. The absence of BSs in a record, and the inherent impossibility to assess the BRS, is not synonymous of an absent BRS, but rather a limitation of the sequences technique to provide an estimate. These difficulties are overcome with the events technique.

The validation of the novel technique is carried out with a comparison with BRS methods traditionally accepted to distinguish the sympathetic and parasympathetic ANS modulations.

First, the novel method is validated with **drug-induced data** following the "Modified Oxford" protocol, involving sequential boluses to stimulate the ANS modulations. The results indicate that spontaneous BRS estimates from BEs (instead of BSs) hold smaller differences and higher correlation with invasive estimates. The dispersion in BRS estimation is a trade-off between the number of beats for slope estimation (N) and the correlation between SBP and RR (r). In comparison with spontaneous, drug-induced data exhibits increased r (due to the drug effect) and diminished N (limited to the time window of the bolus effect). However, the possibility to increase N at the expense of slightly decreasing r in spontaneous recordings (by acquiring stationary recordings longer than the invasive ones) evidences that spontaneous BRS assessment is more advantageous than invasive in terms of dispersion.

The novel technique is finally compared with frequency BRS estimators in **spontaneous data**. This comparison also includes information extracted from respiration and sympathetic activity, the latter measured from the muscle sympathetic nerve activity signal with an automatic burst detector. The sympathetic ANS branch presents oscillations of lower frequency than the parasympathetic one and, consequently, longer data segments are needed to capture sympathetic activity. The sequences technique provides a BRS estimate that reflects only the parasympathetic activity, because BSs are typically of short length. On the contrary, as the events technique is able to provide long BEs, besides BEs of the same length as BSs, BEs are more likely to also capture the sympathetic modulation than BSs. The results indicate that BRS estimates from short and long BEs are able to distinguish the parasympathetic and the sympathetic ANS activities and evidence that BEs of different length carry different information on ANS modulations.

Resumo

A análise conjunta de sinais vitais é actualmente utilizada para estratificação de risco e como auxíliar ao diagnóstico clínico. Em particular, o estudo conjunto da pressão arterial (ABP) e do electrocardiograma (ECG) permite aceder à sensibilidade do reflexo dos baroreceptores arteriais (BRS), como uma medida da actividade e da integridade do sistema nervoso autónomo (SNA). A quantificação do BRS tem-se mostrado útil no estudo de patologias cardíacas: valores de BRS mais baixos estão associados a um aumento da morbilidade e da mortalidade. Adicionalmente, o BRS demonstrou ter um valor de prognóstico independente em comparação com outras medidas cardiovasculares melhor reconhecidas. O valor prognóstico do BRS foi avaliado em dados seguindo o protocolo invasivo de "Oxford", envolvendo bólus intravenoso de fenilefrina. Hoje em dia, a possibilidade geralmente aceite de estudar a função do ANS com métodos espontâneos (sem estimulação induzida do BRS), transforma o BRS numa análise não-invasiva e mais amplamente aplicável. A comparação entre estimativas obtidas por indução de fármacos e as espontâneas mostra que são diferentes embora correlacionadas, e portanto as estimativas espontâneas podem ter o mesmo valor predictivo que as invasivas.

O BRS é quantificado a partir da análise conjunta dos valores batimento-a-batimento da pressão arterial sistólica (SBP) e dos intervalos RR, extraídos dos sinais ABP e ECG, respectivamente. O **método das sequências** é um método popular para estimação do BRS em condição espontânea e no domínio do tempo: a estimativa do BRS é a média dos declives obtidos dos valores de SBP e RR identificados em cada sequência barorreflexa (BS). Apesar da sua simplicidade, essa técnica não consegue fornecer uma estimativa para pacientes com baixo valor de BRS, dependendo dos limiares utilizados. Assim, esta análise é considerada ter um valor limitado em casos de disfunção do ANS, que são os casos fundamentais a identificar. Além disso, as BS têm normalmente 3 batimentos mesmo em casos de função normal do ANS, o que questiona a validade de uma análise de regressão sobre cada BS.

O primeiro passo para avaliação do BRS é a obtenção das séries SBP e RR a partir de pontos de referência detectados no ABP e ECG. Neste trabalho é apresentado um sistema multimodal para detecção desses pontos, baseado na fusão dos resultados decorrentes de análises independentes do ABP e ECG. Este sistema utiliza o detector de batimentos no ECG, anteriormente proposto neste grupo de trabalho. O desempenho do sistema é ilustrado com dados experimentais.

Nesta tese, o **método dos eventos** é proposto para melhorar a avaliação espontânea do BRS no domínio do tempo: a estimativa do BRS é o declive global obtido dos valores de SBP e RR em todas os eventos barorreflexos (BE) identificados. Por um lado, o uso de estimadores globais aumenta a robustez e diminui a dispersão na estimação do declive. Por outro lado, o número de batimentos em BEs é maior do que em BSs e, portanto, o uso de BEs aumenta a probabilidade de obter uma estimativa. Além disso, o maior número de batimentos em BEs aumenta a robustez e a dispersão, porque a influência de um ponto na estimação do declive é menor. Se forem identificadas BSs, as estimativas do BRS apartir de BEs e BSs são correlacionadas e, para os casos de ausência de BSs, as estimativas baseadas nos BEs são menores e exibem reprodutibilidade e variabilidade semelhante às dos restantes casos. A ausência de BSs num registro, bem como a impossibilidade de avaliar o BRS, não é sinónimo de uma função de BRS ausente, mas sim uma lacuna do método das sequências para fornecer uma estimativa. Estas dificuldades são superadas com o método dos eventos.

O método dos eventos é validado a partir da comparação com outros métodos mais correntemente aceites em distinguir as modulações simpática e parasimpática do ANS.

Por um lado, o método dos eventos é validado com **dados invasivos**, obtidos através do protocolo “Modified Oxford”, que involve bolus sequenciais para estimular as modulações do ANS. Os resultado indicam que as estimativas espontâneas a partir de BEs (em vez de BSs) exibem menor diferença e maior correlação com as estimativas invasivas. A dispersão na estimação do BRS é um compromisso entre o número de batimentos para estimação do declive (N) e a correlação entre os valores de SBP e RR (r). Em comparação com os dados espontâneos, os dados invasivos apresentam maior r (devido ao efeito da droga) e menor N (limitado ao tempo de duração do efeito da droga). No entanto, a possibilidade de aumentar N em contrapartida de diminuir r em registros espontâneos (fazendo a aquisição de registros estacionários mais longos do que os invasivos), evidencia que a estimação espontânea do BRS é mais vantajosa do que a estimação invasiva, em termos de dispersão.

O método dos eventos é finalmente comparado com estimadores do BRS no domínio da frequência em **dados espontâneos**, incluindo informação da respiração e da actividade simpática. A modulação simpática apresenta oscilações de frequência mais baixa em comparação com a modulação parasimpática e, por isso, são necessários segmentos mais longos para estimar a actividade simpática. O método das sequências estima um valor para o BRS que reflete predominantemente a actividade parasimpática, uma vez que os BSs são segmentos de duração curta. Pelo contrário, o método dos eventos identifica BEs longos, além dos BEs com a mesma duração dos BSs. Assim, os BEs devem permitir estimar também a modulação simpática. Os resultados indicam que os valores do BRS estimados a partir de BEs curtos e longos permitem distinguir as actividades parasimpática e simpática, evidenciando que BEs de diferentes durações contêm informação diferente acerca das modulações do ANS.

Résumé

L'analyse simultanée des signes vitaux est actuellement utilisée pour la stratification du risque cardiovasculaire et comme aide au diagnostic clinique. En particulier, l'analyse conjointe des variations de la pression artérielle (PA) et du rythme cardiaque (RC) permet d'évaluer la sensibilité du baroréflexe (BRS), laquelle reflète l'intégrité et l'activité du système nerveux autonome (SNA). L'évaluation de la sensibilité du baroréflexe artériel s'est avérée utile dans de nombreuses pathologies cardio-vasculaires, dans lesquelles une diminution de la BRS est associée à une morbi-mortalité accrue. La BRS présente également une valeur pronostique indépendante des mesures connues des facteurs de risque cardio-vasculaire. L'évaluation de la BRS se fait classiquement par la méthode d'Oxford, considérée comme le gold standard, qui implique l'administration intraveineuse et séquentielle de bolus de phényléphrine et de nitroprussiate. Il est à présent possible d'évaluer la BRS d'une manière non invasive, ce qui rend son évaluation davantage accessible. Les études ayant comparé la technique non invasive à la méthode d'Oxford révèlent des résultats différents mais corrélés l'un à l'autre. C'est pourquoi, l'évaluation de la BRS par la méthode non invasive pourrait avoir une valeur prédictive au moins égale à la méthode d'Oxford.

L'estimation de la BRS est réalisée par l'analyse battement par battement des variations de l'intervalle RR par rapport aux variations de la pression artérielle systolique (PAS), obtenus à partir de l'électrocardiogramme (ECG) et de l'enregistrement continu de la pression artérielle (PA) par un finomètre. La **technique des séquences** est une technique populaire d'estimation de la BRS dans le domaine temporel grâce à sa facilité d'interprétation et d'application. L'estimation de la BRS correspond à la moyenne des pentes des relations PAS-intervalle RR dans chaque intervalle identifié, appelé une séquence baroréflexe (SB). Cependant, cette technique est limitée dans l'évaluation de BRS basse. C'est pourquoi cette technique est considérée comme ayant peu de valeur dans l'évaluation des dysfonctions autonomes. De plus, les SBs couvrent habituellement trois battements cardiaques, ce qui relève la question de la validité d'une analyse de régression sur chaque séquence.

La première étape dans l'évaluation de la BRS est la détection des points de référence dans les tracés d'ECG et de PA. Dans ce travail, un système plurimodal de détection des points de référence est présenté. Ce système repose sur l'analyse indépendante des signaux ECG et

PA, et sur la fusion subséquente des résultats. L'efficacité de cette analyse est soutenue par la présentation de données réelles.

Dans ce travail, la **méthode des événements** est proposée afin d'améliorer l'évaluation spontanée de BRS dans le domaine du temps. L'estimation de la BRS correspond à la moyenne des pentes obtenues à partir des variations de PAS et d'intervalle RR dans chaque événement baroréflexe (EB) identifié. L'utilisation d'une pente globale accroît la pertinence de l'estimation de la BRS ainsi qu'elle diminue la dispersion des résultats. De plus, le nombre de battements cardiaques étudiés dans un EB est plus important que dans une SB, ce qui augmente la probabilité d'obtenir une estimation valable de la BRS, mais augmente également la pertinence et diminue la variance de l'estimation BRS en raison de l'influence moindre d'une pente d'un événement sur le résultat final. Si des SBs sont identifiées, l'estimation de la BRS à partir des SBs et EBs est hautement corrélées; dans les cas où les SBs ne sont pas identifiés, les estimations de la BRS à partir des EBs sont inférieures et présentent une reproductibilité et une dispersibilité similaires. L'absence de SB dans un enregistrement et l'impossibilité apparente d'évaluer la BRS ne signifient pas que la BRS est nulle, mais correspond plutôt à une limitation de la technique des séquences. La technique des événements baroréflexe permettrait de pallier à cette limitation.

La validation de cette nouvelle technique est réalisée par la comparaison aux méthodes traditionnelles d'estimation de la BRS, permettant de distinguer les influences parasympathiques et orthosympathiques sur le SNA. D'une part, la technique des EBs est comparée à la méthode d'Oxford modifiée, qui a recours à l'administration intraveineuse séquentielle de bolus de phényléphrine et de nitroprusside afin de moduler l'activité du SNA. Les résultats démontrent que la méthode spontanée d'évaluation de la BRS à partir des EBs présente une meilleure corrélation avec les résultats obtenus par la méthode invasive. Les variations dans l'évaluation de la BRS est un compromis entre le nombre de battements cardiaques utilisé pour l'estimation de la pente (N) et la corrélation entre la PAS et l'intervalle RR (r). La méthode d'Oxford modifiée permet d'obtenir un r élevé (lié aux effets des drogues) et un N bas (lié à la courte période de temps étudiée, restreinte à l'injection des drogues). Cependant, la méthode spontanée permet une évaluation de la BRS en augmentant le N pour une faible diminution de r (en raison de l'obtention d'enregistrements stationnaires plus longs que par la méthode invasive), ce qui démontre que l'évaluation spontanée de la BRS est plus avantageuse que la méthode d'Oxford modifiée en termes de dispersion des résultats.

D'autre part, la technique des EBs est comparée à l'estimation de la BRS par la méthode des SBs aves données comprennent également des informations de l'activité respiratoire et orthosympathique. L'activité orthosympathique est mesurée à partir du signal de l'activité nerveuse sympathique à destinée musculaire, obtenue par la technique de microneurographie, et analysée par un programme de détection de bursts automatique. L'activité nerveuse orthosympathique présente des oscillations de plus basse fréquence que l'activité parasympathique; c'est pourquoi des enregistrements de longue durée sont préconisés. La technique des séquences fournit une estimation de la BRS qui reflète uniquement l'activité parasympathique. En effet, les SBs sont par définition de courte durée alors que les EBs sont de bien plus longue durée. Cependant, pour une durée de EB ou de SB équivalente, les EBs sont plus à même de détecter les modulations orthosympathiques du SNA. Les résultats indiquent que l'estimation de la BRS au départ de courts ou de longs EBs permettent l'appréciation des modulations para- et ortho-sympathiques du SNA, et que les EBs de diverses longueurs apportent des informations différentes quant aux modulations du SNA.

Contents

Contents

Abbreviations and Notation

Physiological Abbreviations

ABP	Arterial Blood Pressure
ANS	Autonomic Nervous System
AV	Atrioventricular
BE	Baroreflex Event
bpm	beats per minute
BPV	Blood Pressure Variability
BRS	Baroreflex Sensitivity
BS	Baroreflex Sequence
CHF	Chronic Heart Failure
CNS	Central Nervous System
DBP	Diastolic Blood Pressure
DM	Diabetes Mellitus
ECG	Electrocardiogram
EMG	Electromiogram
HB	Heart Beat
HF	High Frequency band (0.15 - 0.40 Hz)
HR	Heart Rate
HRV	Heart Rate Variability
L	Lying position
LF	Low Frequency band (0.04 - 0.15 Hz)
LVEF	Left Ventricle Ejection Fraction
MSNA	Muscle Sympathetic Nerve Activity
MI	Myocardial Infarction
NT	Nitroprusside
OX	Modified Oxford protocol
PI	Pulse Interval
PF	Pulse Fluctuation
PH	Phenylephrine
PTT	Pulse Transit Time
RESP	Respiration
RSA	Respiratory Sinus Arrhythmia

Physiological Abbreviations (cont.)

PTT	Pulse Transit Time
RESP	Respiration
RSA	Respiratory Sinus Arrhythmia
S	Standing position
SA	SinoAtrial
SBP	Systolic Blood Pressure
SCD	Sudden Cardiac Death
SP	Spontaneous
VLF	Very Low Frequency band (0 - 0.04 Hz)
TF	Total Frequency band (0 - Nyquist Hz)

Mathematical/Methodological Abbreviations

AIC	Akaike Information Criterion
AR	Autoregressive model
ARMA	Autoregressive Moving Average model
DWT	Discrete Wavelet Transform
FFT	Fast Fourier Transform
G,O	Global approach for slope estimation
G,T	Total approach for slope estimation
L,O	Local approach for slope estimation
LPD	Lowpass Differentiator
MAD	Median Absolute Deviation
MSC	Magnitude Squared Coherence
OLS	Ordinary Least squares
PSD	Power Spectrum Density
TLS	Total Least squares
WT	Wavelet Transform

General Notation

A	approach for slope estimation A = {(L,O),(G,O),(G,T)}
B	frequency band B = {TF,VLF,LF,HF}
C	experimental condition C = {SP,PH,NT}
q	identified segments q = {S,E}, where S stands for sequences and E stands for events
ϑ	nomenclature for series ϑ = {RR,SBP,DBP,PI,PF,PTT,RESP,MSNA}
$\hat{}$	estimate
$\bar{}$	mean
$\tilde{}$	median

Notation (in alphabetic order)

$\mathcal{A}_{\mathrm{HB}}$	burst intensity (area/100HB)
$\mathcal{A}_{\mathrm{T}}$	burst intensity (area/min)
α	frequency domain BRS estimator
$\hat{\alpha}^{\mathrm{B}}$	frequency domain BRS estimate evaluated at B band
b	MSNA burst
$\mathcal{B}$	time domain BRS estimator
$\hat{\mathcal{B}}_{\mathrm{A}}^{\mathrm{q}}[\mathrm{c}]$	BRS estimate from segments q and slope approach A, evaluated in condition C
$\mathcal{B}^{I}$	invasive BRS estimator
$\mathcal{C}$	ratio $\#(x > y)/\#x$ in a dispersion diagram representing x versus y
CV	coefficient of variation
$D_{\hat{\mathcal{B}}}$	Difference between 2 different $\hat{\mathcal{B}}$ values
$\hat{\delta}$	dispersion of $\mathcal{B}$ estimated by bootstrap
Δ^{ϑ}_{min}	threshold value for $x_{\vartheta}(n)$ beat-to-beat changes, $\vartheta = \{\mathrm{RR,SBP}\}$
Δ^{ϑ}_{k}	beat-to-beat $x_{\vartheta}(n)$ changes in segment k
$\mathbf{d}_{\vartheta}$	values of $x_{\vartheta}(n)$ in the identified segments, after local mean detrend
f	frequency (Hz)
f_r	respiratory frequency
F_s	sampling frequency
γ	threshold for the identification of MSNA bursts
$\mathcal{H}(f)$	transfer function between SBP and RR
k	segment number
K	number of identified segments
$\mathcal{K}(f)$	coherence between SBP and RR
κ	threshold in the coherence function
n	# of recordings, # of files or # of subjects
n	beat number
N	number of beats in all identified segments
N_k	Number of beats in the k^{th} segment

Notation (cont.)

N_{max}	maximum number of beats in a recording
N_{min}	minimum number of beats in a segment
$\mathcal{N}_{\text{HB}}$	burst incidence (# bursts/100HB)
$\mathcal{N}_{\text{T}}$	burst frequency (# bursts/min)

p	p-value
p_k	p-value associated with r_k
$\mathcal{P}_{\vartheta}^{\text{B}}$	power of $x_{\vartheta}(n)$ evaluated at B band
$\mathcal{P}_{\vartheta}^{\text{B},nu}$	normalized power of $x_{\vartheta}(n)$ evaluated at B band

$R_{\hat{\mathcal{B}}}$	Ratio between 2 different $\hat{\mathcal{B}}$ values
$\hat{R}_{LS}$	Ratio between the $\hat{\mathcal{B}}$ value estimated in L and S positions
r	Pearson correlation coefficient
r	correlation between $\mathbf{d}_{\text{RR}}$ and $\mathbf{d}_{\text{SBP}}$
r_k	correlation between the SBP and RR values in the k^{th} segment
r_{min}	minimum correlation between the SBP and RR values in a segment

$S_{\vartheta}(f)$	spectrum of series $x_{\vartheta}(n)$
$s_{\text{ABP}}(n)$	standard deviation of ABP signal around the n^{th} heartbeat
$s_{\text{ABP}}(t)$	standard deviation of ABP signal around the time t

$x_{\vartheta}(n)$	beat-to-beat variability series ϑ
$\bar{x}_{\vartheta}$	mean of the $x_{\vartheta}(n)$ series
$\bar{x}_{\vartheta}[\text{C}]$	mean of $x_{\vartheta}(n)$ values in condition C
$\bar{\mathbf{x}}_{\vartheta}$	mean of $x_{\vartheta}(n)$ values across bins of 2 mmHg in $x_{\text{SBP}}(n)$
$\bar{\mathbf{x}}_{\vartheta}^{k}$	mean of $x_{\vartheta}(n)$ values belonging to the k^{th} segment
$\tilde{x}(n)$	median of $x(n)$
$\tilde{x}^{\text{R}}(n)$	robust median of $x(n)$

$t_{\vartheta}(n)$	time occurrence of $\vartheta = \{\text{QRS,SBP,DBP,b}\}$
τ	Delay between the SBP and RR series

ω	frequency (rad)
$w(n)$	window function
W_{2^m}	WT at scale $m = 1, 2, ...$

Chapter 1

Introduction

This chapter comprises the motivation for the work presented in the thesis. The functional aspects of the cardiovascular system are reviewed. In particular, the role of the ANS and the baroreceptors reflex in the regulation of the cardiovascular variables is described, as well as the mechanisms of respiration, and the parasympathetic and sympathetic ANS contributions to the regulation of the cardiovascular variability. A brief introduction to cardiovascular signals is presented, including their physiological interpretation.

This chapter also describes the steps carried out for the analysis of the baroreflex sensitivity (BRS). In particular, the setup for the acquisition of the cardiovascular signals is presented, as well as, the way the cardiovascular series are constructed from beat-to-beat reference points, identified in the acquired signals. The BRS is then estimated from the extracted cardiovascular series. An overview of the existing methods for BRS estimation is also included, with special focus on *spontaneous methods*.

Finally, the objectives of this work and the outline of the thesis are presented.

1.1 Rationale to study the Cardiovascular System

Following recent statistics, cardiovascular disease is the major cause of premature death in Europe (EHN, 2008), and Portugal is no exception (Macedo *et al.*, 2008). In Europe, it accounts for almost half of all deaths causing over 4.3 million deaths every year. Cardiovascular disease is also among the top causes of burden of disease: in EU countries 12 million DALYs[1] are due to cardiovascular disease, accounting for 19% of the total of DALYs, and in Europe the numbers rise up to 34 million DALYs, representing 23% of the total.

Cardiovascular disease has major economic costs (EHN, 2008), apart of the immeasurable cost of a human life. In 2008, it was estimated to cost the EU economy around €192 billion/year - almost half more than €129 billion, the EU's annual budget in 2008. Of the total cost, 60% is due to direct health care costs, 20% due to informal care costs and 20% due to productivity losses, which accounts for the premature deaths and illness of those in working age.

The numbers justify the concern of the EU governments and political changes are in progress. As an example, the Lisbon Treaty[2] introduced amendments to the public health article of the Treaty on EU, which is a clear sign that health protection and disease prevention are imperative to promote. Article 152 states that:

"Union action, which shall complement national policies, shall be directed towards improving public health, preventing physical and mental illness and diseases, and obviating sources of danger to physical and mental health. Such action shall cover the fight against the major health scourges, by promoting research into their causes, their transmission and their prevention, as well as health information and education, and monitoring, early warning of and combating serious cross-border threats to health."

Early Diagnosis of Cardiovascular Disease
The prevention and reduction of cardiovascular disease can be achieved through active support and education for healthier lifestyles and the reduction of associated risk factors, e.g., smoking and excessive consumption of alcohol, lack of physical activity, overweight, diabetes mellitus (DM) and high arterial blood pressure. In particular, DM control is of major importance, because DM substantially increases the risk of cardiovascular disease and amplifies the effect of other risk factors. Over 48 million adults in Europe and 23 million adults in the EU have DM, has a prevalence is 7.8%, with tendency to increase (EHN, 2008).

The early diagnosis of cardiovascular disease is required to prevent the occurrence of sudden and often catastrophic events, such as coronary heart disease, stroke and myocardial

---

[1] The Disability Adjusted Life Years (DALYs) index is the sum of the number of years of life lost due to mortality (YLL) and the number of years of healthy life lost due to disability (YLD).

[2] The Lisbon Treaty was signed in Lisbon on 13 December 2007 and amends the EU Treaty and the Treaty establishing the European Community.

infarction. Additionally, when the risk factors are present, the detection of cardiovascular dysfunction at a stage when intervention is still possible, is crucial to treat lesions, prevent expected serious and incapacitating cardiovascular injuries and, ultimately, to cure the disease or to halt its progression.

1.1.1 Monitoring the Cardiovascular function

The electrocardiogram (ECG) and the arterial blood pressure (ABP) supply important information to interpret the regulation of the cardiovascular system and its interrelation with the autonomic nervous system (ANS). In particular, it is currently accepted that the spectral analysis of heart rate variability (HRV) reflects the autonomic modulation (Akselrod *et al.*, 1981) and the respiratory activity (Brown *et al.*, 1993). Also, the joint study of ECG and ABP variability allows the quantification of the baroreceptor reflex sensitivity (BRS) as a measure of ANS integrity (Mancia and Mark, 1983; La Rovere *et al.*, 2008). Because HRV and BRS characterize different aspects of the ANS activity (modulation and reflex, respectively), it is not surprising that measures extracted from the HRV and BRS analyses have shown to correlate moderately (Klingenheben *et al.*, 2008), or even to have non significant correlation (Farrell *et al.*, 1991), indicating that HRV and BRS indexes are measures of autonomic function which provide complementary information.

The study of HRV is based on the beat-to-beat variations in heart rate, measured from the time series of the heart cycle's length, i.e. the RR intervals extracted from the ECG. The BRS measures the relationship between the RR intervals and the systolic blood pressure (SBP) extracted from the ABP. The evaluation of the RR and SBP values on a beat-to-beat basis provides distinct information on the heart condition and, therefore, the integration of this information may yield a better ability to assess the condition of the cardiovascular system and ANS function. As a matter of fact, studies have shown that BRS indexes provide clinical and predictive power, even beyond that provided by HRV indices:

- BRS is reduced in patients with life-threatening ventricular arrhythmias, long after myocardial infarction (De Ferrari *et al.*, 1995);
- BRS allows identification of patients with chronic heart failure conditions at high risk of nonsustained ventricular tachycardia (Mortara *et al.*, 1997);
- low BRS is a strong risk factor in patients with prior myocardial infarction, and BRS is a prognostic value independent of better recognized measures of cardiovascular outcome (La Rovere *et al.*, 1998);
- BRS is a predictor of arrhythmic events in patients with nonischemic dilated cardiomyopathy (Klingenheben *et al.*, 2008).

More recently, an *expert consensus document* on risk stratification to identify patients at risk for Sudden Cardiac Death – SCD (Goldberger *et al.*, 2008), reports that some studies associate impaired short-term HRV to increased risk and that reduced long-term HRV is a risk factor for mortality, although not being specific for SCD. Some authors point out that low BRS is a risk factor for SCD, nevertheless the clinical utility of HRV and BRS parameters to guide selection of therapy is still to be tested (Goldberger *et al.*, 2008).

1.1.2 Clinical relevance of BaroReflex Sensitivity (BRS) estimates

Over the past years, BRS quantification has been useful in the study of other pathological states, including myocardial infarction, congestive heart failure, hypertension and diabetes (Sleight, 2007; La Rovere *et al.*, 2008). Overall, lower levels of BRS have been associated with an increased cardiovascular disease-related morbidity and mortality.

The ATRAMI study was aimed to assess the predictive value of BRS and HRV in patients with a prior myocardial infarction (MI) and demonstrated that a low BRS is a strong risk factor for cardiac death (La Rovere *et al.*, 1998). The study concluded that the BRS analysis yields a significant prognostic value independent of better recognized measures of cardiovascular outcome, such as Left Ventricular Ejection Fraction – LVEF[3]. Moreover, it has been shown that BRS analysis complements the LVEF prognostic value, indicating the BRS as a new index for risk stratification. More recently, even among the large number of low-risk post-MI patients with preserved LVEF, depressed BRS has been found to identify a subgroup at long-term high risk for cardiovascular mortality (De Ferrari *et al.*, 2007). The complementary prognostic value of BRS to that of LVEF to prevent arrhythmic events has also been confirmed in patients with nonischemic dilated cardiomyopathy (Klingenheben *et al.*, 2008).

BRS quantification has not only been useful to prevent serious cardiovascular events when the cardiovascular disease is already present, but also useful for early detection of cardiovascular dysfunction when risk factors are present. One example is the ANS dysfunction related with diabetes, which is associated with increased mortality (Rathmann *et al.*, 1993). Several studies have shown that BRS is impaired in diabetes and that BRS analysis provides early detection of ANS dysfunction (Frattola *et al.*, 1997; Ziegler *et al.*, 2001). Another example is the high arterial blood pressure (hypertension), where a diminished BRS has been reported since long (Bristow *et al.*, 1969; Takeshita *et al.*, 1975). More recent studies indicate that reduced BRS appears to characterize not only patients with established hypertension, but also normotensive offspring of hypertensive parents, who may display a slight blood pressure increase (Lénárd *et al.*, 2005).

---

[3] LVEF is the percentage of blood ejected from the left ventricle in a heartbeat. An LVEF of 50% indicates that the left ventricle ejects half its volume each time it contracts. A normal LVEF is 50% or higher, whereas a reduced LVEF indicates the presence of abnormal heart function (Guyton and Hall, 2000).

1.2 Physiological Background

In this section the relevant physiological background is resumed. In particular, it comprises a brief description of the electrical and mechanical activity of the heart during a cardiac beat and their connection with the acquired cardiovascular signals. Additionally, it is summarized the role of the ANS and the baroreceptors reflex, responsible for the regulation of the heart rate by the blood pressure.

1.2.1 The heartbeat: electrical/mechanical activity and waveforms

The dynamics of the heartbeat is concerned with the mechanisms by which the heart transfers the blood from the venous to the arterial side, under sufficient pressure to ensure proper circulation in the body. Electrical changes in heart tissue cause mechanical changes, i.e., heart muscle contractions and relaxations: the electrical action potential excites the muscle cells and forces mechanical contraction of the heart chambers (atria and ventricles). The mechanical activity of the heart includes blood flow, vibrations of the chamber walls and opening/closing of the heart valves. It results in the flow of blood to the arteries, returning to the heart through the veins.

The mechanical activity of the heart is controlled by its electrical conducting system. Figure 1.1 outlines a schematic representation of the heart, illustrating the cardiovascular anatomy. The cardiac cycle starts with depolarization at the sinoatrial (SA) node leading to atria contraction and, then, the electrical current is transmitted throughout the ventricles. The contraction of the ventricles (*systole*) causes the closure of the atrioventricular (AV) valves mitral and tricuspid and causes isometric contraction until intraventricular pressures are sufficient to open the pulmonary and aortic valves, when the blood ejection begins. The blood is forced out from their chambers into the arteries leaving the heart: the left ventricle empties into the aorta (and the rest of the body) and the right ventricle into the pulmonary artery (and lungs). The increased pressure due to the contraction of the ventricles is called systolic pressure. Ventricular relaxation (*diastole*) occurs at the end of systole and the pulmonary and aortic valves close. After the isometric relaxation, the ventricular pressures fall to less than atria pressures. This leads to the opening of the atrioventricular valves and to the start of ventricular diastolic filling with the blood from the atria. The decreased pressure due to the relaxation of the ventricles is called diastolic pressure. The whole cycle then repeats following another impulse from the sinoatrial node.

Besides the contraction of the heart muscle, the elasticity of the artery walls also helps in the performance of the heartbeat. Hence they become distended by increased blood volume during systole, or contraction of the heart. During diastole, or relaxation of the heart, blood volume in the arteries decreases and the walls contract, propelling the blood farther along the arterial pathway. The effect is that of a pressure wave initiated by the heartbeat and travelling from the aorta along the walls of all the other arteries.

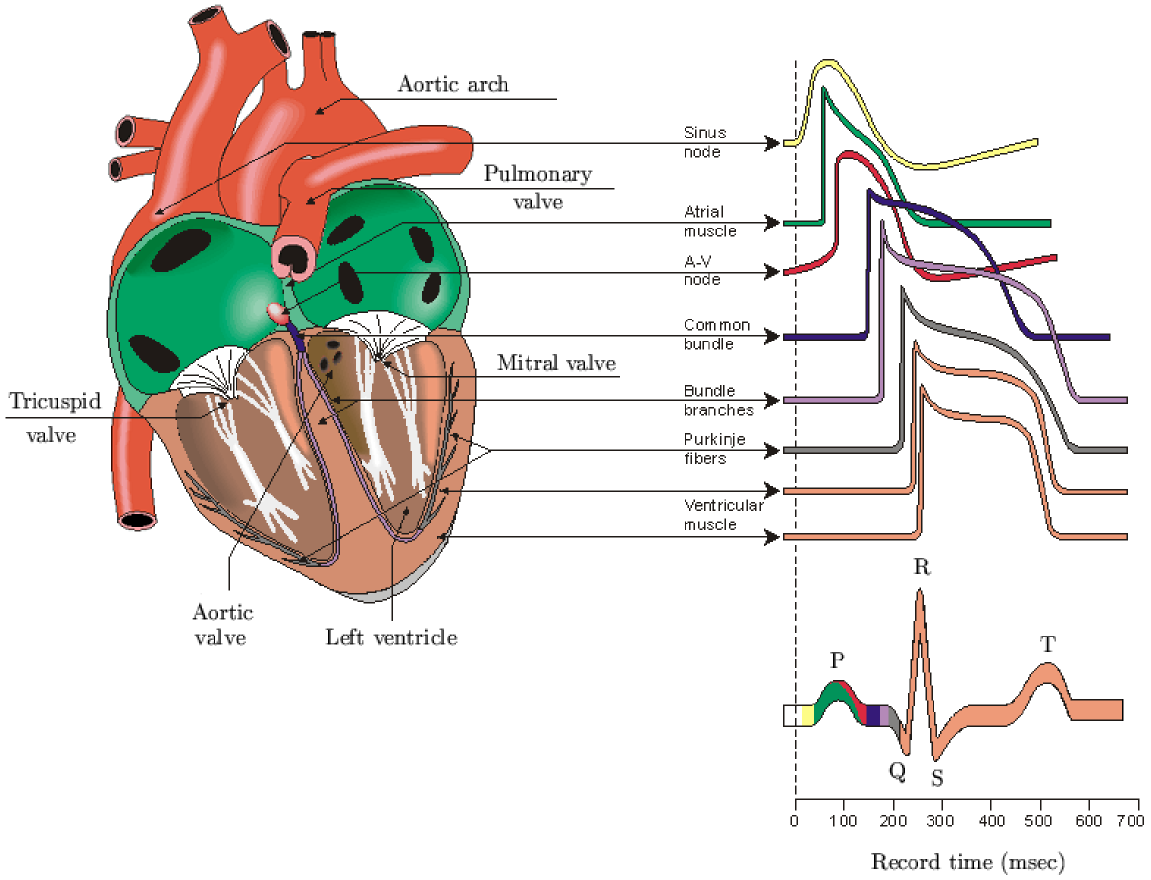

Figure 1.1: Representation of a heart illustrating the cardiovascular anatomy and the heartbeat electrical events reflected in the ECG signal: P, QRS and T waves. Reproduced from Malmivuo and Plonsey (1995).

Electrocardiogram and Arterial Blood Pressure signal

The different phenomena occurring during the heartbeat provide distinct information on the cardiac activity and the integration of this information may yield a better ability to assess the condition of the cardiovascular system. The heart electrical activity can be measured at the skin level with the **ECG**. Changes of the blood pressure in the walls of the arteries (e.g. aorta), being consequence of the mechanical contraction, are reflected in the **ABP** signal.

When the heart muscle is completely polarized or depolarized, the ECG signal is presented as a flat line, whereas, after depolarization, the heart muscle undergoes repolarization to return to its electrical state at rest and an ECG wave is recorded. As illustrated in Fig. 1.1, the ECG in a normal cardiac cycle consists of a P wave, a QRS complex and a T wave. The P wave represents the sequential depolarization of the right and left atria which causes atria contraction. The QRS complex corresponds to the simultaneous right and left ventricular depolarization, which causes ventricular contraction. Finally, the ST segment and the T wave correspond to ventricular repolarization.

As illustrated in Fig. 1.2, the ABP signal exhibits two typical phases: the anacrotic limb (i.e., the rising edge of the pulse) and the dicrotic limb (i.e., the falling edge of the pulse). The first phase is primarily concerned with systole, and the second phase with diastole and wave reflections from the periphery. The ventricular contraction following the R wave in the ECG causes a steep rise in the left ventricular pressure. When the ventricular pressure exceeds the atria pressure the mitral valve closes and, when it exceeds the aortic pressure, the aortic valve opens. Consequently, the blood flows from the ventricle to the aorta. This is the time when the ABP reaches the maximum value (the systolic peak). At the end of blood ejection, the pressure in the ventricle falls below the aortic pressure and the aortic valve closes. The ventricular pressure drops steeply, and when it falls below the atria pressure, the mitral valve opens, and the rapid filling phase begins. This is the time when the ABP reaches the minimum value (the diastolic peak).

A dicrotic notch is usually seen in dicrotic phase of subjects with healthy compliant arteries. The notch is observed as a consequence of the closing of the aortic valve to prevent the backward flow of blood from the aorta, following left ventricular injection, indicating the beginning of the diastolic cycle.

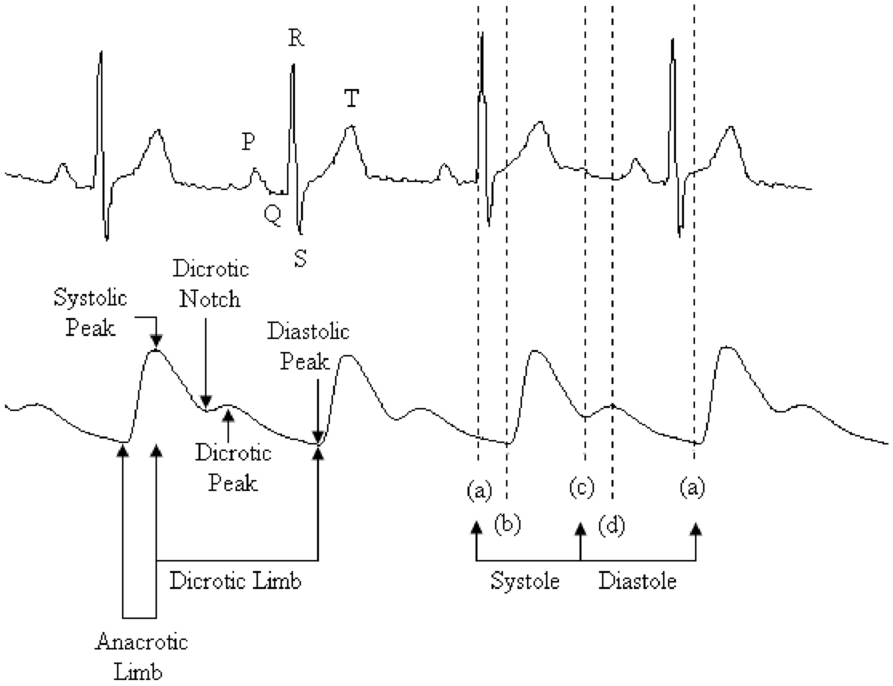

Figure 1.2: ABP and ECG signals with annotation of the most relevant events of the heartbeat reflected in these signals: (a) AV valves opening, (b) aortic valve opening, (c) aortic valve closing and (d) AV valves opening. The time between (b) to (c) corresponds to the ejection time.

1.2.2 Autonomic Nervous System and Baroreflex Mechanism

The autonomic nervous system (ANS) is responsible for the control of the internal organs and of many involuntary human body functions. With respect to the cardiovascular system, the ANS controls the heart rate, the contraction/relaxation of the heart muscle and its force of contraction, constriction/dilatation of blood vessels and glands secretions.

The ANS is predominantly an efferent system transmitting impulses from the central nervous system (CNS) to the peripheral organs and vice-versa (Guyton and Hall, 2000). Figure 1.3 schematizes the anatomy of the ANS concerning the control of the cardiovascular system and of circulation. Autonomic nerves, such as the vagus, constitute almost all of the efferent fibers leaving the CNS and their task is to transmit information on the current state of the system from the periphery to the CNS. The sensory information from the vagus is redirected to the hypothalamus, a higher order CNS structure localized in the brain (Vasomotor center). From there, compensatory changes are initiated, if anything drifts out of the normal function. To complete the required adjustments, the parasympathetic and sympathetic ANS divisions assume a major role.

Most organs are innervated by fibres from both ANS branches. With respect to the cardiovascular system, Fig. 1.3 illustrates that sympathetic nerve fibers are connected directly to the heart, and also to blood vessels. Sympathetic stimulation markedly increases the activity of the heart, both increasing the heart rate and enhancing its strength and the volume of pumping. Parasympathetic stimulation has the opposite effect of sympathetic stimulation. The parasympathetic information is transmitted through the vagus nerve, directly to the heart, and the parasympathetic system has little or no effect on blood vessels. However, an increased parasympathetic activity is associated with a reduced sympathetic stimulation to the vasodilatation of the peripheral vessels.

The parasympathetic and sympathetic systems present functional differences, and their influence is typically opposite: e.g., the parasympathetic slows the heart rate and the sympathetic increases the heart rate and contractility. For the cardiovascular control, the mutual effects of these two systems on the heart rate and on the arterial blood pressure are most significant (Robertson *et al.*, 1996), as following summarized. A fall in blood pressure causes reduced stimulation of the baroreceptors, and consequently reduced discharge from the baroreceptors to the vasomotor centre. This causes an increase in sympathetic discharge leading to vasoconstriction, increased heart rate and contractility, and secretion of adrenaline. The sympathetic constriction of the small arteries and the large arterioles increases the resistance and therefore reduces the blood through the vessels. Sympathetic stimulation of the veins decreases the volume of these vessels and transfers the blood to the heart, forcing increased cardiac activity. Conversely, rises in blood pressure stimulate the baroreceptors, what leads to increased parasympathetic activity, causing slowing of the heart.

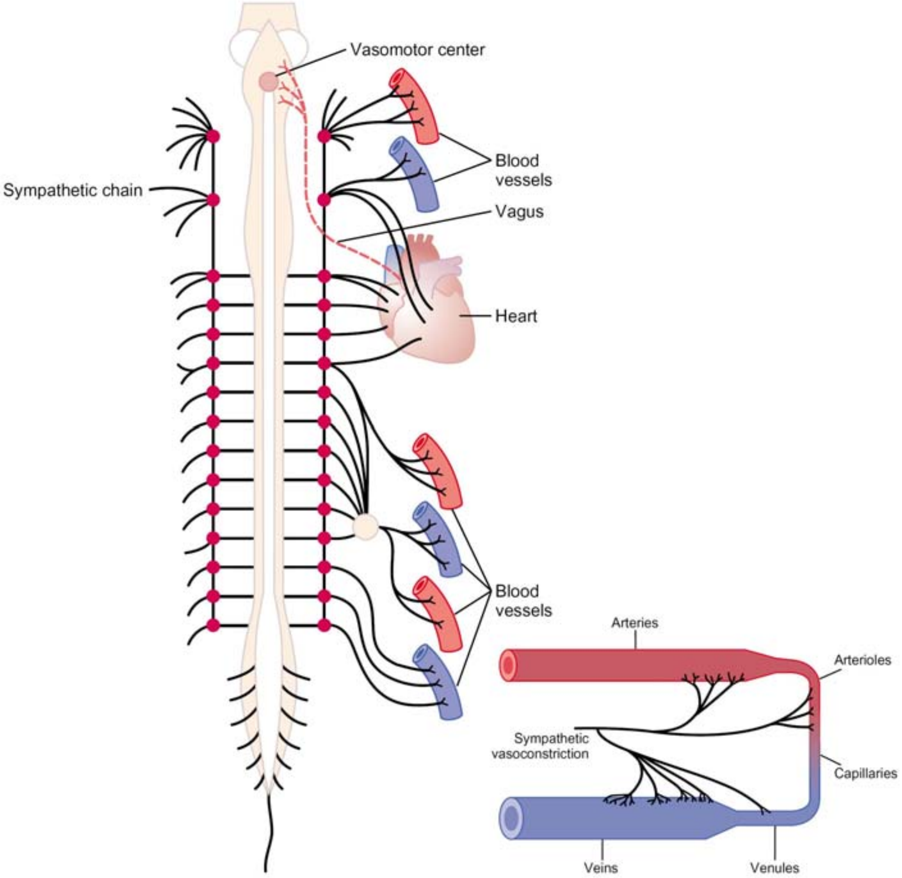

Figure 1.3: Scheme of the anatomy of sympathetic nervous control of the circulation. The full lines represent the sympathetic nerves, while the dotted line represents a vagus nerve that carries parasympathetic signals to the heart. The figure also includes a scheme of the sympathetic innervation of the systemic circulation. Reproduced from Guyton and Hall (2000).

Receptors, Baroreceptors and Baroreflex

To accomplish its task, the ANS actively interprets incoming sensory stimuli from the *receptors*, and produces electrochemical impulses that are distributed to generate responses to the environment and internal conditions. The receptors are a collection of sensory nerve endings that detect the state of the body in the periphery and transmit the corresponding autonomic information.

An example of receptors are the *baroreceptors*, which are the receptors specialized to monitor changes in blood pressure. The main receptors lie strategically in the carotid sinus (neck) and the aortic arch (just outside left ventricle, see Fig. 1.1) to ensure proper blood supply to the brain and periphery; others are found in the walls of other large arteries and veins and some within the walls of the heart. While the arterial baroreceptors found in carotid arteries monitor the pressure of the blood being delivered to the brain, the arterial baroreceptors localized within the aortic arch allow to monitor the pressure of the blood delivered to all other parts of the body [4].

The *baroreflex*, i.e. the reflex of the baroreceptors, is considered the feedback loop in the control of blood pressure: an elevated blood pressure reflexively causes blood pressure to decrease and, then, decreased blood pressure depresses the baroreflex, so that the blood pressure rises. The impulses from the baroreceptors reach centers in the medulla, a part of the brain; from there autonomic activity is redirected to the hypothalamus, so the adjustment process is initiated. The heart rate and resistance of the peripheral blood vessels are then adjusted by the ANS, through its parasympathetic and sympathetic divisions, so that the appropriate blood pressure is maintained.

Cardiovascular variables and baroreflex mechanism

Figure 1.4 presents a block diagram schematizing the interactions between cardiovascular variables (SBP and RR), baroreflex mechanism and respiration (Saul *et al.*, 1991). The interaction between blood pressure and heart rate is regulated by means of the baroreflex, which can be seen as a feedback of this control system and represents the amount of change in heart rate attributable to changes in blood pressure.

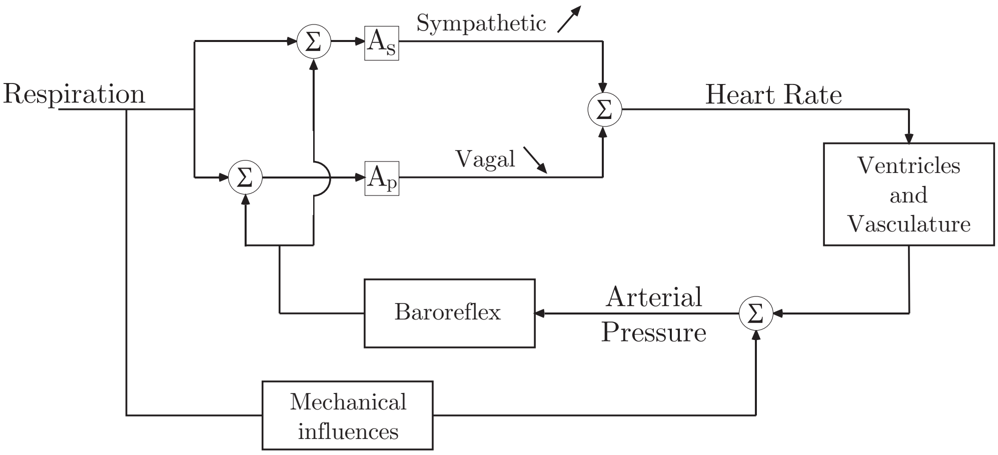

Figure 1.4: Block diagram illustrating the interactions between the cardiovascular variables, baroreflex mechanisms and respiration. The constants A_S and A_P represent the modulation depth of the sympathetic and vagal efferent activity, respectively. Reproduced from Saul *et al.* (1991).

The baroreflex is mainly involved in the control of short-term blood pressure: changes in blood pressure are sensed by the baroreceptors that transmit these changes to brainstem structures, leading to activation/inhibition of parasympathetic and sympathetic ANS afferents in order to adjust the various systems involved in the control of blood pressure e.g., heart rate,

---

[4] Besides arterial baroreceptors, the cardiovascular rhythms are modulated by the central mechanisms and afferent input from chemoreceptors, cardiac receptors, and pulmonary and thoracic stretch receptors.

heart contractility, peripheral resistance and venous blood volume. The parasympathetic and sympathetic nerves are connected to the SA node in order to continuously regulate the function of the heart. Therefore, the heart rate response is the result of a balance between the antagonist functions of the sympathetic and the parasympathetic regulation. In this closed-loop system, the blood pressure determines the heart rate through the baroreflex sensitivity, and the heart rate influences the blood pressure through contraction and dilatation of the ventricles and vasculature.

The faster the blood pressure changes, the more pronounced becomes the baroreceptors reflex, or its sensitivity to the external stimulation. In this way, the baroreflex system attempts to maintain an equilibrium which helps the prevention of cardiac disturbances. In the absence or damage of arterial baroreceptors, this regulation is not possible.

Respiration is one mechanism that can be considered as voluntary and autonomic, being also under the ANS control. Parasympathetic afferents induce constriction inside the lungs, whereas sympathetic activation provokes dilation of the lungs. These interactions are regulated by means of the pulmonary stretch receptors, which are mechanoreceptors found in the lungs. The capacity of the breathing activity and the respiratory system to produce systematic variation in heart rate is referred to respiratory sinus arrhythmia - RSA (Hirsch and Bishop, 1981). Typically, heart rate accelerates during inspiration and decelerates during expiration. Also, respiration influences blood pressure, due to both the mechanical thoracic coupling between respiration and the vasculature and the effects of respiration induced fluctuations of heart rate (Saul *et al.*, 1991).

1.2.3 Cardiovascular Signals

Figure 1.5 shows the cardiovascular signals acquired from a subject in supine position and during the “Modified Oxford” protocol (Gujic *et al.*, 2007), illustrating the baroreflex mechanisms. This protocol consists in a 3 minutes recording: first, the subject is in a spontaneous condition during the initial 60 seconds of the recording, after which follows the successive bolus administration of a vasodilator (nitroprusside) and a vasoconstrictor (phenylephrine). More details about this protocol can be found in Sec. 4.3.1.

The **ECG** is the recording of the electrical activity of the heart over time and the **ABP** signal is the recording of the pressure exerted by the blood circulation on the walls of the blood vessels. Their interactions are directly related with the relation between the electrical and mechanical phenomena occurring in a heart beat, as already described in Sec. 1.2.1.

Breathing occurs by the cyclical contraction of the respiratory muscles, in particular the diaphragm, and can be represented with the respiration - **RESP** signal. As illustrated in Fig. 1.5, the consecutive increasing and consecutive decreasing amplitudes of respiration signal reflect the breathing phases, respectively, inspiration and expiration. The breathing pattern is also characterized by the frequency of the RESP signal, with a faster breathing being reflected in a RESP signal with higher frequency content. In Fig. 1.5, the breathing cycle is completed in 10 sec and, therefore, the respiratory frequency is close to 0.1 Hz. The figure also illustrates that the amplitude of the ECG and inter-heartbeat interval (RR) are modulated at a rate corresponding to the respiratory rate.

The sympathetic function can be assessed by recording the muscle sympathetic nerve activity - **MSNA** signal, which is characterized by synchronous neuronal discharges separated by periods of neural silence. The MSNA is a direct and invasive recording of autonomic activity, with each burst corresponding to the sum of nerve action potential. Increases in sympathetic activity can be evidenced by more frequent occurrence of MSNA bursts (Wallin, 2007; Beloka *et al.*, 2009) and/or increased MSNA burst intensity (Halliwill, 2000). The first case corresponds to neuron firing during higher percentages of cardiac cycles (more bursts), whereas the second case is the output of additional neuron recruitment and/or multiple firings of recruited neurons during a cardiac cycle (larger area or amplitude).

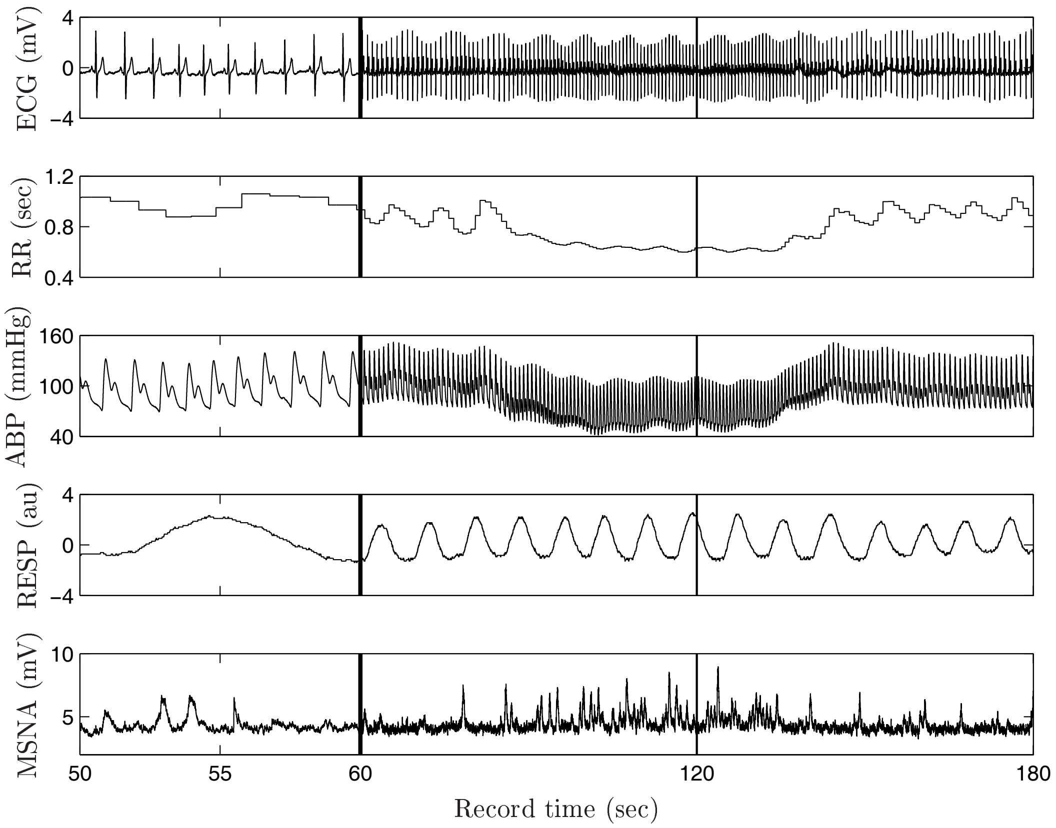

Figure 1.5: ECG, ABP, RESP and MSNA signals from a representative subject in spontaneous condition (first 10 sec) and after the successive boluses of nitroprusside/phenylephrine (bold/light lines). The figure presents a different time scale before and after the bold line, to allow both a detailed visualization of the waveforms and the overall subject's response to the drug administration. Data from the SP/NT/PH dataset.

As illustrated in Fig. 1.5 for the **spontaneous** condition, the respiratory sinus arrhythmia is reflected by physiological modulation that respiration induces in the SBP values and RR intervals. When ABP decreases as a result of expiration, the baroreceptors increase MSNA and, as a response, the RR values increase. The reverse occurs during inspiration. Thus the respiratory oscillations in BP translate into oscillations in MSNA and RR, as a result of baroreflex activity. The MSNA bursts are typically initiated in diastole, as systole elicits baroreceptor afferent inputs that cause the cessation of a sympathetic burst (Wallin and Charkoudian, 2007).

Nitroprusside administration provokes vasodilatation and an acute drop of ABP, into a higher range of amplitudes than of that related with expiration. Therefore, the baroreflex is forced to promote sympathetic activation in order to the ABP to return to its normal levels, which is evidenced by the higher MSNA activity. When the MSNA activity is triggered to high activity levels, the respiratory modulation in the SBP and RR is reduced.

After the **phenylephrine** bolus the effect is reversed. Phenylephrine is an antagonist of nitroprusside, which causes vasoconstriction and forces ABP to increase acutely. The sympathetic activity lowers when the ABP is recovering to its normal level and parasympathetic activity increases. At the end of the drug-induced protocol, the ABP and the sympathetic and parasympathetic balance is returning to its normal functioning levels.

1.3 Assessment of the BRS function

It is currently accepted that the joint analysis of SBP and RR interval series allows BRS assessment, as SBP decreases and increases produce correspondent baroreflex mediated shortening and lengthening of the RR interval, respectively (La Rovere *et al.*, 2008). Therefore, the first step for BRS quantification is the acquisition of the ABP and ECG signals and the detection of the beat-to-beat reference points in each signal, to compute the SBP and RR series. In this section, the main stages for BRS assessment are described in each of the following subsections: the acquisition of the ABP and ECG signals, the extraction of the SBP and RR series from the acquired signals and finally an overview of methods for BRS assessment. Additionally, current acquisition protocols to record RESP and MSNA are also included.

1.3.1 Acquisition of Cardiovascular signals, RESP and MSNA

Figure 1.6 presents a schematic representation illustrating the anatomical position of the ECG electrodes, the finger-cuff and arm-cuff to acquire the ABP signal, the belt to acquire the RESP signal and the MSNA electrodes.

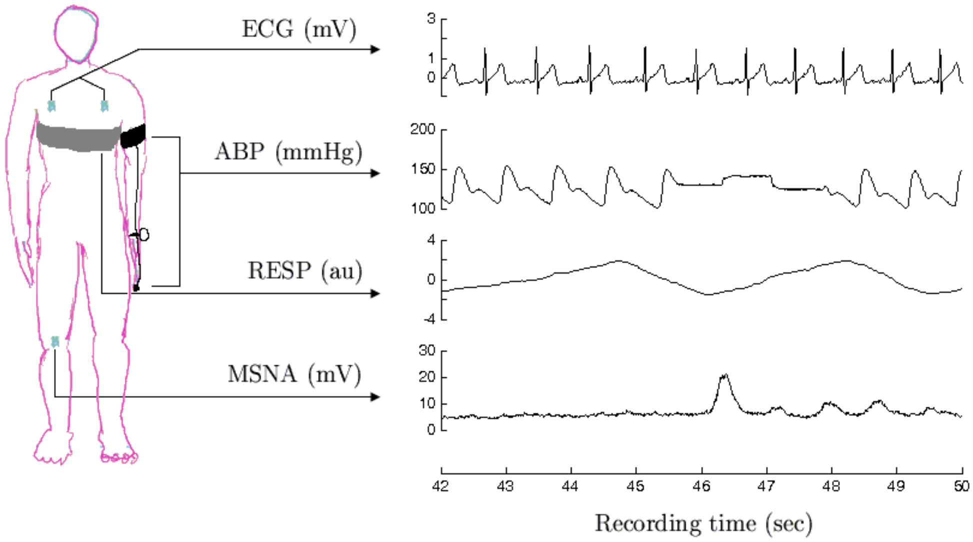

Figure 1.6: Setup for acquisition of the cardiovascular, RESP and MSNA signals, showing anatomical position of the ECG electrodes, the finger-cuff and arm-cuff for ABP acquisition, thoracic belt for RESP acquisition and MSNA electrodes. The signal ABP shows a return-to-flow calibration episode.

Electrocardiogram (ECG)

The ECG can be obtained non invasively via skin electrodes: the heart is triggered to contract by electrical activity and, like any other muscle, produces detectable voltages at the skin level. The ECG shows the changes in the voltage per time, between pairs of electrodes placed at certain points on the skin. The different possibilities to position the ECG electrodes in the thorax determines the *lead*, i.e. the spatial viewpoint from which the electrical activity of the heart is observed (Guyton and Hall, 2000). Figure 1.6 shows two electrodes positioned in the frontal plane of the thorax, left and right arm, which corresponds to the acquisition of the traditional ECG lead I.

Arterial Blood Pressure (ABP)

The ABP can be recorded continuously either directly from the radial/brachial artery by means of an intra-arterial catheter or indirectly and noninvasively from peripheral blood vessel e.g., on ears, toes or fingers by making use of a plethysmograph sensor[5].

There are several devices that can be used for the ABP measurement at the finger level, including the Finapres$^{\mathrm{TM}}$ system that was introduced in the early 1980s. Nowadays, alter-

---

[5] Plethysmography is a simple and low-cost optical technique that is often used non-invasively to make measurements at the skin surface. The finger ABP is measured using a finger cuff and an inflatable bladder in combination with an infrared plethysmograph, which consists of an infrared light source and detector. The infrared light is absorbed by the blood, and the pulsation of arterial diameter during a heart beat causes a pulsation in the light detector signal. Therefore, the acquired waveform comprises a pulsate waveform attributed to cardiac synchronous changes in the blood volume with each heart beat (Allen, 2007).

native acquisition devices with the same acquisition principle are commercially available, in particular, the Portapres and Finometer systems (Finapres Medical Systems BV, Holland). These devices use an inflatable finger-cuff with a built-in plethysmograph sensor (Peñáz, 1973), to measure the pulsate vascular unloading of the arterial walls in the finger.

The ABP signal is known to change in shape as it moves towards the periphery and undergoes amplification and alterations in its shape and temporal characteristics[6]. To correct the distortion in the finger pressure relative to the brachial artery pressure, the acquisition system makes use of software and an arm-cuff (Wesseling *et al.*, 1995; Guelen *et al.*, 2003, 2008). The distortion in finger pressure relative to brachial artery pressure is diminished by real time filtering (with 1 sec delay). The ABP level is corrected by return-to-flow calibration, with an arm-cuff wrapped around the same arm as the finger-cuff. From time to time, the system automatically inflates and deflates the arm-cuff. When the arm-cuff inflates, no pulsations can be sensed in the finger and a flat line is observed in the ABP signal (Fig. 1.6).

Even with distortion correction, ABP measurements at the finger level may differ from invasive ABP. With respect to the BRS quantification, it has been shown that noninvasive ABP measurements accurately reflect intra-arterial pressure (Parati *et al.*, 1989; Hartikaninen *et al.*, 1995; Langewouters *et al.*, 1998). Additionally, the results from the ATRAMI study (La Rovere *et al.*, 1998), showing that the BRS is an independent prognostic value of cardiac death with invasive ABP acquisition, were corroborated in the study of Pinna *et al.* (2000). In that study, using a subset of the ATRAMI data, the BRS obtained from Finapres ABP signals was found to be highly correlated with that of the invasive ABP and to provide equivalent prognostic value.

Respiration (RESP)

Breathing can be monitored in many ways (Folke *et al.*, 2003). Airflow can be measured with a mask over the mouth and nose or by a thermocouple under the nose, measuring the change in temperature of air as it is inhaled and exhaled. Also, airflow can be evaluated by a thorax belt or by electrical impedance.

The impedance of the thorax is affected by several parameters and changes substantially during the respiratory and the cardiac cycle. The impedance changes in a respiratory cycle are due to the changes of air volume in the lungs, and the impedance changes during the cardiac cycle are due to the changes in blood perfusion of the lungs. Additionally, the expansion and contraction of the chest, which accompanies respiration, results in motion of the chest electrodes/belt.

---

[6] Different ABP waveforms can be recorded at different sites of the body: peripheral waveforms are delayed with respect to the ascending aortic ABP waveform (taken as the reference ABP waveform) and present a different contour (Karamanoglu, 1997). Additionally, the pulse propagation in arteries is subjected to a frequency dependent phase distortion, as described in O'Rourke and Gallagher (1996).

The ECG signals recorded from the surface of the chest are influenced by motion of the electrodes/belt with respect to the heart and by changes in the distribution of the electrical impedance in the thoracic cavity. Therefore, changes in the ECG that reflect the filling and emptying of the lungs can be used as an indicator of the respiratory activity. As illustrated in Fig. 1.5, respiration induces an amplitude modulation of the observed ECG. This effect is enhanced in deep breathing, because deep breathing is usually associated with maximal filling and emptying of the lungs, which is reflected in a wider expansion and contraction of the thorax, and larger changes in thoracic impedance. Therefore, when a respiratory signal is not available, the respiratory information can be estimated from ECG signal itself using signal processing techniques (Gouveia *et al.*, 2001; Rocha *et al.*, 2002; Bailón *et al.*, 2006). Yet, these methods do not supply a calibrated respiration signal; only its time evolution and frequency is important. Any automated system for ECG and ABP analysis can use this technique to produce significant and previously unavailable information of clinical value.

Muscle sympathetic nerve activity (MSNA)

The sympathetic activity can be acquired following the micrographic technique, as described in van de Borne *et al.* (1997). The MSNA signal is determined continuously by obtaining multiunit recordings of postganglionic sympathetic activity, measured from a nerve fascicle in the peroneal nerve posterior to the fibular head (localized in the knee) of each subject. Electric activity in the nerve fascicle is measured with the use of tungsten microelectrodes (shaft diameter 200 μm, tapering to a non-insulated tip of 1 to 5 μm). A subcutaneous reference electrode is inserted 2 to 3 cm away from the recording electrode, which is inserted into the nerve fascicle. The neural signals are amplified, filtered, rectified, and integrated to obtain a mean voltage display of sympathetic nerve activity. If a signal-to-noise ratio higher than 3 is achieved, the MSNA recordings are considered for further processing.

1.3.2 Reference points in signals and cardiovascular series

As pointed out in Sec. 1.2.2, the interactions between the beat-to-beat blood pressure and heart rate are regulated by means of the baroreflex and, that is why, traditionally the BRS is quantified from the joint analysis of SBP and RR interval series (La Rovere *et al.*, 2008). Therefore, after the signals acquisition, the timing of the QRS complex in the ECG and the timing of the SBP value in the ABP signal are identified in each cardiac beat, and the corresponding variability series are obtained from those reference points.

The use of automatic systems for the detection of reference points in signals avoids inter and intra observer variability, and facilitates the computation of the SBP and RR series to be used for BRS analysis. For the automatic identification of reference points in the ECG and ABP signals, a multimodal beat detector is presented in Chapter 2. This system is based on independent ABP and ECG analysis with subsequent fusion of the results, and makes use of a wavelet based QRS detector previously evaluated by our group (Martínez *et al.*, 2004).

1.3.3 Overview of methods for BRS assessment

After the acquisition of the cardiovascular signals and the extraction of the SBP and RR series, the BRS can be estimated.

The baroreflex mechanisms exhibit nonlinear characteristics and to characterize the BRS over its entire range, the BRS has to be acutely stimulated (Di Rienzo *et al.*, 2009). As illustrated in Fig. 1.7, the SBP and RR relation over the entire baroreflex range is well described by a sigmoid function (Hunt and Farquhar, 2005). The sigmoid curve includes a lower and a higher plateau and, in between, a range of SBP and RR values exhibiting an approximately linear relation. The SBP changes occurring in the linear part of the sigmoidal produce a more pronounced RR response in comparison with comparable SBP changes occurring in the plateau regions (Di Rienzo *et al.*, 2009; Mancia and Mark, 1983).

As illustrated in Fig. 1.7, the sigmoid function do not exhibit systematic asymmetries and it is likely that the *operating point* of the subject (i.e., the mean baseline SBP and RR values) is localized in the approximately linear portion of the sigmoid (Hunt and Farquhar, 2005). The BRS can be evaluated as the slope of a tangent line to the curve, e.g. at the operating point of the subject, or evaluated separately for the lower and upper arches (Parlow *et al.*, 1995). As illustrated in Fig. 1.7, the sigmoidal shape for BRS failure patients (Group III) is characterized by having a lower RR range and a lower slope in the middle portion of the function in comparison with normal BRS subjects (Mancia and Mark, 1983).

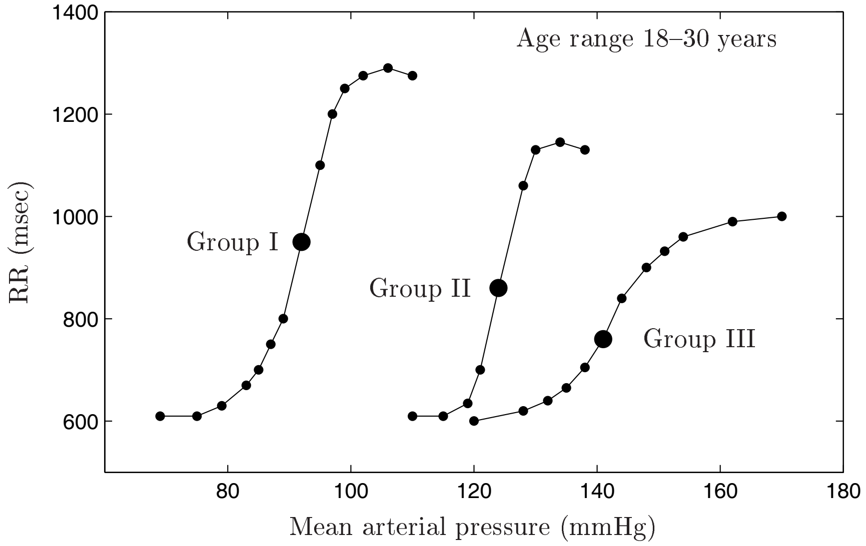

Figure 1.7: Relation between mean arterial pressure (MAP) and RR in normotensive (I), moderately hypertensive (II) and severely hypertensive subjects (III). The curves were constructed by increasing and decreasing MAP from the operating point (large circle), administrating a vasoconstrictor and a vasodilator, respectively. Data correspond to mean values obtained from several young subjects. Reproduced from Korner *et al.* (1974).

There are different classifications of the BRS methods in the literature, e.g., “traditional” versus “modern” (Di Rienzo *et al.*, 2001) or “invasive” versus “noninvasive” (La Rovere *et al.*, 2008). In this work, the distinction of interest is between **induced-stimulation** versus **spontaneous** techniques.

Several methods have been suggested for BRS assessment in induced-stimulation conditions, e.g., pharmacological methods and the neck pressure method.

The **pharmacological methods** make use of vasoactive drugs which change arterial pressure, while having minimal direct effect on the sinus node. Therefore, these drugs induce negligible direct effects on the RR interval, so that the observed RR changes are mediated reflexively via the baroreceptors. The acquisition protocol can include the administration of drugs to provoke either vasoconstriction, vasodilatation or both in the same experimental setting. The lower part of the baroreflex arc in Fig. 1.7, corresponding to the SBP values lower than the SBP operating value, is obtained by bolus injections of a vasodilator administrated at a spontaneous condition, causing the SBP values to acutely decrease to values lower than spontaneous SBP values. Contrarily, the higher part of the baroreflex arc is obtained by the administration of a vasoconstrictor, provoking acute increase of the SBP values and correspondent RR increase mediated via baroreflex.

While the pharmacological methods induce perturbations in the ABP, the **neck pressure method** induces perturbations directly in the carotid baroreceptors, by means of a neck chamber apparatus. The neck chamber allows to create mechanical alteration of transmural carotid sinus pressure stimulating, by suction, the carotid baroreceptors and mimicking ABP changes (Ernsting and Parry, 1957).

Previous comparison between the pharmacological methods (injections of Phenylephrine) and the neck pressure method have reported that both protocols can create artificial SBP ramps, with larger amplitude than that in a spontaneous recording (Ebert *et al.*, 1984). Although the induced-stimulation methods can produce changes across a range of SBP necessary to observe the nonlinear nature of the BRS, the induced SBP range cannot be controlled in such a way as to ensure engagement of the reflex across the entire reflex range. The consequence is that these methods present high failure and, usually, the unsuccessful experiments are discarded and repeated (Davies *et al.*, 1999).

Methods for spontaneous BRS assessment

The drug induced experiments make use of intravenous intubation for the drug administration, what limits the applicability of such techniques besides contributing for the discomfort of the patient. In contrast, the spontaneous techniques are by principle non invasive and do not require drug administration or the use of a neck chamber apparatus. Therefore, the use of spontaneous methods simplifies the test procedure and allows the BRS measurement under a broad range of daily life conditions, with potential applications in ambulatory BRS assessment.

Spontaneous methods provide BRS estimates in a normal physiological range over a time period, rather than in a brief and extreme perturbation, as the BRS induced-stimulation methods. However, they require stationary acquisition conditions and fairly longer periods of recording in comparison with induced-stimulation to provide a steady state BRS estimate.

Most of the spontaneous methods assume that the SBP and RR relation is linear when it is in fact sigmoidal (see Fig. 1.7). However, the relatively reduced SBP changes under spontaneous conditions limit the BRS analysis to a smaller portion of the entire sigmoid reflex arc, in a neighbourhood of the subject's baseline operating point. In this interval, the linear assumption is reasonable to consider because the spontaneous range of SBP and RR amplitudes is much smaller than the entire baroreflex range. Also, the subject's baseline operating point is most likely to lie in the middle portion of the sigmoid function, even for BRS failure patients (Mancia and Mark, 1983). These evidences have been corroborated by studies showing that spontaneous BRS methods are able to provide similar values of BRS to those obtained by the drug-induced methods, within the physiological range of SBP under resting conditions (Parlow *et al.*, 1995).

Table 1.1 presents an overview of the methods that have been proposed for spontaneous BRS assessment, most assuming a linear SBP and RR relation in the operating point. The most recent extensive comparison between spontaneous methods is included in the work of Laude *et al.* (2004), making use of spontaneous data from the EuroBaVar dataset. Besides the methods included in Table 1.1, other methods have been proposed to analyze the nonlinearities of the SBP and RR interactions in spontaneous condition; comprehensive literature reviews of such methods can be found in Porta *et al.* (2009) and Nollo *et al.* (2009).

The sequences technique was introduced in the study of Di Rienzo *et al.* (1985), with the complete description of the methodology presented in Bertineri *et al.* (1988). A more recent and complete review of the sequences technique is presented in Di Rienzo *et al.* (2001). The sequences technique is based on a regression analysis over the SBP and RR values occurring during short segments called "baroreflex sequences" (BSs). These segments consist of SBP and RR values characterized by simultaneous and consecutive decreases (or increases) of amplitude. Following studies confirmed these spontaneous SBP increases and decreases to elicit baroreflex mediated RR responses, due to the similarity of the baroreflex responses measured in such segments to the baroreflex responses provoked experimentally by drug injections (Fritsch *et al.*, 1986; Parlow *et al.*, 1995).

Improvements on time domain BRS assessment have been proposed with the Dual sequence method (Malberg *et al.*, 2002), the "xBRS" estimate (Westerhof *et al.*, 2004) and the events technique (Gouveia *et al.*, 2009).

Method	**Brief description**
Time domain	
Sequences technique Di Rienzo *et al.* (1985) Bertineri *et al.* (1988)	BRS as the average of the slopes between SBP and RR values in each identified baroreflex sequence, considering SBP with one beat lag with respect to RR.
Dual sequence method Malberg *et al.* (2002)	Equivalent to the sequences technique, allowing the identification of baroreflex sequences considering the SBP and RR with a shift up to 3 beats.
xBRS Westerhof *et al.* (2004)	BRS as the slope between the SBP and RR values over 10 sec windows, choosing the shift (up to 5 beats) that maximizes the SBP and RR cross–correlation. SBP and RR series resampled at 1 Hz.
Events technique In this work Gouveia *et al.* (2009)	BRS as one global slope between the SBP and RR values in all identified baroreflex events, considering SBP with one beat lag with respect to RR.
Frequency domain	
Transfer Function Robbe *et al.* (1987)	BRS as the mean value of the transfer function magnitude between SBP and RR in the LF frequency band.
Alpha Technique Pagani *et al.* (1988)	BRS as square root of ratio between RR and SBP powers in the LF frequency band.
Model based	
Closed-loop Bivariate Barbieri and Saul (1999)	Quantification of the feedback/feedforward SBP and RR pathways, assuming a closed-loop SBP and RR system.
Closed-loop Trivariate Barbieri *et al.* (1997)	Quantification of the feedback/feedforward SBP and RR pathways, considering two-way pathways between SBP, RR and RESP.
xAR Porta *et al.* (2000)	Quantification of the feedback/feedforward SBP and RR pathways, considering RESP as an exogenous input in the SBP and RR loop.
Causal analysis Nollo *et al.* (2001)	Quantification of the BRS assuming an exogenous input model, able to separate the RR variability into SBP related and unrelated parts.
Others	
TRS method Rüdiger *et al.* (1999)	Quantification of the open-loop SBP and RR interactions using trigonometric regressive spectral analysis instead of Fourier analysis.
Complex Demodulation Orr and Hoffman (1974) Kim and Euler (1997)	BRS as the ratio between SBP and RR amplitude oscillations estimated by complex demodulation.
Z-analysis Ducher *et al.* (1994) Cerutti *et al.* (1995)	Statistical evaluation of the relationship between SBP and RR based on the calculation of the Z-coefficient.

Table 1.1: Overview of methods for spontaneous BRS assessment, with brief description and indication of comprehensive references with further details of the methods. Table adapted and completed from Di Rienzo *et al.* (2001).

The Dual sequence method is an extension of the sequences technique, by allowing an SBP and RR shift up to 3 beats to identify baroreflex sequences. Because the SBP and RR series are studied in synchronous and shifted modes, this method also considers the delayed baroreflex effects for the BRS estimation.

The xBRS method is more recent than the sequences technique, and is commercially available with the Portapres and Finometer systems (Finapres Medical Systems BV, Holland) for ECG and ABP acquisition. To obtain the xBRS estimate, the regression is performed over 10 sec windows of the SBP and RR series resampled at 1 Hz, considering the delay between the SBP and RR that maximizes their cross–correlation (up to 5 sec). The BRS estimates are accepted if positive valued and statistically significant ($p \leq 0.01$). Finally, the BRS estimate from an entire recording is obtained by geometric averaging of the local estimates. As pointed out in Parati *et al.* (2004), this method provides a higher number of local estimates than the sequences technique because it allows a non-constant SBP–RR delay. However, as the BRS is estimated in relatively long time windows, different effects such as arterial baroreceptor stimulation and deactivation can occur and cannot be separated.

The events technique, the contribution in this thesis, provides a time domain BRS estimate as a global slope computed from the SBP and the RR values in all identified "baroreflex events" (BEs), i.e. segments of high SBP and RR correlation. The use of BEs is introduced as an alternative to BSs, to improve time domain BRS assessment, allowing its quantification in cases of BS absence. Also, global slope estimators combined with BEs are proposed to increase robustness, to increase reproducibility and to decrease dispersion in the BRS estimation. The xBRS method and the events technique provide a time domain BRS estimate that is based on the analysis of data identified by only imposing a criterion based on the SBP and RR correlation. However, the xBRS method is constrained to the analysis of 10 sec segments, while the events technique is based on the analysis of variable length BEs segments.

BRS is also currently estimated from the joint frequency-domain analysis of SBP and RR spontaneous variability, either by Transfer function method or the Alpha technique. The frequency domain methods allow to distinguish baroreflex effects of different frequencies: high frequencies (HF: 0.15–0.4 Hz) are more associated with parasympathetic ANS effects and respiration, if the respiratory frequency remains within the normal limits, whereas low frequencies (LF: 0.04–0.15 Hz) are more associated with sympathetic ANS effects (van de Borne *et al.*, 1997). The Transfer Function method is based on the modulus (or gain) of the transfer function between the SBP and RR series, considering the SBP as the input and the RR as the output of the system, and the BRS estimate is taken as the average of the transfer function values, considering the frequency values in which the SBP and RR series are coupled (expressed by the *squared coherence magnitude* function). A simplified approach to compute a frequency BRS estimate has been proposed by the Alpha Technique (Pagani *et al.*, 1988), by calculating the square root of the ratio between the RR and SBP spectral powers and, thus, only making use of the RR and SBP spectra and avoiding the estimation of the transfer function between SBP and RR. Previous comparisons between frequency BRS methods have pointed out that the Transfer Function method provides lower BRS estimates in comparison with the Alpha Technique, and the BRS estimates obtained by the two methods exhibit greater differences when computed for frequencies presenting lower levels of coherence (Barbieri and Saul, 1999).

Frequency domain BRS methods were first based on non parametric estimation of SBP and RR spectra and cross-spectra, assuming SBP and RR in an open-loop system (Robbe *et al.*, 1987). Therefore, these techniques cannot distinguish between negative and positive feedback interactions or causality between the effects, and cannot account for other influences, e.g., respiration. Extensions of the frequency domain methods assume a closed-loop system, with the SBP and RR relationships parameterized to distinguish the BRS (feedback) from the RR to SBP feedforward pathways. The closed-loop analysis is based on the identification of the model coefficients (e.g. AR or ARMA) and the BRS is then estimated either by the Transfer Function method or by the Alpha technique. The inclusion of respiration (RESP) can also be considered in the closed-loop SBP and RR relation, either assuming feedback/feedforward pathways between RESP and SBP and RESP and RR (Barbieri *et al.*, 1997) or assuming RESP as an exogenous signal (Porta *et al.*, 2000). Finally, the causal SBP and RR dependence has been studied with a model with exogenous input, able to separate the RR variability into SBP related and unrelated parts (Nollo *et al.*, 2001).

Both time and frequency domain methods have been evaluated in sinoaortic denervated conscious cats. Regarding the sequences technique, the BSs appeared to reflect the baroreflex mechanisms as their number (and mean slope) was drastically reduced after denervation (Bertineri *et al.*, 1988). Regarding the frequency domain analysis, denervation increased overall SBP variability and reduced RR variability (Mancia *et al.*, 1999). Also, it was reported that the frequency domain method specifically reflects baroreflex modulation of the RR in the region around 0.1 Hz only, due to the decreased spectral coherence observed only in this frequency band after denervation.

1.4 Objectives and Outline of the Thesis

The first extensively described methods for assessing the BRS were invasive methods involving bolus intravenous injections of phenylephrine or nitroprusside, namely the Oxford technique (Smyth *et al.*, 1969) and the Modified Oxford technique (Ebert and Cowley Jr, 1992; Parlow *et al.*, 1995). Nowadays, the possibility of assess ANS function using spontaneous methods, turns the BRS assessment into a non-invasive test, more convenient and more widely applicable. Previous comparisons between drug induced and spontaneous BRS estimates evidence that they are correlated (Davies *et al.*, 1999) and, therefore, spontaneous BRS estimates can potentially have the same predictive power as the invasive ones.

Several non-invasive methods have been proposed for BRS assessment, including time domain and frequency domain methods. Among these, the **sequences technique** is a frequently used time domain method for spontaneous BRS estimation, thanks to its ease of implementation (Di Rienzo *et al.*, 2001). This method is based on the identification of baroreflex sequences (BSs) and linear regression over the corresponding SBP and RR values. An overall estimate is obtained by averaging the slope estimates from all BSs identified in a record.

In spite of its simplicity, this technique sometimes fails to provide an estimate for low BRS patients, depending of the parameters used. As a result, this method is considered by some authors to have limited value for the BRS evaluation/quantification in ANS dysfunction cases, which are crucial to identify (Oka *et al.*, 2003). Therefore, critical reviews of the existing methods and performance improvements that preserve simplicity are well-justified.

Given the popularity of the sequences technique among the spontaneous methods for BRS assessment, it is surprising that few methodological studies have been reported. The major part of these studies is simply comparative. For example, the spontaneous and drug-induced BRS analysis are reported to provide different estimates, but those differences can be either due to the use of different experimental protocols or due to the use of different BRS estimators. This fact demands a better comparison between the different BRS estimators and the different protocols, in order to assess the limitations of the BRS estimators as well as the limitations of the measured data as representative of the BRS function.

The **main purpose of this work** is the improvement of time domain methods for spontaneous BRS assessment and to contribute to their validation as reliable methods to assess the autonomic reflex function. In particular, this work aims at establishing more accurate BRS methods, offering a higher ability to provide a reliable BRS estimate in ANS dysfunction cases. The aspects evaluated in this study include the ability of the methods to provide a BRS estimate and to discriminate conditions in which the BRS is expected to be modified. Also, the study of reproducibility and of dispersion in the BRS estimation is used to compare the methods. An important objective of the thesis is the validation of the improved methods and to further explore the BRS dependencies with respect to respiration and sympathetic/parasympathetic ANS effects. This validation is carried out from the comparison of the improved estimators with time domain BRS estimators developed for the analysis of drug-induced data and frequency domain estimators developed for the analysis of spontaneous data, both conventionally more accepted to distinguish the respiratory and the sympathetic/parasympathetic ANS effects.

1.4.1 Thesis synopsis

The introduction and the motivation for this work is presented in **Chapter 1**. The functional aspects of the cardiovascular system are reviewed. In particular, the role of the ANS and the baroreceptors reflex in the regulation of the cardiovascular variables is described, as well as the mechanisms of respiration and parasympathetic/sympathetic ANS effects. A brief introduction to cardiovascular signals is presented, including their physiological interpretation. This chapter also comprises the description of the steps carried out for the evaluation of the baroreflex sensitivity (BRS). In particular, the setup for the acquisition of the signals is described, as well as the extraction of the beat-to-beat variability series from the acquired signals. Finally, a short review of existing methods for BRS estimation is presented, with focus on "spontaneous methods".

Chapter 2 describes the automatic system developed to extract the representative beat-to-beat variability from the cardiovascular signals, the first step to perform the BRS quantification and explore the BRS dependencies. The performance of the methods is illustrated with experimental data.

The improvement and validation of the time domain methods for spontaneous BRS assessment is the central contribution of this thesis, being extensively explored in **Chapter 3**. The limitations of the traditional time domain BRS analysis are discussed and the improved BRS analysis is presented and justified. Finally, the traditional and improved BRS analyses are compared in spontaneous data.

Chapters 4 and 5 are dedicated to the validation of the improved methods and to further explore BRS dependencies with respect to respiration and sympathetic activity. In **Chapter 4**, BRS estimators are compared in drug-induced data, obtained by an experimental protocol involving the drug-stimulation of the sympathetic and parasympathetic ANS activity. In **Chapter 5**, the BRS methods are further compared with respect to respiration and sympathetic activity. In particular, the improved time domain BRS estimation is compared with frequency domain methods, more conventionally accepted to distinguish the respiratory and the sympathetic/parasympathetic ANS effects. Finally, **Chapter 6** summarizes the results and presents the most important conclusions of this work.

The characteristics of the datasets used in this work are summarized in Table 1.2 and are further described in the corresponding Chapters/Sections of the thesis.

Table 1.2: Description of the datasets used in this thesis.

Dataset	**# files**	**Signals**	**Ref**
EuroBaVar	46: 23 Lying, 23 Standing	ECG, ABP	Laude *et al.* (2004)
SP/NT/PH	30: 15 Spont, 15 Invasive	ECG, ABP, RESP, MSNA	Gujic *et al.* (2007)

The **EuroBaVar** dataset consists of 46 spontaneous recordings acquired from 23 subjects in Lying and Standing positions. This dataset is available on the internet for the comparison of BRS estimation procedures and, in this thesis, it was used to compare the BRS methods in spontaneous conditions (Chapter 3 and 5).

The **SP/NT/PH** dataset consists of paired spontaneous and drug-induced recordings and it was used for the comparison between spontaneous and invasive BRS analysis, described in Chapter 4. The spontaneous recordings of the SP/NT/PH dataset were also used, together with the RESP and MSNA signals, to further explore the BRS dependencies with respiration and sympathetic activity in Chapter 5.

Additionally, one recording from the **Bisoprolol** dataset was used to illustrate the performance of the automatic MSNA burst detector described in Sec. 2.3.2. This recording consists of the simultanenous acquisition of ECG, ABP, RESP and MSNA signal, after one week of bisoprolol treatment (Beloka *et al.*, 2009). This recording includes manual annotations of the localization of the MSNA bursts (Beloka *et al.*, 2009).

The drug induced experiments were carried out in the Erasme University Hospital, Brussels, Belgium, in the scope of a protocol approved by the Ethics Committee of hospital and with written consent of the participants.

Chapter 2

Series of beat-to-beat variability

The first step for BRS estimation is the detection of the ABP and the ECG heartbeat reference marks, to compute the SBP and RR series. For that purpose, a multimodal beat detector is presented in this chapter. This system is based on independent ABP and ECG analysis with subsequent fusion of the results, and makes use of a wavelet based ECG beat detector, previously evaluated by our group (Martínez *et al.*, 2004). The performance of the system is illustrated with real data.

In this thesis, the BRS analysis was also studied with respect to the respiration (RESP) and sympathetic activity. In this chapter, the methods used to automatically extract measures from the RESP and MSNA signals are described. With respect to respiration, the BRS analysis will be associated with the respiratory frequency of the subject. The BRS estimates will also be associated with measures of sympathetic activity, measured with the muscle sympathetic nerve activity – MSNA signal. The quantification of ANS sympathetic activity is based on burst countings and computation of bursts area, which imply prior identification of the MSNA bursts. The performance of the methods is illustrated with experimental data.

2.1 Reference marks and series of variability

The localization of a heartbeat is identified by a reference mark, usually chosen as the time of the most prominent feature of the ECG and ABP signals occurring during the cardiac cycle. As illustrated in Fig. 2.1, the time of the maximum QRS amplitude, denoted by $t_{\mathrm{QRS}}(n)$, is the mark considered to localize the n^{th} heartbeat in the ECG signal. Similarly, the time of the SBP value, denoted by $t_{\mathrm{SBP}}(n)$, is the mark referencing the heartbeat in the ABP signal. The series of values expressing the beat-to-beat variability of the cardiovascular signals are then obtained from these reference marks. Figure 2.1 also illustrates that the RESP and MSNA signals do not exhibit variability on a beat-to-beat basis. Therefore, the beat-to-beat RESP and MSNA series are extracted with the use of the heartbeat reference marks previously identified in the ECG and/or ABP signals.

This procedure allows to obtain variability series from the acquired ECG, ABP, RESP and MSNA signals, which are synchronous with each other on a beat-to-beat basis.

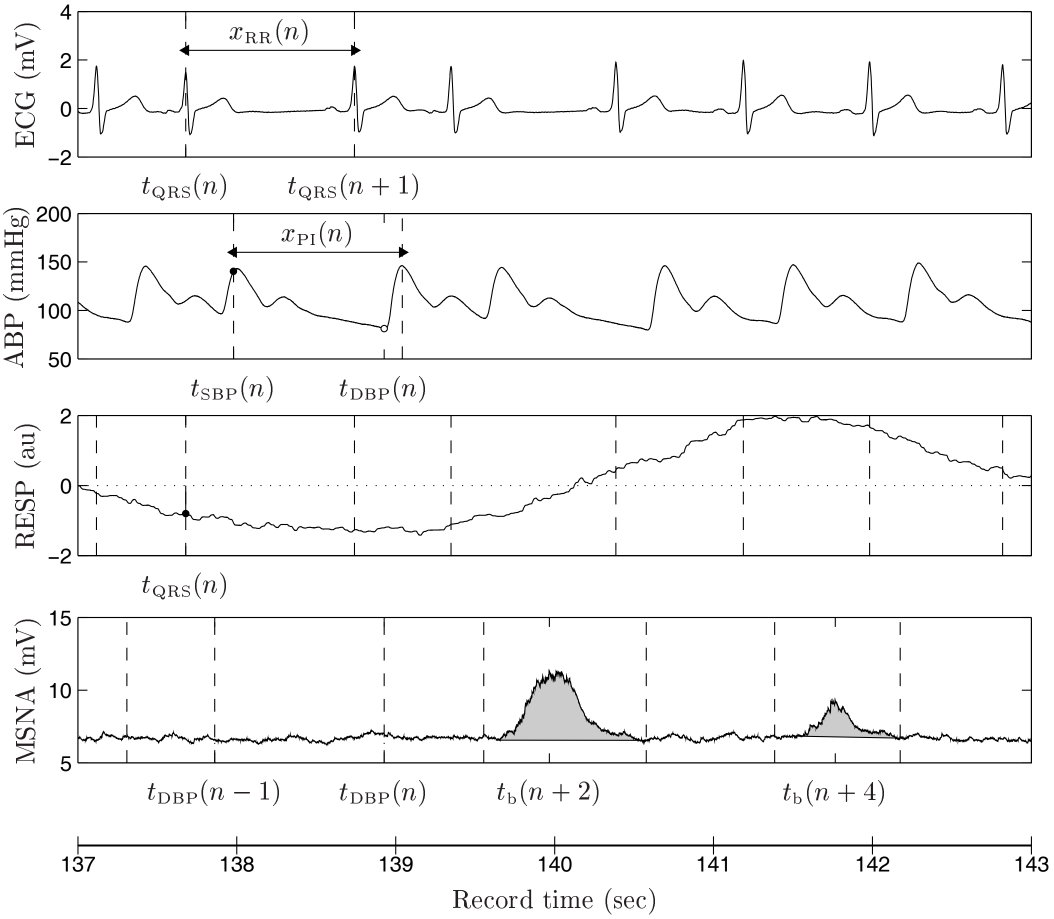

Figure 2.1: Reference marks in the ECG, ABP, RESP and MSNA signals, associated with the n^{th} heartbeat. Data showing a long RR interval and evidencing the ECG, ABP and MSNA phase dependencies. Notation in accordance with Pagani *et al.* (1997).

For an adequate cross-analysis of the variability series, it is crucial to reproduce in the series the phase relationships that the cardiovascular signals exhibit. These dependencies are evident in Fig. 2.1, with the longer interval between two QRS complexes in the ECG and following longer interval between two systolic ABP peaks. This is accompanied by a lower amplitude diastolic ABP value, what triggers a MSNA burst that contributes for the ABP to return to its normal levels. The notation adopted in this work, and presented in Fig. 2.1, follows the expected physiology (Mancia and Mark, 1983) and is in accordance with the studies of Pagani *et al.* (1997), van de Borne *et al.* (1997) and Baselli *et al.* (1988)[1].

In this work, the ECG, ABP, RESP and MSNA denote sampled signals, i.e., signals function of a discrete time $t_{i+1} = t_i + \Delta_t$, $i > 0$ with $\Delta_t = F_s^{-1}$ and F_s their sampling frequency. Accordingly, t_{E} refers the time of the occurrence of E, e.g., t_{QRS} denoting the time of the occurrence of a QRS complex in the ECG signal.

Figure 2.1 illustrates how the variability series are obtained from the heartbeat reference marks identified in a recording. The **tachogram** $x_{\mathrm{RR}}(n)$ is obtained after beat detection in the ECG signal, as the series of successive time duration between two consecutive QRS complexes, i.e.,

$$x_{\mathrm{RR}}(n) = t_{\mathrm{QRS}}(n+1) - t_{\mathrm{QRS}}(n), \tag{2.1}$$

with $t_{\mathrm{QRS}}(n)$ denoting the time of the occurrence of the n^{th} QRS complex in the ECG signal.

The **systogram** $x_{\mathrm{SBP}}(n)$ is the series of the successive systolic/maximum ABP values. Each $x_{\mathrm{SBP}}(n)$ value can be obtained as the maximum ABP value after its corresponding QRS complex and delimitated by the current heart beat interval, i.e.,

$$x_{\mathrm{SBP}}(n) = max \text{ ABP(t) for } t \in [t_{\mathrm{QRS}}(n), t_{\mathrm{QRS}}(n+1)]. \tag{2.2}$$

The **diastogram** $x_{\mathrm{DBP}}(n)$ is the series of successive diastolic/minimum ABP values. Each $x_{\mathrm{DBP}}(n)$ value can be obtained as the global minimum ABP value in between each consecutive occurrences of the SBP values $t_{\mathrm{SBP}}(n)$ and $t_{\mathrm{SBP}}(n+1)$, i.e.,

$$x_{\mathrm{DBP}}(n) = min \text{ ABP(t) for } t \in [t_{\mathrm{SBP}}(n), t_{\mathrm{SBP}}(n+1)]. \tag{2.3}$$

In this work, additional series of interest are obtained from the ECG and/or the ABP signal, in particular, the $x_{\mathrm{PI}}(n)$, $x_{\mathrm{PF}}(n)$ and $x_{\mathrm{PTT}}(n)$ series, defined as follows.

The **Pulse Interval** series $x_{\mathrm{PI}}(n)$ is defined as the series of time duration between two

---

[1] Other notations were proposed in the literature. As an example, with respect to the notation in the figure, deBoer *et al.* (1987) denotes $x_{\mathrm{SBP}}(n)$ and $x_{\mathrm{DBP}}(n+1)$, Korhonen *et al.* (1996) denotes $x_{\mathrm{SBP}}(n-1)$ and $x_{\mathrm{DBP}}(n)$ and Almeida *et al.* (2006) considers $x_{\mathrm{RR}}(n+1)$.

consecutive SBP values in the ABP signal, i.e.,

$$x_{\mathrm{PI}}(n) = t_{\mathrm{SBP}}(n+1) - t_{\mathrm{SBP}}(n) \tag{2.4}$$

and it constitutes a *surrogate* series of the $x_{\mathrm{RR}}(n)$ extracted from the ECG signal.

The **Pulse Fluctuation** series $x_{\mathrm{PF}}(n)$ is defined as

$$x_{\mathrm{PF}}(n) = x_{\mathrm{SBP}}(n) - x_{\mathrm{DBP}}(n-1) \tag{2.5}$$

and it represents the beat-to-beat ABP amplitude range.

Finally, the **Pulse Transit Time** series $x_{\mathrm{PPT}}(n)$ represents the time taken for the pulse wave to travel from the aortic valve to the periphery (Smith *et al.*, 1999). Due to the ease of measurement, $x_{\mathrm{PPT}}(n)$ is usually approximated by the time duration between the R wave of the ECG and the corresponding systolic peak in the ABP signal[2], i.e.,

$$x_{\mathrm{PPT}}(n) \approx t_{\mathrm{SBP}}(n) - t_{\mathrm{QRS}}(n). \tag{2.6}$$

In this work, a multimodal system is used for the detection of the heartbeat reference marks in the ECG and ABP signals, taking advantage of the redundancy presented in the ECG and ABP signals (e.g., the fact that $x_{\mathrm{RR}}(n)$ and $x_{\mathrm{PI}}(n)$ series provide similar information on the heart function). The system makes use of a method developed for QRS detection in the ECG signal, previously implemented and validated by our group (Martínez *et al.*, 2004). The overall multimodal system is described in Sec. 2.2.

Because the RESP signal does not exhibit variability on a beat-to-beat basis, it is usually analyzed with the use of the heartbeat reference mark $t_{\mathrm{QRS}}(n)$, identified in the ECG signal. The **respirogram** $x_{\mathrm{RESP}}(n)$ is obtained by sampling the RESP signal at the time of the occurrence of a QRS complex in the ECG signal, i.e.,

$$x_{\mathrm{RESP}}(n) = \mathrm{RESP}\left(t_{\mathrm{QRS}}(n)\right). \tag{2.7}$$

As previously referred, respiration is reflected by the breathing phase (inspiration and expiration), but also by the respiratory frequency. Section 2.3.1 details the methods to estimate the respiratory frequency from the $x_{\mathrm{RESP}}(n)$ series.

---

[2] By definition, $x_{\mathrm{PPT}}(n)$ should be measured from a plethysmograph signal collected with the finger-cuff (periphery), before the correction of the distortion in the finger pressure relative to brachial artery pressure (see Sec. 1.3.1). In this work, the $x_{\mathrm{PPT}}(n)$ interval is approximated with the ABP wave after correction, with no consequences for the purpose that it is used. Some authors consider a more robust $x_{\mathrm{PPT}}(n)$ estimation, as the distance from $t_{\mathrm{QRS}}(n)$ to the time that the ABP amplitude reaches a fraction of the $x_{\mathrm{PF}}(n)$ value, instead of $t_{\mathrm{SBP}}(n)$. This definition avoids the introduction of spurious variability in the $x_{\mathrm{PPT}}(n)$ series due to the inherent variability of the peak localization in a flat wave (Foo and Lim, 2006).

The MSNA signal is composed by a succession of bursts, which might occur on a beat-to-beat basis: in a condition of increased sympathetic activity it is expected a larger number of bursts, with occurrence of up to 100 bursts per 100 cardiac beats (Wallin, 2007). A higher sympathetic activity can also evidenced by higher burst area (Halliwill, 2000). This is why the beat-to-beat series of sympathetic activity, the neurogram $x_{\text{MSNA}}(n)$, is obtained by numerical integration of the MSNA signal in the time window corresponding to a cardiac beat. The MSNA signal is usually integrated between two DBP values because this interval contains one existing MSNA burst (Halliwill, 2000) and also because sympathetic activity correlates closely with diastolic but not with systolic pressure (Sundlöf and Wallin, 1978).

The amplitude of the MSNA signal is not calibrated and not restricted to be positive, which might have effects in the computation of the MSNA area. Therefore, in this work, the **neurogram** $x_{\text{MSNA}}(n)$ is computed as

$$x_{\text{MSNA}}(n) = \frac{1}{T_I} \int_I \mathcal{M}_{\text{C}}(t)dt, \tag{2.8}$$

where T_I is the width of the MSNA integration interval $I = [t_{\text{DBP}}(n-1), t_{\text{DBP}}(n)]$ and $\mathcal{M}_{\text{C}}$ is a baseline corrected signal obtained from the acquired MSNA signal, as described in Sec. 2.3.2.

Interval MSNA measures able to account for increases/decreases of sympathetic activity in a recording are also considered (Table 2.1). These measures are based on burst countings and burst area calculation. For the computation of such measures, the MSNA bursts have to be identified and the reference mark for the MSNA burst was taken as the time of the burst peak $t_{\text{b}}(n)$. To allow the use of the index n, associated with the n^{th} heartbeat, the notation $t_{\text{b}}(n) = 0$ was adopted to denote the absence of a MSNA burst in the n^{th} beat.

The method developed for MSNA processing is presented in Sec. 2.3.2. The MSNA signal is first subjected to noise reduction: in this step, $\mathcal{M}_{\text{C}}$ is obtained after baseline correction and background noise reduction from the acquired MSNA signal. The $\mathcal{M}_{\text{C}}$ signal is then used to automatically identify the MSNA bursts and to compute the $x_{\text{MSNA}}(n)$ series. The performance of the methods is illustrated with experimental data including manual burst annotations, in this thesis, referred as *bisoprolol* recordings (Beloka *et al.*, 2009).

2.2 Multimodal system to identify ECG/ABP reference marks

QRS detection is a well-studied problem and several methodologies have been proposed since the 80s (Köhler *et al.*, 2002; Sörnmo and Laguna, 2005). The continuous improvement of signal processing techniques together with the advancement of signal acquisition technology and the growth of computer resources have allowed the development of QRS detection methodologies not only to become more efficient/effective but also more robust to noise sources of physiological and nonphysiological origin.

Although many beat detection algorithms have been developed for ECG signals, there are only a few proposed for ABP (Kinias *et al.*, 1981; Antonelli *et al.*, 1994*a*,*b*; Karamanoglu, 1997; Navakatikyan *et al.*, 2002; Aboy *et al.*, 2005). This is one of the reasons why the ABP beat-to-beat information is usually obtained either manually or after performing QRS detection in the ECG signal (Pagani *et al.*, 1997). Specifically, the QRS complex is first identified and then the maximum and minimum ABP values are evaluated in the time interval between two consecutive QRS complexes. Obviously, these approaches for ABP processing are highly dependent on the accuracy of the ECG processing stage.

For the purpose of BRS assessment, the development of an ABP beat detector independent of the ECG is well-justified, because it is possible to extract from the ABP signal the two required series to accomplish it. However, in the cases that the ECG is acquired together with the ABP, a more robust beat detection can be achieved if the ECG and ABP information is combined. As is illustrated in Fig. 2.1, the ECG and ABP signals show variability on a beat-to-beat basis. Consequently, the $x_{\mathrm{RR}}(n)$ series obtained from the ECG has surrogate series that can be obtained from the ABP, e.g., the $x_{\mathrm{PI}}(n)$ series obtained as the time difference between two consecutive systolic values. These series provide redundant but independent measures of the heart rate. Therefore, parallel analysis of the ECG and ABP signal with following fusion of the results allows a more robust beat detection, taking advantage of the multimodal acquisition usually carried out for the BRS analysis. As a matter of fact, in intensive care monitoring, the use of ECG and ABP relationships have already been proposed for the reduction of ABP false alarms (Zong *et al.*, 2004) and the independent analysis of multilead ECGs and an invasive ABP waveform has been recently proposed for robust heart rate estimation (Li *et al.*, 2008).

The fusion of the results obtained from independent ECG and ABP analysis is expected to minimize the effects of the noise sources. This is because the noise likely to occur in the ECG and ABP signals are typically uncorrelated, mainly due to the different technical principles underlying the signals acquisition. For example, it is expected that the ECG signal, measuring the electrical activity of the heart at the skin level, is more susceptible to electrical activity of other origin rather than of the heart, such as electrical activity of skeletal muscles during periods of contraction (electromyographic – EMG noise) and powerline interference[3]. The methods for QRS detection are typically based on the analysis of the bandpass filtered ECG. Such filtering enhances the QRS complex while attenuating the P and T waves as well as certain types of noise and artifacts. These methods are naturally more susceptible to noise with frequency range overlapping with that of the QRS complex, such as EMG

---

[3] Other examples of contaminated ECG records can be found in Pahlm and Sörnmo (1984), including artifacts of physiological and of technical origin, such as beat-to-beat changes in QRS morphology, occurrence of ventricular extrasystoles, drastic changes in QRS amplitude due to technical problems and situations where P and T waves can be misinterpreted as QRS complexes.

noise[4] and electrode motion artifacts. Figure 2.2(a) shows an excerpt of an ECG signal corrupted with noise of muscular origin and the corresponding ABP signal, evidencing that with independent systems for ECG and ABP processing, the ABP processing errors due to errors in ECG processing can be avoided and that beat detection can be enhanced.

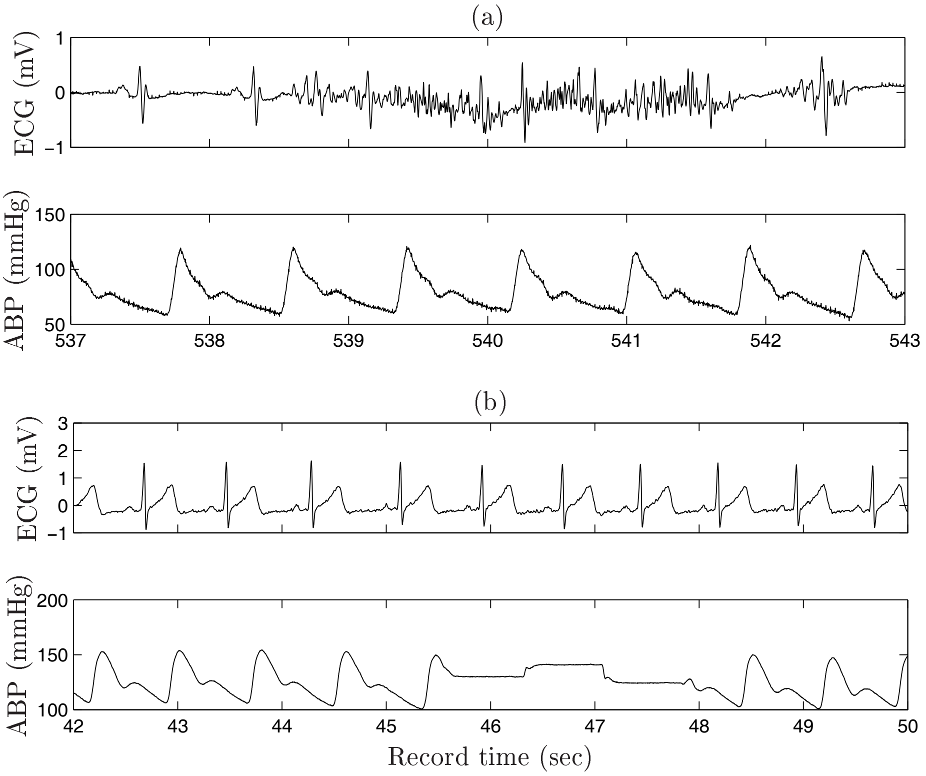

Figure 2.2: ECG and ABP signals with (a) EMG noise contamination in the ECG and (b) ABP signal lost due to automatic calibration of the acquisition device. The excerpt in (a) is from the EuroBaVar file "B010LC" and in (b) is from the Bisoprolol dataset.

The effects of other types of ECG artifacts can be diminished with the independent ABP analysis and subsequent fusion of the results. At least, independent ABP analysis would avoid the repercussion of ECG detection errors in an ECG-dependent method for ABP analysis, allowing a more robust beat detection. Besides the EMG noise contamination, other noise sources in the ECG signal include movement artifacts, improper lead contact and improper lead connection, likely to occur in ambulatory recordings, sleep apnoea studies or intensive care unit monitoring.

---

[4] The frequency range of EMG noise and electrode motion artifacts considerably overlaps the QRS complex frequency range (Sörnmo and Laguna, 2005), what limits the utility of linear techniques for noise removal. Recent studies indicate that independent component analysis (ICA) and nonlinear filtering seem to offer some potential in removing EMG contamination from the ECG (He *et al.*, 2006) and removing the ECG contamination from the EMG signal (Liang *et al.*, 2005). Typical shapes of EMG spectrum depending on contraction levels can be found in Jones and Lago (1982). For moderate levels, a narrow peak can often be detected above the 15 Hz and often also at twice this frequency. With increasing contraction force, the frequency at which the peaks occur increases up to 40 Hz.

The noise sources influencing ABP signals are commonly mechanical, including improper cuff size or position, cuff compression and hand/cuff movement. The finger cuff technology for ABP acquisition is immune to muscular noise and powerline interference, although being as susceptible as the ECG to movement artifacts. For both the ECG and the ABP signals, motion artifacts constitute a problematic situation to deal with, because also in this case the noise spectral content overlaps that of the ECG/ABP information. However, it is less probable for the ECG and ABP signals to be simultaneously corrupted, even less with movement artifacts that have different origins: electrodes movements in the case of the ECG and finger cuff motion in the case of the ABP.

The difficult problems to deal with in ABP processing are motion artifacts and calibration episodes[5]. Figure 2.2(b) presents an ABP excerpt in a calibration episode, showing that the ABP signal is completely lost. If the calibration mode is switched on, the Finapres device interrupts the ABP measurement for a few seconds, approximately every 80 heart beats, in which the ABP signal appears to be a staircase signal with steps around the mean ABP value of the subject. In these cases, the correction can be resolved with the use of proper interpolation techniques (Keselbrener and Akselrod, 1995), if possible, keeping the total time-duration of the corrected signal equal to that of the original signal. Another approach to deal with this problem is to simply ignore/remove the unwanted parts of the ABP signal containing artifacts or other random-like physiological disturbances, as it is advised for the ECG signal (Task Force of ESC & NASPE, 1996).

In addition to a more robust beat detection, an independent system for ECG and ABP analysis is able to discard possible time delays between them due to the setup of the acquisition machines, if the time delay exceeds the length of one cardiac beat. This can be verified, e.g., from cross-correlation analysis of $x_{\mathrm{RR}}(n)$ and $x_{\mathrm{PI}}(n)$ series.

Multimodal system to detect reference points in ABP and ECG signals

Figure 2.3 outlines the multimodal system for automatic identification of beat-to-beat ECG and ABP reference marks. The ECG beat detection is performed by means of a wavelet based methodology previously proposed (Li *et al.*, 1995; Martínez *et al.*, 2004) and its main features are summarized in Sec. 2.2.1. The ABP beat detection developed in this work is detailed in Secs. 2.2.2 and 2.2.3. The ECG and ABP beat detection is followed by the time alignment of the QRS and SBP marks identified by the independent analyses, as described in Sec. 2.2.4. In this step, the time alignment of the QRS and SBP marks is carried out and possible misdetections are corrected.

---

[5] Examples of contaminated ABP records can be found in Moody and Mark (1996) and Zong *et al.* (2004). Other examples can be found in Navakatikyan *et al.* (2002), including irregular position of the systolic peak, arrhythmia and a large dicrotic peaks, chaotic ABP waveform with rapid changes of amplitude and interval.

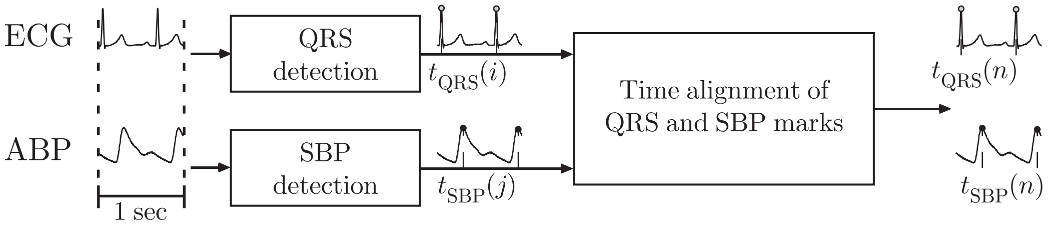

Figure 2.3: Block diagram schematizing the steps of the system developed to jointly detect reference points in the ECG and ABP signals. Indexes i and j denote the order numbers of the QRS and SBP marks obtained by the independent ECG and ABP beat detectors. Index n denotes the order number of the marks after time alignment of the QRS and SBP marks.

2.2.1 QRS detection in the ECG signal

The QRS detector used in this work is a part of the *Wavedet* system, a fully automatic system for ECG waves delineation based on wavelet analysis (Li *et al.*, 1995; Martínez *et al.*, 2004). This system has as a first step the identification of each QRS complex, taken as the reference for the location of the cardiac beat, for further delineation of the ECG waves, namely delimiting the onset/peak/end of each QRS complex, T and P waves, see Fig. 2.4. This system has been used, e.g., to extract the $x_{\mathrm{RR}}(n)$ and $x_{\mathrm{QT}}(n)$[6] series from the ECG in order to explore the interactions between their variabilities (Almeida *et al.*, 2006).

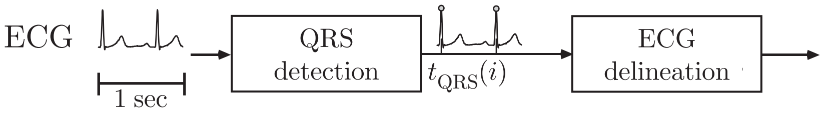

Figure 2.4: Block diagram displaying the two major steps of the Wavedet system for ECG waves detection/delineation.

The beat detector implemented in this system is a detector of singularities on wavelet transforms of the original signal, combined with posterior rules/conditions adjusted to the inherent characteristics of the ECG signal. These rules enhance the performance of the system, avoiding the detection of false positive/negative cardiac beats in this signal.

A prototype wavelet is a fast-decaying oscillating waveform Ψ, which is scaled in amplitude by a factor of $a \in \mathbb{R}^+$ and translated by a factor of $b \in \mathbb{R}$, in order to produce a wavelet $\Psi_{a,b}$ at the scale a and centred at time b (Mallat, 1999). A wavelet transform (WT) provides a description of a signal in the time-scale domain, allowing the representation of its temporal

---

[6] The $x_{\mathrm{QT}}(n)$ is the series of successive distances between the Q wave onset to the T wave offset (QT interval). It includes the total interval of ventricular depolarization and repolarization of the cardiac muscle.

features at different resolutions according to their frequency content. The discrete wavelet transform (DWT) is obtained by using discrete values for a and b. One of the most popular choices for these parameters follows a dyadic grid in the time-scale plane, by constraining the parameters values to $a = 2^m$ and $b = 2^m l$, with $m \in \mathbb{N}$ and $l \in \mathbb{Z}$.

As illustrated in Fig. 2.5, the shift parameter b adjusts the time resolution whereas the scale parameter a adjusts the WT frequency content: a larger value of a produces a wider wavelet and therefore the WT will contain the lower frequencies of the signal. Also, as is possible to observe from the tiling pattern, smaller scales decrease the time spread but increase the frequency support. Therefore, higher temporal resolution is achieved at high frequencies whereas higher frequency resolution is achieved at low frequencies.

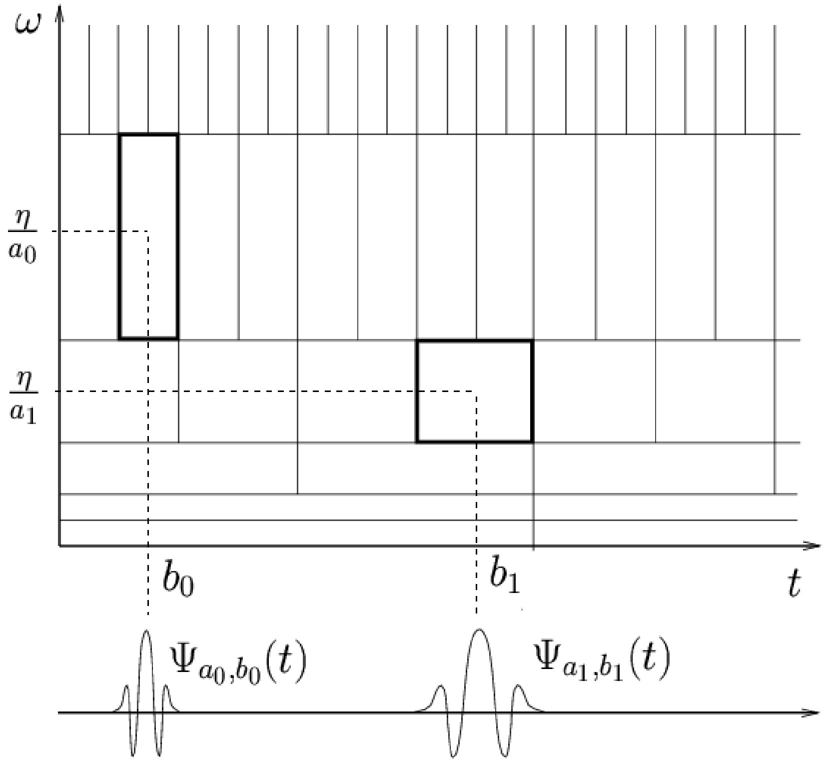

Figure 2.5: Time-frequency boxes of a wavelet, defining the resolution tiling of the time-frequency plane (t and ω axis, respectively). The variable η represents the fundamental/central frequency of Ψ. Adapted from Mallat (1999).

The prototype wavelet used in the Wavedet system corresponds to the derivative of the convolution of four rectangular pulses, i.e., a lowpass differentiator filter (Li *et al.*, 1995; Martínez *et al.*, 2004). In the first step/scale, the signal is decomposed into *approximation* and *detail*, which include the low and the high frequency content of the input signal, respectively. In the next scale, only the *approximation* is considered to be once more decomposed into its *approximation* and *detail*. This procedure is repeated m times to achieve the $a = 2^m$ scale. For its practical use, the dyadic DWT is implemented as a cascade of FIR filters with varying cutoff frequencies (Mallat, 1999), presenting a shorter bandwidth (approximately half of the previous) and a lower central frequency for increasing WT scales (Fig. 2.6(b)).

Figure 2.6 presents the power spectral density of the main ECG waves and the DWT equivalent frequency responses at the various scales. It can be observed that most of the ECG power goes up to 50 Hz, the QRS complex energy extends to a frequency of 40 Hz and the smoother P and T waves have most of their power only up to 10 Hz (Fig. 2.6(a)). Also, most of the ECG energy lies within scales 2^1 to 2^5, with the QRS complex being more visible in scales 2^1 to 2^4, whereas the P and T waves are more perceptible in scales 2^4 and 2^5 (Fig. 2.6(b)). Therefore, the identification of the QRS complex is carried out across the scales that maximize its power, avoiding artifacts and other ECG waves that can lead to misdetections. Finally, it is worthwhile to refer that the DWT equivalent frequency responses represented in Fig. 2.6 were obtained assuming a sampling frequency of the signal $F_s = 250$ Hz. For other F_s values, the coefficients of the new set of filters are obtained by resampling adequately the equivalent filter impulse responses at $F_s = 250$ Hz (Martínez *et al.*, 2004).

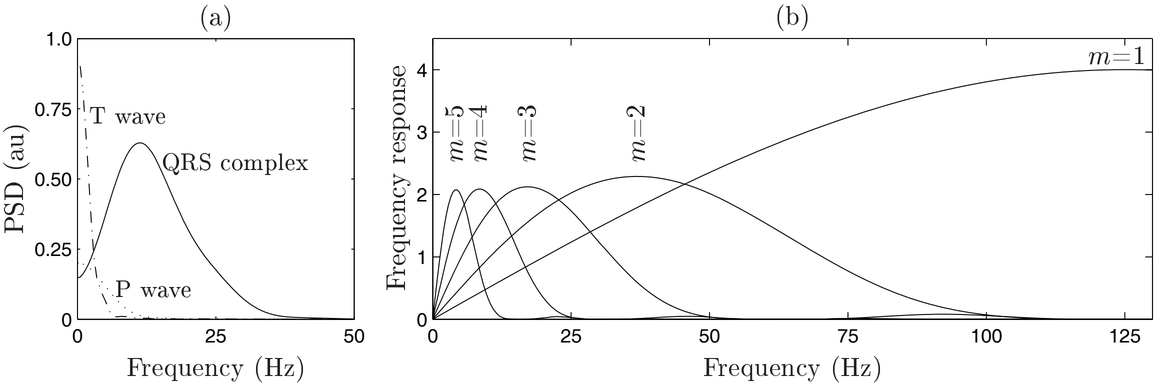

Figure 2.6: (a) Indicative power spectral density (PSD) of the main ECG waves. Reproduced from Sörnmo and Laguna (2005). (b) DWT equivalent frequency responses at scales $a = 2^m$, $m \leq 5$ for $F_s = 250$ Hz. Reproduced from Martínez *et al.* (2004).

Figure 2.7 shows simulated waves, similar to those in the ECG signal, together with the corresponding first five DWT scales. It can be observed that the WT at the scale a is proportional to the derivative of the filtered signal with the smoothing impulse response at scale a (Mallat and Zhong, 1992). In this way, signal peaks correspond to WT zero crossings, whereas maximum/minimum slopes correspond to WT maximum/minimum values.

As illustrated in Figs. 2.7(e–f), the QRS complex is characterized by a pair of values with opposite polarity and largest amplitude. The fiducial mark of each QRS complex (or any other ECG wave) is determined as the zero crossing between these WT paired values, evaluated at scale 2^1, which is the WT scale that presents better temporal resolution (see Fig. 2.5).

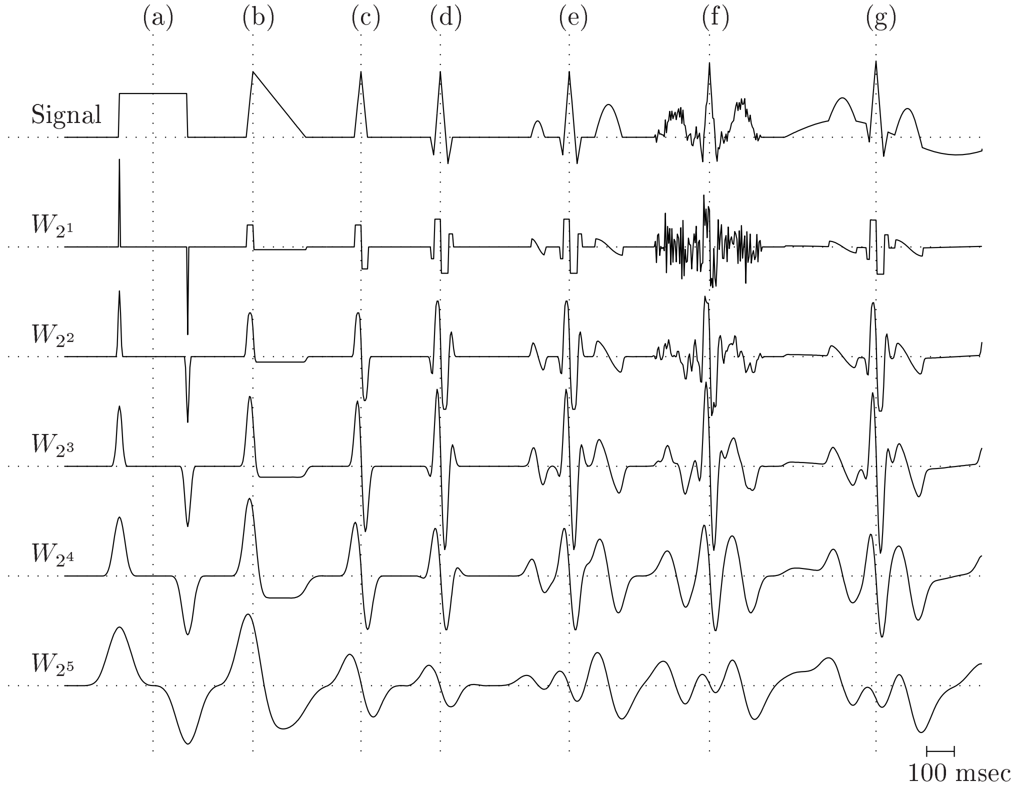

Figure 2.7: WT scales of simulated shapes (a–d) and ECG beats (e–g), showing the correspondence between the characteristic points of the simulated waves and those of their W_{2^m}, $m \leq 5$ scales. Shapes: (a) squared, (b) asymmetric, (c) symmetric and (d) QRS like; ECG beats: (e) clean, (f) with HF noise and (g) with baseline wandering. Adapted from Martínez *et al.* (2004).

All details of the QRS detection methodology and its evaluation can be found in Li *et al.* (1995) and Martínez *et al.* (2004). The signal is processed in windows of 2^{16} samples, following the generic steps after the WT computation:

1. *Identify candidate peaks* by searching across the WT scales 2^1 to 2^4 for maximum modulus peaks exceeding a constant threshold;

2. *Identify significant peaks*, i.e., 2 or more peaks presented in all scales (starting from 2^4 and moving to 2^1 to save computational time), that satisfy an apriori defined time neighbourhood;

3. *Remove isolated peaks* in 2^1 scale, i.e., peaks with distance[7] to its closest neighbour longer than 150 msec;

4. *Remove redundant peaks*, keeping the pairs of peaks with different polarity that satisfy apriori defined amplitude and time distance thresholds;

---

[7] The 150 msec value corresponds to the maximum QRS complex width (Hamilton and Tompkins, 1986).

5. *Search for the fiducial mark of the QRS complex* in 2^1 scale, as the zero crossing between each pair of significant peaks;
6. *Remove false positives*, if the distance[8] between 2 consecutive fiducial marks is shorter than the refractory period of 275 msec. This rule excludes prominent T waves detected shortly after a QRS complex;
7. *Correct false negatives.* If there was no detection during the time window of 1.5 times the median difference between the last 3 consecutive fiducial marks, a search back procedure in that time window is performed by starting (1) with lower thresholds.

Wavelet based QRS detection restricts the analysis to scales 2^1 to 2^4, which include the highest frequencies of the ECG signal in each scale (Fig. 2.6). Therefore, it is expected that QRS detection is more sensitive to HF noise, while being more robust to VLF noise sources, which are more noticeable in WT scales higher than W_{2^4} (Fig. 2.7(e–g)).

Typical HF contamination sources of the ECG signal include powerline interference and EMG noise. The PSD of powerline interference is characterized by a narrow band frequency content centred around 50/60 Hz which do not overlap the QRS complex indicative frequency band (Fig. 2.6(a)). However, it is expected that the effects of this type of noise will be present in scales 2^1 and 2^2, which are the scales with frequency content higher than 50 Hz (Fig. 2.7(f)). Nevertheless, the effects of powerline interference will not be present in scales 2^3 and 2^4, which contain the frequencies of the signal lower than 50 Hz. Consequently, false positive detections due to this type of noise are unlikely to occur, because the beat detection obliges the identification of significant pairs of peaks simultaneously in scales 2^1 to 2^4.

The EMG noise contamination is a more difficult problem to deal with than the powerline interference. This is because the frequency content of the EMG noise overlaps with that of the QRS complex, as already pointed out and discussed in Sec. 2.2. Figure 2.8 shows the WT scales for the EMG contaminated ECG excerpt presented in Fig. 2.2(a). As can be observed, the EMG noise contamination is present in scales 2^1 to 2^4 used for QRS detection and, therefore, false positive ECG detections can occur.

2.2.2 SBP detection in the ABP signal

In general, QRS detectors make use of the higher frequency content of the QRS complex with respect to the other ECG waves. Transformations are applied to the ECG in order to enhance the QRS complex characteristics and finally a threshold-dependent detection scheme is applied. The ABP beat detectors also rely on similar features of the ABP signal, by enhancing the anacrotic limb, which contains the higher frequency content with respect to the other ABP waves.

---

[8] The threshold value of 275 msec was set as the minimum distance between 2 consecutive QRS complexes, which corresponds to a heart rate of 210 bpm, unlikely to occur in human adults.

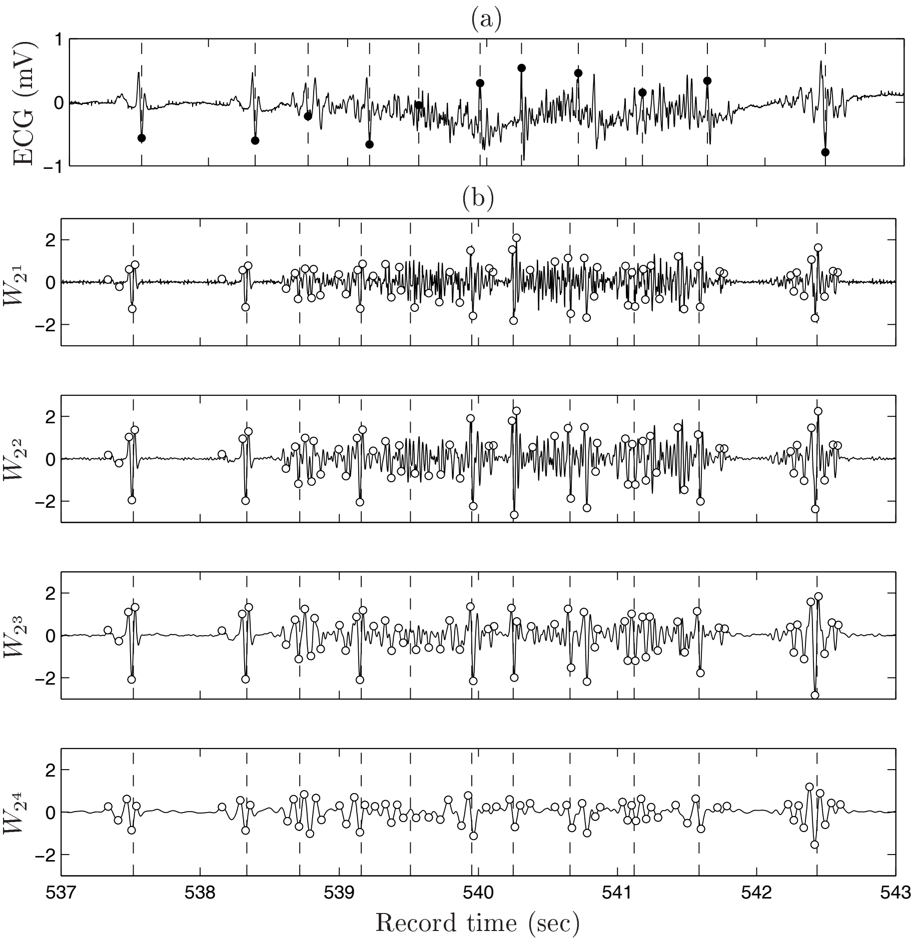

Figure 2.8: ECG presenting EMG contamination and its corresponding WT scales $a = 2^m$, $m \leq 4$. The white circles in each WT scale localize the identified significant peaks and the dashed lines indicate the position of an identified beat. Same data as in Fig. 2.2(a).

The ABP signal exhibits different morphology in comparison to the ECG signal. In particular, the ABP waves are smoother than the ECG ones and the ABP signal contains typically lower frequencies than the ECG: the highest frequency segment is the anacrotic limb, which is less steep than the QRS complex (Fig. 2.1). It has been reported that the ABP frequency content is typically concentrated below 10 Hz (Aboy *et al.*, 2005), although presenting significant frequencies up to 20 Hz (Lee and Wei, 1983).

Because the ABP signal presents detectable peaks and contains frequencies in the interval 5–15Hz, considered as the suitable passband for QRS detection (Thakor *et al.*, 1983), it is reasonable to expect that a beat detector suitable for QRS detection may be functional in ABP signals. However, it is not straightforward that a QRS detection method can be successfully applied to the problem of ABP beat identification. The reasons include the shape dissimilarities of the ECG and ABP waves, in particular, the fact that the anacrotic limb is less steep than the uprising slope of the QRS complex and the ABP signal is more asymmetric than the QRS complex. Also, QRS methodologies usually include thresholds/criteria based on known durations and distances between the ECG waves (such as the steps in Sec. 2.2.1). These rules are set to avoid beat misdetections in the ECG signal and may not be suitable for the same purpose in the ABP signal.

In the literature, few attempts have been presented in which a QRS detector has been adapted to the purpose of ABP beat detection. For example, the ABP beat detector in Zong *et al.* (2003*b*) is an adaptation of the QRS detector described in Zong *et al.* (2003*a*). In both detectors, the ABP and ECG signals are enhanced using the same filter. Also, the following processing steps are the same, but using different threshold values, which for the ABP detector were tuned to an experimental dataset. Both studies were inspired by previously proposed QRS methodology (Nygårds and Sörnmo, 1983; Pan and Tompkins, 1985), also studied by our group (Gouveia *et al.*, 2000).

For the purpose of SBP detection, either an already existing ABP beat detector can be used or a QRS detector can be adapted to the characteristics of the ABP signal, e.g., the one described in Sec. 2.2.1. In this work, the approach that has been considered for ABP beat detection consists of using the wavelet based QRS detector exactly as described for ECG beat detection (Sec. 2.2.1). However, to avoid false negative detections and enhance the ABP beat detection, the ABP signal is first preprocessed with a lowpass differentiator.

The combined use of differentiation and wavelet transforms has already been proposed for dicrotic notch detection in ABP signals (Antonelli *et al.*, 1994*a*,*b*). In those studies, the Haar, Morlet, Shannon and Spline wavelet functions were tested to process the ABP signal, and the authors reported that the *best* results were obtained with a cubic spline wavelet function. The method described in those studies allows to obtain a low pass version of an approximation of the ABP first derivative (see Fig.1 from Antonelli *et al.* (1994*b*)), in which the dicrotic peak is accentuated with respect to the other ABP waves. In this work, the cascade use of differentiation and Wavedet beat detector allows to obtain filtered versions of the approximations of ABP second derivative, because the prototype wavelet used in Wavedet exhibits derivative characteristics (see Fig. 2.6(b)).

System for beat detection/delineation in the ABP signal

The steps of the ABP beat detector developed in this work are resumed in Fig. 2.9, being detailed in the following sections. First, the ABP signal is preprocessed using the lowpass differentiator (LPD) presented in Sec. 2.2.2.2. Beat detection is then carried out with the QRS detector described in Sec. 2.2.1 and further delineation of the ABP signal in each cardiac beat is performed, as detailed in Sec. 2.2.2.3. Finally, Sec. 2.2.3 describes the outlier rejection rules employed to avoid beat misdetections in the ABP signal.

The need of the LPD before ABP beat detection is motivated in Sec. 2.2.2.1. This step essentially transforms the problem of ABP beat detection to the well-known problem of QRS

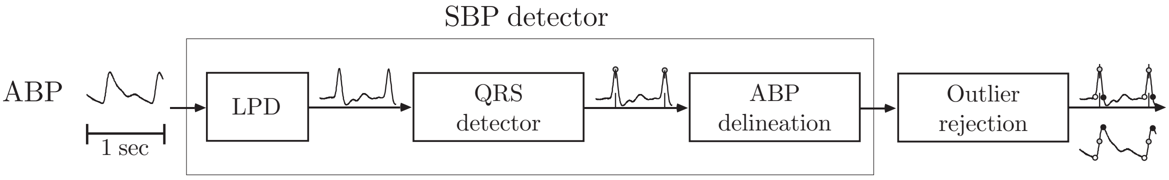

Figure 2.9: Block diagram displaying the steps of the system developed for ABP waves detection/delineation. LPD stands for lowpass differentiator filter.

detection. The QRS detector described in Sec. 2.2.1 is based on a lowpass approximation of the first derivative of the input signal. Therefore, the cascade of the LPD and Wavedet beat detection is comparable to the analysis of an approximation of the second derivative of the input signal. In this way, the ABP beat detection proposed in this work corresponds to the problem of searching zero crossings in the ABP second derivative, which correspond to peaks in the ABP first derivative and inflection points in the ABP signal.

2.2.2.1 SBP detection using the QRS Wavedet detector

The Wavedet beat detector performs successfully when applied directly to ABP signals exhibiting sharp anacrotic and dicrotic limbs, see Fig. 2.10. In such signals, all the ABP beats are correctly identified because pairs of significant WT maximum and minimum values are identified in all WT scales and the following steps are satisfied, so that fiducial marks are provided.

However, the morphology of ABP waves depends on several variables and less sharp/steep waves are more likely to occur. Also, ABP waves can exhibit a longer distance between the maximum and minimum derivative values in each heartbeat, see Fig. 2.11. Although in these cases, significant WT maximum and minimum values can be still identified, the distance between them is higher than the temporal threshold of 150 msec (step 3 in Sec. 2.2.1). Consequently, no fiducial marks are identified because these values are considered as isolated peaks and removed from the analysis.

Analysis of Wavedet beat detection in ABP signals
The Wavedet beat detector searches across WT scales for significant peaks in order to identify pairs of values with different polarity. The amplitude thresholds to consider a WT peak as significant are set regardless if the peak is a maximum or a minimum, being evaluated in terms of a modulus. This is because the QRS complex is expected to have a symmetric shape, leading to WT shapes with similar absolute amplitude maximum and minimum values, see Fig. 2.7(c) and (d). In contrast to the QRS complex, the ABP waveform has an asymmetric shape, exhibiting a much steeper anacrotic limb than dicrotic limb. Therefore, the WT of an ABP signal presents prominent maxima and less perceptible minima (Fig. 2.7(b))

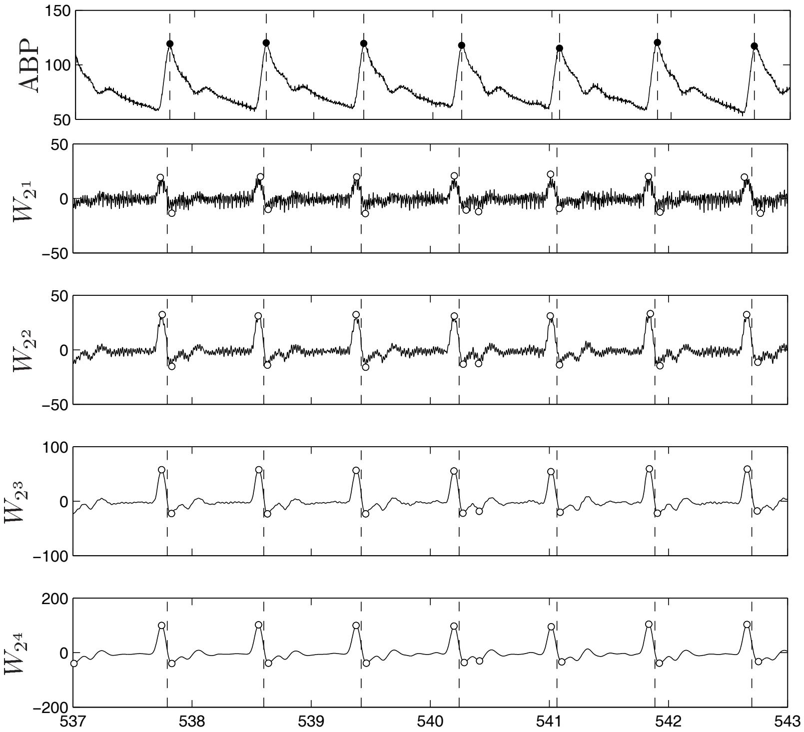

Figure 2.10: ABP waves exhibiting a sharp shape and the corresponding WT scales. The white circles in each scale localize the identified significant peaks and the dashed lines indicate the position of an identified beat. Same data as in Fig. 2.2(a).

and, consequently, false negative detection of minima or false labelling as non–significant are expected to occur.

After the identification of significant peaks, amplitude/temporal conditions are imposed to avoid misdetections (steps 3 to 7 in Sec. 2.2.1). In particular, the maximum distance between two consecutive significant peaks of 150 msec allows to remove isolated peaks. For each significant peak i, $\delta_{min}(i)$ is defined as the distance of the peak i to its closest neighbour. Figure 2.12(a) presents an ECG signal with its W_{2^1} scale, in which significant minima were identified due to a steep T wave. As presented in Fig. 2.13(a), these values have $\delta_{min}(i) >$ 150 msec and, therefore, are removed from subsequent analysis. If the T wave would also present a steep ascending limb, significant maxima would be identified and, together with a significant minima, would form significant pairs of WT peaks. Consequently, fiducial marks in the T wave would be provided. However, they would be finally discarded because its distance to the fiducial mark of the previous QRS complex would be shorter than the refractory period of 275 msec (step 6 in Sec. 2.2.1).

Figure 2.12(b) presents the ABP signal for the same time window as in Fig. 2.12(a). For the beats in which the WT minima are not identified (or not labelled as significant), the $\delta_{min}(i)$ values associated with the maxima are naturally longer than 150 msec. When such

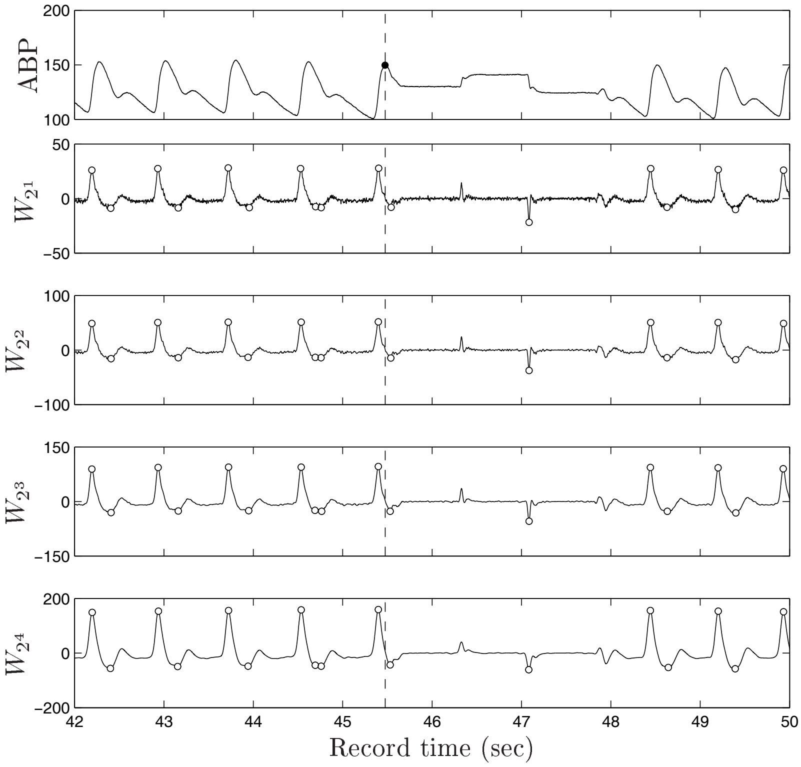

Figure 2.11: ABP waves exhibiting a less sharp shape and the corresponding WT scales. The white circles in each scale localize the identified significant peaks and the dashed lines indicate the position of an identified beat. In this recording, only one ABP beat was identified. Same data as in Fig. 2.2(b).

minima are identified, the WT maxima and minima do not satisfy a maximum distance of 150 msec. The histogram in Fig. 2.13(b) shows that more than 80% of the significant peaks have $\delta_{min}(i) > 150$ msec, being 205 msec in median. As a consequence, these values are discarded from subsequent analysis and no fiducial mark is provided.

How to use the QRS Wavedet detector in ABP signals

There are several ways to use a QRS detector to ABP signals, depending on the QRS detector considered. Regarding the Wavedet beat detector, one intuitive way is to revise the proper WT scales to analyze the ABP signal and tune all the thresholds values to the characteristics of the ABP waves instead of the ECG ones. Additionally, some of the rules/steps in Sec. 2.2.1 would have to be removed and other rules would have to be introduced.

Regarding the proper scales to analyze the ABP signal, possibly only the scales higher than W_{2^2} should be considered to avoid ABP noise with frequency content higher than that of the anacrotic limb (Figs. 2.6, 2.10 and Fig. 2.11). However, the WT scales $a = 2^m, m = 1, ..., 4$ considered for QRS detection are also suitable for ABP beat detection, because the highest frequency of the ABP signal is the anacrotic limb and, therefore, it is presented across these scales (Figs. 2.10 and Fig. 2.11). Also, other adjustments in the QRS Wavedet detector should be considered for its use in ABP signals. In particular,

- *to increase the maximum distance between two consecutive max/min WT values* (step 3 in Sec. 2.2.1) to allow the detection of significant pairs (See Fig. 2.11),
- *to lower the threshold to identify a significant minimum WT value* (step 1 in Sec. 2.2.1), to avoid false negatives (See Fig. 2.12(b)),
- *to adjust the refractory period* (step 6 in Sec. 2.2.1) to avoid the misdetection of dicrotic peaks as systolic peaks (See Fig. 2.13(b))[9].

Another way to apply the Wavedet detector to ABP signals is to find an ABP transformation to reduce the dissimilarities between the ECG and the ABP signals, in particular, to transform the asymmetric ABP signal into a succession of prominent waves with a more symmetrical shape and shorter distance between two corresponding consecutive significant WT peaks. The fulfilment of such conditions will identify significant WT maxima and minima (with equal probability) and significant pairs of peaks so that, ultimately, fiducial marks can be provided.

One of such transformations is the differentiation of the ABP signal. Figure 2.12(c) shows the differentiated ABP signal in Fig. 2.12(b), accomplished with the lowpass differentiator (LPD) described in Sec. 2.2.2.2. As can be observed, the LPD enhances the anacrotic limb, transforming the ABP signal into a symmetric-like signal. Also, an adequate choice for the LPD bandpass shapes the ABP signal to have similar frequency content to that of the QRS complex, making the analysis of the WT scales 2^1 to 2^4 suitable for the new purpose.

The restriction of the ABP analysis to the time window of the anacrotic limb has also the advantage of shortening the maximum distance between two consecutive significant WT peaks. As previously referred, this distance is constrained to be shorter than 150 msec, which is reported as a value corresponding to the maximum width of a QRS complex (Pan and Tompkins, 1985; Hamilton and Tompkins, 1986). As presented in Fig. 2.13(c), all beats exhibit $\delta_{min}(i) < 150$ msec. Although there seems to be no well-established relationship between the QRS width and the duration of the anacrotic limb in the literature, the duration of the anacrotic limb was found to be lower than 150 msec for all files considered in this study. This result is in accordance with the anacrotic limb duration of 128 msec reported in the study by Zong *et al.* (2003*b*). Nevertheless, it is worthwhile to say that the shape of the ABP waveforms change from subject to subject depending, e.g., on age and clinical condition (O'Rourke, 2009).

---

[9] The refractory period of 275 msec is imposed to avoid the misdetection of T waves as QRS complexes. The distance between systolic and following dicrotic peaks is higher than the distance between the peaks of the QRS complex and T wave and, therefore, this threshold value should be increased for ABP signals. However, dramatic increases of this value might lead to the removal of systolic peaks at high heart rate.

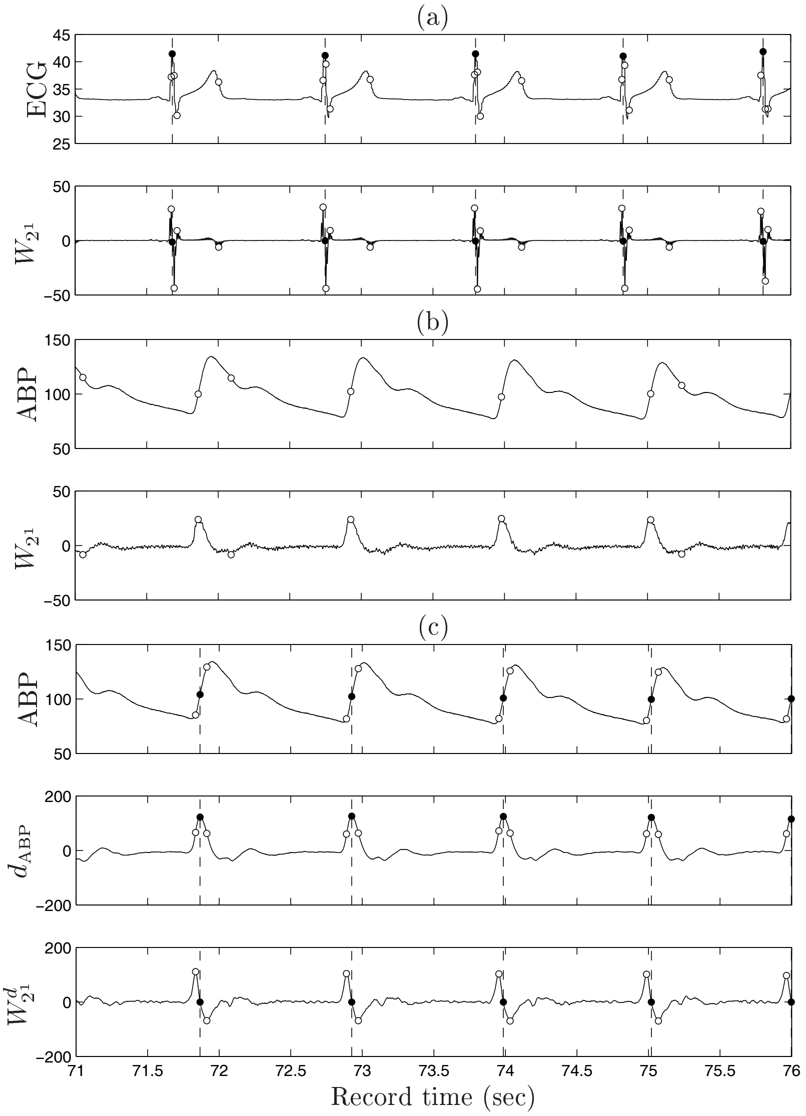

Figure 2.12: Plot of (a) ECG, (b) ABP and (c) ABP and d_{ABP} signals, with corresponding 2^1 scale. The white circles localize the WT significant peaks and the black circles identify the final fiducial marks. Notice that the ABP beats were not identified in (b).

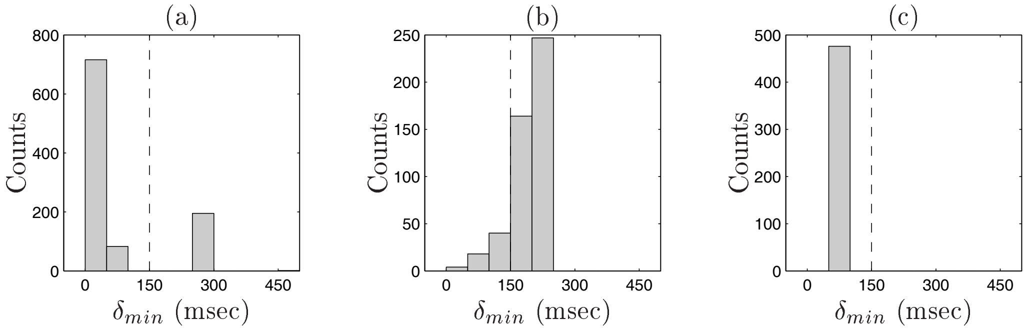

Figure 2.13: Histograms of $\delta_{min}(i)$ for the entire (a) ECG, (b) ABP and (c) d_{ABP} signals in Fig. 2.12. The dashed line locates the 150 msec threshold value. Horizontal axis zoomed from –50 to 500.

2.2.2.2 Lowpass differentiator to preprocess the ABP signal

The lowpass differentiator (LPD) used in this work to preprocess the ABP signal was originally designed for the purpose of QRS detection in the ECG signal (Laguna *et al.*, 1990). In this context, its main feature is to enhance the fast amplitude changes in the QRS frequency band to improve detection. The filter was designed bearing in mind real-time signal processing and its use in long term recordings. Therefore, low order, linear phase and integer filter coefficients were some of the restrictions in its design. Since it was not possible to directly design the LPD with such restrictions, the LPD is implemented as a cascade of two filters: a differentiator filter and a lowpass filter to reduce the high frequency noise amplified by the differentiator. The system function of the LPD is given by the product $G(z) = G_1(z)G_2(z)$ where

$$G_1(z) = 1 - z^{-6} \tag{2.9}$$

and

$$G_2(z) = \frac{1 - z^{-8}}{1 - z^{-1}}, \tag{2.10}$$

with z^{-k} representing the delay operator $z^{-k}x(n) = x(n-k)$. Figure 2.14 shows the frequency response of $G_1(z)$, $G_2(z)$ and their product $G(z)$. The first derivative is usually approximated by the difference between successive samples, i.e., a filter with system function $1 - z^{-1}$. However, the frequency response of $G_1(z)$ approximates that of the true derivative in the range up to approximately 20 Hz, which is the important frequency range to keep since frequencies higher than 30 Hz are attenuated by $G_2(z)$. Additionally, $G_1(z)$ has the advantage over $1 - z^{-1}$ of further attenuate HF noise.

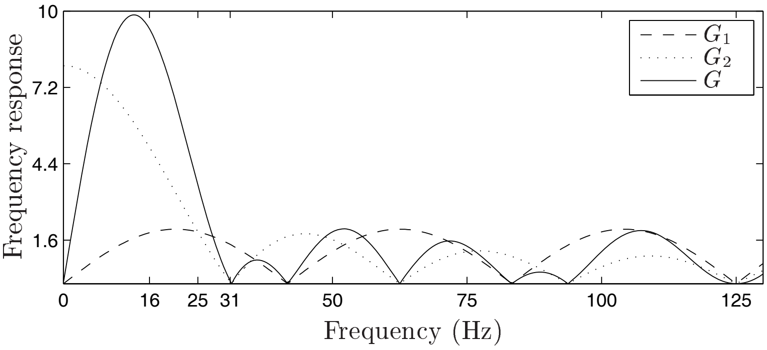

Figure 2.14: Frequency response of the LPD for $F_s = 250$ Hz. The filter coefficients for other F_s values were obtained by interpolation (Martínez *et al.*, 2004).

Figures 2.15 and 2.16 present the approximation of the ABP first derivative (d_{ABP}) obtained by the LPD and the corresponding WT scales for the same ABP signals in Fig. 2.10 and Fig. 2.11, respectively. The use of the LPD helps to shape the ABP signal so that its frequency content resembles to that of the QRS complex (Fig. 2.15(b) and Fig. 2.16(b)). Even if the frequency content of the anacrotic limb is lower than that of the QRS complex, both are the highest frequency content of the ABP and ECG signals, respectively. Therefore, the scales 2^1 to 2^4 considered for QRS detection are also suitable for ABP beat detection because, similar to the QRS complex, the anacrotic limb is enhanced across all these scales (Fig. 2.15(b) and Fig. 2.16(b)). The LPD, in particular its differentiation characteristic, changes the morphology of the anacrotic limb, transforming the ABP signal into a more symmetric signal. In this way, the scales of the d_{ABP} signal ($W^d_{2^m}$, $m = 1, 2, 3, 4$) present significant maxima and minima with similar amplitude. Additionally, the restriction of the ABP analysis to the anacrotic limb shortens the distance between the significant maxima and minima to a value shorter than 150 msec so that, finally, fiducial marks are identified.

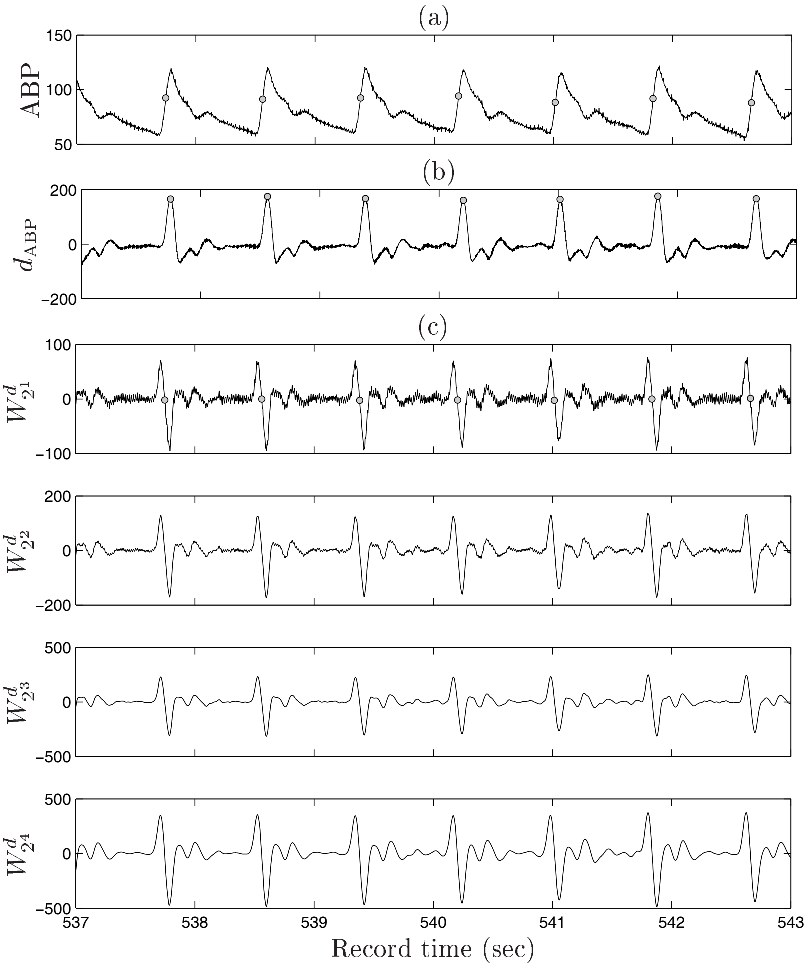

Figure 2.15: Plot of (a) ABP, (b) d_{ABP} and (c) d_{ABP} WT scales ($W^d_{2^m}$, $m = 1, 2, 3, 4$). The grey circles localize the detected fiducial marks. Same data as in Fig. 2.10.

Figures 2.15 and 2.16 additionally show the beat detection output, illustrating that the use of the LPD continues to return a successful output for the ABP signals exhibiting sharp anacrotic and dicrotic limbs (Fig. 2.10), while for the ABP signals exhibiting less sharp waves the beat detection is now correctly carried out (Fig. 2.11).

Figure 2.16: Plot of (a) ABP, (b) d_{ABP} and (c) d_{ABP} WT scales ($W^d_{2^m}$, $m = 1, 2, 3, 4$). The grey circles localize the detected fiducial marks. Same data as in Fig. 2.11.

2.2.2.3 Beat delineation in ABP signals

The cascade use of the LPD filter and the QRS detector in the ABP signals allows to obtain fiducial marks that localize the heartbeat. These fiducial marks correspond to the peaks in the $d_{\text{ABP}}(t)$ signal, around which further delineation of the cardiac cycle can be carried out. In particular, the maximum and minimum ABP values in each beat, respectively, $x_{\text{SBP}}(n)$ and $x_{\text{DBP}}(n)$ are obtained.

As referred in Sec. 2.2.1, the QRS detector allows the detection of positive and/or inverted QRS complexes in the same recording and, therefore, the fiducial marks can be either positive or negative amplitude, as is illustrated in Fig. 2.17. A positive fiducial mark is associated with an ABP shape presenting a steeper slope in the anacrotic limb than in the dicrotic limb (Fig. 2.17(a)). In these cases, $x_{\text{SBP}}(n)$ and $x_{\text{DBP}}(n)$ are the $d_{\text{ABP}}(t)$ zero crossings localized to the right and left of the fiducial mark n, respectively. By other hand, a negative mark is associated with an ABP signal presenting a steeper slope in the dicrotic limb than in the anacrotic limb (Fig. 2.17(b)). For this case, $x_{\text{SBP}}(n)$ and $x_{\text{DBP}}(n)$ are identified as the first and second $d_{\text{ABP}}(t)$ zero crossings anterior to the fiducial mark n, respectively.

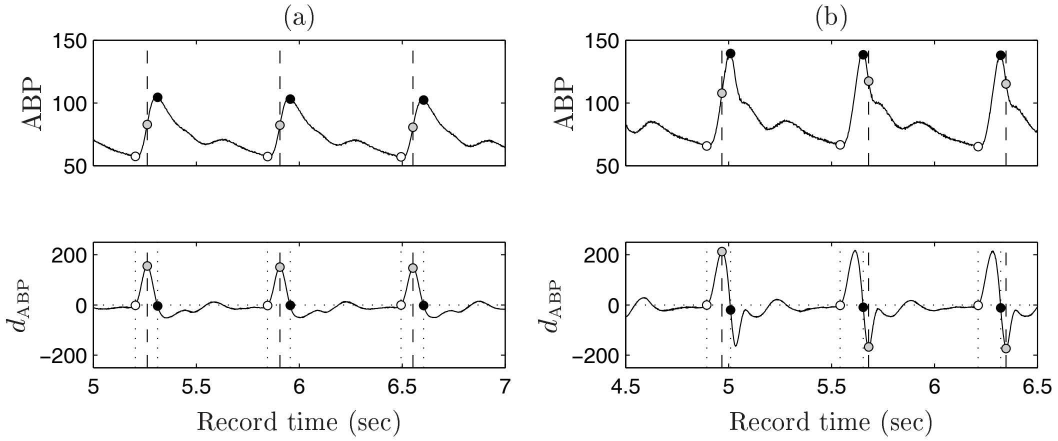

Figure 2.17: Illustrative example of ABP heartbeat delineation for (a) positive and (b) negative fiducial marks (grey circles). The white and black circles localize respectively the $x_{\text{DBP}}(n)$ and $x_{\text{SBP}}(n)$ values obtained after delineation.

2.2.3 Rejection of outlier SBP marks

Figure 2.18 presents two ABP recordings illustrating the SBP detection in ABP signals with prominent dicrotic peaks following the systolic peaks and calibration episodes. These artifacts are likely to produce false positive detections, thus motivating the development/inclusion of rules able to identify and reject outlier SBP marks.

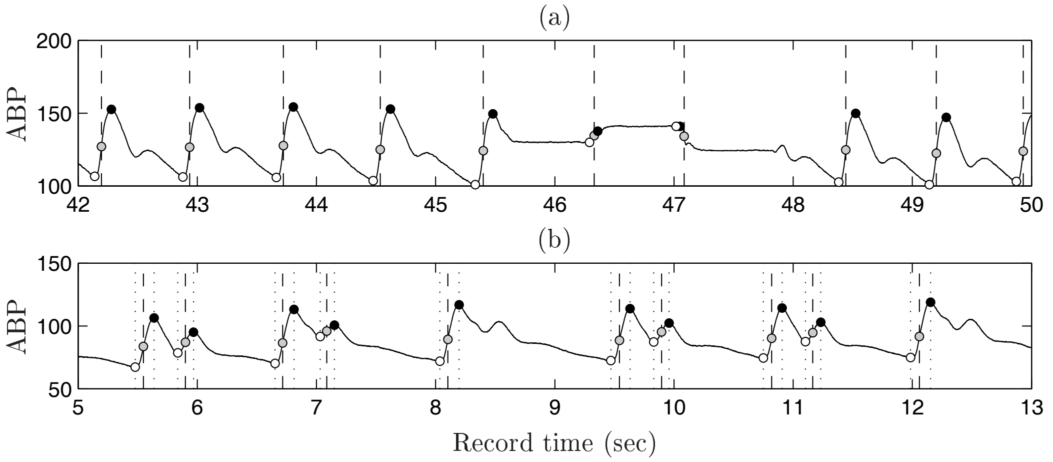

Figure 2.18: Delineation in ABP signals exhibiting (a) calibration episodes and (b) prominent dicrotic peaks following the systolic peak. To notice that in (b) two dicrotic peaks were not identified.

The SBP outlier rejection rules considered in this work were specifically developed to remove prominent dicrotic peaks and peaks in calibration episodes, by this order. Other outlier cases in SBP detection will be corrected together with the output of the QRS detection, in the step of time alignment of the QRS and SBP marks described in Sec. 2.2.4.

2.2.3.1 Removal of prominent dicrotic peaks

The Wavedet detector includes a refractory period of 275 msec set as the minimum acceptable distance between two consecutive peaks (step 6 in Sec. 2.2.1). As highlighted in Fig. 2.18(b) some dicrotic peaks are not detected, because its time distance to the previous systolic peak is lower than 275 msec. The histograms in Fig. 2.19 present the distribution of the distances between each detected peak to its closest neighbour before the verification of step 6, for the ABP signals in Fig. 2.18. In the case of detected prominent peaks (Fig. 2.19(b)), around 90% of the distances are above 275 msec and, therefore, this value is not sufficient to avoid the detection of prominent dicrotic peaks in ABP signals. However, increasing excessively the refractory period might lead to the removal of systolic peaks at high heart rates and, by this reason, alternative rejection rules have to be considered.

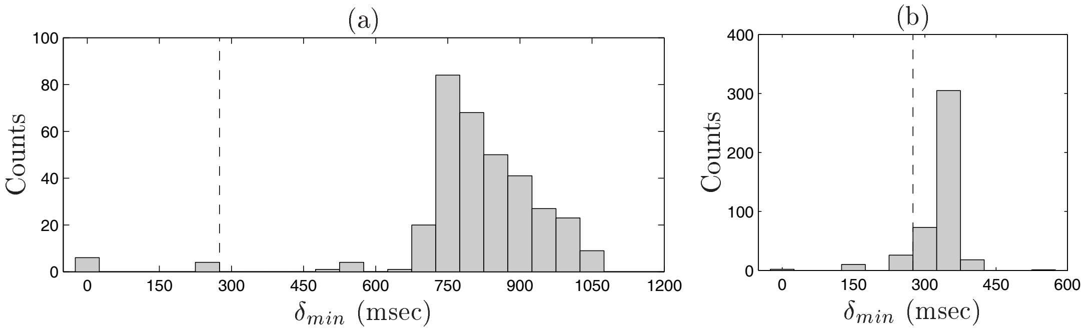

Figure 2.19: Histogram of the distances between each peak to its closest neighbour before the verification of step 6 of the Wavedet system. The dashed line localizes the threshold value of 275 msec. Same data as in Fig. 2.18(a) and 2.18(b), respectively.

The rejection rules to avoid the detection of prominent dicrotic peaks are conservative rules, which are based on complementary amplitude and temporal conditions, such as the beat-to-beat statistics $x_{\mathrm{PF}}(n)$ and $x_{\mathrm{PI}}(n)$ values associated with each cardiac beat n. As illustrated in Fig. 2.20, the dicrotic peaks are characterized by their shorter $x_{\mathrm{PI}}(n)$ and lower $x_{\mathrm{PF}}(n)$ values when compared with the systolic peaks. In practice, the candidate marks to remove are the ones that present short $x_{\mathrm{PI}}(n)$ and low $x_{\mathrm{PF}}(n)$ values, following the time-variant threshold described in Sec. 2.2.3.3. These fiducial marks are removed only if their removal does not introduce an updated $x_{\mathrm{PI}}(n)$ identified as long, following the same definition.

The systematic detection of dicrotic peaks might affect the thresholds considered to label a fiducial mark as long/short and large/small. Therefore, the first marks considered to be remove are the marks that with more confidence correspond to prominent dicrotic peaks: besides short $x_{\mathrm{PI}}(n)$ and low $x_{\mathrm{PF}}(n)$ values, these marks additionally present long $x_{\mathrm{PI}}(n-1)$ and large $x_{\mathrm{PF}}(n-1)$. After threshold update, fiducial marks with short $x_{\mathrm{PI}}(n)$ and low $x_{\mathrm{PF}}(n)$ values were then considered to be removed.

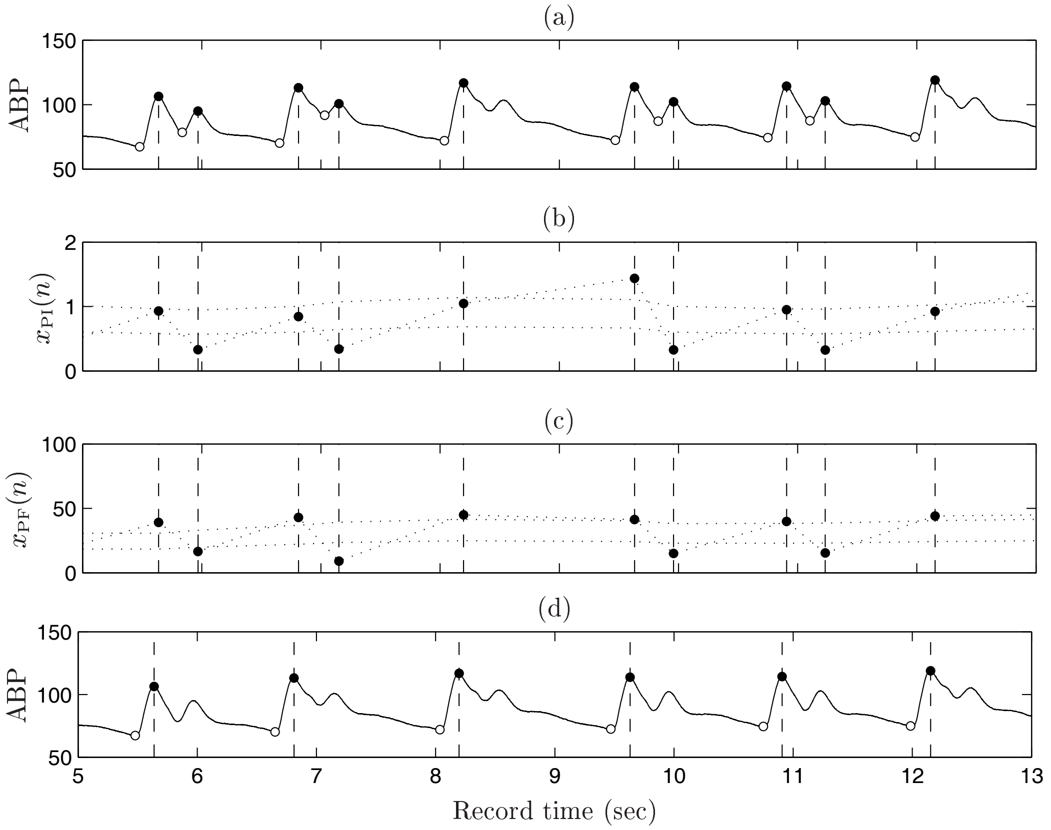

Figure 2.20: ABP delineation in a case of prominent dicrotic peaks (a) before and (d) after outlier rejection. In (b–c), the $x_{\mathrm{PI}}(n)$ and $x_{\mathrm{PF}}(n)$ estimates are plotted together with the time-variant thresholds (horizontal dotted lines) to label a beat as longer/shorter and larger/smaller, respectively. Same data as in Fig. 2.18(b).

2.2.3.2 Removal of peaks in calibration episodes

As observed in Fig. 2.18(a), ABP calibration episodes are characterized by the lower amplitude variance in comparison with the ABP signal. Therefore, dispersion measures on ABP amplitude can be used to identify such episodes.

In an early attempt to develop and implement a rule to exclude peaks in calibration episodes, the series $x_{\mathrm{PF}}(n)$ was considered together with a threshold (either constant or time variant, as the one described in Sec. 2.2.3.3). This approach would serve for signals in which the $x_{\mathrm{PF}}(n)$ is low for the peaks in calibration episodes, such as the example in Fig. 2.21(a). However, in more challenging signals, such as data acquired in sleep studies (Fig. 2.23(a)), the $x_{\mathrm{PF}}(n)$

statistics can be similar in smaller variance ABP waves and very steep calibration stairs occurring in the same recording. Therefore, an alternative approach had to be developed to avoid, by one hand, removing peaks in ABP waves and, by the other, keeping peaks in calibration episodes.

In this work, the detection of the calibration episodes was based on the standard deviation of the ABP amplitudes, s_{ABP}, and it was performed in two steps to save computational load. Briefly, in the first step the candidate peaks to remove are identified based on a beat-to-beat variability statistics $s_{\mathrm{ABP}}(n)$. In the second step, a more refined delineation of the calibration episode (onset/end) is carried out based on a sample-to-sample statistics $s_{\mathrm{ABP}}(t)$. Finally, the peaks to be removed are chosen based on the onset/end of the identified calibration episode.

Figure 2.21 illustrates the two steps to remove fiducial marks in calibration episodes, which are detailed below. For illustration purposes, Figs. 2.21(a) and 2.21(d) show the peaks before and after outlier removal.

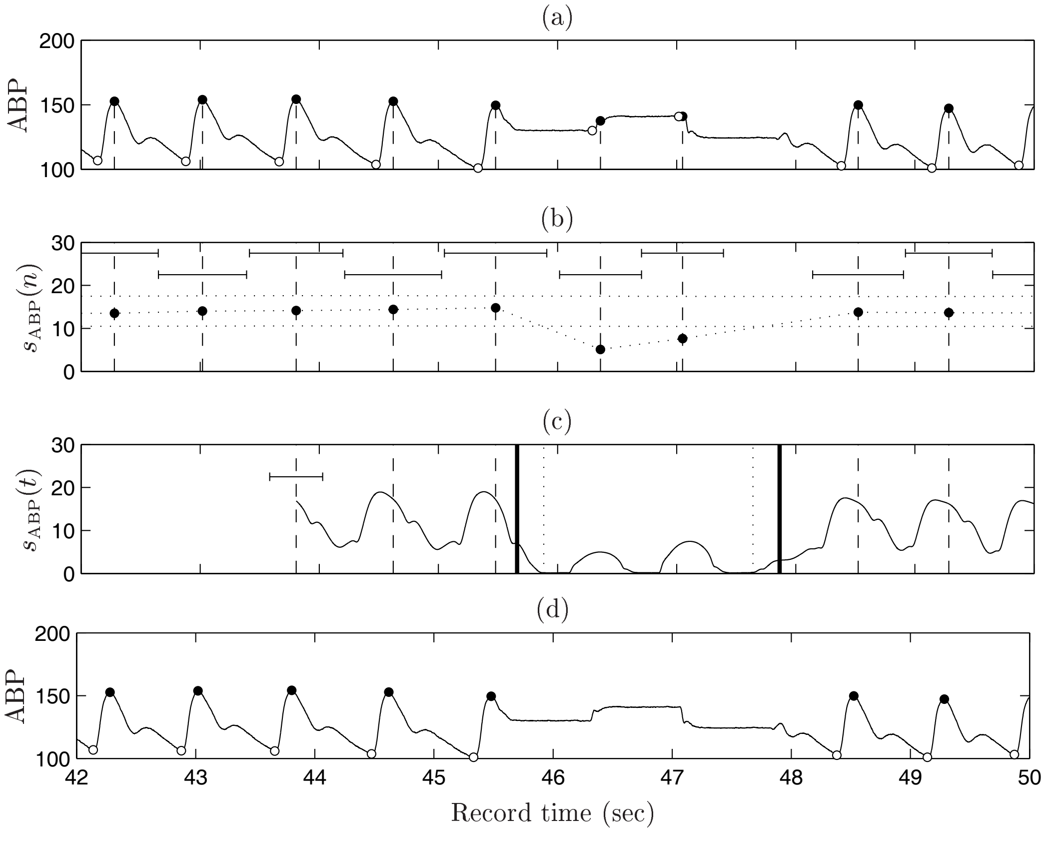

Figure 2.21: Plot of (a) ABP and the identified marks, (b) $s_{\mathrm{ABP}}(n)$ estimates and time windows for its computation, (c) $s_{\mathrm{ABP}}(t)$ estimates and sliding window for its computation, (d) ABP and marks after outlier rejection. In (c), the thick vertical lines delineate the onset/end of the episode. Same data as in Fig. 2.18(a).

Identification of the candidate marks to remove – Fig. 2.21(b)
The candidate peaks to remove are the ones that have lower $s_{\text{ABP}}(n)$ in comparison with the remaining peaks, based on the time-variant threshold presented in Sec. 2.2.3.3. The beat-to-beat $s_{\text{ABP}}(n)$ estimates are computed as the standard deviation of the ABP values at the time window $w(n)$, centred in each mark n with variable width $l_n = min\,\{x_{\text{PI}}(n), x_{\text{PI}}(n+1)\}$, i.e.,

$$s_{\text{ABP}}(n) = std\ \text{ABP}(w(n)) \text{ where } w(n) \in [t_{\text{SBP}}(n) - \frac{l_n}{2}, t_{\text{SBP}}(n) + \frac{l_n}{2}]. \tag{2.11}$$

Refined delineation of the beginning/end of the calibration episode – Fig. 2.21(c)
The sample-to-sample $s_{\text{ABP}}(t)$ values are calculated in the neighbourhood of the candidate marks $t \in [t_{\text{SBP}}(k_1 - 3), t_{\text{SBP}}(k_2 + 3)]$, where k_1 and k_2 are the order number of the first and the last mark of a set of consecutive candidates. The $s_{\text{ABP}}(t)$ estimates are computed as the standard deviation of the ABP values at a sliding time window $w(t)$, centred in each t and with fixed width $l/2$ for each calibration episode, i.e.,

$$s_{\text{ABP}}(t) = std\ \text{ABP}(w(t)) \text{ where } w(t) \in [t - \frac{l}{4}, t + \frac{l}{4}]. \tag{2.12}$$

where $l = mean\,\{x_{\text{PI}}(k_1 - 3), x_{\text{PI}}(k_1 - 2), x_{\text{PI}}(k_2 + 1), x_{\text{PI}}(k_2 + 2)\}$. The onset of the calibration episode is the first zero crossing of the $s_{\text{ABP}}(t)$ derivative (approximated by its successive differences), after $s_{\text{ABP}}(t)$ decreasing to values lower than 1 mmHg (dotted line in Fig. 2.21(c)). From this position, the onset of the episode is corrected taking into account the width of the time window w_t, i.e., $\frac{l}{4}$ (thick line in Fig. 2.21(c)). The end of the episode is found in the same way by reversing the time order.

2.2.3.3 Robust thresholds to label a mark

In this work, $x(n)$ is labelled as "long/large" if $x(n)$ exceeds $1.25\tilde{x}(n)$, where $\tilde{x}(n)$ is a statistics based on the moving average of the neighbouring $x(n)$ values, obtained as follows

$$\tilde{x}(n) = \frac{1}{8} \sum_{\substack{k=n-4 \\ k \neq \{n, n+1\}}}^{n+5} x(k), \tag{2.13}$$

i.e., mean of 8 neighbour values of $x(n)$ (4 samples before and 4 samples after). Analogously, $x(n)$ is labelled as "short/small" if $x(n)$ falls below $0.75\,\tilde{x}(n)$.

The zero coefficients for samples n and $n+1$ allow to increase the robustness in teh computation of $\tilde{x}(n)$, to occurring patterns of shorter/longer and smaller/larger values in $x(n)$, e.g., smaller/larger $x_{\text{PF}}(n)$ due to the detection of dicrotic peaks as systolic peaks.

The computation of $\tilde{x}(n)$ is more critical if outliers of very small or very large amplitude occur. As illustrated in Fig. 2.22(a) and 2.22(b), very large amplitude $x(n)$ lead to overestimation of

$\tilde{x}(n)$, so that neighbour values can be mislabelled as "short". In this work, $\tilde{x}(n)$ is recomputed to obtain a robust threshold to larger amplitude outliers $\tilde{x}^{\mathrm{R}}(n)$, if outlier values are found, i.e., if $x(k) > 1.25\,\tilde{x}(k)$ or $x(k) < 0.75\,\tilde{x}(k)$, for some k. In this case, $\tilde{x}(k)$ is updated by replacing the previously identified outliers $x(k)$ by $\hat{x}(k)$, obtained by cubic spline interpolation from the non outlier $x(n)$ values. The $\tilde{x}(n)$ is updated until one of the following conditions is met:

- the identified outliers are the same in two consecutive steps,
- more than 10% updated higher threshold values are larger than the previous higher threshold values,
- more than 10% updated lower threshold values are smaller than the previous lower threshold values.

The two latter conditions were imposed to avoid update errors: if outliers are not included in the computation of $\tilde{x}(n)$, it is expected that the updated confidence band $[0.75\,\tilde{x}(n), 1.25\,\tilde{x}(n)]$ is narrower than the previous. In this work, updated confidence bands wider than the previous were associated with recordings exhibiting outlier values in the beginning/end of the files, and the use of spline interpolation lead to misleading estimates.

Figure 2.22(c) shows the same excerpt of data as in Fig. 2.22(a) and 2.22(b), illustrating that the use of robust thresholds offers a more correct identification of the longer/shorter $x_{\mathrm{PI}}(n)$ values, in particular for the beats close to higher amplitude outliers.

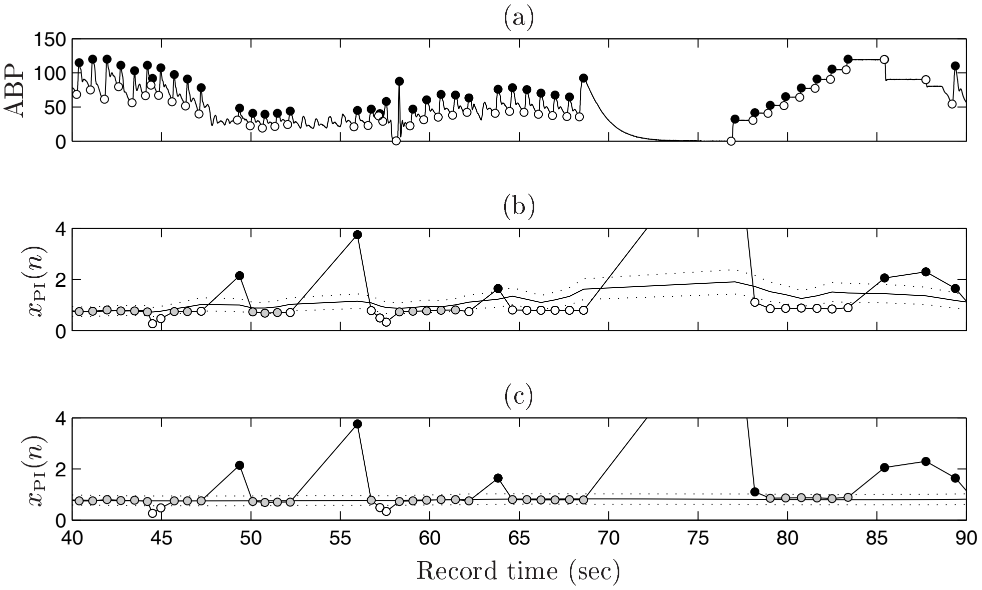

Figure 2.22: Plot of (a) ABP and (b–c) $x_{\mathrm{PI}}(n)$ series. In (b), $\tilde{x}(n)$ and $[0.75\,\tilde{x}(n), 1.25\,\tilde{x}(n)]$ are represented by the full and dotted lines. The same representation is presented in (c), for $\tilde{x}^{\mathrm{R}}(n)$ and $[0.75\,\tilde{x}^{\mathrm{R}}(n), 1.25\,\tilde{x}^{\mathrm{R}}(n)]$. In (b–c), the grey dots identify the values inside each confidence band, while the white and the black dots identify the shorter and larger $x_{\mathrm{PI}}(n)$ values, respectively.

2.2.3.4 Illustrative example of SBP outlier rejection

Figure 2.23(a) presents the identified marks for an excerpt of data from a sleep Apnoea study, showing false positives, smaller variance ABP waves and very steep calibration stairs.

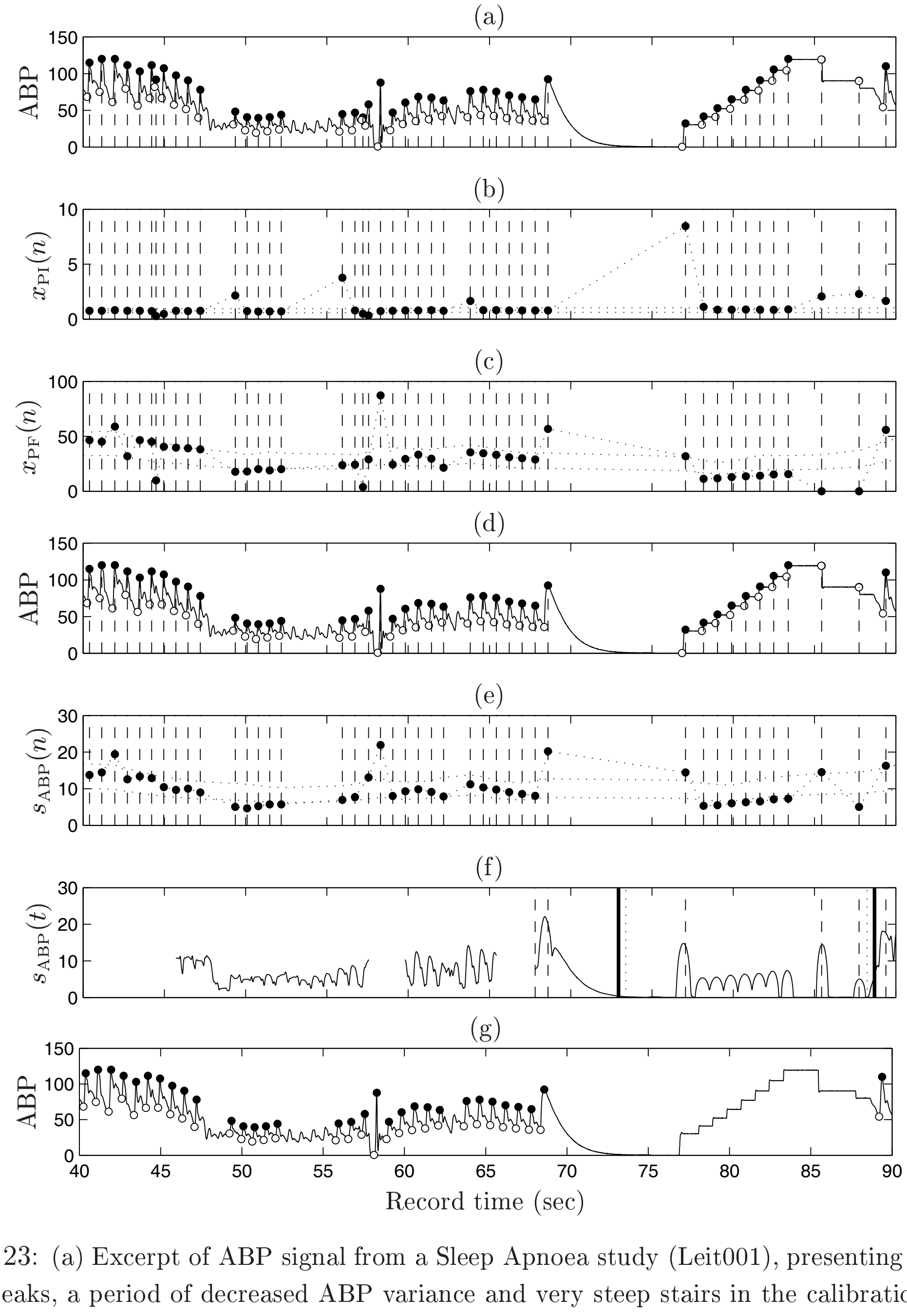

Figure 2.23: (a) Excerpt of ABP signal from a Sleep Apnoea study (Leit001), presenting prominent dicrotic peaks, a period of decreased ABP variance and very steep stairs in the calibration episode. (d) Same excerpt after removing the prominent dicrotic peaks and (g) after removing also the marks in calibration episodes. Figures (b–c) and (e–f) illustrate the evaluated statistics used for removal of prominent dicrotic peaks and calibration episodes, respectively.

After beat delineation, the identified dicrotic peaks are removed, based on $x_{\text{PI}}(n)$ and $x_{\text{PF}}(n)$ values, as illustrated in Fig. 2.23(b–c) and described in Sec. 2.2.3.1. The output of this step is presented in Fig. 2.23(d), where it is possible to observe that these false positive marks are correctly removed. The identified peaks in ABP calibration episodes are then removed, based on the beat-to-beat $s_{\text{ABP}}(n)$ and sample-to-sample $s_{\text{ABP}}(t)$ values, as illustrated in Fig. 2.23(e–f) and described in Sec. 2.2.3.2. As can be observed in Fig. 2.23(g), this step removes correctly the marks in calibration episodes, while keeping the fiducial marks the unexpected lower variance ABP waves.

Figure 2.23(a) also shows that there were systolic peaks of very low variance that were not identified by the beat detector. These false negative detections could be solved by changing the threshold in the beat detector, from constant in a window of 2^{16} samples (step 1 in Sec. 2.2.1), e.g., to a constant threshold based on a more robust statistics. In this work, the missing marks are introduced by interpolation, after the time alignment of the QRS and the SBP marks, as described in Sec. 2.2.4.

2.2.4 Time alignment of QRS and SBP marks

The fusion of the QRS and SBP marks obtained from the independent ECG and ABP beat detectors is carried out by time alignment of the marks and correction of eventual time alignment errors. If there are no misdetections, it is expected that for the n^{th} cardiac beat, the condition

$$t_{\text{SBP}}(n-1) < t_{\text{QRS}}(n) < t_{\text{SBP}}(n) < t_{\text{QRS}}(n+1) \tag{2.14}$$

is satisfied, i.e., the identified QRS and SBP marks alternate, each QRS complex matches one (and only one) SBP value and a SBP value occurs after its corresponding QRS complex.

If misdetections occur, the obtained QRS and SBP marks will not be orderly matched and have to be time aligned. Figure 2.24 presents two examples of misdetections, showing a different numbering in the QRS and SBP marks. In Fig. 2.24(a) is possible to observe that $t_{\text{QRS}}(677)$ matches $t_{\text{SBP}}(673)$ after the noisy ECG episode. In Fig. 2.24(b), the QRS and SBP matching is quite obvious, apart of the different QRS and SBP numbering.

Based on the condition (2.14), the i^{th} QRS complex and j^{th} SBP value are said to be *time aligned* if $t_{\text{QRS}}(i)$ and $t_{\text{SBP}}(j)$ satisfy

$$t_{\text{SBP}}(j-1) < t_{\text{QRS}}(i) < t_{\text{SBP}}(j) < t_{\text{QRS}}(i+1), \tag{2.15}$$

where i and j represent the order number of the QRS and SBP marks obtained by the independent systems. If the condition (2.15) is not satisfied there is a time alignment error.

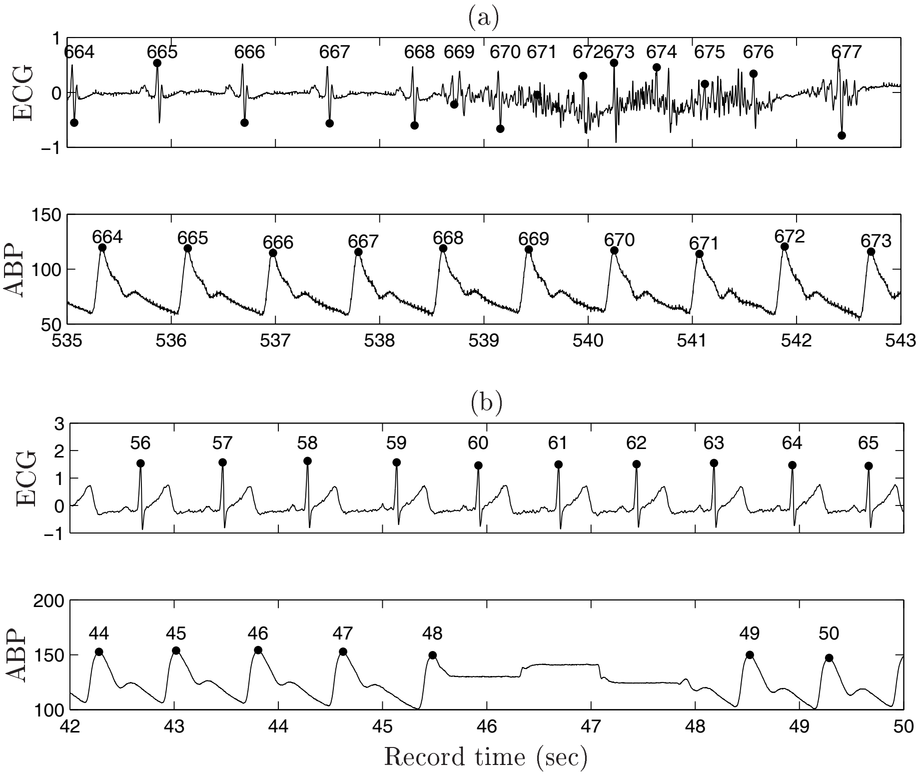

Figure 2.24: Same data as in Fig. 2.2 showing the order number of the identified QRS and SBP marks by the independent ECG and ABP beat detectors. The QRS and SBP marks in (b) do not start with the same numbering due to prior misdetections.

For the time alignment verification, the $t_{\text{QRS}}(i)$ and $t_{\text{SBP}}(j)$ values are sorted in ascending order and renumbered, to maintain the QRS and SBP matching after an eventual noisy episode. The following examples illustrate how the sorting and renumbering is carried out and the indexes (i, j) are replaced with a common index n' both QRS and SBP marks.

Figure 2.25 shows the same examples as in Fig. 2.24 after sorting and renumbering the values $t_{\text{QRS}}(i)$ and $t_{\text{SBP}}(j)$. The figure illustrates that in the case of misdetection in the ECG and/or in the ABP detection systems, the cumulative errors due to previous misdetections will be avoided and the resulting QRS and SBP values will be still orderly matched after a noisy interval.

Figure 2.25 presents two distinct situations in which the condition (2.15) is not satisfied, i.e., there are time alignment errors. For both cases, the following condition

$$t_{\text{SBP}}(n'-1) < t_{\text{QRS}}(n') < t_{\text{QRS}}(n'+1) < ... < t_{\text{QRS}}(n'+k) < t_{\text{SBP}}(n'+k) < t_{\text{QRS}}(n'+k+1)$$

is satisfied for some n' and k. This condition indicates that there are more QRS than SBP marks. In Fig. 2.25(a), there are three false positive detections in the ECG signal identified for the pairs of values (n', k)=$(669, 1), (671, 2), (675, 1)$. For each misdetection, only one of

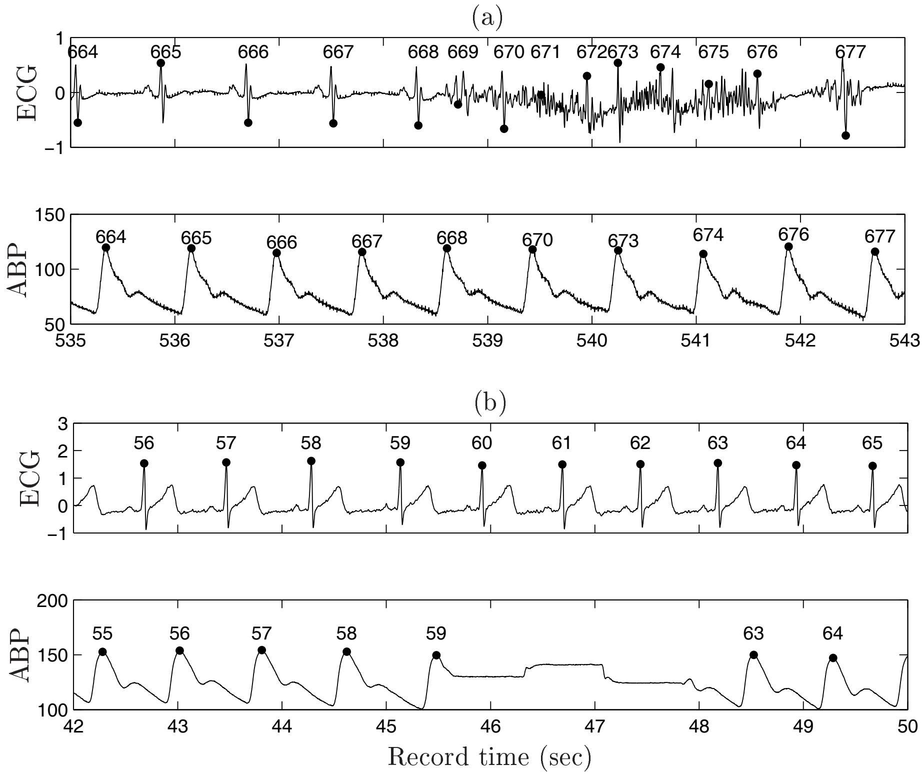

Figure 2.25: Same data as in Fig. 2.24 with the numbers above each mark representing the order number of the marks after sorting and renumbering.

the $t_{\mathrm{QRS}}(n')$, $t_{\mathrm{QRS}}(n'+1)$, ... $t_{\mathrm{QRS}}(n'+k)$ has to be chosen while removing the remaining marks, so to keep the time alignment of the QRS and SBP marks. In Fig. 2.25(b) there are false negative detections in the ABP signal for the pair of values $(n', k)=(60, 3)$ and three SBP values have to be inserted to satisfy condition (2.14).

For illustration purposes, Fig. 2.26 shows the same data as in Fig. 2.25, with indication of the marks after correction of the time alignment errors. The procedure for detection/correction of time alignment errors is following described.

Figure 2.27 schematizes the procedure for the detection of time alignment errors. An error occurs in one of the two situations: either a $t_{\mathrm{QRS}}(n')$ or a $t_{\mathrm{SBP}}(n')$ does not exist. The distinction between the situation of a false positive (FP) or false negative (FN) in each signal is performed from the evaluation of the $x_{\mathrm{RR}}(n')$ and $x_{\mathrm{PI}}(n')$ values. For example, Step (2) corresponds to the detection of a FN in the ECG signal, which is identified by a missing $t_{\mathrm{QRS}}(n')$ mark and a $x_{\mathrm{RR}}(n')$ labelled as long (see Sec. 2.2.3.3 for methods to label a mark). The remaining situations are detected in a similar way.

The detections/corrections of the time alignment errors are performed by the order indicated in the flowchart of Fig. 2.27. Step (1) consists of the correction of FN in ABP, due to calibration episodes. The heartbeat n' is in an ABP calibration episode if the $t_{\mathrm{SBP}}(n')$ is

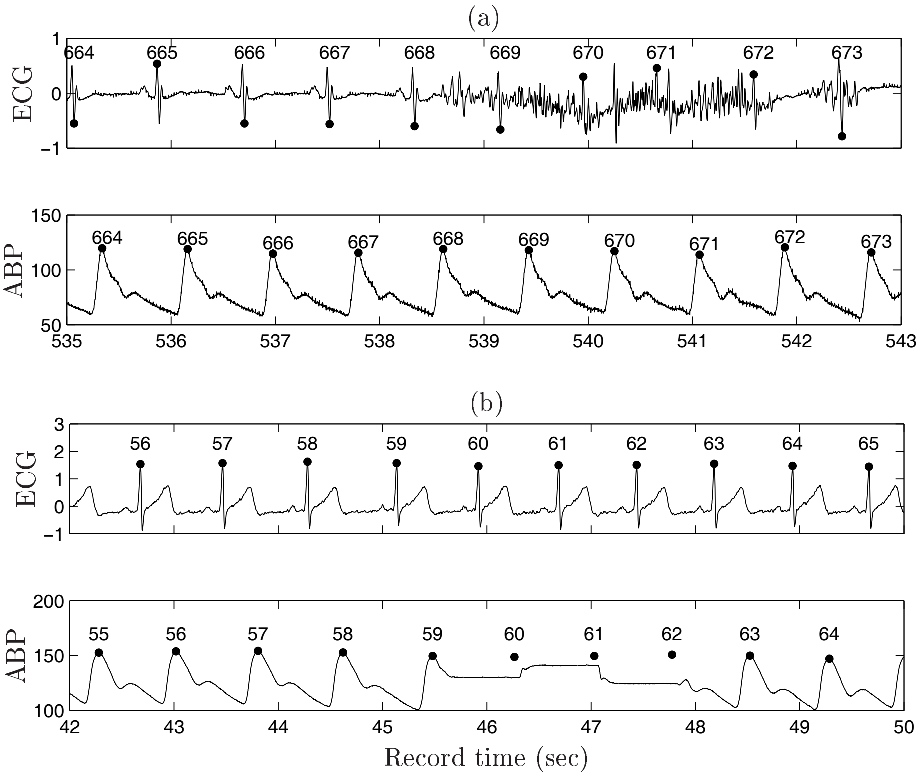

Figure 2.26: Same data as in Fig. 2.25, showing the QRS and SBP marks after the correction of time alignment errors.

missing, the $x_{\mathrm{PI}}(n')$ is labelled as long and $s_{\mathrm{ABP}}(n')$ is labelled as low. The correction due to calibration episodes is the first one to be carried out because the ABP signal is lost from time to time, if the calibration mode is switched on, and the occurrence of many of these episodes might affect the accuracy of the $\hat{x}_{\mathrm{RR}}(n')$ labelling as short/long intervals. Next, steps (2) and (3) consist of the detection of FN in the ECG and ABP signals, respectively. Regarding step (3), it comprises the detection of FN in the ABP signal due to other reasons besides the occurrence of calibration episodes (e.g., due to unexpected lower variance in the ABP amplitudes, see Fig. 2.23). Finally, steps (4) and (5) are related with the detection of FP in the ECG and ABP signals, respectively.

After the detection of time alignment errors, FN detections are corrected by inserting marks and FP detections of FP are corrected by removing marks, as detailed ahead. After the execution of each step of detections/corrections, the $t_{\mathrm{QRS}}(n')$ and $t_{\mathrm{SBP}}(n')$ are renumbered and the $x_{\mathrm{RR}}(n')$, $x_{\mathrm{PI}}(n')$ and $s_{\mathrm{ABP}}(n')$ series are updated. Finally, the time alignment condition (2.14) is verified between the execution of each step.

Correction of FN detections: inserting marks

Missing SBP marks are inserted such that the condition (2.14) is satisfied. A missing $t_{\mathrm{SBP}}(n)$ mark obliges the computation of both $\hat{t}_{\mathrm{SBP}}(n)$ and $\hat{x}_{\mathrm{SBP}}(n)$ values. First, the timing of the

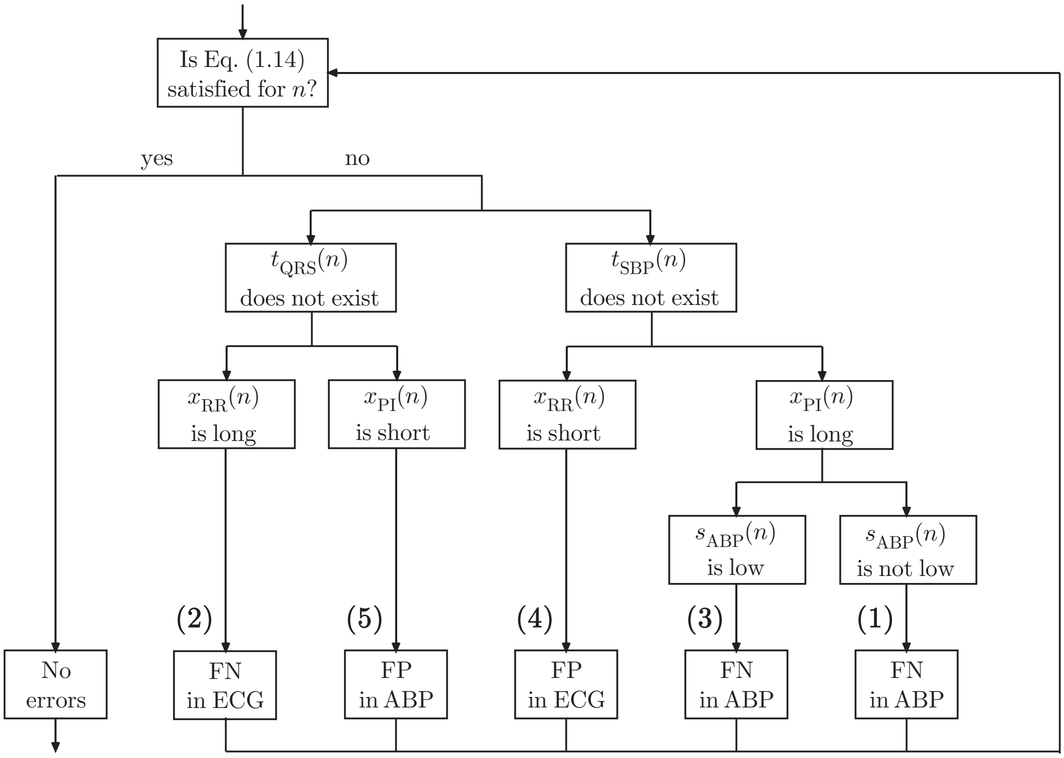

Figure 2.27: Flowchart providing an overall view of the procedure implemented to detect time alignment errors. The numbers indicate the execution order of the detections/corrections: FP stands for False Positives and FN stands for False Negatives.

mark is estimated as

$$\hat{t}_{\mathrm{SBP}}(n) = t_{\mathrm{QRS}}(n) + \hat{x}_{\mathrm{PPT}}(n), \tag{2.16}$$

where $\hat{x}_{\mathrm{PPT}}(n)$ is obtained by cubic spline interpolation from the existing x_{PPT} values. After, the corresponding $\hat{x}_{\mathrm{SBP}}(n)$ is obtained by cubic spline interpolation from the existing x_{SBP} values. The missing $t_{\mathrm{SBP}}(n)$ marks are inserted by interpolation if the episodes are up to 12 beats length. In the case of the ECG, the procedure is the analogous with

$$\hat{t}_{\mathrm{QRS}}(n) = t_{\mathrm{SBP}}(n) - \hat{x}_{\mathrm{PPT}}(n). \tag{2.17}$$

This way of inserting marks maintains the tendency in $x_{\mathrm{PPT}}(n)$ series and preserves the cumulative sum of the distances between consecutive peaks, expressed in the $\hat{x}_{\mathrm{RR}}(n)$ and $\hat{x}_{\mathrm{PI}}(n)$ series, equal to the overall record time.

Correction of FP detections: removing marks

The correction of false positive assume that the *true* marks were detected by one of the beat detection systems. The $t_{\mathrm{SBP}}(n')$ marks to be removed are chosen such as their removal does not introduce an updated $x_{\mathrm{PI}}(n')$ value labelled as long. In the case of the ECG, the procedure is the same.

2.3 Measures extracted from RESP and MSNA signals

As previously referred, the BRS estimate is computed from the SBP and RR beat-to-beat series. In this thesis, the BRS analysis was also associated with respiration and sympathetic activity. The methods used to extract measures from the beat-to-beat RESP and MSNA series are described in the following sections. With respect to respiration, the BRS analysis was studied with respect to the respiratory frequency, estimated with the use of the methods described in Sec. 2.3.1. On the other hand, the quantification of the sympathetic activity in a recording was based on an automatic detector of MSNA bursts, presented in Sec. 2.3.2.

2.3.1 Estimation of the respiratory frequency

The respiratory signal reflects the breathing phases, inspiration and expiration. The breathing pattern is also characterized by the frequency of the RESP signal (f_r), with faster breathing being reflected in a RESP signal with a higher frequency content. In a stationary breathing condition, the RESP signal is similar to a sinusoidal of a certain amplitude and frequency f_r, and this value can be estimated from the power spectral density (PSD) function of either the RESP signal itself or the $x_{\text{RESP}}(n)$ series (see Fig. 2.1).

There are nonparametric and parametric methods for PSD estimation (Manolakis *et al.*, 2000). The basic idea of parametric methods is that if a $x(n)$ series depends on a finite set of parameters, then all of its statistical properties can be expressed in terms of the model, including its autocorrelation and PSD function. Additionally, parametric methods for PSD estimation allow to automatically identify the central frequency of each spectral component (Zetterberg, 1969). This property facilitates the estimation of the respiratory frequency in a recording once, in stationary breathing conditions, the RESP signal and the $x_{\text{RESP}}(n)$ series exhibit one dominant frequency.

In this work, the estimation of the respiratory frequency f_r was carried out from the PSD of the respirogram $x_{\text{RESP}}(n)$, which was computed from autoregressive (AR) modelling. The AR order p model of a series $x(n)$ can be written as

$$x(n) = -\sum_{k=1}^{p} a_p(k)x(n-k) + b(0)w(n), \tag{2.18}$$

where $w(n)$ is a zero-mean stationary white noise process with unit variance, and the PSD function of an AR model is estimated by

$$\widehat{S}_{xx}\left(e^{j\omega}\right) = \frac{\left|\hat{b}(0)\right|^2}{\left|1 + \sum_{k=1}^{p} \hat{a}_p(k) e^{-jk\omega}\right|^2} \tag{2.19}$$

where $\hat{a}_p(1), \hat{a}_p(2), ..., \hat{a}_p(p)$ and $\hat{b}(0)$ are the estimates of the model coefficients in Eq. (2.18). In this work, the coefficients of the model were estimated by solving the Yule-Walker equations via Levinson-Durbin algorithm (Marple, 1987).

If the model order p is not known a priori, the optimal model order can be estimated using an automatic criteria, such as the Akaike Information Criterion (Akaike, 1974). In the case of stationary respiration, only one spectral component will be exhibit in the PSD of the $x_{\text{RESP}}(n)$ series. Therefore, a fixed model order of $p = 2$ can be used. In this work, $p = 4$ was used to avoid errors in f_r estimation due to, e.g., the presence of two breathing frequencies in the same recording (non stationary respiratory frequency). The respiratory frequency is then taken as the central frequency of the component that exhibits the largest variance.

Figure 2.28 shows an excerpt of the $x_{\text{RESP}}(n)$ obtained from a 5 minute recordings together with the corresponding PSD, computed from AR modelling and $p = 4$. It is possible to

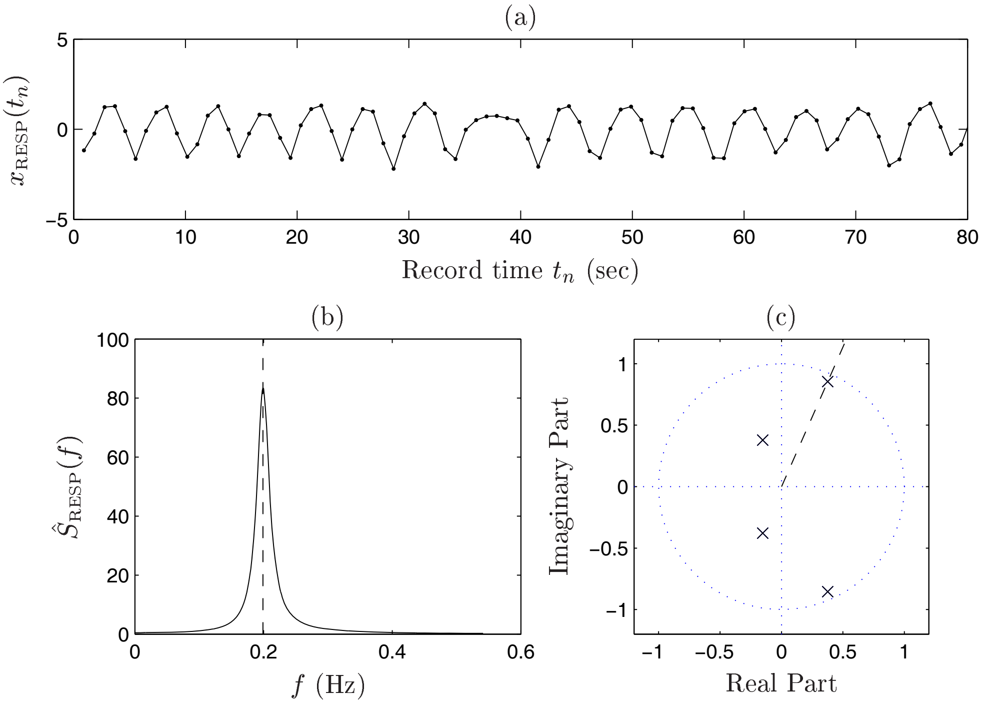

Figure 2.28: RESP series $x_{\text{RESP}}(n)$ (a), spectra (b) and correspondent zero-pole representation (c). Spectra computed from AR modelling, Yule-Walker equations and $p = 4$. The time axis in (a) was obtained by multiplication of the sample number by RR mean. Frequency axis in (b) was normalized by RR mean, i.e., $f = \frac{\omega}{2\pi}\frac{1}{\bar{x}_{\text{RR}}}$.

observe in Fig. 2.28(b–c) that one of the spectral components exhibits much higher variance than the other (in linear scale, the component of lowest variance is not perceptible). The central frequency of the largest variance component is $f_r = 0.2$ Hz, and is taken as the respiratory frequency for that recording. Figure 2.28(c) shows the zero-pole representation in the unit circle, illustrating that the poles associated with f_r are closer to the unit circle, thus, indicating a sharp component in the spectra. This evidences that the respiratory frequency is stable along the recording.

One possible drawback of estimating the respiratory frequency from the $x_{\mathrm{RESP}}(n)$ series is that, unlike the RESP signal, it exhibits non uniform sampling and its values are indexed to the heartbeat occurrence. However, as the PSD estimation method assumes that the discrete series are wide-sense stationary, the frequency axis in the spectra can be normalized assuming a uniform sampling period equal to the mean RR interval, i.e., the mean duration of a heartbeat. The approximation $F_s \approx 1/\bar{x}_{\mathrm{RR}}$ for the sampling frequency of the $x_{\mathrm{RESP}}(n)$ series allows to estimate a respiratory frequency from the $x_{\mathrm{RESP}}(n)$ series similar to that of the RESP signal, in stationary recordings.

2.3.2 Measures extracted from the MSNA signal

As already referred, the MSNA signal is characterized by synchronous neuronal discharges separated by periods of neural silence, see Fig. 2.29(a), and increases in sympathetic activity can be evidenced by greater MSNA burst occurrence and/or increased MSNA burst intensity, see Fig. 2.29(b).

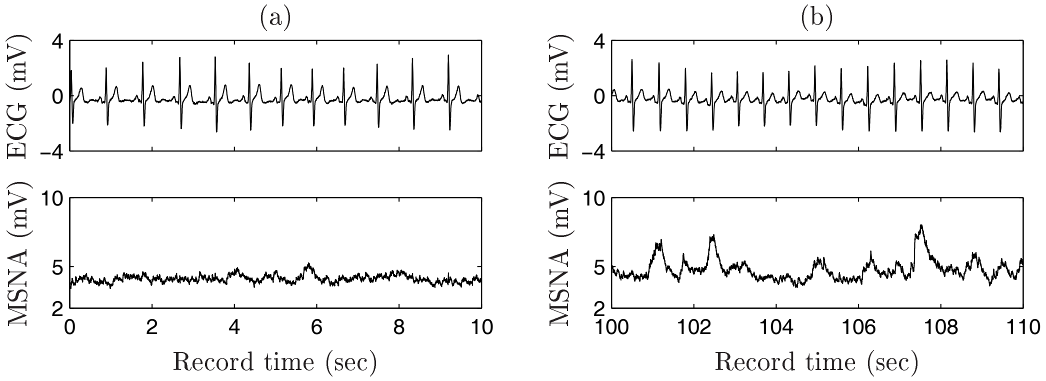

Figure 2.29: ECG and MSNA signals from one subject in (a) spontaneous and in (b) increased sympathetic activity condition by a nitroprusside bolus. Same data as in Fig. 1.5.

In this work, the sympathetic activity in a recording was quantified with measures based on bursts counting ($\mathcal{N}$) and bursts area ($\mathcal{A}$). As summarized in Table 2.1, the *burst incidence* and *burst frequency* are computed as the number of MSNA bursts normalized by the number of heart beats ($\mathcal{N}_{\mathrm{HB}}$) and the recording length in min ($\mathcal{N}_{\mathrm{T}}$), respectively. The burst incidence determines the number of multiunit sympathetic discharge over a given number of cardiac cycles, and provides an index of sympathetic activity that is independent of changes in heart rate (Wallin, 2007). The *burst intensity* is calculated by integrating the MSNA signal over the entire experimental recording and, analogously to $\mathcal{N}$, the area $\mathcal{A}$ is normalized for either the number of heart beats ($\mathcal{A}_{\mathrm{HB}}$) or the recording length in min ($\mathcal{A}_{\mathrm{T}}$).

Table 2.1: Summary of MSNA variables evaluated for each recording (HB stands for heartbeat).

Var	**Description**	**Units**
$\mathcal{N}_{\mathrm{HB}}$	burst incidence	# bursts/100HB
$\mathcal{N}_{\mathrm{T}}$	burst frequency	# bursts/min
$\mathcal{A}_{\mathrm{HB}}$	burst intensity	area/100HB
$\mathcal{A}_{\mathrm{T}}$	burst intensity	area/min

The estimation of the variables $\mathcal{N}_{\mathrm{HB}}$ and $\mathcal{N}_{\mathrm{T}}$ in Table 2.1 requires the counting of the bursts and, indirectly their detection. Additionally, the burst delineation is required to estimate the variables $\mathcal{A}_{\mathrm{HB}}$ and $\mathcal{A}_{\mathrm{T}}$. Traditionally, the detection of MSNA bursts is done by careful visual inspection of a trained observer (van de Borne *et al.*, 1997; Beloka *et al.*, 2009). Semi-automatic algorithms have been proposed for the same purpose, with a MSNA burst being recognized on the basis of an apriori user-defined voltage (Pagani *et al.*, 1997) and time thresholds (Hamner and Taylor, 2001). In particular, the algorithm proposed by Hamner and Taylor (2001) requires the apriori user definition of burst latency with respect to the QRS complex in the ECG signal to obtain a search time window for the MSNA burst.

The method developed in this work for automatic MSNA burst identification, was inspired in the description of a MSNA burst provided in the work of Hamner and Taylor (2001):

"The generally accepted criteria for burst identification are based mainly on morphology to discriminate sympathetic activity from background noise (i.e., a relatively gradual rise followed by a similarly sloped fall with a peak amplitude at least two times greater than random fluctuations)."

Figure 2.30 outlines the method developed from MSNA burst detection and delineation. The MSNA signal is first subjected to noise reduction: in this step, $\mathcal{M}_{\mathrm{C}}$ is obtained after baseline correction and background noise reduction from the acquired MSNA signal. The $\mathcal{M}_{\mathrm{C}}$ signal is then used to automatically identify the MSNA bursts and to compute the $x_{\mathrm{MSNA}}(n)$ series.

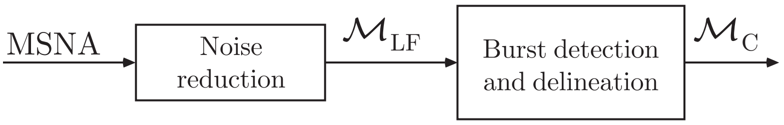

Figure 2.30: Block diagram displaying the two major steps of the method developed for MSNA burst detection and delineation.

The stages of the method are also illustrated in Fig. 2.31: from the acquired MSNA signal (a), the $\mathcal{M}_{\text{LF}}$ signal is obtained by noise reduction, i.e., removal of the zero nerve activity level and the baseline. Once the MSNA bursts are identified and delineated (b), the sections of signal between the offset of bursts and the onset of the next burst are set to zero, providing a clean $\mathcal{M}_{\text{C}}$ signal for further analysis (c). The $x_{\text{MSNA}}(n)$ beat-to-beat series and the interval measures given in Table 2.1 are then estimated.

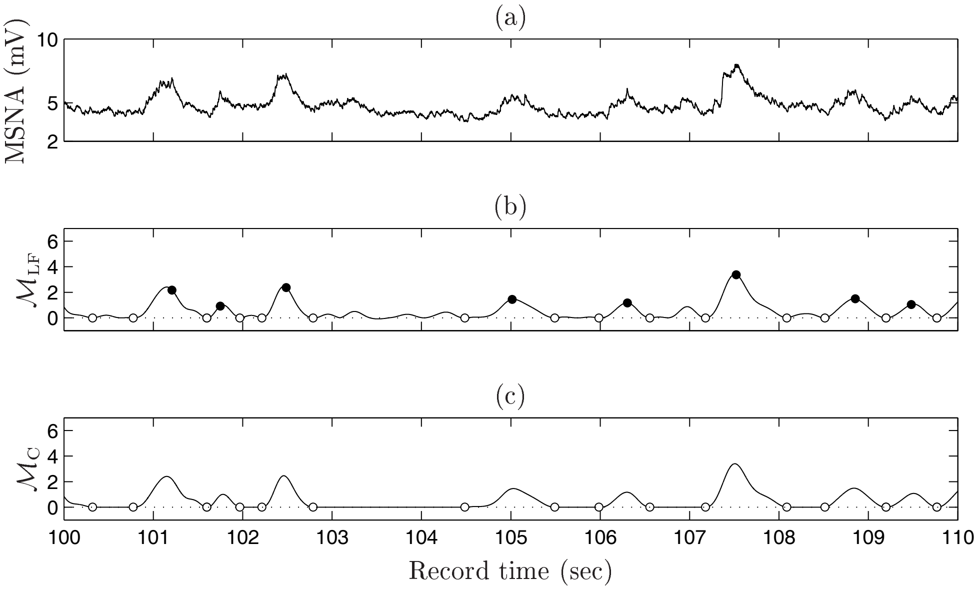

Figure 2.31: MSNA processing steps illustrated with experimental data. The black circles localize the peak of the identified burst, while the white circles delimitate the beginning/end of each burst. Same data as in Fig. 2.29.

2.3.2.1 Noise reduction

Before burst detection and delineation, the MSNA is subjected to noise removal, in particular, removal of the zero nerve activity and baseline.

Estimation and removal of zero nerve activity level

In manual burst detection, the background noise (or zero nerve activity level) is usually determined from the mean voltage during a period of neural silence between sympathetic bursts. As an example, Halliwill (2000) found manually in each recording a period in which sympathetic bursts were absent for >5 sec and used it to estimate the zero nerve activity level. In automatic burst identification, algorithms based on apriori user-defined voltage have been proposed (Pagani *et al.*, 1997).

However, to determine periods of neural silence, the MSNA bursts have to de identified, what is by turn, the purpose of the method. Nevertheless, the zero nerve activity level can be estimated by means of signal processing techniques. As a matter of fact, the zero nerve activity level corresponds to the HF content of the MSNA signal and, therefore, it can be obtained by means of high pass filtering of the MSNA signal. The frequency response of the filter used is represented in Figure 2.32. The cutoff frequency of 4 Hz was chosen in accordance with the work of Hamner and Taylor (2001) and the non constant delay of the filter was corrected by processing the input data in both the forward and reverse directions, such as the output of these operations has zero-phase distortion and double the filter order (Sörnmo and Laguna, 2005).

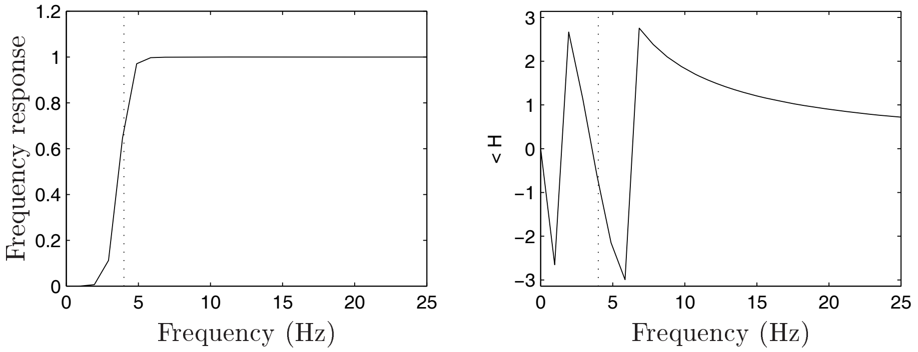

Figure 2.32: Frequency response of the filter used for the estimation of the zero nerve activity level: Butterworth high pass filter with order 7 and cutoff frequency of 4 Hz (F_s=1000Hz).

Figure 2.33 shows the output of the high-pass filter which represents the zero nerve activity level $\mathcal{M}_{\mathrm{HF}}$. The background noise free signal $\mathcal{M}_{\mathrm{LF+VLF}}$ is obtained by subtraction of the $\mathcal{M}_{\mathrm{HF}}$ to the original MSNA signal.

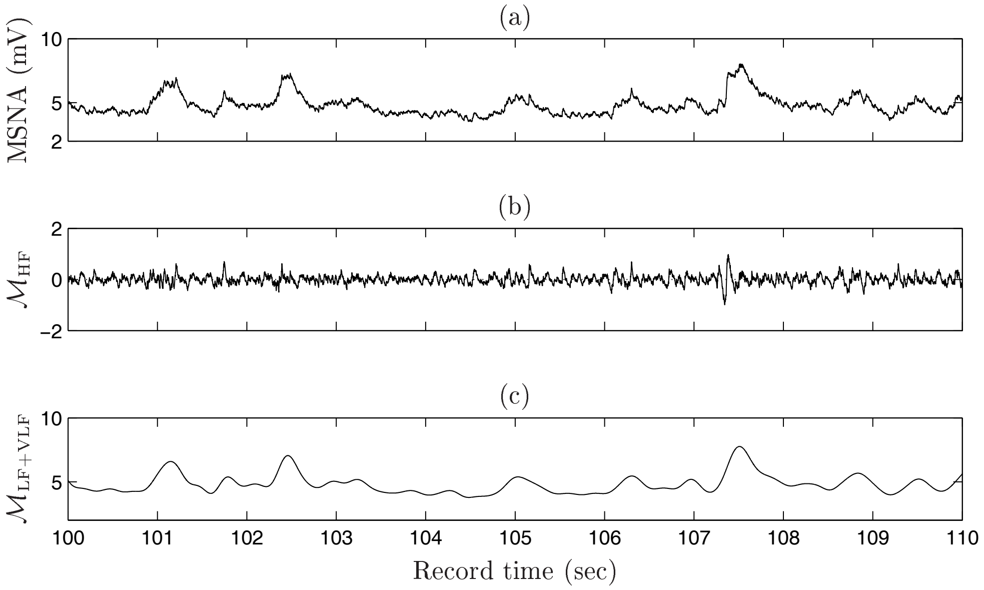

Figure 2.33: Example of MSNA noise reduction due to background noise. Same data as in Fig. 2.31.

Estimation and removal of MSNA baseline

The MSNA baseline corresponds to the very low frequency content of the MSNA signal and, therefore, it could be obtained by means of low pass filtering of the MSNA signal. The work of Hamner and Taylor (2001) proposes the cutoff frequency of 0.05 Hz for signals sampled at 500 Hz and no further details on the type of the filter are provided. However, the choice of a suitable cutoff frequency is quite difficult, because it is dependent on the sympathetic activity present in the recording. Figure 2.34 shows the $\mathcal{M}_{\text{LF+VLF}}$ signal superimposing a baseline obtained by filtering, illustrating that, in a condition of increased sympathetic activity, the baseline estimated by low pass filtering *overestimates* the baseline of the signal.

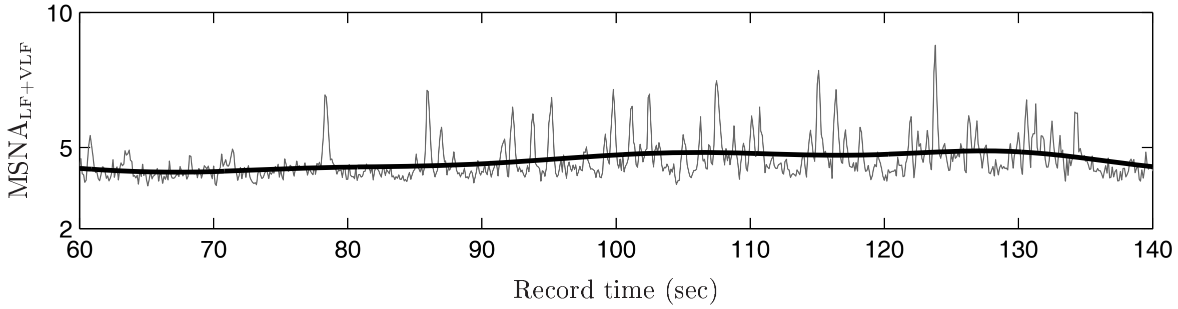

Figure 2.34: $\mathcal{M}_{\text{LF+VLF}}$ signal superimposing the baseline estimated by filtering: Butterworth low pass filter with order 7 and cutoff frequency of 0.05 Hz (F_s=100Hz). Same data as in Fig. 2.29.

An alternative approach, independent of the amount of sympathetic activity in a recording, is here presented. The method is based on the observation that after the removal of the background noise, the minimum values of the $\mathcal{M}_{\text{LF+VLF}}$ can be used to estimate the baseline.

As illustrated in Fig. 2.35, the identification of the local minimum in $\mathcal{M}_{\text{LF+VLF}}$ is performed by searching the zero crossings in its first derivative. As the $\mathcal{M}_{\text{LF+VLF}}$ is a smooth signal, the first derivative was approximated by its successive differences. The baseline $\mathcal{M}_{\text{VLF}}$ is then obtained by linear interpolation using the identified minimum values as the anchor points. The signal $\mathcal{M}_{\text{LF}}$ is finally obtained by subtracting $\mathcal{M}_{\text{VLF}}$ to $\mathcal{M}_{\text{LF+VLF}}$.

2.3.2.2 Burst detection and delineation

After noise reduction, the peaks of the burst candidates are identified between each pair of the $\mathcal{M}_{\text{LF+VLF}}$ local minimums, previously identified for the purpose of baseline removal (see Fig. 2.35). From the candidates, only the significant bursts are chosen. MSNA bursts are characterized by a gradual rise and fall that is usually constrained by a cardiac cycle and exhibits at least twice the amplitude of random fluctuations (Hamner and Taylor, 2001).

The amplitude of random fluctuations was quantified from the standard deviation of the estimated zero nerve activity level $\mathcal{M}_{\text{HF}}$. The cutoff threshold for the identification of significant peaks was considered to be γs, where γ represents a constant value and s estimates the $\mathcal{M}_{\mathrm{HF}}$ standard deviation. To achieve a more robust estimate for s, only the $\mathcal{M}_{\mathrm{HF}}$ negative values were considered and s is computed as the square root of the mean square difference of each negative amplitude to zero (the expected value of the noise). This procedure avoids bias introduced by the positive $\mathcal{M}_{\mathrm{HF}}$ values, which are more likely to be associated with MSNA bursts than the negative ones. In this work, $\gamma = 3$ was considered, because $3s$ includes more than 99% of the distribution of the noise values assuming a normal distribution.

After the identification of the significant candidates, as is illustrated in Fig. 2.36, the burst onset and offset are delineated as the nearest local minima on either side of the peak of the detected burst in the second derivative of $\mathcal{M}_{\mathrm{LF}}$.

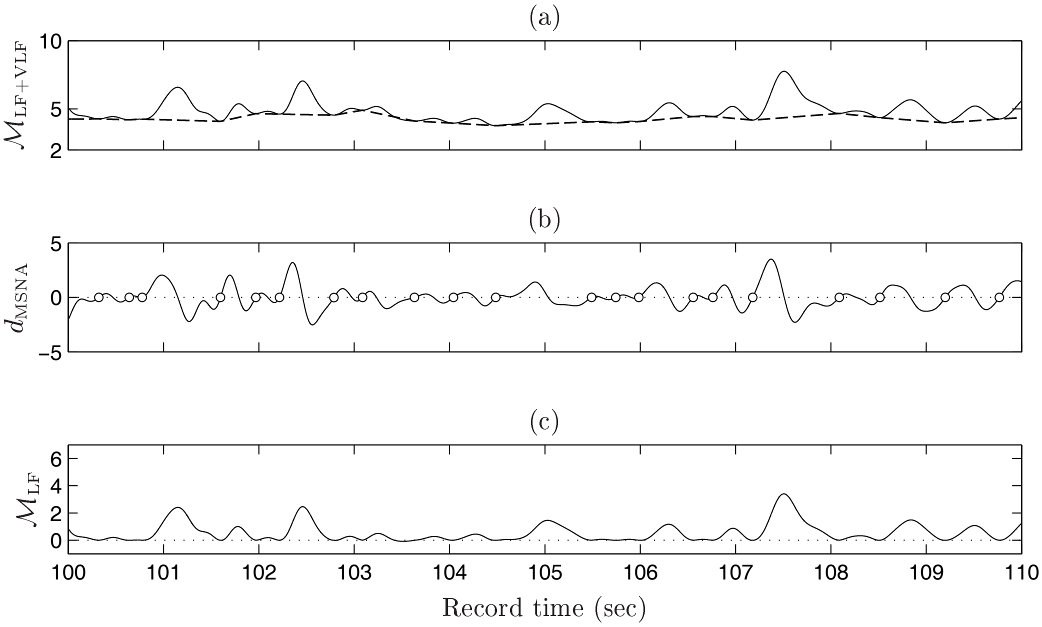

Figure 2.35: Example of MSNA noise reduction due to baseline. Same data as in Fig. 2.31.

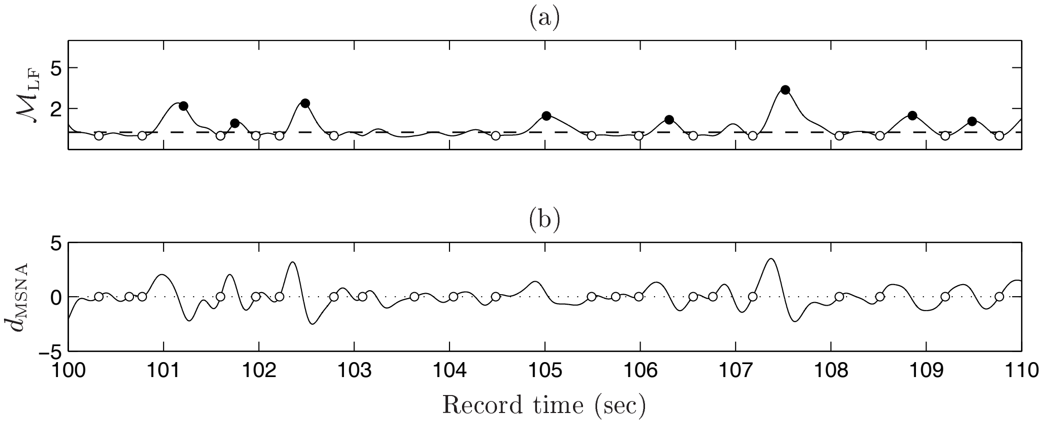

Figure 2.36: Illustrative example of the MSNA burst detection and delineation. The black circles localize the peak of the identified burst, while the white circles delimitate the beginning/end of each burst. Same data as in Fig. 2.31.

2.3.2.3 Illustrative examples

The performance of the MSNA burst detector is illustrated with experimental data that included manual burst annotations in *bisoprolol* recordings (Beloka *et al.*, 2009). As is illustrated in Fig. 2.37 for one MSNA recording, the automatic MSNA burst detector identifies most of the manually annotated burst, except the bursts exhibiting very low amplitudes.

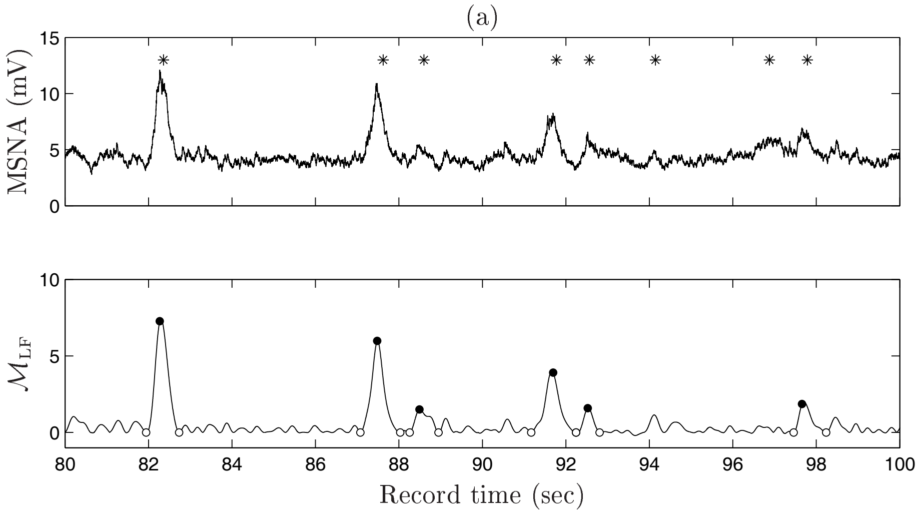

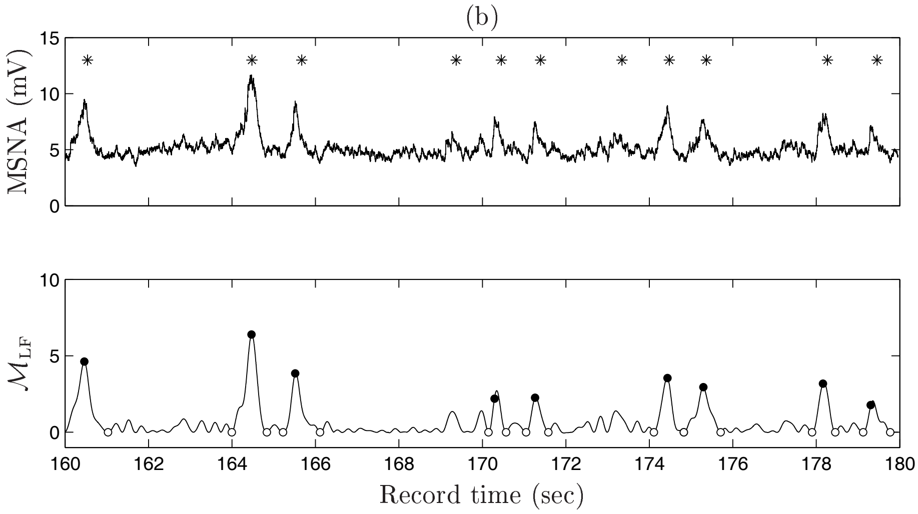

Figure 2.37: MSNA signal showing marks provided by manual burst identification (black stars) and by automatic burst detection/delineation (black circles, $\gamma = 3$). The white circles delimitate the beginning/end of each burst provided by the automatic delineation.

2.4 Concluding remarks

In this chapter, the methods used to extract series of beat-to-beat variability from the acquired signals are described. By one hand, the series extracted from the ABP and ECG signals (SBP and RR series, respectively) are used to compute the BRS. By the other hand, the series extracted from the RESP and MSNA signals are used to evaluate the BRS interactions with respiration and ANS sympathetic activity.

The parallel ECG and ABP analysis with following fusion of the results allows a more robust beat detection. As a matter of fact, this approach is expected to minimize the effects of the noise sources, because those likely to occur in the ECG and ABP signals are typically uncorrelated. Also, the development of methods to process the ABP signal independently of the ECG is well-justified in the scope of this work, because it is possible to extract from the ABP signal the two beat-to-beat series required to compute a BRS estimate. The performance of the multimodal beat detector is illustrated with experimental data including periods of EMG noise contamination in the ECG and ABP calibration episodes.

The ECG beat detection is carried out with the Wavedet beat detector, i.e., the QRS detector previously implemented and evaluated by our group (Martínez *et al.*, 2004). This detector is based on the Wavelet multiscale decomposition of the input signal and processing of the wavelet scales that exhibit most of the QRS energy. This system was validated using several standard annotated databases and has been shown to be robust to noise non overlapping the QRS complex frequency band, outperforming other algorithms (Martínez *et al.*, 2004). The ABP beat detection is carried out with the Wavedet beat detector, as well. However, because the ABP exhibits different frequency content in comparison with the ECG, the ABP signal is first preprocessed with a LPD filter. The use of the Wavedet beat detector in ABP signals highlights the properties of this system as a versatile tool for peak detection. Finally, the fusion of the QRS and SBP marks obtained from the independent ECG and ABP beat detectors is carried out by time alignment of the marks and correction of eventual time alignment errors.

In this work, the interactions between the BRS analysis (carried out from the SBP and RR series) were also explored with respect to respiration and ANS sympathetic activity. On one hand, the BRS analysis is associated with the respiratory frequency of the subject. The RESP frequency is estimated from parametric spectral analysis of the RESP beat-to-beat series, which allows to automatically identify the central frequency of each spectral component of the series. On the other hand, the BRS analysis is associated with measures of ANS sympathetic activity. The quantification of the sympathetic activity is based on burst countings and computation of bursts area, which imply prior identification of the MSNA bursts. The MSNA signal is first subjected to noise reduction and then the bursts are identified with a constant threshold based on the MSNA background noise. The performance of the methods is illustrated with experimental data, showing that the automatic MSNA burst detector identifies most of the manually annotated bursts.

Chapter 3

Time Domain BRS Estimation from Spontaneous Data

This chapter comprises the description and the study of the time domain methods for spontaneous BRS assessment.

The limitations of the well established sequences technique are discussed. In a first study, a sensitivity analysis on the thresholds used for the identification of baroreflex sequences is carried out, what motivated and justified the use of the improved BRS analysis proposed in this thesis (the events technique).

The traditional BRS analysis by the sequences technique and the improved BRS analysis by the events technique are then compared in spontaneous data from the EuroBaVar dataset. It is discussed the ability of the methods to provide a BRS estimate and to distinguish conditions in which the BRS is expected to be changed, as well as the reproducibility and the dispersion in the BRS analysis. The sequences and events technique estimates are finally compared with other time domain methods.

3.1 Motivation to improve time domain BRS assessment

The **sequences technique** is a frequently used time domain method for spontaneous BRS estimation, thanks to its ease of interpretation and implementation (Di Rienzo *et al.*, 2001). This method is based on the identification of baroreflex sequences (BSs) and linear regression over the corresponding SBP and RR values. An overall estimate is obtained by averaging the slope estimates from all BSs identified in a record. In spite of its simplicity, this technique fails to provide an estimate for low BRS patients, depending of the parameters used. As a result, this method is considered by some authors to have limited value for the BRS quantification in autonomic dysfunction cases (Oka *et al.*, 2003), which are the crucial cases to identify. Therefore, performance improvements that preserve simplicity are needed.

The sequences technique was first used in sinoaortic denervated cats (Di Rienzo *et al.*, 1985; Bertineri *et al.*, 1988). The spontaneous BSs appeared to reflect baroreflex mechanisms as their number (and mean slope) was drastically reduced after denervation. Studies in humans confirmed the existence of such BSs and reported similar results in subjects with poor BRS function (Frattola *et al.*, 1997). In practice, several thresholds are imposed for BSs identification and no consensual opinion about their values can be found in the literature. Slight modifications in threshold values can change the number of BSs and the BRS estimate (Davies *et al.*, 2001), and the elimination of certain thresholds has also been suggested (Davies *et al.*, 2001; Westerhof *et al.*, 2004). Moreover, the need of establish reference threshold values is evident, because the threshold values originally derived for cats are most likely non-optimal for humans. Literature studies argue that changes should be made to the sequences technique, to optimize its validity in conscious humans, particularly when applied to patients with attenuated BRS (Davies *et al.*, 2001) and also to establish reference BRS values to evaluate impaired baroreflex function in individual patients (Tank *et al.*, 2000).

In normal cases, the overall number of beats in BSs is approximately one fourth of the total number of beats (Bertineri *et al.*, 1988) and, consequently, a large part of the acquired data is discarded from BRS analysis. Also, more than half of the BSs have 3-beat length (Parlow *et al.*, 1995), implying that the BRS estimate is more likely to be influenced by outlier values. In cases of BRS dysfunction, the number of BSs is further reduced so that the slope estimate will exhibit higher dispersion. In cases of BSs being unavailable, the BRS cannot be quantified. The validity of BRS estimates obtained from short and few segments remains to be addressed (Laude *et al.*, 2004).

The sequences technique already benefits from its use in many clinical trials and in many experimental settings (Parati *et al.*, 2000): the full description of the sequences technique was first published in the work of Bertineri *et al.* (1988) and since then it has been used in many clinical studies in baroreflex field of research. However, given the popularity of this method among the spontaneous methods for BRS assessment, it is surprising that few methodological studies have been reported. The major part of these studies are simply comparisons of the BRS estimates obtained by different methods (Laude *et al.*, 2004) or the use of different thresholds (Davies *et al.*, 2001), and studies of BRS reproducibility (Davies *et al.*, 1999), either using datasets of recordings acquired from normal subjects or patients.

In this work, reference threshold values are established to identify alternative baroreflex related segments, here referred as baroreflex events (BEs). The use of BEs is introduced as an alternative to BSs, to improve time domain BRS assessment in normal conditions and to allow its quantification in cases of BS absence. Also, alternative slope estimators combined with BEs are proposed to increase robustness, to increase reproducibility and to decrease dispersion in the BRS estimation. The joint use of BEs and global slope estimators constitutes the **events technique**.

The BRS estimation methods are presented in Sec. 3.3. In this work, there was an effort to formalize the methods for time domain BRS assessment and to explain the differences between the BRS estimators and the data transformations involved. The illustrative comparison of the different BRS methods is also provided. The sensitivity analysis on the thresholds used for BSs identification is the first study carried out (Sec. 3.4). The results obtained further motivate and justify the use of the BEs instead of the BSs, for an improved BRS analysis. The novel methods are then compared to the traditional methods for BRS estimation in Sec. 3.5. The BRS methods were compared regarding their ability to provide a BRS estimate able to distinguish conditions in which the BRS is expected to be changed (e.g. lying and standing positions). Besides the quantification of the BRS reproducibility with the novel methods, the time domain BRS estimators are additionally studied with respect to dispersion, which is usually disregarded in BRS analysis. Finally, the results obtained are discussed in Sec. 3.6 and the main conclusions are resumed in Sec. 3.7.

3.2 Experimental protocol and data: the EuroBaVar dataset

The EuroBaVar dataset consists of spontaneous recordings, available for the comparison of BRS estimation procedures.

This dataset has 46 paired records of spontaneous ECG and ABP recordings, acquired from 21 subjects in lying and standing positions (Laude *et al.*, 2004). The data is provided in 10 minute records of ABP and ECG signals, acquired at 500 Hz. The data is additionally provided on a beat-to-beat basis, with the length of the RR and SBP series ranging from 553 to 1218 beats. For illustration purposes, Fig. 2.2 shows an excerpt of one of the files included in the dataset.

The recordings were acquired in stationary conditions: quiet room, constant temperature and luminosity; only one person in the room besides the subject; disturbance, such as noise or entry in the room, was avoided. Each subject was first recorded in standing position and the recording started after 5 min standing. After followed the supine position and the recording started after 5 min supine. In between conditions, there was a 10 min rest period, when the ABP finger cuff was removed and patients could speak. The ABP and ECG signals were acquired following the acquisition protocol presented in Sec. 1.3.1.

The EuroBaVar dataset is non-homogenous: one subject is diabetic with evident cardiac autonomic neuropathy and another is recently heart transplanted, both classified as cardiac baroreflex failure patients by the Ewing score. The remaining 19 subjects are 12 normotensive outpatients, 1 untreated hypertensive, 2 treated hypertensive and 4 healthy volunteers. In addition, replica records of two subjects were incorporated to test reproducibility. There is no information about the match of each subject to its corresponding records.

3.3 The Sequences and the Events techniques

The time domain methods for BRS assessment are based on 2 steps: first the identification of baroreflex related segments (sequences or events) and then BRS estimation from SBP–RR slope. The sequences technique is based on BSs identification and on the average of the slopes computed at each BS (Di Rienzo *et al.*, 2001), here referred as local approach for slope estimation. The events technique, proposed as an alternative to the sequences technique to improve BRS assessment, introduces the baroreflex events (BEs) and the use of global/total slope estimators.

The BRS analysis is performed over the SBP and RR series, denoted here as $x_{\text{SBP}}(n)$ and $x_{\text{RR}}(n)$ respectively, with $n = 1, 2, \ldots, N_{max}$ indicating the beat number. The BRS analysis is carried out considering the series with one beat lag, i.e., $x_{\text{SBP}}(n-\tau)$ is paired with $x_{\text{RR}}(n)$ for $\tau = 1$. The lag $\tau = 1$ is in accordance with the baroreflex physiology (see SBP and RR phase dependencies in Sec. 2.1 and Fig. 2.1) and with the SBP and RR lag considered in previous BRS studies (Di Rienzo *et al.*, 2001).

In this section, the methods for BRS estimation are illustrated with the EuroBaVar "A001LB" file, using the first N_{max}=512 beats.

3.3.1 The Sequences technique

A diversity of threshold values is used in the literature for BS identification (Davies *et al.* (2001) and references therein included). In general, the k^{th} BS must have a minimum length in beats ($N_k \geq N_{min}$), with the composing beats satisfying a minimum SBP and RR beat-to-beat changes in the same direction ($\Delta_k^{\text{SBP}} \geq \Delta_{min}^{\text{SBP}}$ and $\Delta_k^{\text{RR}} \geq \Delta_{min}^{\text{RR}}$), and a minimum correlation between the SBP and RR values in BSs ($r_k \geq r_{min}$). In this work, the threshold values $\Delta_{min}^{\text{SBP}} = 1$ mmHg, $\Delta_{min}^{\text{RR}} = 5$ msec and $r_{min} = 0.8$ were chosen as referred by group that originally proposed the sequences technique for BRS estimation (Di Rienzo *et al.*, 2001).

Figure 3.1 displays $x_{\text{SBP}}(n-1)$ and $x_{\text{RR}}(n)$ in BSs identified in a record, illustrating that BSs are simultaneous SBP and RR ramps over time and that BSs are short segments, typically with length up to 5 beats.

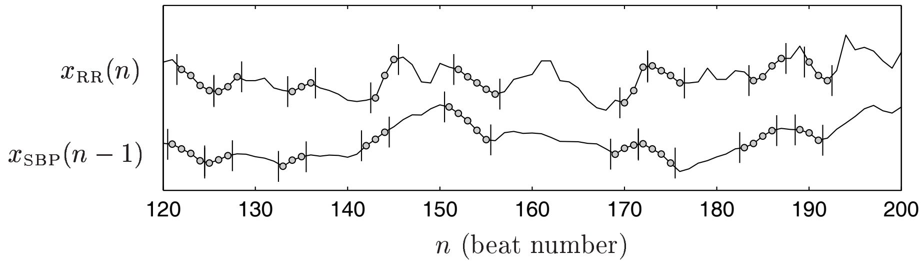

Figure 3.1: Values of $x_{\text{SBP}}(n-1)$ and $x_{\text{RR}}(n)$ for BS identified in the EuroBaVar “A001LB” file.

After SBP and RR segmentation, each identified BS$_k$, $k = 1, 2, \ldots, K$ is characterized by N_k pairs of values $(\mathbf{x}_{\text{SBP}}^k, \mathbf{x}_{\text{RR}}^k)$ beginning at index n_k, that is,

$$\begin{aligned}
\mathbf{x}_{\text{SBP}}^k &= \Big[x_{\text{SBP}}(n_k - 1) \quad x_{\text{SBP}}(n_k) \quad \cdots \quad x_{\text{SBP}}(n_k + N_k - 2) \Big] \\
\mathbf{x}_{\text{RR}}^k &= \Big[x_{\text{RR}}(n_k) \quad x_{\text{RR}}(n_k + 1) \quad \cdots \quad x_{\text{RR}}(n_k + N_k - 1) \Big] .
\end{aligned}$$

The local approach provides a local BRS measure b_k associated to the k^{th} baroreflex related segment, assuming the linear regression

$$\mathbf{x}_{\text{RR}}^k = b_k \, \mathbf{x}_{\text{SBP}}^k + c_k \, \mathbf{1}_{N_k} + \boldsymbol{\epsilon}_k, \quad k = 1, 2, \ldots, K \tag{3.1}$$

where $\boldsymbol{\epsilon}_k$ is a vector of residuals and $\mathbf{1}_{N_k}$ is a vector of ones with length N_k. The parameters b_k and c_k are estimated by ordinary least squares (OLS) minimization. Finally, an overall estimator is obtained from the mean of the K local slopes

$$\mathcal{B}_{\text{L,O}} = \frac{1}{K} \sum_{k=1}^{K} b_k. \tag{3.2}$$

However, the arithmetic average of the local slopes may not be the most suitable measure to describe the location of the distribution of the BRS slopes. As a matter of fact, as is illustrated in Fig. 3.2, the distribution of b_k is not symmetric and presents a positive skewness, so evidencing the inadequacy of the mean to obtain an overall BRS slope. Because of the positive skewness, the $\hat{\mathcal{B}}_{\text{L,O}}$ value is affected by the b_k values in the longer tail of the distribution and tends to provide a higher value than other robust measures of location (Wilcox, 2005).

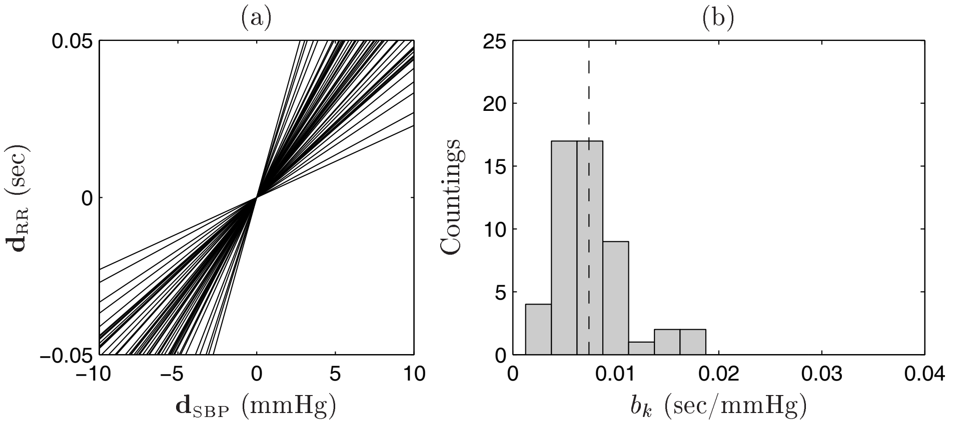

Figure 3.2: Dispersion diagram of the SBP and RR range around the mean SBP and RR value in each BS, represented by the 0 value, together with the regression lines with slope b_k and passing through the origin. (b) Histogram of the estimated local slopes with the dashed line locating the average slope $\hat{\mathcal{B}}_{\mathrm{L,O}}$. Same data as in Fig. 3.1.

3.3.2 The Events technique

As previously referred, the events technique is based on baroreflex events (BEs), instead of BSs, and it makes use of global/total slope estimators, instead of a local estimator.

In this section, the analysis of the methods is illustrated simultaneously for BSs and BEs, in order to provide an illustrative comparison of the different BRS estimators and the data transformations involved.

3.3.2.1 Identification of Baroreflex Events

The new criterion for SBP–RR segmentation consists of the identification of segments that exhibit positive and high correlation between the $x_{\mathrm{SBP}}(n-1)$ and $x_{\mathrm{RR}}(n)$ values. That is, for the identification of each baroreflex event BE_k only the thresholds N_{min} and r_{min} are enforced, as pointed out in Table 3.1.

Table 3.1: Lower thresholds values for BS and BE identification.

Threshold (Units)	BS	BE
N_{min} (beats)	3	3
$\Delta_{min}^{\mathrm{SBP}}$ (mmHg)	1	–
$\Delta_{min}^{\mathrm{RR}}$ (msec)	5	–
r_{min} (no units)	0.8	0.8

Since no minimum values for Δ_k^{SBP} and Δ_k^{RR} are required, the SBP and RR values in a BEs may not be consecutively increasing or decreasing on a beat-to-beat basis as in BSs. Instead, by only imposing the r_{min} threshold, BEs are characterized by having a similar $x_{\text{SBP}}(n-1)$ and $x_{\text{RR}}(n)$ trend over time. Therefore, for such clear conceptual differences and potentially different clinical information between BSs and BEs, it is reasonable to use a different name for the new segments.

Figure 3.3 displays the SBP and RR values in BSs and BEs identified in a record, illustrating that BEs are not necessarily simultaneous $x_{\text{SBP}}(n-1)$ and $x_{\text{RR}}(n)$ ramps over time, as BSs. Instead, BEs are segments characterized by having similar $x_{\text{SBP}}(n-1)$ and $x_{\text{RR}}(n)$ trend over time. Also, it can be observed that BEs usually achieve a longer length than BSs and that the SBP and RR values in BEs exhibit higher dispersion as a consequence of less restrictive identification thresholds.

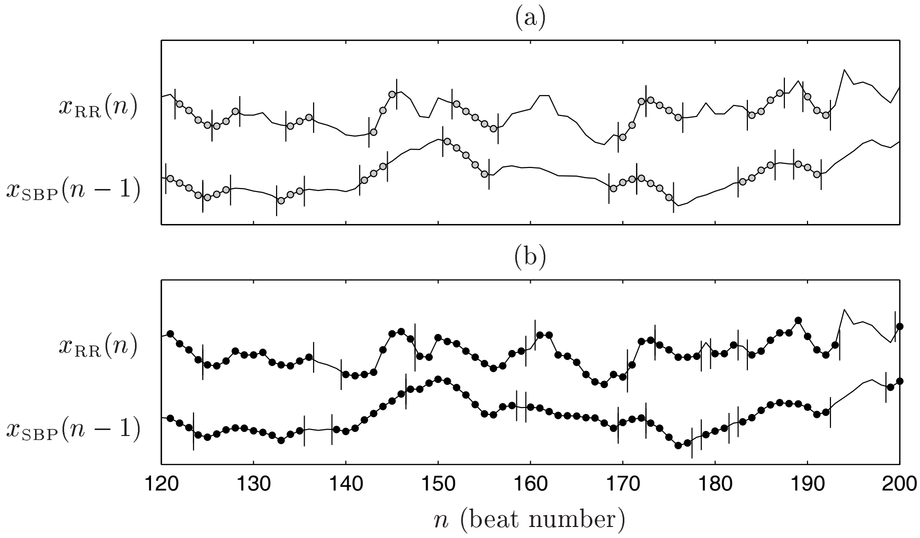

Figure 3.3: Values of $x_{\text{SBP}}(n-1)$ and $x_{\text{RR}}(n)$ for the identified (a) BS and (b) BE in the EuroBaVar "A001LB" file. There are 171 beats in 52 BSs and 448 beats in 57 BEs, in the first 512 beats of the record. Thresholds for BS and BE identification given in Table 3.1.

3.3.2.2 Global approach for slope estimation

The global approach is an alternative method for the BRS computation that has been used by our group. This approach is based on a global regression slope over the local mean detrended baroreflex related segments (Gouveia *et al.*, 2005).

After the segments identification, the corresponding pairs of values can be represented in a dispersion diagram with $\mathbf{x}_{\text{SBP}}^k$ displayed against $\mathbf{x}_{\text{RR}}^k$, as in Fig. 3.4(a–b). The k^{th} local mean detrended segment $(\mathbf{d}_{\text{SBP}}^k, \mathbf{d}_{\text{RR}}^k)$ is obtained from the original segment $(\mathbf{x}_{\text{SBP}}^k, \mathbf{x}_{\text{RR}}^k)$ by

$$\mathbf{d}_{\vartheta}^{k} = \mathbf{x}_{\vartheta}^{k} - \bar{x}_{\vartheta}^{k}\,\mathbf{1}_{N_k}, \quad \vartheta = \{\text{SBP,RR}\} \tag{3.3}$$

where $\bar{x}_{\vartheta}^{k}$ represents the mean value of $\mathbf{x}_{\vartheta}^{k}$, i.e.,

$$\bar{x}_{\vartheta}^{k} = \frac{1}{N_k}\sum_{i=1}^{N_k}\mathbf{x}_{\vartheta}^{k}(i), \tag{3.4}$$

A global BRS measure $\mathcal{B}_{\text{G,O}}$ can be considered as the slope obtained from the SBP and RR values in the identified segments, after local mean detrending, i.e.,

$$\mathbf{d}_{\text{RR}} = \mathcal{B}_{\text{G,O}}\,\mathbf{d}_{\text{SBP}} + \boldsymbol{\epsilon}, \tag{3.5}$$

where $\mathbf{d}_{\vartheta} = [\mathbf{d}_{\vartheta}^{1} \cdots \mathbf{d}_{\vartheta}^{K}]$ are vectors concatenating the $\vartheta = \{\text{SBP,RR}\}$ detrended values and $\boldsymbol{\epsilon}$ is a vector of residuals. The parameter $\mathcal{B}_{\text{G,O}}$ is estimated by OLS minimization.

Regarding the local mean detrend, since the mean value $(\bar{x}_{\text{SBP}}^{k}, \bar{x}_{\text{RR}}^{k})$ is naturally not the same for all K segments, each segment is moved to the origin by a different factor. Therefore, the relative position of points in the same segment is not altered, but the relative location of all segments is changed. As illustrated in Fig. 3.4(c–d), the local mean detrending allows the correction of the differences in SBP and RR baselines, emphasizing their fluctuations around their local mean value. Also, from the comparison between Figs. 3.4(a–b) and 3.4(c–d), local mean detrending enhances the global linear relationship between SBP and RR.

The local mean detrend of the data before global slope estimation is of major importance. This transformation allows to put together the pairs of SBP and RR values identified in BSs and BEs (and slopes) obtained at different operating points of the sigmoidal SBP and RR relation (Fig. 1.7). Therefore, the underlying hypothesis of local mean detrend is that the BRS slopes obtained along a stationary recording are of similar value, i.e., the BRS is stationary in spontaneous condition. As a matter of fact, the BRS slopes can be considered as similar, because the operating point of one subject is more likely to lye in the SBP range in which the SBP and RR sigmoidal relation is approximately linear, rather than in the plateau range (Hunt and Farquhar, 2005). Moreover, the different operating points occurring in a spontaneous recording exhibit small changes and therefore, even if the operating point of the subject is not lying in the central portion of the sigmoidal, the slopes are likely similar.

Erroneous conclusions can be drawn if local mean detrend is not carried out before a global regression. As a matter of fact, the global slope estimation without local mean detrended has already been applied in rats data (Moffitt *et al.*, 2005). In that study, the BRS estimate was taken as the global regression slope computed from all beats identified in BSs without local mean detrending (i.e., in this thesis from the data represented in Fig. 3.4(a)). The authors concluded that the BRS assessment was not reliable, due to the lower correlation that the SBP and RR data exhibited. The authors later clarified that the negative conclusion was due to the misinterpretation of the computational algorithm of the sequences technique, and confirmed the usefulness of the sequences technique (mean of the local slopes) to provide a BRS estimate (Stauss *et al.*, 2006).

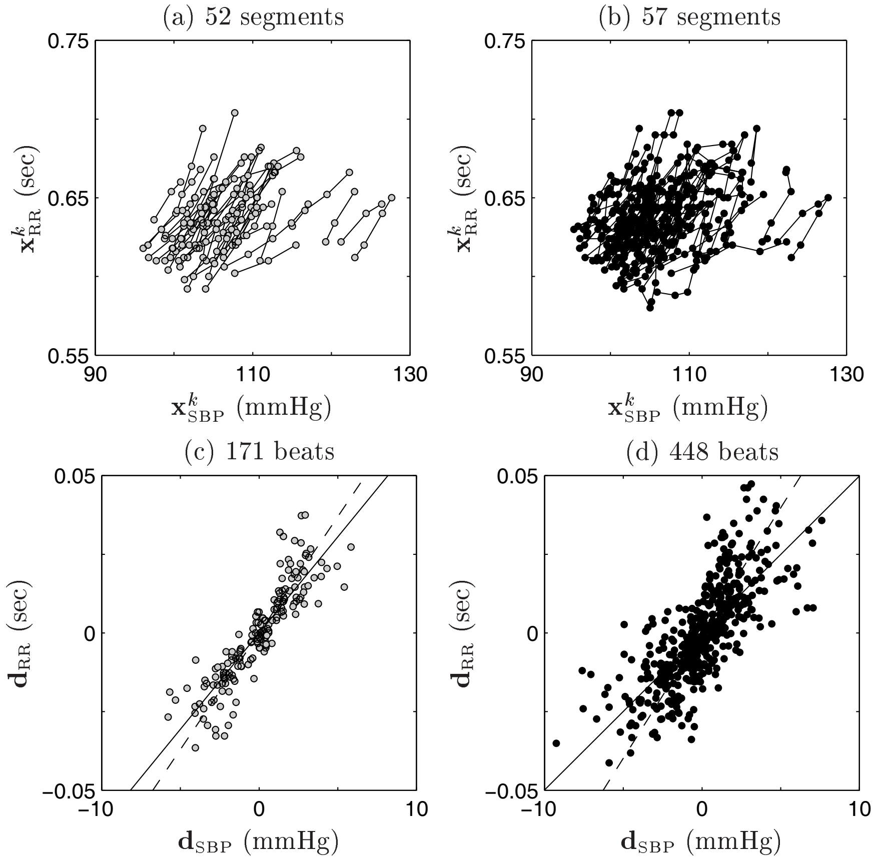

Figure 3.4: Dispersion diagram of $x_{\mathrm{SBP}}(n-1)$ and $x_{\mathrm{RR}}(n)$ for (a) BSs and (b) BEs. Dispersion diagram of $\mathbf{d}_{\mathrm{SBP}}$ and $\mathbf{d}_{\mathrm{RR}}$ for (c) BSs and (d) BEs. The dashed line has slope $\hat{\mathcal{B}}_{\mathrm{L,O}}$ and passes through the origin. The solid line is the global regression line with slope $\hat{\mathcal{B}}_{\mathrm{G,O}}$, estimated by OLS minimization. Same data as in Fig. 3.3.

3.3.2.3 Total approach for slope estimation

Figure 3.5 shows the distribution of the slopes $b_k, k = 1, 2, ..., K$, computed for each identified BE. Comparing to Fig. 3.2, it is possible to observe that the distribution of b_k computed from BEs exhibits more skewness than that evaluated for BSs. Also, Fig. 3.5(b) illustrates that the use of a global slope (instead of the mean of the local slopes) provides an overall BRS estimate more robust to the b_k values in the longer tail of the distribution.

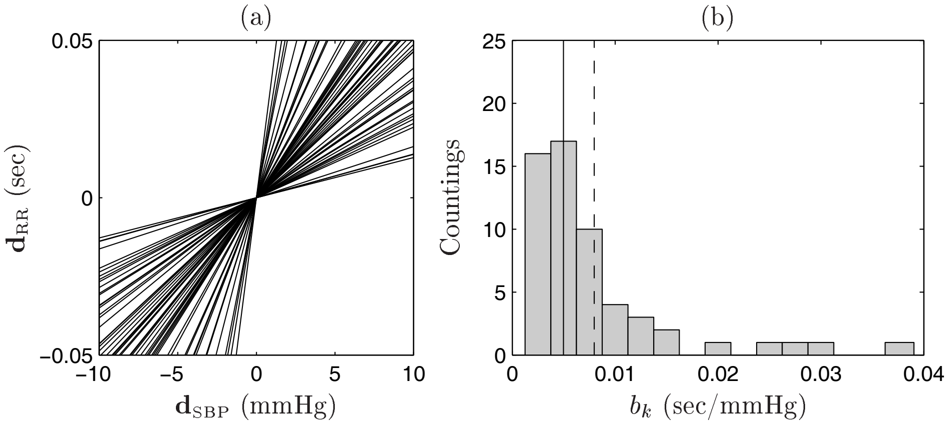

Figure 3.5: Dispersion diagram of the SBP and RR range around the mean SBP and RR value in each BE, represented by the 0 value, together with the regression lines with slope b_k and passing through the origin. (b) Histogram of the estimated local slopes with the lines locating the average slope $\hat{\mathcal{B}}_{\mathrm{L,O}}$ (dashed line) and the global slope $\hat{\mathcal{B}}_{\mathrm{G,O}}$ (full line). Same data as in Fig. 3.3.

In this work, a robust global approach was also considered for BRS estimation: the total approach. This approach consists of an outlier rejection rule combined with the slope estimation in Eq. (3.5) using total least squares (TLS) minimization (Gouveia *et al.*, 2006).

The total approach avoids the effect of outlier segments on global slope estimation. On one hand, to achieve more robustness in BRS estimation, the outlier segments are removed before global slope estimation. On the other hand, to allow a better identification of the outlier segments (since errors in both SBP and RR series can occur), the slope is estimated by TLS minimization, instead of OLS minimization. In linear regression, the OLS method attributes all errors to the dependent variable and the solution minimizes the sum of squared vertical direction errors (see Fig. 3.6(a)). On the contrary, the TLS method minimizes the sum of squared orthogonal direction errors (van Huffel and Vandewalle, 1991), accounting for errors in both the dependent and independent variables (see Fig. 3.6(b)).

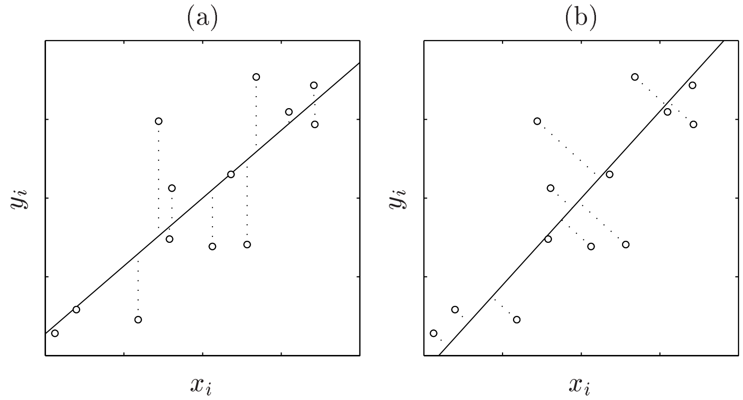

Figure 3.6: (a) OLS and (b) TLS slope estimation: OLS minimizes the sum of squared vertical errors $(y_i - \hat{y}_i)^2$ and TLS minimizes the sum of squared orthogonal errors $(y_i - \hat{y}_i)^2 + (x_i - \hat{x}_i)^2$.

The outlier segments are removed from BRS analysis as follows. The influence of the k^{th} segment is evaluated by g_k, as the ratio between the *TLS slope estimated when the k^{th} segment is omitted from BRS analysis* and the *TLS slope estimated when all segments are used for BRS analysis.* A value of g_k near 1 indicates no excessive influence of that segment in the BRS estimation. The k^{th} segment is an outlier if g_k exceeds the median value more than twice the median absolute deviation (MAD) divided by 0.6745 (Wilcox, 2001). As illustrated in Fig. 3.7, the rejection criteria allows the identification of BSs and BEs with unusual high influence on the slope estimation. Also, as there are more BEs with influence near 1, the 95% robust acceptance band associated with BEs is narrower. This indicates more homogeneity between the influences of BEs in the slope estimation.

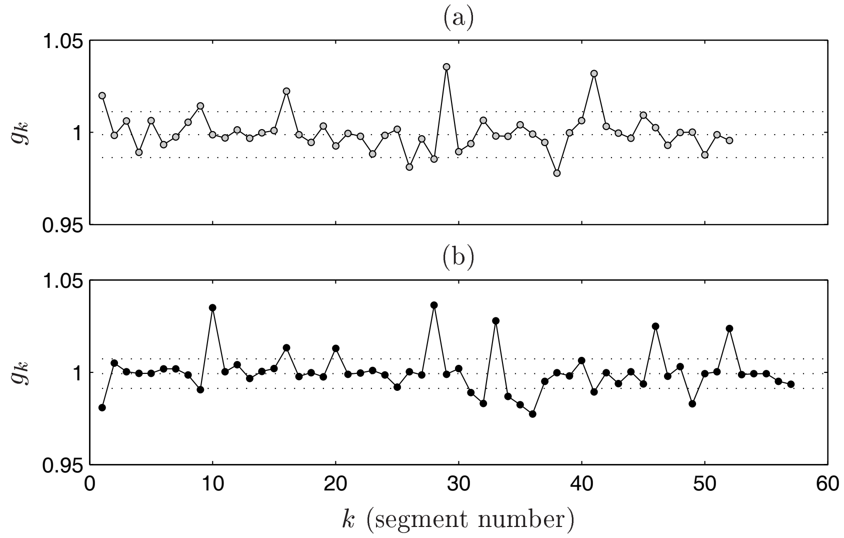

Figure 3.7: Influence function for (a) BSs and (b) BEs, with 95% robust acceptance band, assuming a normal distribution (Wilcox, 2001). Same data as in Fig. 3.3.

The total slope $\mathcal{B}_{\mathrm{G,T}}$ is estimated after the removal of outlier segments, with the remaining pairs $(\mathbf{d}_{\mathrm{SBP},\alpha}, \mathbf{d}_{\mathrm{RR},\alpha})$. As the TLS approach is sensitive to scale changes in the data (van Huffel and Vandewalle, 1991), the use of a multiplicative factor in one of the variables will not produce a proportional slope. To deal with this shortcoming, $\mathbf{d}_{\mathrm{SBP},\alpha}$ and $\mathbf{d}_{\mathrm{RR},\alpha}$ must be normalized and to guarantee the same order of magnitude in $\mathbf{d}_{\mathrm{SBP},\alpha}$ and $\mathbf{d}_{\mathrm{RR},\alpha}$ errors, the correction factors are defined by the corresponding MAD values. The slope α_{T} is estimated using TLS minimization over the normalized values from

$$\frac{\mathbf{d}_{\mathrm{RR},\alpha}}{\mathrm{MAD}(\mathbf{d}_{\mathrm{RR},\alpha})} = \alpha_{\mathrm{T}} \frac{\mathbf{d}_{\mathrm{SBP},\alpha}}{\mathrm{MAD}(\mathbf{d}_{\mathrm{SBP},\alpha})} + \boldsymbol{\epsilon}_{\alpha}, \tag{3.6}$$

where $\boldsymbol{\epsilon}_{\alpha}$ is a vector of residuals and the total approach estimator is

$$\mathcal{B}_{\mathrm{G,T}} = \frac{\mathrm{MAD}(\mathbf{d}_{\mathrm{RR},\alpha})}{\mathrm{MAD}(\mathbf{d}_{\mathrm{SBP},\alpha})} \, \alpha_{\mathrm{T}}. \tag{3.7}$$

Figure 3.8 illustrates the dispersion of $\mathbf{d}_{\mathrm{SBP},\alpha}$ and $\mathbf{d}_{\mathrm{RR},\alpha}$ together with the corresponding total regression line. Comparing to Fig. 3.4(c–d), it can be observed that the identified outlier segments have their extreme points outside the mass center of the data.

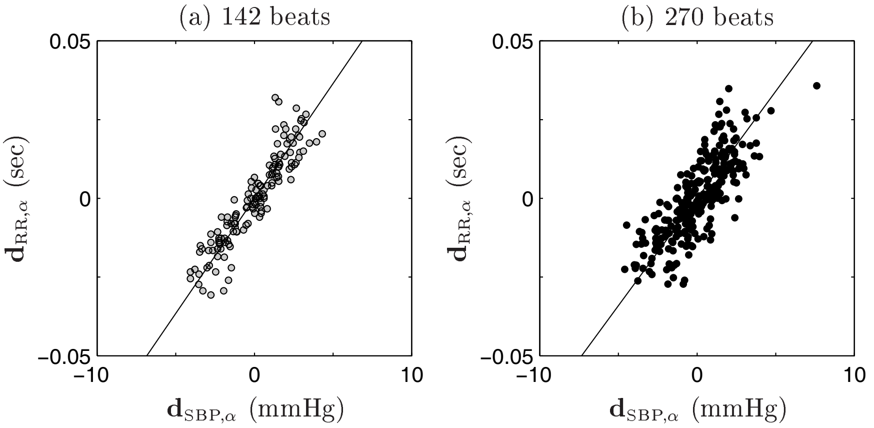

Figure 3.8: Dispersion diagram of $\mathbf{d}_{\mathrm{SBP},\alpha}$ and $\mathbf{d}_{\mathrm{RR},\alpha}$ for (a) BSs and (b) BEs. The solid line is the total regression line with slope $\hat{\mathcal{B}}_{\mathrm{G,T}}$. Same data as in Fig. 3.3.

3.3.3 Variables extracted from the BRS analysis

Besides the $\hat{\mathcal{B}}$ values obtained by the different approaches, the variables in Table 3.2 can be retrieved from time domain BRS analysis. For the comparison of the methods, the upper index S or E was added to each variable according to its evaluation in BSs or BEs, e.g., N^{S} and N^{E} indicate the number of beats available for BRS analysis using BSs and BEs.

Table 3.2: Summary of BRS variables evaluated for each recording.

Var	**Description**	**Units**
N	# of beats	beats
K	# of segments	segments
N/K	segments mean length	beats per segment
r	$\mathbf{d}_{\mathrm{SBP}}$ – $\mathbf{d}_{\mathrm{RR}}$ correlation	no units
$\hat{\mathcal{B}}_{\mathrm{L,O}}$	*local* BRS estimate	sec/mmHg
$\hat{\mathcal{B}}_{\mathrm{G,O}}$	*global* BRS estimate	sec/mmHg
$\hat{\mathcal{B}}_{\mathrm{G,T}}$	*total* BRS estimate	sec/mmHg

The Sequences and Events techniques are evaluated and compared using the recordings of the EuroBaVar dataset (Sec. 3.2). As the recordings length range from 553 to 1218 beats, the BRS analysis was based on the first N_{max}=512 beats of each file, to set comparable results for all recordings.

3.4 Threshold sensitivity analysis: from Sequences to Events

This section includes the sensitivity analysis on the thresholds used for BSs identification. The results here reported further motivate and justify the use of BEs instead of BSs, to achieve an improved BRS estimation.

The analysis presented in **Sec. 3.4.1** corroborates the previous studies that the simultaneous use of $\Delta_{min}^{\mathrm{SBP}}$, $\Delta_{min}^{\mathrm{RR}}$ and r_{min} thresholds is redundant (Davies *et al.*, 2001). One alternative to solve the thresholds redundancy would be to remove the r_{min} threshold, as already been suggested in the literature (Davies *et al.*, 2001). However, the setting of the optimum $\Delta_{min}^{\mathrm{SBP}}$ and $\Delta_{min}^{\mathrm{RR}}$ values is still dependent on the subjects BRS condition, being expected that lower optimal values would be obtained for low BRS cases (Davies *et al.*, 2001). It would be desirable to consider thresholds which could be set independently of the subjects BRS condition.

The other alternative to solve the thresholds redundancy is to remove the $\Delta_{min}^{\mathrm{SBP}}$ and $\Delta_{min}^{\mathrm{RR}}$ thresholds and keep the r_{min} threshold, as in the case of BEs. The results presented in **Sec. 3.4.2** point out that r_{min}=0.8 for BEs identification is an optimum trade-off between N^{E} and r^{E}, for normal BRS subjects. Moreover, the results obtained for the BRS dysfunction cases indicates that r_{min}=0.8 is also an optimum value for these cases, so suggesting that the optimum r_{min} value can be set independently of the BRS condition of the subject.

Finally, in **Sec. 3.4.3** the BEs segmentation is compared with other segmentation strategies, based on r_{min} threshold. In particular, the need of including a statistical significant threshold on BEs identification is discussed.

3.4.1 Effect of changing $\Delta_{min}^{\mathrm{SBP}}$ and $\Delta_{min}^{\mathrm{RR}}$ threshold values

The distribution of the BRS variables in Table 3.2 was first studied as a function of $\Delta_{min}^{\mathrm{SBP}}$ and $\Delta_{min}^{\mathrm{RR}}$ values. Figure 3.9 shows the distribution of the median values obtained considering r_{min}=0.8, as in BSs. As evidenced in Figs. 3.9(a–b) by the light colors, $\tilde{N}$ and $\tilde{K}$ are small for any combination of threshold values considered: $\tilde{N}<200$ and $\tilde{K}<50$ (in files with N_{max}=512 beats length). The similar color pattern of $\tilde{N}$ and $\tilde{K}$ distributions indicates that $\tilde{N}/\tilde{K}$ is fairly constant and lower than 4 beats/segment (ratio of $\tilde{N}$ and $\tilde{K}$ majorant values). As presented in Fig. 3.9(c), $\tilde{r}>0.8$ for all $\Delta_{min}^{\mathrm{SBP}}$ and $\Delta_{min}^{\mathrm{RR}}$ values, probably due to the small N and N/K values.

The BRS estimates are highly sensitive to changes in the $\Delta_{min}^{\mathrm{SBP}}$ and the $\Delta_{min}^{\mathrm{RR}}$ values. As is illustrated in Figs. 3.9(d–f), the lower $\Delta_{min}^{\mathrm{SBP}}$ and higher $\Delta_{min}^{\mathrm{RR}}$ values lead to higher median $\hat{\mathcal{B}}$, whereas the higher $\Delta_{min}^{\mathrm{SBP}}$ and lower $\Delta_{min}^{\mathrm{RR}}$ values lead to lower median $\hat{\mathcal{B}}$ values. The similar but darker color pattern in Fig. 3.9(d) when compared to Fig. 3.9(e) evidences that $\hat{\mathcal{B}}_{\mathrm{L,O}}$ are higher than $\hat{\mathcal{B}}_{\mathrm{G,O}}$ and correlated. The $\hat{\mathcal{B}}_{\mathrm{G,T}}$ values have similar pattern as the previous, except for $\Delta^{\mathrm{SBP}}_{min}$ or $\Delta^{\mathrm{RR}}_{min}$ around zero, which present more variability.

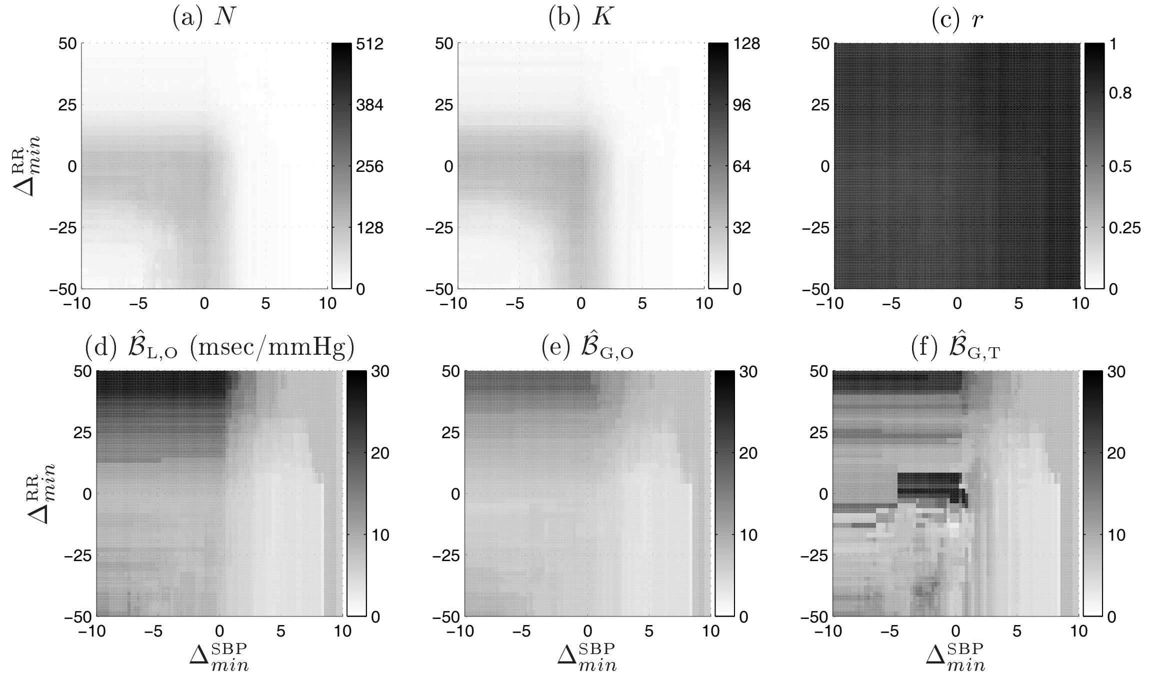

Figure 3.9: Distribution of BRS variables as a function of $\Delta^{\mathrm{SBP}}_{min}$ and $\Delta^{\mathrm{RR}}_{min}$ with setting $r_{min} = 0.8$. The $\Delta^{\mathrm{SBP}}_{min}$ values range within the interval [–10:0.25:10] mmHg and $\Delta^{\mathrm{RR}}_{min}$ changes cover the interval [-50:0.5:50] msec. The figures show the median of the values obtained for each EuroBaVar record. Darker indicates higher density.

Figure 3.10 shows the same representation as in Fig. 3.9 considering r_{min}=–1, instead of r_{min}=0.8. The comparison between Figs. 3.9 and 3.10 shows the similarity of the distributions for some $\Delta^{\mathrm{SBP}}_{min}>0$ or $\Delta^{\mathrm{RR}}_{min}>0$ either considering r_{min}=0.8 or r_{min}=–1. For such $\Delta^{\mathrm{SBP}}_{min}$ and $\Delta^{\mathrm{RR}}_{min}$ values, the identified segments are the same either considering r_{min}=0.8 or r_{min}=–1, what indicates that the corresponding SBP and RR values present correlation exceeding r_{min}=0.8. With the setting of r_{min}=0.8 (Fig. 3.9), decreasing $\Delta^{\mathrm{SBP}}_{min}$ and $\Delta^{\mathrm{RR}}_{min}$ values lead to increasing $\tilde{N}$ and decreasing $\tilde{K}$ values, so that $\tilde{N}/\tilde{K}$ increases (up to N_{max}=512). The $\tilde{r}$ values decrease almost to 0 because the negative $\Delta^{\mathrm{SBP}}_{min}$ and $\Delta^{\mathrm{RR}}_{min}$ values allows the identification of the entire SBP and RR series as one valid segment. The median $\hat{\mathcal{B}}$ values also tend to 0 with decreasing $\Delta^{\mathrm{SBP}}_{min}$ and $\Delta^{\mathrm{RR}}_{min}$ values.

The threshold sensitivity analysis indicates that for some $\Delta^{\mathrm{SBP}}_{min}>0$ or $\Delta^{\mathrm{RR}}_{min}>0$ values, the simultaneous use of the $\Delta^{\mathrm{SBP}}_{min}$, $\Delta^{\mathrm{RR}}_{min}$ and r_{min} thresholds can be avoided (Gouveia *et al.*, 2007). One alternative to solve the thresholds redundancy would be to remove the r_{min} threshold, as already been suggested in the literature (Davies *et al.*, 2001). However, even by removing r_{min}, if restrictive $\Delta^{\mathrm{SBP}}_{min}$ or $\Delta^{\mathrm{RR}}_{min}$ values are considered, N and N/K would still be diminished and so it would the probability of obtaining a BRS estimate. But then, the

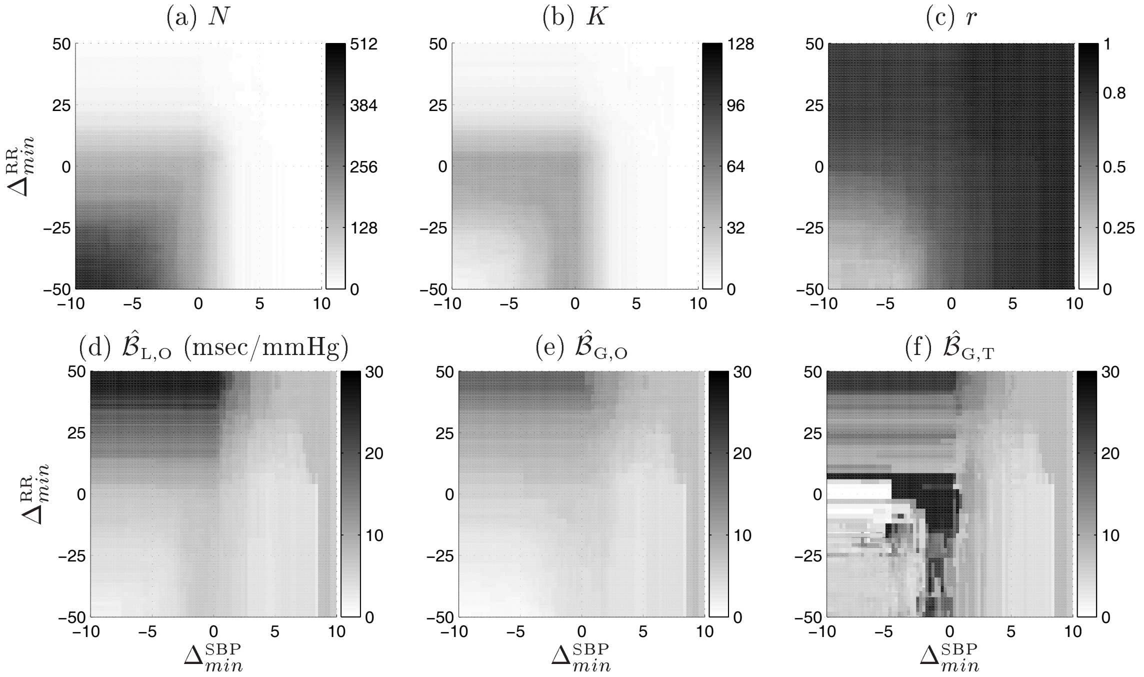
(a) N (b) K (c) r

(d) $\hat{\mathcal{B}}_{\mathrm{L,O}}$ (msec/mmHg) (e) $\hat{\mathcal{B}}_{\mathrm{G,O}}$ (f) $\hat{\mathcal{B}}_{\mathrm{G,T}}$

Figure 3.10: Distribution of BRS variables as a function of $\Delta_{min}^{\mathrm{SBP}}$ and $\Delta_{min}^{\mathrm{RR}}$ with setting $r_{min} = -1$. Darker indicates higher density. Same caption as in Fig. 3.9.

$\Delta_{min}^{\mathrm{SBP}}$ and $\Delta_{min}^{\mathrm{RR}}$ values could neither be *too* unrestrictive: as illustrated in Figs. 3.10(a-c), the use of low $\Delta_{min}^{\mathrm{SBP}}$ and $\Delta_{min}^{\mathrm{RR}}$ values would increase N up to N_{max} and decrease r down to zero. Therefore, the adequateness of the linear regression model in such data would be questionable.

The optimum $\Delta_{min}^{\mathrm{SBP}}$ and $\Delta_{min}^{\mathrm{RR}}$ values could be set as a trade-off between N and r, using experimental data. However, these optimum values would highly depend on the subject condition, being expected that lower optimum values would be obtained for attenuated BRS subjects. In normal cases, the optimum values obtained for the low BRS cases would lead to higher N at the expense of a lower r value. Therefore, it would be desirable to consider thresholds (and threshold values) which could be set independently of the subjects condition.

3.4.2 Effect of changing the r_{min} threshold value

The other alternative to solve the thresholds redundancy is to remove the $\Delta_{min}^{\mathrm{SBP}}$ and $\Delta_{min}^{\mathrm{RR}}$ thresholds instead of r_{min}, as is the case of BEs.

Figure 3.11 shows the distribution of the BRS variables as a function of r_{min} values, either evaluated for BSs or BEs. For BSs, all variables are constant for $r_{min} < 0.8$ indicating that the SBP and RR values in BSs present $r_{min} > 0.8$. In median, N^{S} is close to 128 of the 512 beats, $N^{\mathrm{S}}/K^{\mathrm{S}}$ is lower than 4 beats/segment and r^{S} is very high, probably due to the small values of N^{S} and $N^{\mathrm{S}}/K^{\mathrm{S}}$. Regarding BEs, as r_{min} increases, N^{E} decreases and K^{E} increases such that $N^{\mathrm{E}}/K^{\mathrm{E}}$ decreases and tends to $N_{min} = 3$. As illustrated in Fig. 3.11(c), r^{E} increases linearly with r_{min}, being approximately r_{min} for $0.2 < r_{min} < 0.8$.

Regarding the BRS estimates, $\hat{\mathcal{B}}^{\mathrm{E}}_{\mathrm{L,O}}$ increases with increasing r_{min} (Fig. 3.11(d)), because the mean of the local slopes estimate is calculated from more segments that exhibit shorter duration ($N^{\mathrm{E}}/K^{\mathrm{E}}$) and higher slope. As illustrated in Fig. 3.11(e), the $\hat{\mathcal{B}}^{\mathrm{E}}_{\mathrm{G,O}}$ values also increase with increasing r_{min}, because the BEs with lower SBP and RR correlation (and slope) are more unlikely to be identified for higher r_{min} values and $\hat{\mathcal{B}}^{\mathrm{E}}_{\mathrm{G,O}}$ tends to $\hat{\mathcal{B}}^{\mathrm{S}}_{\mathrm{G,O}}$. Finally, as presented in Fig. 3.11(f), the robust estimates $\hat{\mathcal{B}}^{\mathrm{E}}_{\mathrm{G,T}}$ do not seem to be much affected by r_{min}, mainly due to the outlier rejection rule.

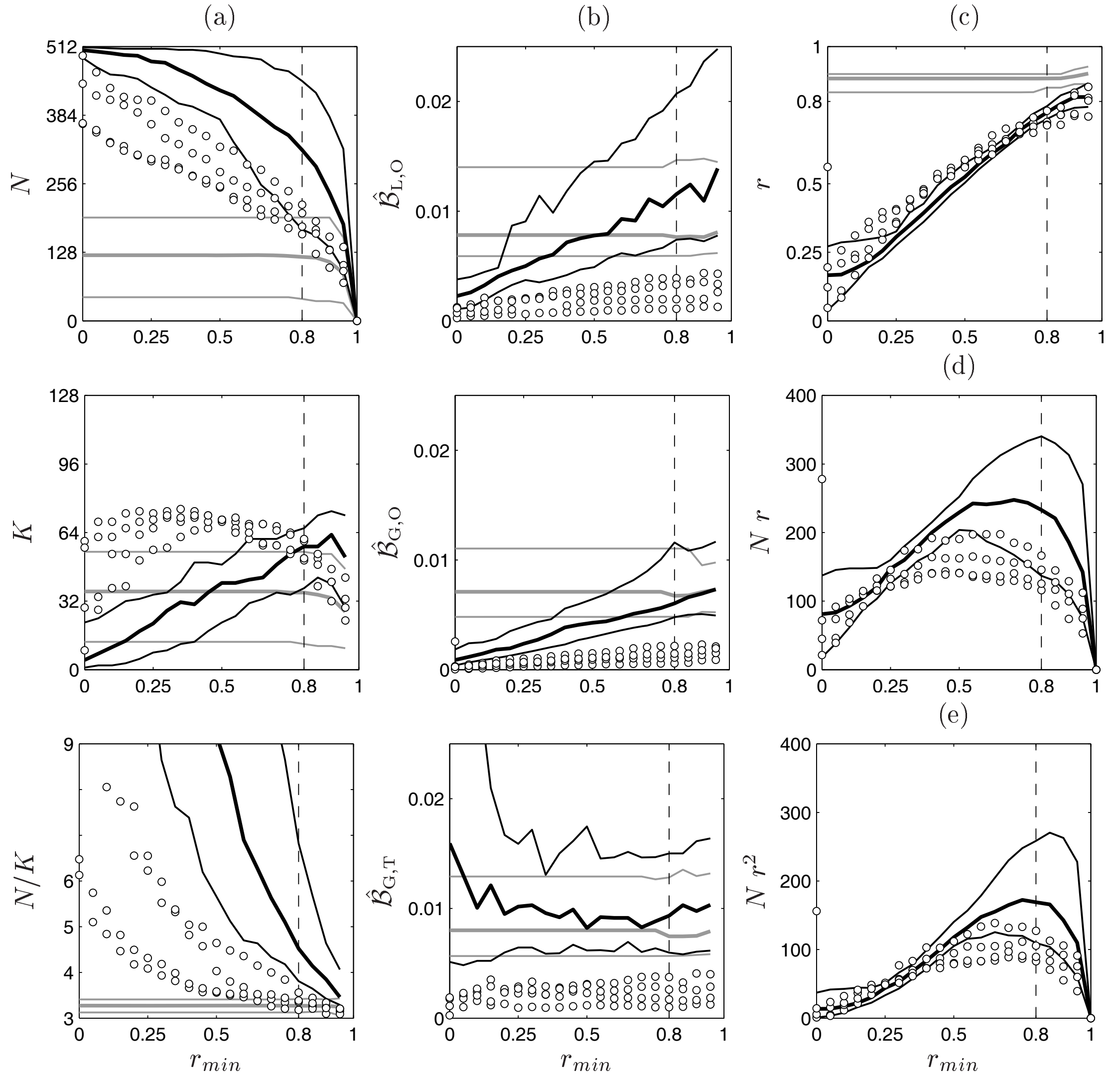

Figure 3.11: Distribution of BRS variables as a function of r_{min} (in the interval [0:0.05:1]) showing lower/upper quartiles and median values. Values obtained from BSs (grey) and BEs (black). The white circles localize the files without BSs and with BEs.

The four EuroBaVar files without BSs present BEs; these files, identified by circles in Fig. 3.11, show the same trend in N^{E}, $N^{\mathrm{E}}/K^{\mathrm{E}}$ and $\hat{\mathcal{B}}^{\mathrm{E}}$ as for the remaining files, although presenting lower values. As illustrated in Fig. 3.11(c), the files without BSs have r^{E} values similar to the remaining files, indicating that the choice of the r_{min} value is not dependent of the subjects condition, as desirable.

The optimum r_{min} value can be set as a trade-off between N^{E} and r^{E}. Since N^{E} decreases and r^{E} increases when r_{min} increases, r_{min} can be set to a value that maximizes the product $N^{\mathrm{E}}\, r^{\mathrm{E}}$. Alternatively, the product $N^{\mathrm{E}}(r^{\mathrm{E}})^2$ can be considered, once the squared correlation coefficient r^2 corresponds to the fraction of $\mathbf{d}_{\mathrm{RR}}$ variance accounted for the $\mathbf{d}_{\mathrm{SBP}}$ and $\mathbf{d}_{\mathrm{RR}}$ linear regression. For both optimization functions considered, Figs. 3.11(d) and 3.11(e) suggest that $r_{min} = 0.8$ for BEs identification is an optimum trade-off between N^{E} and r^{E}.

As remarked in Fig. 3.11, the threshold values $\Delta^{\mathrm{SBP}}_{min} = 1$ mmHg and $\Delta^{\mathrm{RR}}_{min} = 5$ msec used for BSs identification led to difficulties in providing a BRS estimate. These values were chosen to follow the most recent publication with focus on the methodological aspects of the sequences technique (Di Rienzo *et al.*, 2001). Also, the values (1mmHg, 5msec) are similar to the values (1mmHg, 4msec) originally proposed for cats data (Di Rienzo *et al.*, 1985; Bertineri *et al.*, 1988). Because these threshold values are the most used in the literature, the comparison presented in Fig. 3.11 is the imperative to present.

Nevertheless, other $\Delta^{\mathrm{SBP}}_{min}$ and $\Delta^{\mathrm{RR}}_{min}$ values could have been considered for the BS identification. As a matter of fact, the sequences technique has been applied considering other threshold values, with $\Delta^{\mathrm{SBP}}_{min}$ ranging from 0 to 2 mmHg and $\Delta^{\mathrm{RR}}_{min}$ varying from 0 to 6 msec (Davies *et al.* (2001) and references therein included), and it has been shown that both the BSs number and the BRS estimate are sensitive to changes in these threshold values (Davies *et al.*, 2001; Gouveia *et al.*, 2007). In particular, by decreasing the $\Delta^{\mathrm{SBP}}_{min}$ and $\Delta^{\mathrm{RR}}_{min}$ values down to 0, it is expected an increased number of identified BSs and, consequently, an increased probability of the sequences technique to provide a BRS estimate. Therefore, the comparison between the BRS variables obtained from BSs identified by imposing $\Delta^{\mathrm{SBP}}_{min} = \Delta^{\mathrm{RR}}_{min} = 0$ and the variables obtained from BEs is well justified.

Figure 3.12 presents the same representation as in Fig. 3.11, considering $\Delta^{\mathrm{SBP}}_{min} = \Delta^{\mathrm{RR}}_{min} = 0$ in BSs identification instead of $\Delta^{\mathrm{SBP}}_{min} = 1$ and $\Delta^{\mathrm{RR}}_{min} = 5$. As is possible to observe, lowering the threshold values for BSs identification, increases N^{S} and N^{S}, without introducing major changes in the distribution of the $\hat{\mathcal{B}}$ as a function of r_{min}. However, the four files without BSs for $\Delta^{\mathrm{SBP}}_{min} = 1$ and $\Delta^{\mathrm{RR}}_{min} = 5$ present BSs if $\Delta^{\mathrm{SBP}}_{min} = \Delta^{\mathrm{RR}}_{min} = 0$ is considered instead. As illustrated by the grey circles, the N, the N/K and the $\hat{\mathcal{B}}$ values for these four files are lower than those evaluated for the remaining files. Also, the $\hat{\mathcal{B}}$ values are lower for these files in comparison with the remaining. The BRS analysis from BEs provides comparable BRS estimates. However, the results indicate that the N^{E} values are still higher than N^{S}, the K^{E} are similar to K^{S} values, and $N^{\mathrm{E}}/K^{\mathrm{E}}$ are still higher than the $N^{\mathrm{S}}/K^{\mathrm{S}}$.

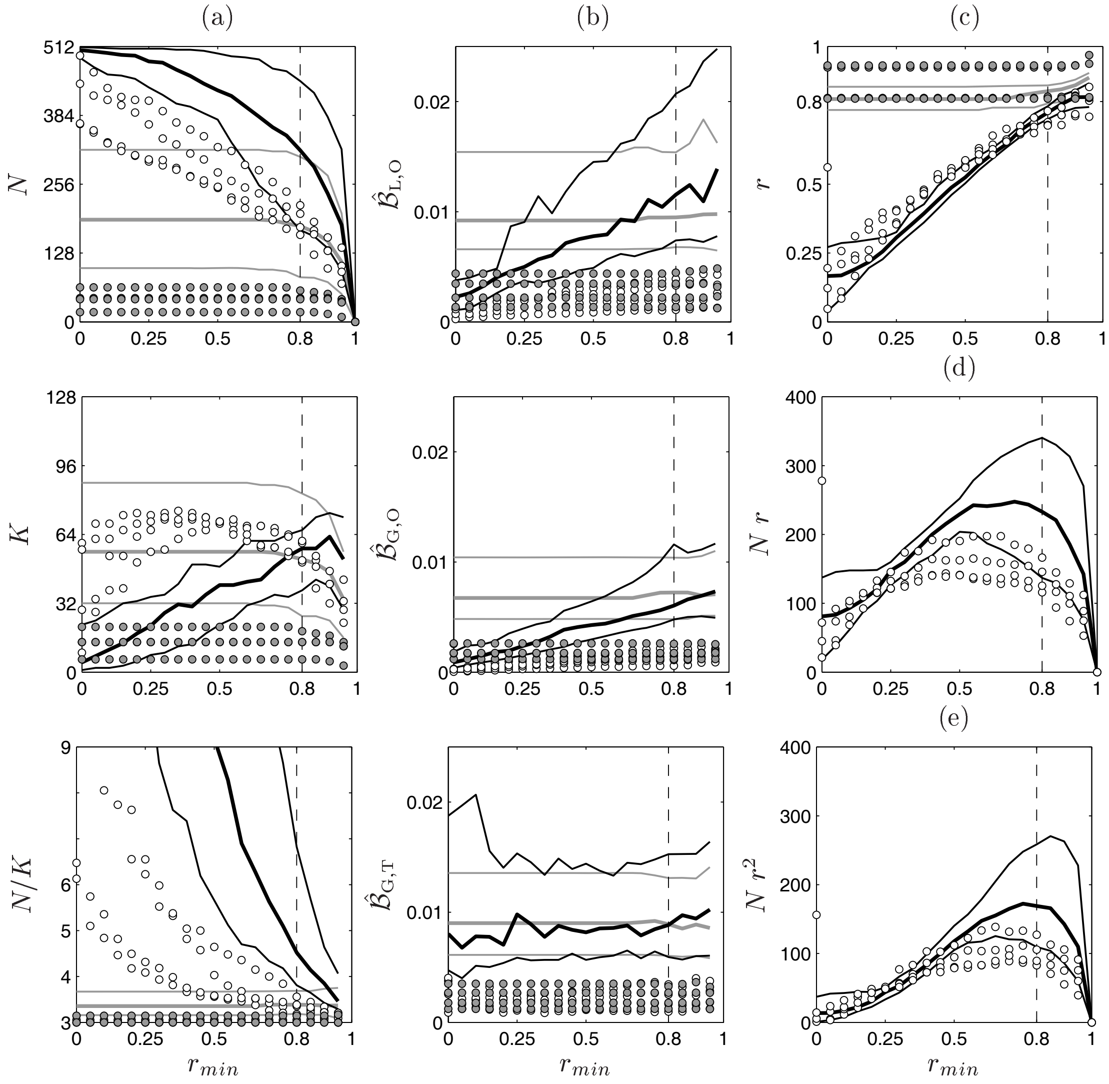

Figure 3.12: Distribution of BRS variables as a function of r_{min} (in the interval [0:0.05:1]) showing lower/upper quartiles and median values. Values obtained from BSs considering $\Delta^{\mathrm{SBP}}_{min}=\Delta^{\mathrm{RR}}_{min}=0$ (grey) and BEs (black). The white circles localize the files without BSs and with BEs.

3.4.3 The r_{min} value and related statistical significance

As previously referred, the k^{th} baroreflex segment is identified by imposing $r_k \geq r_{min}$, regardless of its statistical significance p_k[1]. In this section, it is discussed the utility of a statistical p_k based criterion for BEs identification and its non inclusion is justified.

As presented in Table 3.3, 60% of the BSs identified in the EuroBaVar files present a r_k value considered as not statistically significant ($p_k > 0.05$). For BEs, the corresponding proportions are 61% and 38%. That is, the results evidence that the majority of identified

---

[1] In this work, p_k is defined as the probability of having a correlation between the SBP and RR values in the k^{th} segment as large as the observed value r_k by random chance, when the true correlation ρ_k is zero.

segments, both BSs and BEs, do not exhibit statistically significant correlation. However, the majority of points in with the BRS analysis from BEs is based (N^{E}) is from BEs that present significant correlation. The inclusion of non-significant segments in the BRS analysis can turn into a disadvantage if $\mathcal{B}_{\mathrm{L,O}}$ is used, because $\hat{\mathcal{B}}_{\mathrm{L,O}}$ considers slopes estimated from non-significant segments to compute the average slope. If the $\mathcal{B}^{\mathrm{E}}_{\mathrm{G,O}}$ and $\mathcal{B}^{\mathrm{E}}_{\mathrm{G,T}}$ estimators are used instead, the BRS estimate is obtained as a global slope based on data that presents r^{E} close to 0.8, being obviously statistically significant due to the large N^{E} value (see Fig. 3.11).

Table 3.3: Countings and percentage of K and N evaluated for BSs and BEs, distinguishing the segments with $p_k > 0.05$ and with $p_k \leq 0.05$.

	$p_k > 0.05$	$p_k \leq 0.05$	**Total**
$\sum K^{\mathrm{S}}$	903 (60%)	611 (40%)	1514 (100%)
$\sum N^{\mathrm{S}}$	2786 (54%)	2369 (46%)	5155 (100%)
$\sum K^{\mathrm{E}}$	1464 (61%)	918 (39%)	2382 (100%)
$\sum N^{\mathrm{E}}$	4969 (38%)	7982 (62%)	12951 (100%)

Figure 3.13 presents the distribution of the number of segments identified in the EuroBaVar dataset, as a function of the segments length (N_k). As illustrated in Fig. 3.13(a–b), the non-significant BEs are typically 3-beat segments that have their beats located around the origin of the $\mathbf{d}_{\mathrm{SBP}}$ and $\mathbf{d}_{\mathrm{RR}}$ dispersion diagrams (see Fig. 3.4(b) and Fig. 3.8(b)). Therefore, it is expected that these short segments have small weight in the global slope estimation.

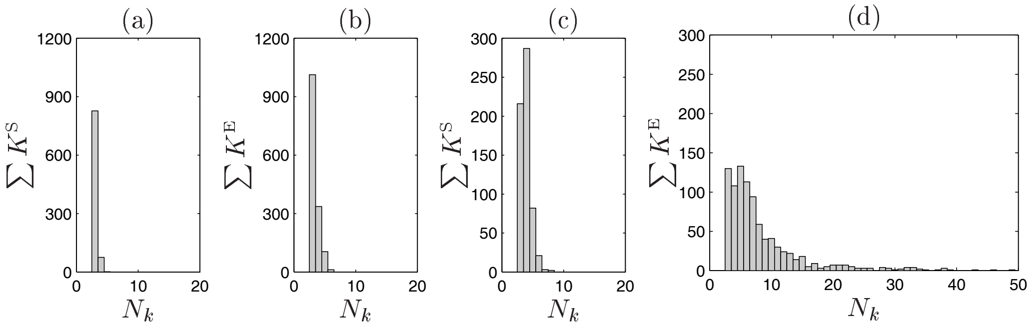

Figure 3.13: Distribution of $\sum K$ by segment length (N_k) evaluated for BSs and BEs, distinguishing the segments with (a–b) $p_k > 0.05$ and with (c–d) $p_k \leq 0.05$. Values obtained for the entire EuroBaVar dataset.

To illustrate that non-significant BEs have small weight in BRS estimation, Fig. 3.14(a–c) present the comparison between the BRS analysis from BEs and from segments satisfying simultaneously $r_k \geq 0.8$ and $p_k \leq 0.05$ (segments P1, a subset of BEs). It can be observed that N^{E} is higher at the expense of a lower r^{E} in comparison with those evaluated for segments P1, without changing the $\hat{\mathcal{B}}_{\mathrm{G,O}}$ value: the correlation between the $\hat{\mathcal{B}}^{\mathrm{E}}_{\mathrm{G,O}}$ and $\hat{\mathcal{B}}^{\mathrm{P1}}_{\mathrm{G,O}}$ values is 0.98 and their median paired differences is not significantly different from zero (p > 0.35).

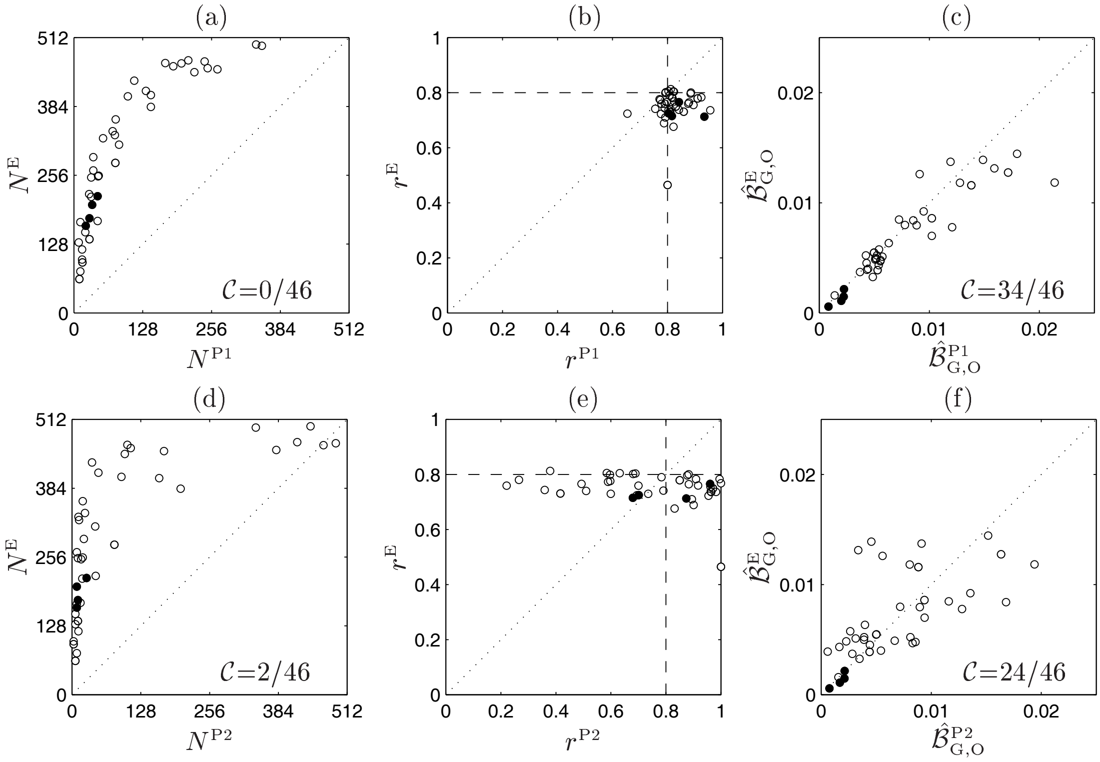

Figure 3.14: Dispersion diagrams comparing N, r and $\hat{\mathcal{B}}_{\mathrm{G,O}}$ evaluated from BEs (index E), from segments satisfying $r_k \geq 0.8$ and $p_k \leq 0.05$ (P1) and from segments satisfying $r_k > 0$ and $p_k \leq 0.05$ (P2). The black circles localize the files without BSs and with BEs.

Patients with a weak baroreflex response are expected to present a lower SBP and RR coupling in comparison with the normal cases. Figures 3.14(d–f) present the comparison between the BRS variables evaluated from BEs and from segments satisfying $r_k \geq 0$ and $p_k \leq 0.05$ (segments P2), illustrating that both N^{P2} and r^{P2} are much lower than those evaluated for BEs, inclusive for normal cases. Therefore, in comparison with BEs, the BRS analysis from segments P2 has a diminished ability to provide a BRS estimate (due to the lower N^{P2}), as well as, a diminished ability to provide an adequate BRS estimate (due to the lower r^{P2}). Moreover, BRS analysis from BEs and from segments P2 provide distinct BRS estimates that, although presenting a correlation of 0.87, their median paired differences is significantly different from zero (p < 0.001). As presented in Fig. 3.11, the normal and BRS dysfunction cases in the EuroBaVar dataset present r^{E} close to 0.8, which is statistically significant due to large N^{E}. For the BRS dysfunction cases, the expected lower SBP and RR coupling is not reflected in lower r^{E}, and instead it is reflected in lower $N^{\mathrm{E}}/K^{\mathrm{E}}$ values, i.e., shorter segments of high correlation.

Figure 3.15 shows the dispersion diagrams of the data used for global BRS estimation, in a normal and a BRS dysfunction case. The use of BEs, i.e., the unique setting of $r_k \geq 0.8$, allows to maximize N^{E} while keeping r^{E} sufficiently *high*, making the global linear regression suitable to use in this data (Figs. 3.15(a) and 3.15(d)).

With the additional setting of $p_k \leq 0.05$, N^{P1} decreases and r^{P1} slightly increases in comparison with BEs (Figs. 3.15(b) and 3.15(e)). However, the similarity between $\hat{\mathcal{B}}^{\mathrm{E}}$ and $\hat{\mathcal{B}}^{\mathrm{P1}}$ remark that there is no need of considering the $p_k \leq 0.05$ criterion in BEs identification. Finally, the setting of $r_k \geq 0$ and $p_k \leq 0.05$ leads to different results depending on the subject's condition. In the normal case, N^{P2} is maintained while N^{P1} is drastically reduced in comparison with BEs (Fig. 3.15(b–c)). The $\hat{\mathcal{B}}^{\mathrm{P2}}_{\mathrm{G,O}}$ is much lower than $\hat{\mathcal{B}}^{\mathrm{E}}_{\mathrm{G,O}}$ and $\hat{\mathcal{B}}^{\mathrm{P2}}_{\mathrm{G,T}}$ is similar to $\hat{\mathcal{B}}^{\mathrm{E}}_{\mathrm{G,T}}$, because $\mathcal{B}_{\mathrm{G,T}}$ is a more robust estimator than $\mathcal{B}_{\mathrm{G,O}}$. In the BRS dysfunction case, N^{P2} is reduced whereas r^{P2} is increased and the global/total BRS estimates are maintained (Fig. 3.15(f)). Therefore, the data obtained segments P2 may not be suitable for global regression analysis. Finally, from the comparison between Figs. 3.15(e) and 3.15(f), it can be observed that segments P1 and P2 are the same for the BRS dysfunction cases. This result points out that, for the BRS dysfunction cases, the segments presenting a statistically significant correlation are short segments of correlation higher than 0.8, highlighting once more that the inclusion of a threshold based on p_k is not needed.

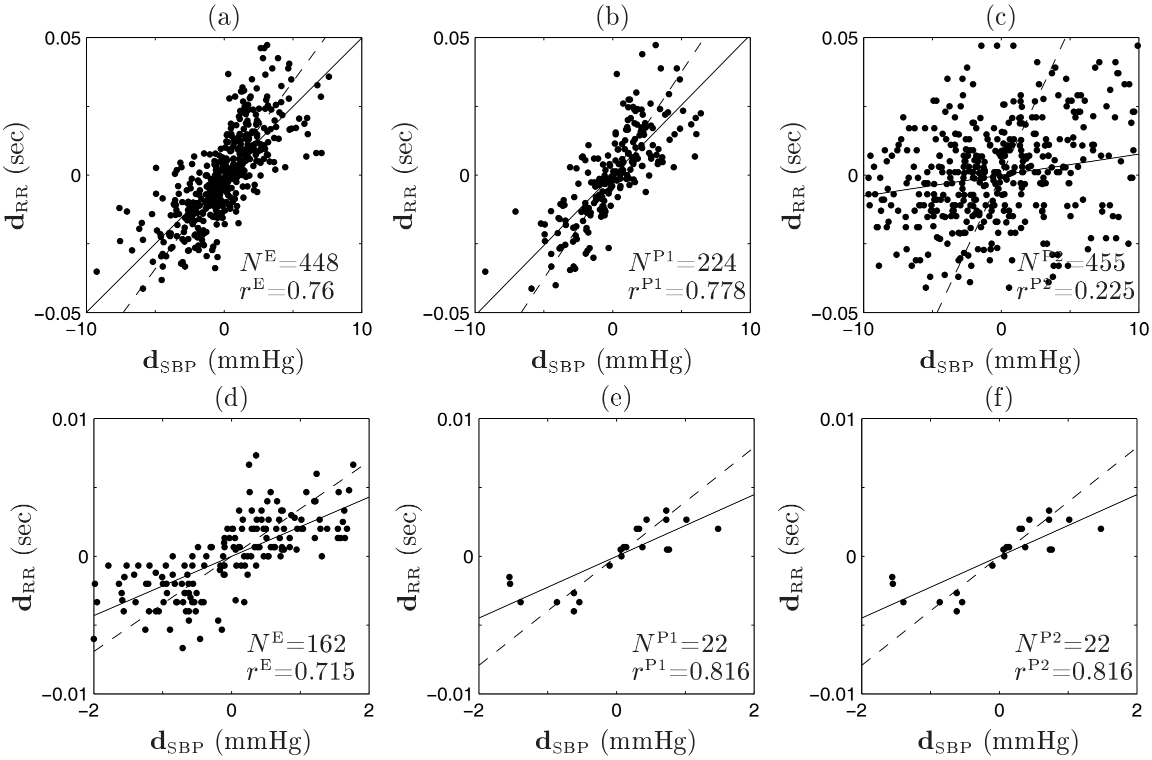

Figure 3.15: Dispersion diagram of $\mathbf{d}_{\mathrm{SBP}}$ and $\mathbf{d}_{\mathrm{RR}}$ for BEs, P1 and P2 segments. The solid/dashed line is the global/total regression line. Figures (a–c) are from the "A001LB" file, while (d–f) are from the "B005LB" file, which does not present BSs.

3.5 Results

The methods were compared with respect to the variables given in Table 3.2 and their ability to discriminate Lying (L) and Standing (S) positions for each subject (Secs. 3.5.1 and 3.5.2). Also, the reproducibility of the novel BRS estimators is quantified and compared with that evaluated for the traditional BRS methods (Sec. 3.5.3). The time domain BRS estimators are additionally studied with respect to their dispersion, which is usually disregarded in BRS analysis (Sec. 3.5.4).

As before, the upper index S or E was added to each variable according to its evaluation in BSs or BEs. With respect to the display of results, in a dispersion diagram representing x versus y, e.g., Fig. 3.16, the percentage $\mathcal{C}$ is defined as the ratio $\#(x > y)/\#x$ where # stands for the counting numbers, is indicated at the lower right corner of the figure.

The results here reported are based in the first N_{max}=512 beats of each EuroBaVar file. The BRS analysis of the EuroBaVar files “B005”, “B010”, “B013”, “B014” and “B015” produced results which deserves a comment. In the paired L and S evaluations of “B005” and “B010” files, it was not possible to identify BSs and, therefore, these files may correspond to the cardiac baroreflex failure subjects. File “B013” resulted in very high $\hat{\mathcal{B}}$ estimates for the L position. Files “B014” and “B015” were found to be replicas of files “A003” and “A008”, respectively, giving the same results for every analyzed variable.

3.5.1 Number of beats and segments in BRS analysis

As illustrated in Fig. 3.16, N^{E} is highly correlated with N^{S} and is always higher than N^{S}, because BEs are in larger number for most of the files (open circles in the figure) and are longer than BSs. The files that exhibit $K^{\mathrm{S}}>K^{\mathrm{E}}$ (filled circles) are the files that present the highest N^{E} and N^{S} values and still satisfy $N^{\mathrm{E}}>N^{\mathrm{S}}$ because, in these cases, BEs are much longer than BSs. As displayed in Fig. 3.16(c) for BSs, N^{S} is fairly proportional to K^{S} with $N^{\mathrm{S}}/K^{\mathrm{S}}$ between 3 and 4 beats/segment. As shown in Fig. 3.16(d) for BEs, there is a linear relation between N^{E} and K^{E} for files with $N^{\mathrm{E}}<3/4\,N_{max}$ (384 in the figure), with $N^{\mathrm{E}}/K^{\mathrm{E}}$ higher than the corresponding $N^{\mathrm{S}}/K^{\mathrm{S}}$. In addition, there are 14 files with $N^{\mathrm{E}}>3/4\,N_{max}$. As illustrated with the filled circles in Fig. 3.16, the files satisfying $K^{\mathrm{S}}>K^{\mathrm{E}}$ are associated with N^{E} values close to N_{max}, therefore, indicating mean $N^{\mathrm{E}}/K^{\mathrm{E}}$ values between 8 and 9 beats. These files also exhibit the highest N^{S} and K^{S} values of the dataset.

Figure 3.17 shows the distribution of the median of K and the number of EuroBaVar records (out of 46) as a function of N_k (the segments length in beats), evidencing that BEs are longer segments than BSs. For BSs, 12 records have one 6-beat BS and none present BSs longer than 8 beats, whereas 24 records have one 10-beat BE and 21 records one 15-beat BE.

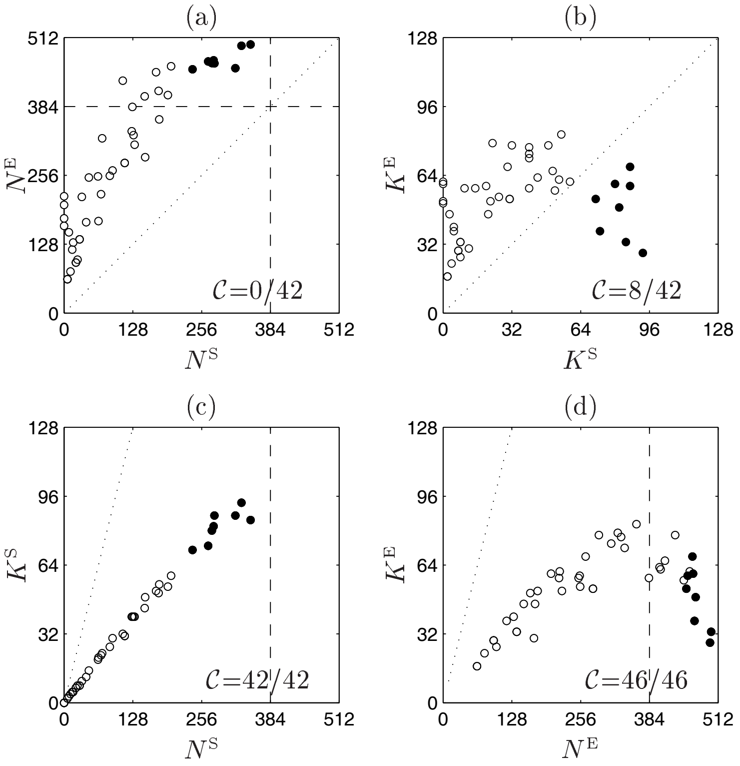

Figure 3.16: Dispersion diagrams comparing N and K produced by BS and BE. Values equal to 0 correspond to the files without BSs and with BEs. The filled circles localize the files that satisfy $K^{\mathrm{S}} > K^{\mathrm{E}}$. The dotted line is the identity line and the dashed line represents 3/4 of the N_{max} value.

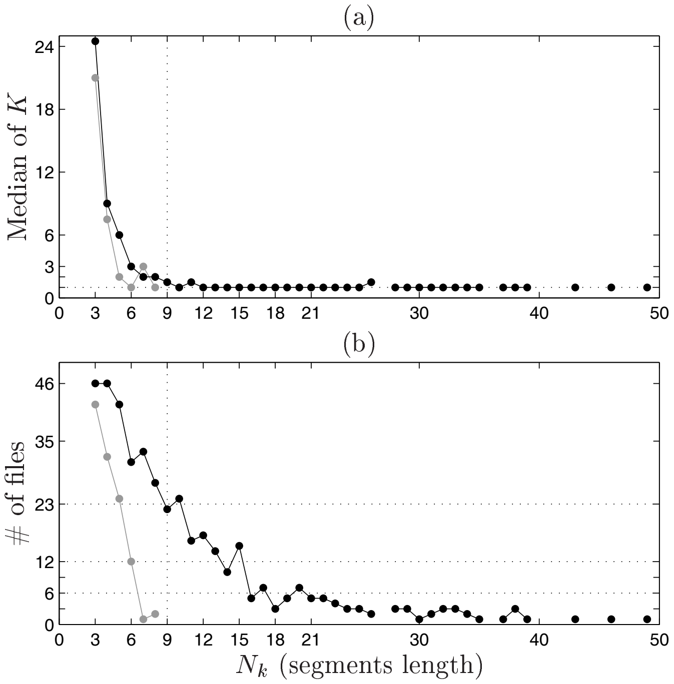

Figure 3.17: Distribution of (a) median of K and (b) number of EuroBaVar files (out of 46) as a function of N_k, for BS/BE (grey/black). There are 5 files with BEs longer than 50 beats.

3.5.2 BRS estimates and L from S discrimination

Regarding the BRS estimates, Fig. 3.18 presents the comparison between the different $\hat{\mathcal{B}}$ values and r produced by BS and BE. Figures 3.18(a–b) illustrate the comparison between $\hat{\mathcal{B}}^{\mathrm{S}}$ values: the results evidence that $\hat{\mathcal{B}}^{\mathrm{S}}_{\mathrm{L,O}} > \hat{\mathcal{B}}^{\mathrm{S}}_{\mathrm{G,O}}$, due to the fact that the global approach emphasizes BSs with lower slopes; also, there are no significant statistical differences between the mean of paired $\hat{\mathcal{B}}^{\mathrm{S}}_{\mathrm{L,O}} - \hat{\mathcal{B}}^{\mathrm{S}}_{\mathrm{G,T}}$ values and zero ($p > 0.7$). Figures 3.18(c–d) show the comparison of $\hat{\mathcal{B}}^{\mathrm{E}}_{\mathrm{G,O}}$ and $\hat{\mathcal{B}}^{\mathrm{E}}_{\mathrm{G,T}}$ with the traditional $\hat{\mathcal{B}}^{\mathrm{S}}_{\mathrm{L,O}}$: $\hat{\mathcal{B}}^{\mathrm{S}}_{\mathrm{L,O}} > \hat{\mathcal{B}}^{\mathrm{E}}_{\mathrm{G,O}}$ is observed in 34/42 of the files and 26/42 of the files exhibit $\hat{\mathcal{B}}^{\mathrm{E}}_{\mathrm{G,T}} > \hat{\mathcal{B}}^{\mathrm{S}}_{\mathrm{L,O}}$, so that $\hat{\mathcal{B}}^{\mathrm{E}}_{\mathrm{G,T}} > \hat{\mathcal{B}}^{\mathrm{S}}_{\mathrm{L,O}} > \hat{\mathcal{B}}^{\mathrm{E}}_{\mathrm{G,O}}$ is observed in 18/42 of the dataset files.

With the use of BSs, all approaches produce $\hat{\mathcal{B}}^{\mathrm{S}}$ values with pairwise correlations exceeding $\mathrm{r} = 0.97$. With the use of BEs instead of BSs, the pairwise correlations between estimates are lower, but still exceeding $\mathrm{r} = 0.8$. Figure 3.18(e) shows the dispersion of $\hat{\mathcal{B}}^{\mathrm{S}}_{\mathrm{G,T}}$ and $\hat{\mathcal{B}}^{\mathrm{E}}_{\mathrm{G,T}}$, which attained the highest correlation between estimates using BSs and BEs ($\mathrm{r} = 0.94$). Finally, as illustrated in Fig. 3.18(f), $r^{\mathrm{S}} > r^{\mathrm{E}}$ for all files that present BSs.

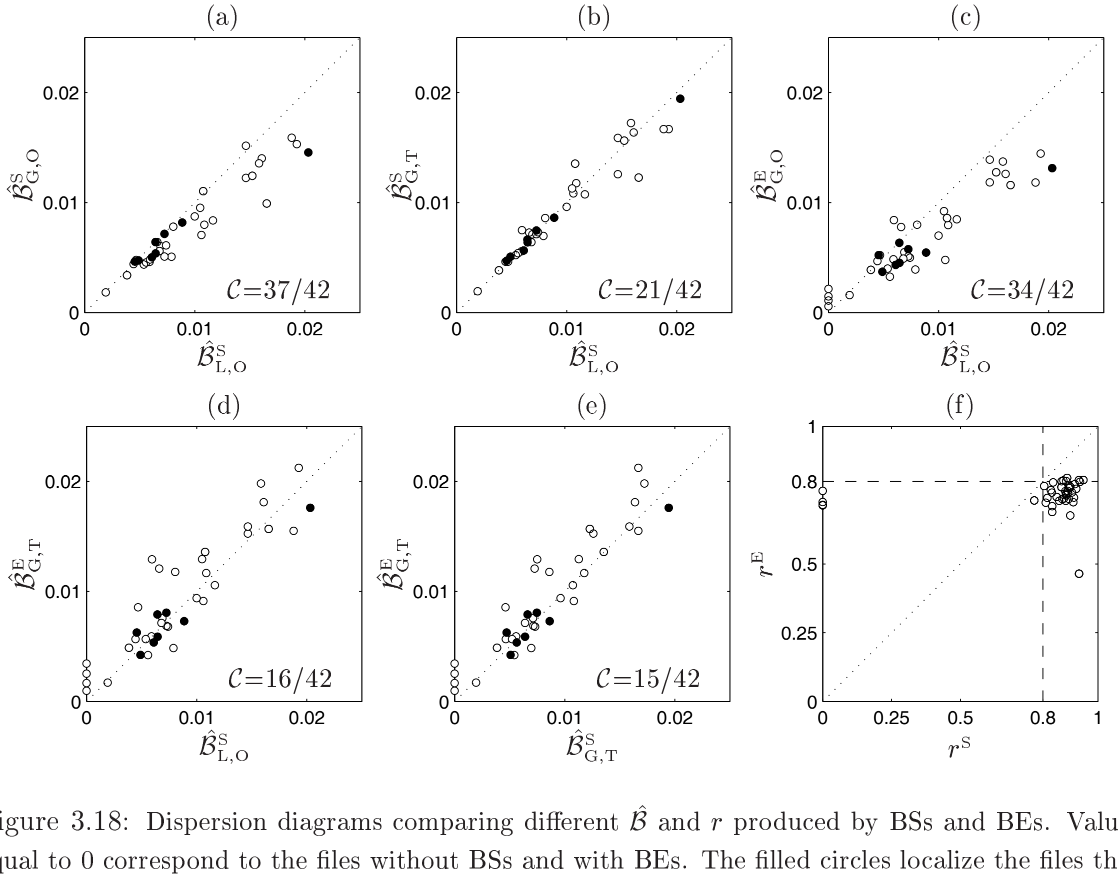

Figure 3.18: Dispersion diagrams comparing different $\hat{\mathcal{B}}$ and r produced by BSs and BEs. Values equal to 0 correspond to the files without BSs and with BEs. The filled circles localize the files that satisfy $K^{\mathrm{S}} > K^{\mathrm{E}}$. The dotted line is the identity line.

The empirical distribution of $\hat{\mathcal{B}}$ obtained from the EuroBaVar files is presented in Fig. 3.19(a). The $\hat{\mathcal{B}}^{\mathrm{E}}_{\mathrm{L,O}}$ values are higher than $\hat{\mathcal{B}}^{\mathrm{S}}_{\mathrm{L,O}}$ and show larger interindividual differences. With the use of the global/total approaches, $\hat{\mathcal{B}}^{\mathrm{S}}$ and $\hat{\mathcal{B}}^{\mathrm{E}}$ have similar distributions.

The BRS analysis based on BEs is also capable of providing a BRS estimate when BSs cannot be identified. The 4 files without BSs correspond to the paired L and S evaluations of 2 subjects (B005 and B010) and, therefore, these files may correspond to the BRS dysfunction cases. For these files, identified in Fig. 3.19(a) with the open circles, the $\hat{\mathcal{B}}^{\mathrm{E}}$ values are lower than the 5^{th} percentile of the BRS estimates empirical distribution of the remaining files.

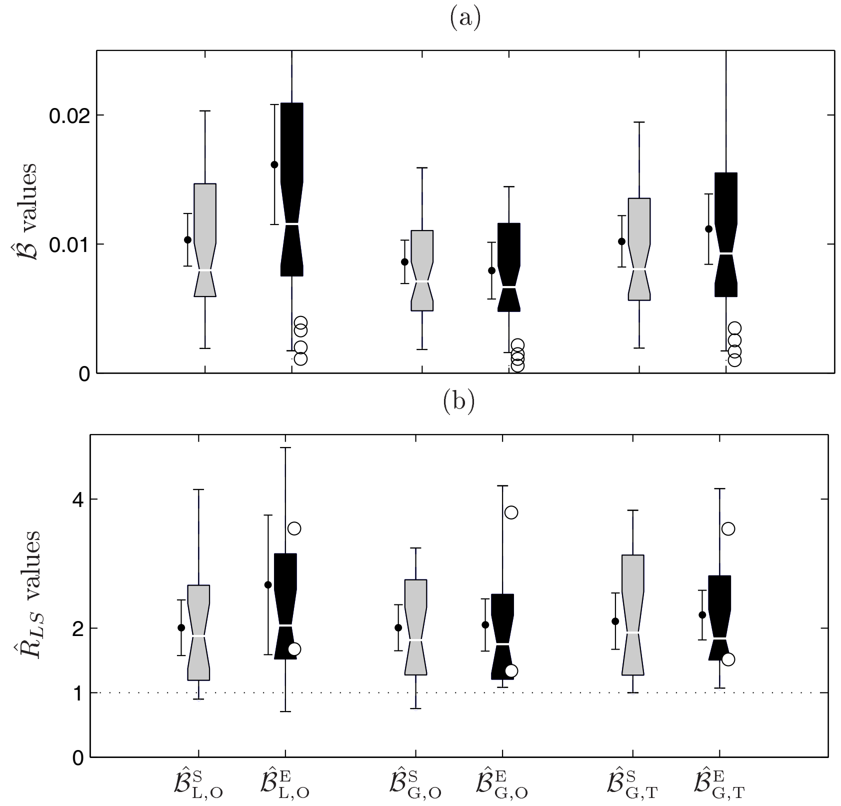

Figure 3.19: Boxplots of (a) $\hat{\mathcal{B}}$ and (b) L to S ratio of $\hat{\mathcal{B}}$ ($\hat{R}_{LS}$). Median and mean 95% confidence intervals represented by the notch and by the interval displayed at the left of each boxplot. Values estimated with BSs (grey) and BEs (black). The circles localize the files without BSs and with BEs.

For the discrimination between L and S, it is expected that the L to S ratio of $\hat{\mathcal{B}}$ ($\hat{R}_{LS}$) is above 1 (Laude *et al.*, 2004). As shown in Fig. 3.19(b) there is strong evidence that both the mean and median of $\hat{R}_{LS}$ are above 1 for all approaches, being approximately twice greater in L than in S. Of the 23 pairs of records, 21 present BSs in both positions and $\hat{R}_{LS}$ from local/global/total approach is above 1 in 18/20/20 of the pairs, respectively. All 23 pairs present BEs, and $\hat{R}_{LS}$ is above 1 in 20/23/23 of the pairs, respectively. The use of global/total approach combined with BEs is able to distinguish L from S also for the files without BSs, but not able to differentiate them from the remaining files.

Table 3.4 resumes the additional comparison between the events technique and other time domain BRS methods, including the sequences technique used with the thresholds referred in Laude *et al.* (2004) and the xBRS method Westerhof *et al.* (2004). The effect of changing the threshold values in the sequences technique was already discussed in Sec. 3.4 and, in this comparison, the sequences technique is used with the following thresholds Laude *et al.* (2004): method [13] $\Delta^{\mathrm{SBP}}_{min} = 1$, $\Delta^{\mathrm{RR}}_{min} = 4$ and $r_{min} = 0.7$, method [15] $\Delta^{\mathrm{SBP}}_{min} = \Delta^{\mathrm{RR}}_{min} = 0$ and $r_{min} = 0.85$ and method [18] $N_{min} = 4$, $\tau = 0$, $\Delta^{\mathrm{SBP}}_{min} = 1$, $\Delta^{\mathrm{RR}}_{min} = 5$. The comparison with the xBRS method is also included (See Sec. 1.3.3 for details on the methodology).

The results in Table 3.4 point out that all techniques are able to differentiate L from S positions in most of the subjects (mean $\hat{R}_{LS} > 1$), with the $\hat{\mathcal{B}}^{[15]}$ and $\hat{\mathcal{B}}^{\mathrm{E}}_{\mathrm{G,T}}$ estimates achieving a higher $\hat{R}_{LS}$ mean value (better discrimination). The $\hat{R}_{LS}$ values obtained from $\hat{\mathcal{B}}^{\mathrm{E}}_{\mathrm{G,T}}$ present a similar dispersion and lower amplitude range in comparison to that evaluated for the xBRS estimates. Both $\hat{\mathcal{B}}^{\mathrm{E}}_{\mathrm{G,O}}$ and $\hat{\mathcal{B}}^{\mathrm{E}}_{\mathrm{G,T}}$ are able to distinguish L and S conditions for all subjects.

Table 3.4: Events technique compared with other time domain BRS methods (description in the text). The xBRS values were taken from Table 2 of Westerhof *et al.* (2004). The mean, SD (standard deviation) and range (in msec/mmHg) were computed over the non-repeated 21 EuroBaVar files.

	$\hat{\mathcal{B}}^{[13]}$	$\hat{\mathcal{B}}^{[15]}$	$\hat{\mathcal{B}}^{[18]}$	xBRS	$\hat{\mathcal{B}}^{\mathrm{E}}_{\mathrm{G,O}}$	$\hat{\mathcal{B}}^{\mathrm{E}}_{\mathrm{G,T}}$
Lying						
n	20	21	16	21	21	21
Mean	11.5	18.5	13.4	12.4	10.5	15.3
SD	7.8	14.8	6.7	12.1	9.4	11.1
Range	2.3-38.9	3.1-64.6	5.5-30.6	2.0-60.0	1.4-49.8	2.6-55.4
Standing						
n	19	21	19	21	21	21
Mean	5.7	8.2	8.0	6.2	5.4	7.3
SD	2.6	6.1	3.1	3.9	3.1	4.3
Range	1.7-12.8	1.4-26.6	2.9-14.1	0.8-16.3	0.57-11.8	0.99-15.8
$\hat{R}_{LS}$						
n	19	21	16	21	21	21
Mean	2.20	2.49	1.80	1.96	2.05	2.24
SD	0.97	1.16	0.77	0.92	0.94	0.92
Range	0.77-3.95	0.80-5.31	0.81-3.57	0.85-4.20	1.08-4.20	1.17-4.31

3.5.3 BRS reproducibility

The intra-method reproducibility relates to the concordance of the results obtained from different experimental data, acquired from the same subject and in the same conditions. In this work, the BRS reproducibility was evaluated from the paired comparison between the BRS analysis obtained from different recordings of the same subject. As the EuroBaVar data was collected in stationary conditions, it is expected that smaller parts of the original file are still distinctive of that subject. Therefore, each of the 512 beats recordings was divided into two consecutive and non-overlapping spontaneous test recordings of 256 beats, [SP$_1$] and [SP$_2$]. Subsequently, the BRS analysis was carried out in each test recording and the results were paired/compared within subject.

Figure 3.20 shows the comparison between the variables given in Table 3.2 evaluated from BSs for the two test recordings [SP$_1$] and [SP$_2$]. As is possible to observe, N^{S} and K^{S} in the recording tests are correlated, as well as the $\hat{\mathcal{B}}$ estimates, with the larger $\hat{\mathcal{B}}$ values exhibiting larger differences between their evaluation in the two test recordings.

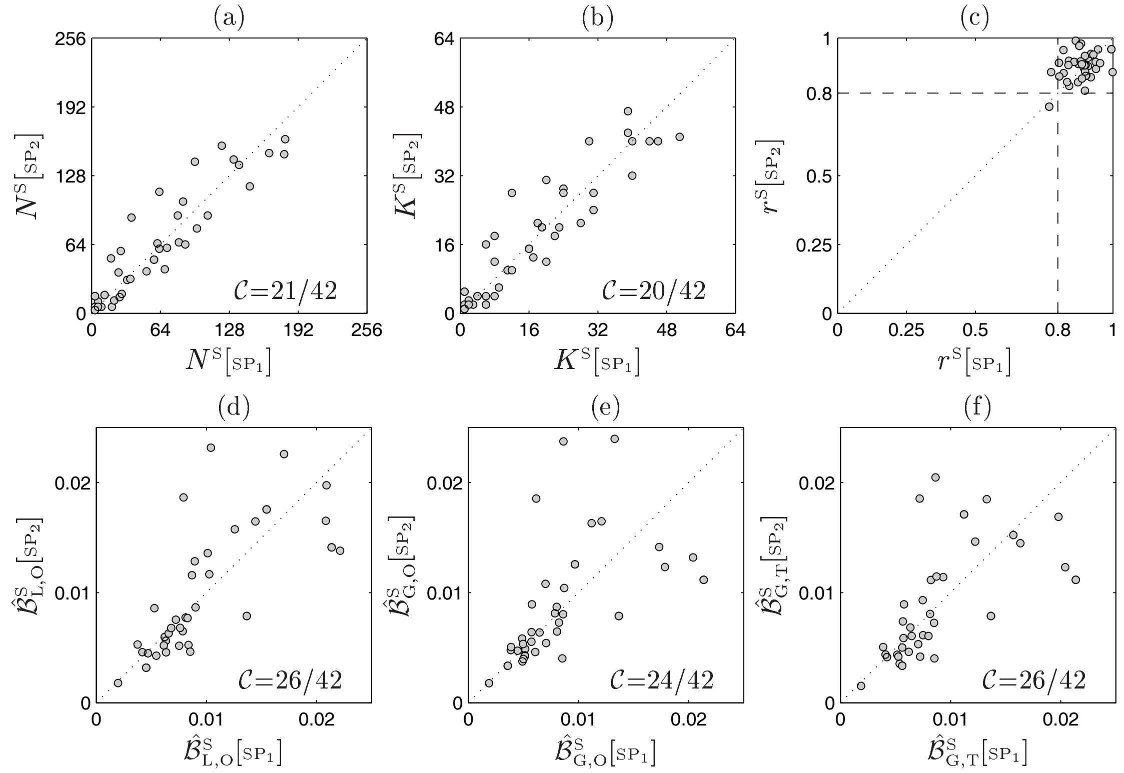

Figure 3.20: Comparison between the BRS variables from BSs, obtained for the two test recordings [SP$_1$] and [SP$_2$]. The dotted line is the identity line.

Figure 3.21 shows the same comparison as in Fig. 3.20 for the variables evaluated from BEs. The N^{E} and K^{E} obtained in the test recordings are correlated, as well as the $\hat{\mathcal{B}}$ values. In comparison with the BRS analysis from BSs (Fig. 3.20), the larger $\hat{\mathcal{B}}$ values show less differences between their evaluation in the two test recordings. Also, the BRS analysis from BEs for the files that do not exhibit BSs, was found to provide comparable values for both test recordings.

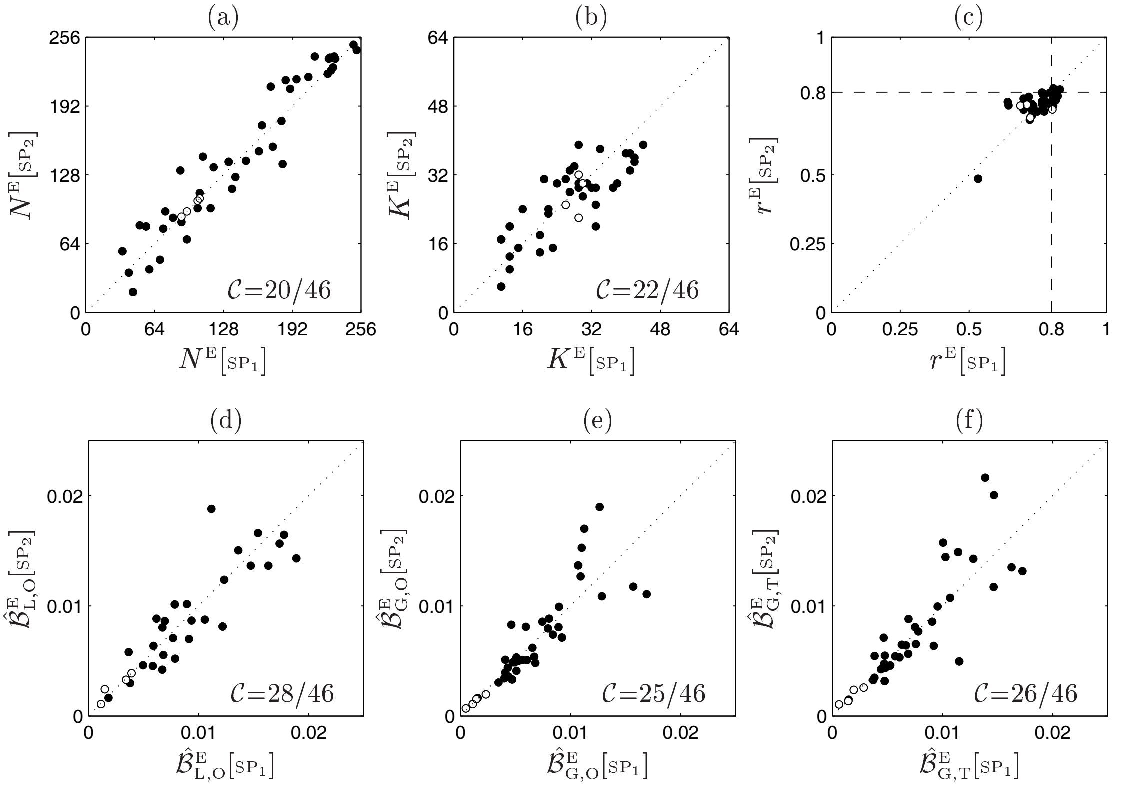

Figure 3.21: Comparison between the BRS variables from BEs, obtained from the two test recordings [SP$_1$] and [SP$_2$]. The dotted line is the identity line. The white circles localize the files without BSs and with BEs.

The BRS reproducibility was quantified from the distribution of the difference between the $\hat{\mathcal{B}}$ values evaluated from the two test recordings, i.e.,

$$\mathrm{D}_{\hat{\mathcal{B}}} = \hat{\mathcal{B}}[\mathrm{SP}_2] - \hat{\mathcal{B}}[\mathrm{SP}_1]. \tag{3.8}$$

As the EuroBaVar dataset includes a wide range of $\hat{\mathcal{B}}$ values and the different BRS estimators provide different mean $\hat{\mathcal{B}}$ values, the reproducibility was also quantified from the $\hat{\mathcal{B}}$ coefficient of variation, here denoted by $\mathrm{CV}_{\hat{\mathcal{B}}}$, which quantifies the intra-method dispersion as a percentage of the $\hat{\mathcal{B}}$ mean value.

The distributions of the $\mathrm{D}_{\hat{\mathcal{B}}}$ and $\mathrm{CV}_{\hat{\mathcal{B}}}$ values obtained for each BRS estimator are presented in Fig. 3.22. As illustrated in Fig. 3.22(a), all approaches present 95% confidence intervals over the median/mean $\mathrm{D}_{\hat{\mathcal{B}}}$ values including zero and, therefore, the hypothesis of the true median/mean intra-method difference being equal to zero cannot be rejected (at a significance level of 5%). The estimates $\hat{\mathcal{B}}^{\mathrm{E}}_{\mathrm{G,O}}$ and $\hat{\mathcal{B}}^{\mathrm{E}}_{\mathrm{G,T}}$ achieve the lowest $|\mathrm{D}_{\hat{\mathcal{B}}}|$ values (Fig. 3.22(a)) and the lowest $\mathrm{CV}_{\hat{\mathcal{B}}}$ values (Fig. 3.22(b)) in comparison with the remaining estimates. Figure 3.22(b) shows that around 75% of the files exhibit a $\mathrm{CV}_{\hat{\mathcal{B}}}$ value below 25%, for $\hat{\mathcal{B}}^{\mathrm{S}}_{\mathrm{L,O}}$, $\hat{\mathcal{B}}^{\mathrm{E}}_{\mathrm{G,O}}$ and $\hat{\mathcal{B}}^{\mathrm{E}}_{\mathrm{G,T}}$ values. This percentage increases to values above 30% for the remaining estimates.

The 4 EuroBaVar files without BSs and with BEs have smaller $\left|\mathrm{D}_{\hat{\mathcal{B}}}\right|$ values in comparison with the $\left|\mathrm{D}_{\hat{\mathcal{B}}}\right|$ values for the files with BSs (Fig. 3.22(a)), mainly due to their smaller $\hat{\mathcal{B}}$ values (Fig. 3.19(a)). The $\mathrm{CV}_{\hat{\mathcal{B}}}$ values are comparable to that of the remaining cases (Fig. 3.22(a)), indicating that the estimators reproducibility may not be dependent on the BRS condition.

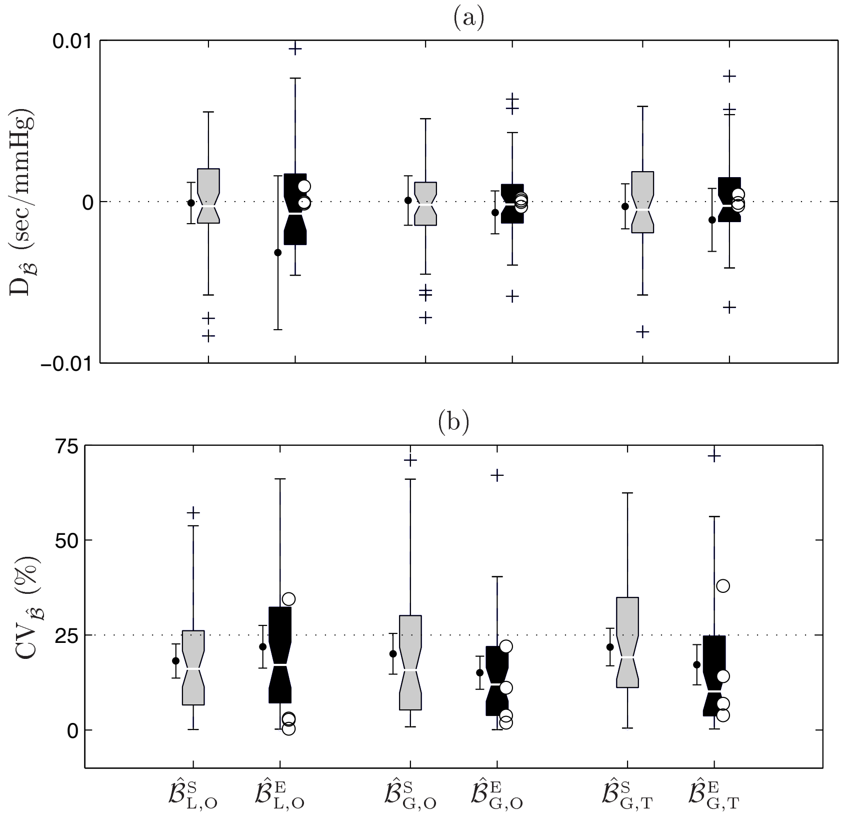

Figure 3.22: Boxplots of (a) $\mathrm{D}_{\hat{\mathcal{B}}}$ and (b) $\mathrm{CV}_{\hat{\mathcal{B}}}$ evaluated from the $\hat{\mathcal{B}}$ obtained in the two test recordings. Median and mean 95% confidence intervals represented by the notch and by the interval displayed at the left of each boxplot. Values estimated with BSs (grey) and BEs (black). The circles localize the files without BSs and with BEs.

The reproducibility study of the sequences technique ($\hat{\mathcal{B}}^{\mathrm{S}}_{\mathrm{L,O}}$) has already been carried out in two homogenous datasets, one of 21 patients with chronic heart failure and another of 16 control subjects (Davies *et al.*, 1999). It is reported in Davies *et al.* (1999) that $\mathrm{CV}_{\hat{\mathcal{B}}}$=30.7% in the patients and $\mathrm{CV}_{\hat{\mathcal{B}}}$=40.4% in the control subjects, with the $\mathrm{CV}_{\hat{\mathcal{B}}}$ being calculated as one value for all the dataset files. In this study, for the EuroBaVar files presenting BSs, $\mathrm{CV}_{\hat{\mathcal{B}}}$=38.6% and for the files not presenting BSs (i.e., patients) the $\mathrm{CV}_{\hat{\mathcal{B}}}$ could not be calculated, because no BRS estimate was provided.

The EuroBaVar is a non-homogenous dataset and, therefore, the analysis of the $\mathrm{CV}_{\hat{\mathcal{B}}}$ empirical distribution carries much more information than a single statistics. The reproducibility limits for the BRS estimators, quantified from the $\mathrm{D}_{\hat{\mathcal{B}}}$ range and $\mathrm{CV}_{\hat{\mathcal{B}}}$ percentiles, are provided in Table 3.5. The $\hat{\mathcal{B}}^{\mathrm{S}}_{\mathrm{L,O}}$ estimates provided a median $\mathrm{CV}_{\hat{\mathcal{B}}}$ value lower than 20% and, of the six estimators, the $\mathcal{B}^{\mathrm{E}}_{\mathrm{G,O}}$ and $\mathcal{B}^{\mathrm{E}}_{\mathrm{G,T}}$ presented the highest reproducibility for all files, either presenting or not BSs.

Table 3.5: Reproducibility limits for the BRS estimators in spontaneous condition, quantified from $\mathrm{D}_{\hat{\mathcal{B}}}$ and $\mathrm{CV}_{\hat{\mathcal{B}}}$. The variable P_k, $k = \{50, 75, 95\}$ is the value below which k% of the observations fall, and n indicates the # of files from which the statistics were computed.

		$\mathrm{D}_{\hat{\mathcal{B}}}$ (msec/mmHg)		$\mathrm{CV}_{\hat{\mathcal{B}}}$ (%)		
	n	[P_{25}, P_{75}]	[$\mathrm{P}_{2.5}$, $\mathrm{P}_{97.5}$]	P_{50}	P_{75}	P_{95}
$\hat{\mathcal{B}}^{\mathrm{S}}_{\mathrm{L,O}}$	42	[-1.3, 2.0]	[-7.7, 11.6]	16.1	26.1	46.5
$\hat{\mathcal{B}}^{\mathrm{S}}_{\mathrm{G,O}}$	42	[-1.5, 1.2]	[-10.2, 13.6]	15.8	30.1	56.8
$\hat{\mathcal{B}}^{\mathrm{S}}_{\mathrm{G,T}}$	42	[-1.9, 1.9]	[-10.2, 11.6]	19.1	34.9	53.4
$\hat{\mathcal{B}}^{\mathrm{E}}_{\mathrm{L,O}}$	46	[-2.5, 1.5]	[-66.3, 20.3]	16.1	32.3	63.0
$\hat{\mathcal{B}}^{\mathrm{E}}_{\mathrm{G,O}}$	46	[-1.0, 1.0]	[-18.8, 6.0]	11.4	21.9	45.7
$\hat{\mathcal{B}}^{\mathrm{E}}_{\mathrm{G,T}}$	46	[-1.0, 0.7]	[-29.0, 6.4]	10.2	24.7	59.4

3.5.4 Dispersion in time domain BRS estimation

Regardless of the slope estimator, the BRS analysis from BEs has shown to be advantageous as it provides a larger number of beats for slope estimation, allowing BRS analysis in cases where BSs cannot be identified. However, the higher number of beats (N) is obtained at the expense of a lower SBP-RR correlation (r) although remaining close to 0.8, with possible repercussion on the dispersion of the BRS estimator. In this study, the dispersion in BRS estimation was quantified from the estimated $\hat{\mathcal{B}}$ standard deviation ($\hat{\sigma}_{\hat{\mathcal{B}}}$) as follows

$$\delta = \frac{\hat{\sigma}_{\hat{\mathcal{B}}}}{\hat{\mathcal{B}}} \times 100. \tag{3.9}$$

Regarding the global approach, standard parametric confidence intervals (CIs) over the regression slope could have been considered to quantify the dispersion in BRS analysis. However, these CIs can only be applied if the regression residues ($\hat{\boldsymbol{\epsilon}}$) satisfy the classic assumptions of zero mean, normal distribution, non correlation and homoscedasticity. In this work, the $\hat{\boldsymbol{\epsilon}}$ analysis did not support these assumptions, either considering BSs or BEs, except for a zero mean normal distribution (with 95% confidence). Therefore, these parametric CIs were not considered for global approach.

The heteroscedasticity exhibited by the data can over/underestimate $\hat{\sigma}_{\hat{\mathcal{B}}}$, depending on the heterocedasticity pattern. In the case of the BRS analysis, the higher concentration of points lies near the origin and the residuals of the global regression analysis show larger dispersion for more extreme SBP values (like a "*butterfly*" pattern, as illustrated in Fig. 3.4(c–d)). Therefore, more points exhibit a lower dispersion, leading to $\hat{\sigma}_{\hat{\mathcal{B}}}$ underestimation. The lack of homoscedasticity in the residuals could be overcome either by changing the regression model (if the heterocedasticity pattern is known) or by using weighted least squares regression instead of OLS (Wilcox, 2005). Because the aim of this work is to quantify the dispersion in the BRS analysis from more conventional slope estimators, an alternative simulation-based methodology was considered for such purpose. Similarly, the same technique was used to evaluate the BRS variability when using the local and total approach, attending to the specificities of each slope estimator.

Bootstrap-based methodology to quantify the BRS variance

Bootstrapping is a general approach to perform statistical inference. It is based on building a sampling distribution for a statistic, by resampling with replacement the data (Efron and Tibshirani, 1993). The advantage of bootstrapping over analytical methods is its great simplicity, because it does not require any apriori knowledge about the sample besides its values, and they have been shown to be useful in the resolution of several signal processing problems (Zoubir and Boashash, 1998).

The method produces the bootstrap replicas, mimicking the original data, by resampling with replacement the original data[2]. Each bootstrap replica is taken from the original sample and, therefore, it is considered to be independent and identical distribution (i.i.d.), i.e., it is assumed that the bootstrap replica come from the same distribution of the population and that each replica is drawn independently from the other replicas. The statistics in study is then recomputed for each bootstrap replica and the mean value of the bootstrapped recomputations is taken as an estimate of the statistics.

There are several ways to carry out a bootstrap simulation, including nonparametric bootstrapping of the observation pairs, nonparametric bootstrapping of the residuals, and parametric bootstrapping of the residuals (assuming a distribution in the regression residuals). With respect to the BRS analysis, there is the question to carry out the bootstrap by resampling over the segments or over the beats. For example, if the bootstrap is carried out by segments it is not guaranteed that the bootstrap replicas have the same number of beats and, therefore, the bootstrap by segments is not suitable for the evaluation of the BRS dispersion in global and total slope estimators. On the other hand, resampling by beats is not suitable for the analysis of the local slope estimator, because the segments unit is lost.

---

[2] The bootstrap replicas are created by random selection of the elements in the original set. The elements of the original set have equal probability of being chosen, even if previously chosen. Therefore, a bootstrap replica of the same size as the original set likely has repeated elements from the original set.

In order to attend the specificities of each estimator and to mimic the size of the original data in each bootstrap replica, the bootstrap technique has to be used differently for each slope estimation approach. In this application, the original sample size should be used in each bootstrap replica, reproducing also the length of the original data. This is because the lower BRS estimates are associated with reduced number of beats in the identified segments; therefore, the number of beats for slope computation also characterizes the BRS function.

Figure 3.23 shows the dispersion diagrams of one generated bootstrap replica for one subject, considering BSs and BEs and the different slope estimators. The bootstrap replicas were generated by resampling with replacement the segments (BSs or BEs) or the beats in those segments, depending on the slope approach:

- for the local approach, the replicas were composed by resampling the segments presented in Fig. 3.4(c–d) for BSs and BEs, respectively;
- for the global approach, the replicas were composed by resampling the beats presented in Figs. 3.4(c–d) for BSs and BEs, respectively;
- for the total approach, the replicas were composed by resampling the beats after the removal of outlier segments presented in Figs. 3.8(a–b) for BSs and BEs, respectively.

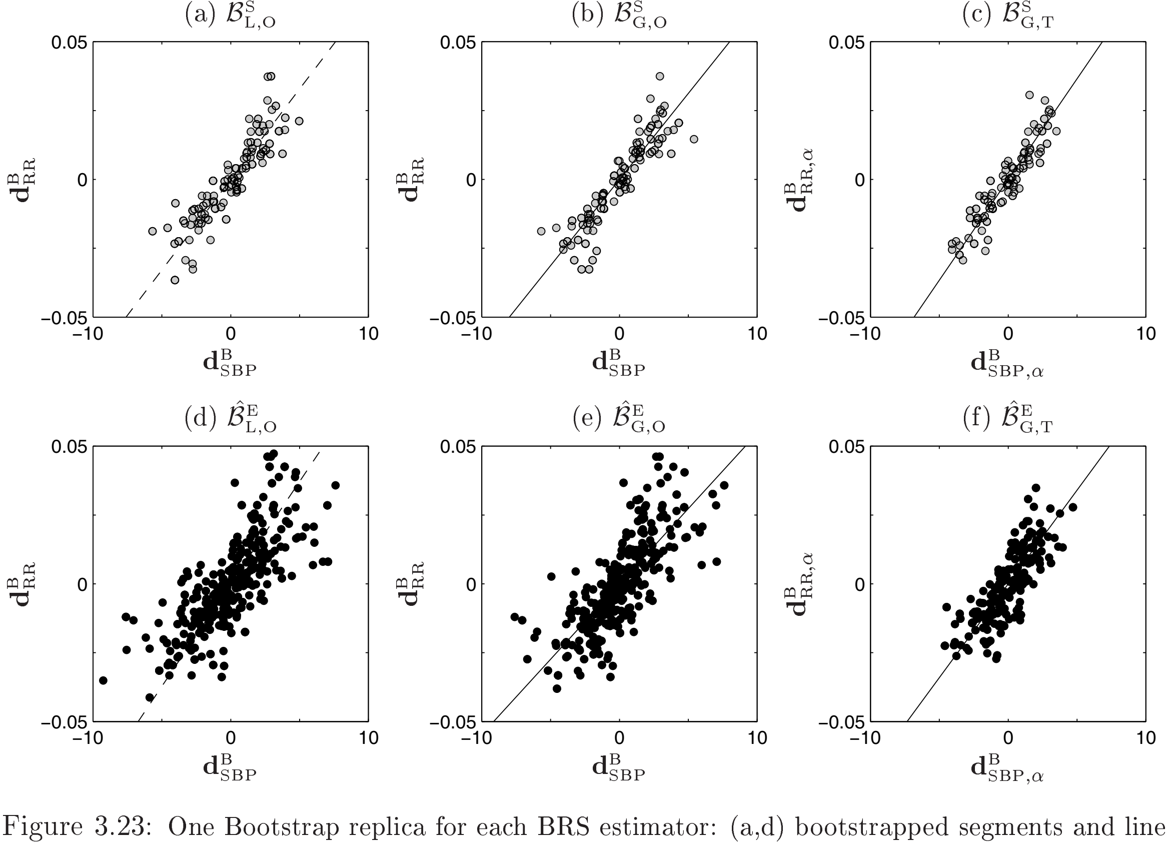

(a) $\hat{\mathcal{B}}^{\mathrm{S}}_{\mathrm{L,O}}$ (b) $\hat{\mathcal{B}}^{\mathrm{S}}_{\mathrm{G,O}}$ (c) $\hat{\mathcal{B}}^{\mathrm{S}}_{\mathrm{G,T}}$

(d) $\hat{\mathcal{B}}^{\mathrm{E}}_{\mathrm{L,O}}$ (e) $\hat{\mathcal{B}}^{\mathrm{E}}_{\mathrm{G,O}}$ (f) $\hat{\mathcal{B}}^{\mathrm{E}}_{\mathrm{G,T}}$

Figure 3.23: One Bootstrap replica for each BRS estimator: (a,d) bootstrapped segments and line with slope $\hat{\mathcal{B}}_{\mathrm{L,O}}$, (b,e) bootstrapped beats and line with slope $\hat{\mathcal{B}}_{\mathrm{G,O}}$ and (c,f) bootstrapped beats and line with slope $\hat{\mathcal{B}}_{\mathrm{G,T}}$. Replicas for (a–c) BSs and for (d–f) BEs. Same data as in Fig. 3.3.

The choice of the number of replicas B is crucial, depending on the sample length and the distribution of the data (Efron and Tibshirani, 1993). Because the bootstrap technique is based on an asymptotic result, at a formal level, the bootstrap requires an infinite B. However, the bootstrap statistics converges in terms of B, and so having a finite B is good enough, assuming the number of replications chosen is large enough. The larger the B, the more reproducible the results will be when a different set of samples is used. So if redoing the bootstrap analysis, it is more likely to see the same results if a high number of bootstrap replicas is used.

For illustration purposes, Fig. 3.24(a) shows the estimated $\delta^{\mathrm{E}}_{\mathrm{G,O}}$ as a function of B, varying B from 20 to 2000. For B lower than 500, $\delta^{\mathrm{E}}_{\mathrm{G,O}}$ is variable, while for B higher than 500 the $\delta^{\mathrm{E}}_{\mathrm{G,O}}$ stabilizes. Similar analysis was performed for the remaining BRS estimators, leading to similar results. Therefore, in this work B=1000 was considered. Figure 3.24(b) presents the histogram of the bootstrapped $\hat{\mathcal{B}}^{\mathrm{E}}_{\mathrm{G,O}}$ values considering B=1000, from which the $\delta^{\mathrm{E}}_{\mathrm{G,O}}$ in Eq. (3.9) is computed.

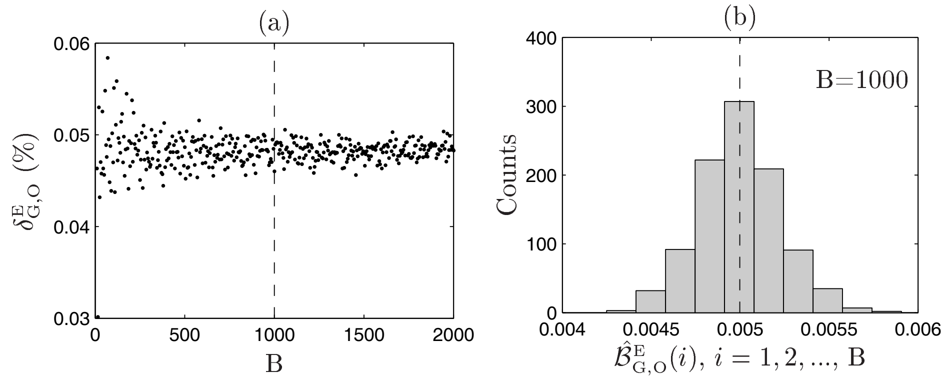

Figure 3.24: Bootstrap computation of $\delta^{\mathrm{E}}_{\mathrm{G,O}}$: (a) $\hat{\delta}^{\mathrm{E}}_{\mathrm{G,O}}$ as a function of B=[20:5:2000]; (b) histogram of the bootstrapped $\hat{\mathcal{B}}^{\mathrm{E}}_{\mathrm{G,O}}$ for B=1000 with the dashed line locating the $\hat{\mathcal{B}}^{\mathrm{E}}_{\mathrm{G,O}}$ value.

Figure 3.25 presents the distribution of δ obtained for each BRS estimator, illustrating that the $\hat{\mathcal{B}}_{\mathrm{G,O}}$ and $\hat{\mathcal{B}}_{\mathrm{G,T}}$ are the estimates that achieve the lowest δ values. Around 50% of the files present $\delta^{\mathrm{S}}_{\mathrm{L,O}}$ below 10%, while only 25% of the files exhibit $\delta^{\mathrm{E}}_{\mathrm{L,O}}$ lower than 10%. This percentage increases considerably for $\delta_{\mathrm{G,O}}$ and $\delta_{\mathrm{G,T}}$, indicating that the use of global and total approaches for slope estimation is clearly an advantage over the use of the traditional local approach, in terms of dispersion. In particular, the $\hat{\mathcal{B}}^{\mathrm{S}}_{\mathrm{G,T}}$ values achieve the lowest variability, with around 50% of the files presenting $\delta^{\mathrm{S}}_{\mathrm{G,T}}$ lower than 5%. However, the BRS analysis from BSs is not able to provide a BRS estimate for all subjects. Considering the $\hat{\mathcal{B}}^{\mathrm{E}}_{\mathrm{G,O}}$ and $\hat{\mathcal{B}}^{\mathrm{E}}_{\mathrm{G,T}}$ values, the δ values obtained for the 4 EuroBaVar files without BSs and with BEs are comparable to that of the remaining files, indicating that the estimators variability may not be dependent on the subject's BRS condition. Finally, the median $\delta^{\mathrm{E}}_{\mathrm{G,O}}$ and $\delta^{\mathrm{E}}_{\mathrm{G,T}}$ values are slightly higher than the median $\delta^{\mathrm{S}}_{\mathrm{G,T}}$ value for the files presenting BSs.

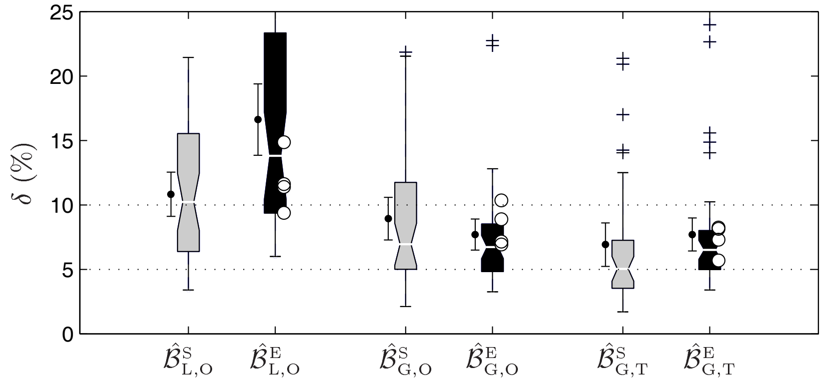

Figure 3.25: Boxplots of δ evaluated for each BRS estimator. Median and mean 95% confidence intervals represented by the notch and by the interval displayed at the left of each boxplot. Values estimated with BSs (grey) and BEs (black). The circles localize the files without BSs and with BEs.

The dispersion limits for the BRS estimators, quantified from the percentiles of the δ empirical distribution are provided in Table 3.6. As already referred, the $\hat{\mathcal{B}}^{\mathrm{S}}_{\mathrm{L,O}}$ estimates provide a median δ value around 10% and, of the estimators able to provide a BRS estimate for all subjects, the $\mathcal{B}^{\mathrm{E}}_{\mathrm{G,O}}$ and $\mathcal{B}^{\mathrm{E}}_{\mathrm{G,T}}$ yield the lowest dispersion attending the entire distribution: more than 75% of the EuroBaVar files present a δ value below 10%.

Table 3.6: Dispersion limits for the BRS estimators in spontaneous condition, quantified from δ. The variable P_k, $k = \{50, 75, 95\}$ is the value below which k% of the observations fall, and n indicates the # of files from which the statistics were computed.

	δ (%)			
	n	P_{50}	P_{75}	P_{95}
$\hat{\mathcal{B}}^{\mathrm{S}}_{\mathrm{L,O}}$	42	10.2	15.5	20.8
$\hat{\mathcal{B}}^{\mathrm{S}}_{\mathrm{G,O}}$	42	6.9	11.7	21.1
$\hat{\mathcal{B}}^{\mathrm{S}}_{\mathrm{G,T}}$	42	5.0	7.2	19.5
$\hat{\mathcal{B}}^{\mathrm{E}}_{\mathrm{L,O}}$	46	13.6	21.2	38.5
$\hat{\mathcal{B}}^{\mathrm{E}}_{\mathrm{G,O}}$	46	6.8	8.9	14.7
$\hat{\mathcal{B}}^{\mathrm{E}}_{\mathrm{G,T}}$	46	6.6	8.1	17.0

Figure 3.26 presents the comparison between the different δ, illustrating that the use of $\hat{\mathcal{B}}^{\mathrm{S}}_{\mathrm{G,O}}$ instead of $\hat{\mathcal{B}}^{\mathrm{S}}_{\mathrm{L,O}}$ reduces the BRS dispersion in the majority of the cases (Fig. 3.26(a)). The BRS estimation from $\hat{\mathcal{B}}^{\mathrm{E}}_{\mathrm{G,O}}$ instead of $\hat{\mathcal{B}}^{\mathrm{S}}_{\mathrm{G,O}}$ is advantageous for the files that do not present BSs and for the files that exhibit higher $\delta^{\mathrm{S}}_{\mathrm{G,O}}$ values (open circles in Fig. 3.26(b)). The comparison between the $\hat{\mathcal{B}}^{\mathrm{E}}_{\mathrm{G,O}}$ and $\hat{\mathcal{B}}^{\mathrm{E}}_{\mathrm{G,T}}$ (Fig. 3.26(c)) indicates that the mean paired differences between the $\delta^{\mathrm{E}}_{\mathrm{G,O}}$ and $\delta^{\mathrm{E}}_{\mathrm{G,T}}$ values do not significantly differ from zero ($p > 0.9$).

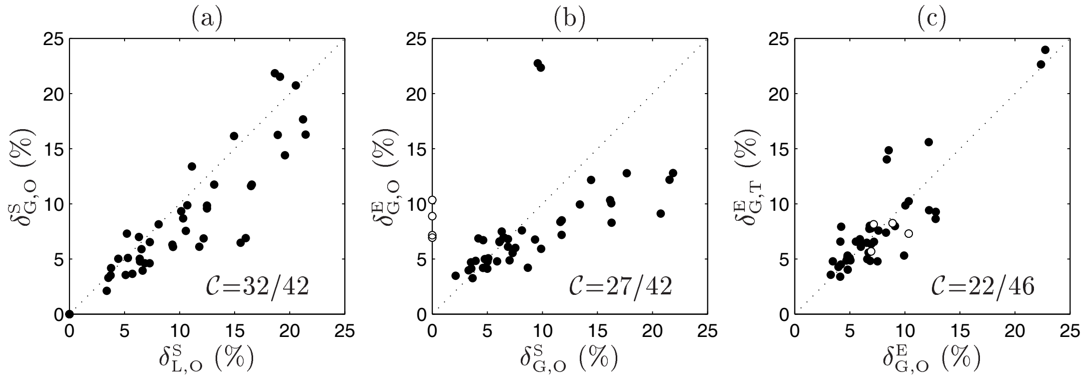

Figure 3.26: Dispersion diagrams comparing δ evaluated for different BRS estimators. The white circles localize the files without BSs and with BEs.

Figure 3.26(b) illustrates that the BRS estimation from BEs instead of BSs leads to $\delta^{\mathrm{E}}_{\mathrm{G,O}} < \delta^{\mathrm{S}}_{\mathrm{G,O}}$ for the files exhibiting the highest $\delta^{\mathrm{S}}_{\mathrm{G,O}}$. As illustrated in Figs. 3.27(a) and 3.27(c), these files present the lowest N^{S} values, although presenting similar r^{S} values to that of the remaining files. This result indicates that the decreased N^{S} is the main reason for an increased $\delta^{\mathrm{S}}_{\mathrm{G,O}}$. As illustrated in Figs. 3.27(b) and 3.27(d), these files also exhibit the lowest N^{E} values and present r^{E} similar to that of the remaining files.

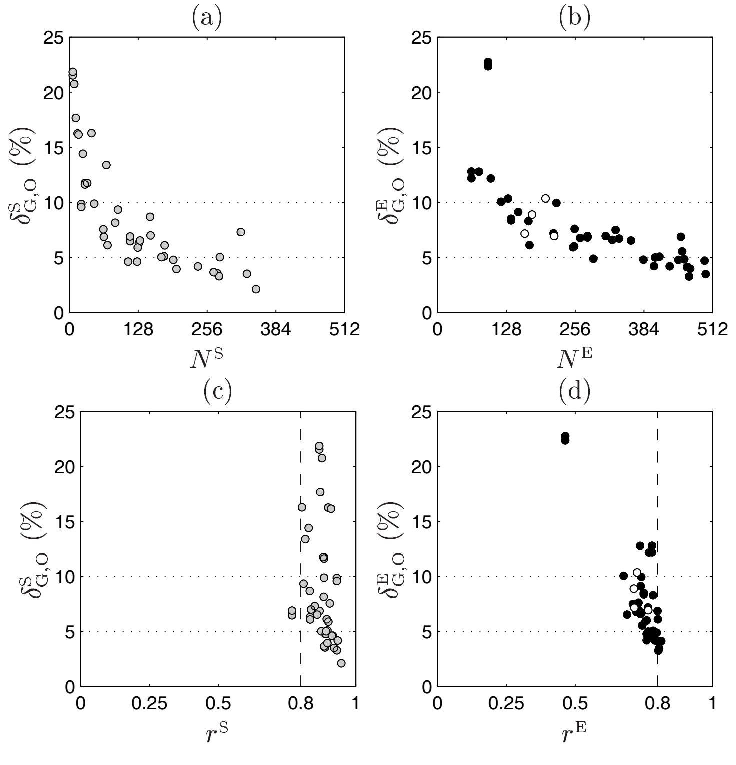

Figure 3.27: Plot of δ as a function of N and r for $\hat{\mathcal{B}}^{\mathrm{S}}_{\mathrm{G,O}}$ (grey) and $\hat{\mathcal{B}}^{\mathrm{E}}_{\mathrm{G,O}}$ (black). The white circles localize the files without BSs and with BEs.

As previously referred, the less restrictive thresholds for BE identification lead to $N^{\mathrm{E}} > N^{\mathrm{S}}$ and $r^{\mathrm{E}} < r^{\mathrm{S}}$ for all EuroBaVar files (Fig. 3.16 and Fig. 3.18). Therefore, with the used of BEs instead of BSs, the increased N^{E} obtained at the expense of a lower r^{E}, not only increases the probability of providing a BRS estimate, but also compensates in terms of dispersion, because $\delta^{\mathrm{E}}_{\mathrm{G,O}} \approx \delta^{\mathrm{S}}_{\mathrm{G,O}}$ for the files with higher N^{S} and $\delta^{\mathrm{E}}_{\mathrm{G,O}} < \delta^{\mathrm{S}}_{\mathrm{G,O}}$ for the files with lower N^{S}.

3.6 Discussion

The thresholds regarding the minimum beat-to-beat changes ($\Delta^{\mathrm{SBP}}_{min}$ and $\Delta^{\mathrm{RR}}_{min}$) and minimum correlation (r_{min}) required for SBP and RR segmentation are chosen to increase the reliability of the identified BS to be a segment clearly baroreflex related. In this way, there is an increased assurance that the corresponding slope is quantifying a real baroreflex effect. However, their use may also reduce the ability of providing an individual estimate, particularly if the thresholds values are very restrictive and/or the analyzed subject has poor BRS function.

Thresholds and threshold values to identify baroreflex related segments

The simultaneous use of the $\Delta^{\mathrm{SBP}}_{min}$, $\Delta^{\mathrm{RR}}_{min}$ and r_{min} can be avoided (Gouveia *et al.*, 2007). In fact, SBP and RR segments satisfying restrictive $\Delta^{\mathrm{SBP}}_{min}$ and $\Delta^{\mathrm{RR}}_{min}$ values present high correlation between the SBP and RR values. The correlation is usually higher than r_{min}, suggesting that the simultaneous use of these 3 thresholds is redundant. This fact is in accordance with results in cats data (Bertineri *et al.*, 1988), where it is reported that the correlation between SBP and RR values that fulfill $\Delta^{\mathrm{SBP}}_{min} = 1$ mmHg and $\Delta^{\mathrm{RR}}_{min} = 4$ msec exceeds 0.92; the authors state that such a high correlation supports a true baroreflex nature of BSs rather than random coupling. However, the high correlation is clearly a consequence of BSs being chosen as to satisfy restrictive values on $\Delta^{\mathrm{SBP}}_{min}$ and $\Delta^{\mathrm{RR}}_{min}$. In the EuroBaVar data, 85% of the SBP and RR segments that fulfill $N_{min} = 3$, $\Delta^{\mathrm{SBP}}_{min} = 1$ and $\Delta^{\mathrm{RR}}_{min} = 4$ also satisfy $r_{min} = 0.92$. This percentage increases to 99% for $r_{min} = 0.8$, either setting $\Delta^{\mathrm{RR}}_{min} = 4$ or $\Delta^{\mathrm{RR}}_{min} = 5$ msec.

As a matter of fact, it is more adequate to remove $\Delta^{\mathrm{SBP}}_{min}$ and $\Delta^{\mathrm{RR}}_{min}$ thresholds and only impose the r_{min} threshold. Removing $\Delta^{\mathrm{SBP}}_{min}$ and $\Delta^{\mathrm{RR}}_{min}$ for SBP and RR segmentation (as in BEs), there are more beats available for the slope estimation in the files that present BSs. It also enables to identify segments in cases of BSs absence and, therefore, it is possible to provide a BRS estimate. The results of the r_{min} sensitivity analysis show that $r_{min} = 0.8$ is an adequate value for BEs identification, achieving a trade-off between N^{E} and r^{E} and maximizing r^{E} (see Figs. 3.11(c–e)). Also, the stationarity of BRS over segments in this dataset (a priori setting of $r_{min} = 0.8$ leading to r^{E} close to 0.8) supports the use of global/total approach for BRS estimation, which implicitly assume stationarity.

BRS estimates obtained from the use of different approaches

Regarding the BRS values, it was shown that local estimates from BEs are higher and present higher dispersion than local estimates from BSs. The higher inter-subject dispersion in BEs estimates simply indicates that, in the EuroBaVar dataset (a heterogeneous dataset), the inter-subject variability measured by BEs analysis is greater than the inter-subject variability measured by BSs analysis. These results can be explained by the weight of 3-beat BEs in the slopes averaging, once they present higher slopes than the 3-beat BSs (as a result of avoiding $\Delta_{min}^{\mathrm{SBP}}$ and $\Delta_{min}^{\mathrm{RR}}$ thresholds). This fact was corroborated by recalculating local estimates from BEs considering $N_{min} = 4$ and observing that the differences disappear (both in median and dispersion). Concerning the global/total approach with $N_{min} = 3$, the median and dispersion differences in the BSs/BEs estimates are smaller (see Fig. 3.19).

In general, local estimates are higher than global estimates (both with BSs and BEs) and there are no significant statistical differences between local and total estimates. All estimates present pairwise correlation with the sequences technique estimates exceeding 0.8. With the use of the global/total approaches, BRS estimates from BSs and BEs have similar distributions and the total approach presents the highest correlation between BSs and BEs estimates with no significant statistical differences.

The fact that BRS estimates from BSs and BEs are correlated, though in the latter case obtained from a higher number of beats, indicates that both are measuring the same phenomenon but with a more visible expression in BEs. The absence of BSs in a record, and the impossibility to assess the BRS, is not synonymous to an absent BRS function, but rather a shortcoming of the sequences technique to provide a BRS estimate. In EuroBaVar recordings without BSs, the number of beats in BEs is around 200 out of 512 beats with r^{E} exceeding 0.75. The corresponding BRS estimates are lower than the 5^{th} percentile of the BRS estimates empirical distribution for the remaining files, therefore indicating a poorer BRS function of these subjects.

BRS estimates and ability to discriminate between Lying and Standing positions

The ratio $\hat{R}_{LS}$ obtained from BEs allows the discrimination of L and S positions in all subjects, whether obtained with the global or the total approach. However, the median of the ratios is higher when the total approach is used. In general, the total approach is preferred since it is more robust than the global approach and can handle nonstationary data. It should be noticed that for the single purpose of L and S discrimination, simpler statistical measures over the whole $x_{\mathrm{RR}}(n)$ series can be considered. For example, the L to S ratio of $x_{\mathrm{RR}}(n)$ mean value (or any quartile) discriminates 22/23 of the cases and the L to S ratio of $x_{\mathrm{RR}}(n)$ maximum value (or minimum) discriminates 21/23 of the cases.

The use of BEs in BRS analysis also allows L and S discrimination for the subjects without BSs and it is not possible to differentiate these cases from the remaining ones. The location of the ratio $\hat{R}_{LS}$ for these files in separate tails of the overall distribution could be explained by the fact that the ratio of two small values is more sensitive to a small variation in one of the values. Another explanation could be the different origins of the baroreflex failure (one diabetic with cardiac neuropathy and another after heart transplantation). This work suggests that clinical interpretation studies facing pathological/control cases should be carried out in order to further investigate this behavior.

Reproducibility in spontaneous BRS analysis

The reproducibility of the BRS analysis was studied from the comparison between the BRS analysis carried out in two different recordings of the same subject in the same condition. The BRS variables obtained from the two test recordings were found to be more correlated when the BRS analysis was carried out from BEs instead of BSs. Regarding the BRS estimates, the global/total estimates from BEs in the two test recordings were found to be more correlated and holding the highest reproducibility.

Dispersion in spontaneous BRS analysis

The dispersion in BRS analysis was studied from a simulation-based methodology. A shorter length of BSs leads to a higher dispersion in the BRS estimate when the sequences technique is used (local approach with BSs), since each slope is typically estimated from 3 points. This shortcoming can be reduced if BEs are used together with global/total approach. First, with the global/total approach the slope is estimated from the overall number of SBP and RR pairs in all of the identified segments. Second, as BEs are longer segments and usually in higher number than BSs, the overall number of beats in BEs is higher than in BSs. The higher N^{E} obtained at the expense of a slightly lower r^{E}, not only increases the likelihood of providing a BRS estimate, but also provides a lower dispersion in the BRS analysis, in particular for the files presenting lower N^{S} values. For the files without BSs, the dispersion of the global/total estimator combined with BEs was found to be similar to that for the files with BSs. The BRS analysis from BEs provides a larger N^{E} obtained at the expense of a lower r^{E} in comparison with that evaluated from BSs, leading to a decrease in the dispersion of the BRS estimator based on BEs (see Fig. 3.25). In spontaneous condition, r^{S} is higher than 0.8 and r^{E} is will tend to be 0.8 in stationary recordings. In contrast, the longer the recordings the higher is the difference between the N^{E} and N^{S} values. Therefore, if the SP stationary conditions are satisfied (i.e., r^{E} remain close to 0.8), it is expected that $\hat{\mathcal{B}}^{\mathrm{E}}_{\mathrm{G,O}}$ outperforms $\hat{\mathcal{B}}^{\mathrm{S}}_{\mathrm{G,O}}$ in terms of dispersion.

3.7 Conclusions

The events technique is proposed in this work to improve time domain BRS assessment. This novel technique consists of the joint use of baroreflex events (BEs) and global/total slope estimators.

The performance of the methods is compared with the recordings from the EuroBaVar dataset, including two subjects with autonomic dysfunction. These subjects were expected to exhibit lower BRS estimates in comparison with the remaining subjects.

With the use of BEs instead of baroreflex sequences (BSs), the BRS analysis benefits from more and longer segments of data, leading to a higher number of beats available for the slope estimation. As a matter of fact, the higher number of beats in BEs allows to provide a BRS estimate for all EuroBaVar subjects, including for those recordings in which BSs were not identified. The BRS estimates from BEs and BSs are highly correlated, if BSs are identified. For the cases of BSs absence (the subjects with poor BRS function), BRS estimates based on BEs are lower than the 5^{th} percentile of the remaining BRS estimates empirical distribution. This result indicates that in the case of BSs absence, the events technique provides a BRS estimate in accordance with the autonomic dysfunction reported for these EuroBaVar subjects.

The events technique also provides BRS estimates with higher inter-subject variability, which allows to distinguish lying from standing positions in all EuroBaVar subjects, including for those without BSs (23/23 against 18/23 for the sequences technique). Finally, the events technique produces BRS estimates with higher reproducibility and lower dispersion than the sequences technique estimates, as a result of the increased number of beats in BEs obtained without decreasing the SBP–RR correlation. For the files without BSs, the reproducibility and the dispersion in BRS analysis from BEs is similar to those of the BRS analysis from BEs for the files with BSs.

The BRS estimates provided by the events technique are now going to be validated in the following chapters. On one hand, the BRS methods are going to be further compared with invasive data in Chapter 4. By the other hand, the time domain BRS methods are going to be associated with respiration and ANS sympathetic activity in Chapter 5.

Chapter 4

BRS Estimation from Drug-induced Data

The comparison between the BRS analysis from BSs and from BEs pointed out that the estimates are different and exhibit a high pairwise correlation. However, without a reference BRS value, it was impossible to quantify the bias of the methods. The drug-induced protocols involve the stimulation of the BRS function, and are considered as a *gold standard* for BRS quantification. Consequently, the spontaneous BRS estimates from BSs and from BEs were further compared with invasive BRS estimates derived from drug-induced data.

The comparison between invasive and spontaneous BRS estimates considered the fact that the invasive estimates are based on different estimators and different data comparing to spontaneous ones. Therefore, it is possible that the reported differences between BRS estimates are due to methodological and physiological differences between the methods.

Regarding the BRS dispersion, the results in the previous chapter indicate that spontaneous BRS analysis from BEs provides larger N and lower r in comparison with BSs, leading to a decrease in the BRS dispersion. In drug-induced data, the trade-off between N and r is more unbalanced when compared with spontaneous data, because N is diminished and constrained to the time window of the drug effect, while r is increased due to the drug effect. Hence, the dispersion in BRS estimation from drug-induced data was also studied and compared with that evaluated in spontaneous condition.

The chapter starts with the motivation to study the BRS in invasive settings, including a first comparison between the BRS analysis from BSs and BEs with the drug-induced. This comparison is illustrated with the data published in the pioneer work of Smyth *et al.* (1969), providing evidences that BEs should be used for BRS analysis, instead of BSs.

4.1 Motivation to study the BRS in invasive settings

Time domain BRS is currently quantified as the regression slope obtained from the cross-analysis between SBP and RR interval values, either using drug induced or spontaneous data. The advantages and limitations of these techniques have been reviewed elsewhere (Parati *et al.*, 2000; La Rovere *et al.*, 2008) and an overview is presented in Sec. 1.3.3.

The pharmacological methods allow BRS assessment under a controlled baroreflex stimulation. The principle of these techniques is to make use of vasoactive drugs which change arterial pressure by producing vasoconstriction (or vasodilatation) while having minimal direct effect on the sinus node. Thus, these drugs induce negligible direct effects on the RR interval, so that the observed RR changes are mediated reflexively via the baroreceptors. In comparison with the spontaneous, drug induced techniques stimulate a larger and clearer SBP increase (or decrease) in order to force a pronounced RR response (i.e., a clearer baroreflex activation). Therefore, the pharmacological methods allow to explore the baroreflex function over the entire range of SBP values, whereas the spontaneous methods allow the BRS assessment at the subject's operating point.

It is not clear which BRS method and experimental protocol (spontaneous or invasive) should be considered as *gold standard* for BRS assessment and divergent opinions are found in the literature. Some authors support that the spontaneous BRS assessment should not be used in clinical practice as an alternative to pharmacological ones (Pitzalis *et al.*, 1998*a*), whereas others argue that spontaneous experiments are viable alternatives to the pharmacological (Watkins *et al.*, 1996). The drug induced protocols are considered a gold standard due to the increase in control that can be obtained with the vasoactive drugs (Lipman *et al.*, 2003). However, drugs actions are complex and can exert influences on baroreflex function which are independent of the ABP changes they provoke (Watkins *et al.*, 1996; Pitzalis *et al.*, 1998*a*). Also, others debate which "quality of gold is that provided by forcing one mechanism probably beyond its normal play" (Malliani and Montano, 2004). Nevertheless, because drug-induced protocols allow the BRS stimulation, the comparison between invasive and spontaneous BRS estimates cannot be avoided for the *validation* of a reference BRS method.

Experimental protocols for drug-induced BRS assessment

The pioneer method for invasive BRS assessment, known as the *Oxford technique*, used bolus of angiotensin to provoke constriction of the blood vessels and increase the blood pressure (Smyth *et al.*, 1969). Following studies from the same research group have used phenylephrine[1] to induce ABP rises (Gribbin *et al.*, 1971) and amyl nitrite[2] combined with

---

[1] Phenylephrine is a vasoconstrictor with immediate onset of action and 2.5 hours of half-life elimination (Brunton *et al.*, 2007).

[2] Amyl nitrite is a vasodilator administered by inhalation. It is prepared in small ampoules that are crushed, freeing the vapours to be inhaled. The effects are felt within 30 sec of inhalation and last for 2–3 min (Brunton *et al.*, 2007).

phenylephrine to provoke ABP decreases and increases (Pickering *et al.*, 1972). Nowadays, the BRS estimate obtained from Oxford technique refers to the slope of the SBP and RR values after the administration of a phenylephrine bolus.

Other experimental BRS studies have used nitroprusside[3] to provoke ABP falls (Chen *et al.*, 1982) and sequential injections of nitroprusside and phenylephrine to stimulate acute ABP falls and rises in the same experimental setting. The protocol consisting of sequential injections of nitroprusside and phenylephrine is known as the *Modified Oxford technique.* However, it is relevant to point out that there are several descriptions of this protocol, because different studies make use of different dosages and consider different time intervals between the successive injections. The time gap between injections is a characteristic particularly important in the protocol. By only allowing 1 minute between injections, the second injection is administrated when the subject is still under the effect of the first (Ebert, 1990; Ebert and Cowley Jr, 1992). In this experiment, the SBP and RR values of the subjects are acutely lowered (first nitroprusside, then phenylephrine) or raised (first phenylephrine, then nitroprusside) with respect to the baseline values and, therefore, only one branch of the SBP–RR sigmoidal relationship is determined. On the contrary, by allowing at least 5 minutes between the boluses, the SBP and RR values return fully to their baseline values after the first injection, and the second injection is given when the effect of the first is already diminished (Parlow *et al.*, 1995). Thus, a larger gap between injections allows to assess the 2 branches of the SBP–RR sigmoidal.

Comparison between invasive and spontaneous BRS estimates

Time domain spontaneous techniques, in particular the sequences technique (Di Rienzo *et al.*, 1985; Bertineri *et al.*, 1988), were introduced after the pharmacological methods. Despite of their obvious advantages, the wide spread use of spontaneous protocols has been limited because of their poor agreement with the invasive ones (Davies *et al.*, 2001). Several comparisons between spontaneous and drug induced BRS estimates obtained from bolus of phenylephrine (i.e., Oxford technique) evidence that they are different although significantly correlated (Davies *et al.*, 1999; Pitzalis *et al.*, 1998*a*; Watkins *et al.*, 1996)[4].

However, the spontaneous/invasive differences found in those studies can be due to the experimental protocol used. As a matter of fact, the correlation between spontaneous BRS estimates from the sequences technique and the slope of the SBP–RR sigmoidal tangent line in the SBP rest level was found to be 0.96 for 21 normal subjects (Parlow *et al.*, 1995). Moreover, the authors found no statistically significant differences between the estimated slopes and concluded that the invasive and spontaneous BRS estimates are in agreement at

---

[3] Sodium Nitroprusside is a vasodilator with onset of action within 30 sec and hypotensive effect occurring within 2 min. Its effect disappears within 3 min after the end of the infusion. (Brunton *et al.*, 2007).

[4] The correlation between the spontaneous and phenylephrine slopes was estimated as 0.67 in a dataset combining normal and chronic heart failure (CHF) patients (Davies *et al.*, 1999), 0.64 in post-myocardial infarction patients (Pitzalis *et al.*, 1998*a*) and 0.5 in hypertensive patients (Watkins *et al.*, 1996).

the operating point of the subject.

The comparisons between spontaneous and invasive BRS estimation methods have been focused on the study of the information that spontaneous and invasive data carries out, by comparing BRS estimates obtained from different data and from different estimators. Obviously, it is possible that the reported differences between spontaneous and invasive BRS estimates are due to physiological and methodological differences between the methods. Consequently, the comparison between BRS analysis from spontaneous and invasive data must consider these two aspects.

In this chapter, the methods for invasive BRS assessment are studied and compared with spontaneous BRS analysis evaluated from BSs and from BEs. Moreover, the differences observed between spontaneous and invasive BRS estimates are further studied. On one hand, the invasive BRS estimates are compared with the spontaneous BRS estimates. On the other hand, the BRS methods are compared from the evaluation of the different BRS estimators in the same data and the evaluation of the same BRS estimator in different data.

The BRS estimators are then validated with respect to the ability to provide different estimates in conditions of different BRS stimulations (either due to sympathetic or parasympathetic activation). The obtained estimates are also compared with respect to the expected relation between the BRS values and the mean RR interval.

Spontaneous BRS analysis from BEs has shown to provide larger N and lower r in comparison with BSs, leading to a decrease in the BRS dispersion. The trade-off between N and r is more unbalanced in drug-induced data, when compared with spontaneous data, because N is diminished and constrained to the time window of the drug effect, while r is increased due to the drug effect. Hence, the dispersion in BRS estimation from drug-induced data was also studied and compared with results obtained in spontaneous condition.

The invasive BRS estimates are typically based on all the data provided by the experimental protocol, either slope estimation as in Smyth *et al.* (1969) or sigmoidal estimation as in Parlow *et al.* (1995), with the BRS estimates being obtained by OLS minimization. Therefore, the global approach for slope estimation was considered for BRS evaluation, both in invasive and spontaneous condition. Due to the diminished number of segments observed in the invasive data and the expected repercussions in robustness of the local approach estimate (mean of slopes) and in the performance of the outlier segments removal in the total approach, the local and total slope estimators were not considered for BRS evaluation in drug-induced data.

4.2 Literature evidences to use Events instead of Sequences

The pioneer study of Smyth *et al.* (1969) presented the results upon the SBP and RR interaction after an intravenous bolus of a vasoconstrictor (angiotensin – AG). As illustrated in Fig. 4.1 with the data retrieved from Table 1 of that study, the method was based in the simple observation that a rise of arterial blood pressure following a vasoconstrictor bolus is accompanied by cardiac slowing, as a reflex from the baroreceptors. It was found a strong linear relation between $x_{\text{SBP}}(n-1)$ and $x_{\text{RR}}(n)$ during the drug induced changes, and the slope estimated by OLS minimization was taken as the BRS index. The experiments were discarded if a no statistical significant correlation was found between the $x_{\text{SBP}}(n-1)$ and $x_{\text{RR}}(n)$ values in the chosen beats (p > 0.05).

The non consecutive beats used for BRS estimation were chosen from the time window of the drug effect, extending from 20 to 30 sec from the start of the $x_{\text{SBP}}(n)$ rise to just before the $x_{\text{SBP}}(n)$ peak (in the Fig. 4.1 example was 23 sec). In this time window, only the beats in the expiratory phase of respiration were chosen, because it was observed that the $x_{\text{SBP}}(n-1)$ and $x_{\text{RR}}(n)$ correlation is higher in a concordant respiratory phase (because expiration is associated with $x_{\text{SBP}}(n-1)$ and $x_{\text{RR}}(n)$ rises).

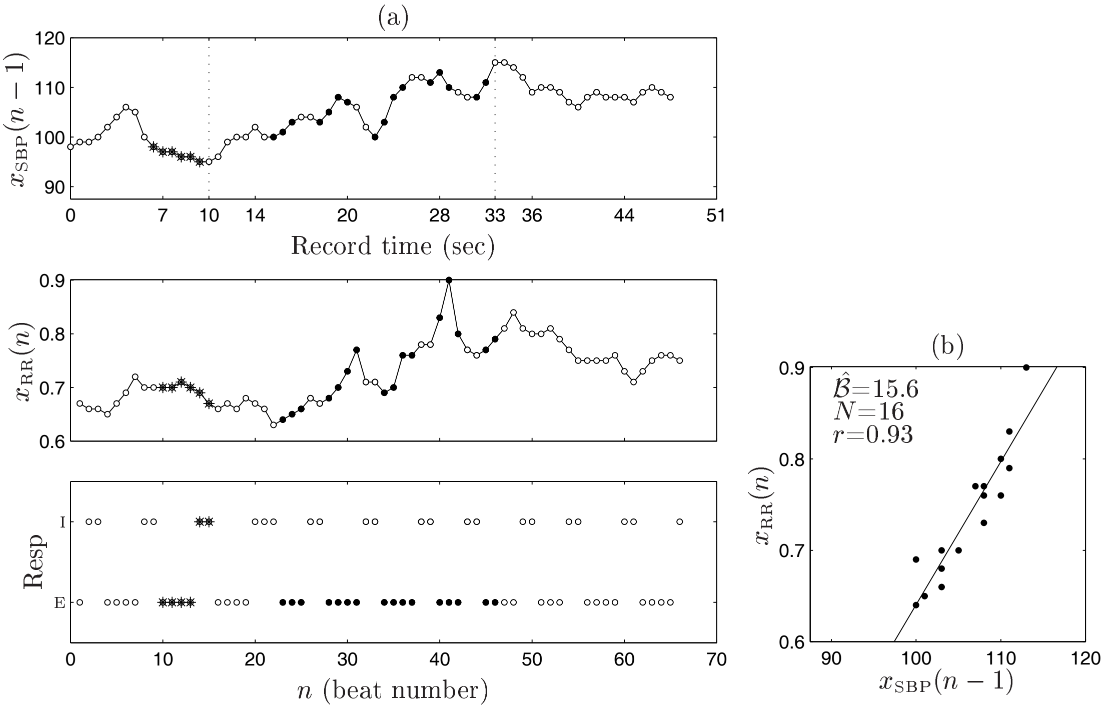

Figure 4.1: SBP and RR response to an angiotensin injection [Smyth *et al.* (1969), Table 1], with indication of the bolus period (*) and the beats chosen for BRS estimation (●). The dotted lines delimitate the analysis window and the solid line is the global regression line with slope $\hat{\mathcal{B}}$ (in msec/mmHg), obtained by OLS minimization. Letters I and E in the Resp signal stand for Inspiration and Expiration phases, respectively.

One observation that can be depicted from Fig. 4.1 is that the beats chosen for BRS analysis are not necessarily in $x_{\mathrm{SBP}}(n-1)$ and $x_{\mathrm{RR}}(n)$ ramps over time. As illustrated in Fig. 4.2, if the beats were chosen regardless of the respiratory phase, N would be higher and r would be slightly lower, but still close to 0.9. This segmentation procedure has been used in Watkins *et al.* (1996), and the BRS estimate was considered as valid for the regressions exhibiting r>0.8. It should be remarked that, the minimum r value was imposed only after the selection of the beats for regression analysis and not stipulated as an apriori threshold for segments identification, as it is with BEs.

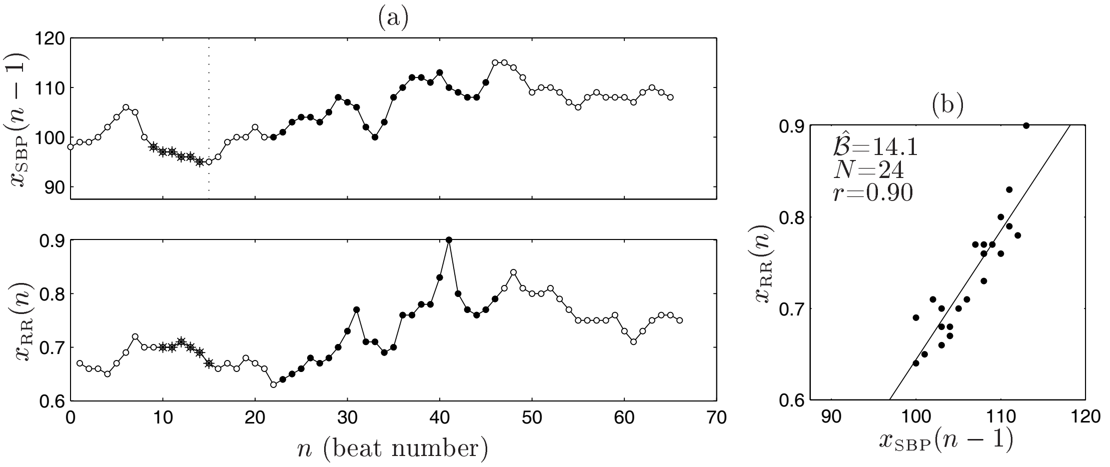

Figure 4.2: Plot of (a) the SBP and RR pairs from the first to the last beat within the BRS analysis window considered in Smyth *et al.* (1969) and (b) corresponding dispersion diagram. The dotted lines delimitate the analysis window and the solid line is the global regression line with slope $\hat{\mathcal{B}}$.

In spontaneous protocols there is no acute stimulation of the baroreceptors and, therefore, it is natural to impose numerical thresholds for the identification of baroreflex related segments (either BSs or BEs). These thresholds are set to increase the reliability of the identified segment to be a real baroreflex related segment. However, their use may also reduce the ability to perform the BRS analysis, particularly if the threshold values are very restrictive. Figure 4.3 illustrates the application of the methodologies developed for the segmentation of spontaneous $x_{\mathrm{SBP}}(n-1)$ and $x_{\mathrm{RR}}(n)$ series in the drug induced data from Smyth *et al.* (1969), illustrating that the BSs threshold values are quite restrictive, even in a condition of a clear baroreflex stimulation, with only 2 BSs being identified (N=6). In contrast, N=48 for BEs is higher than for either BSs or for the $x_{\mathrm{SBP}}(n-1)$ and $x_{\mathrm{RR}}(n)$ segmentation initially proposed by Smyth *et al.* (1969) (N=16). From the comparison between Figs. 4.1(b), 4.2(b) and 4.3(b), it can be observed that 4.3(d) is a more populated version of the previous. The slope obtained from the data plotted in Fig. 4.3(d) is lower than the slope evaluated for the data in Figs. 4.1(b) and 4.2(b), because the beat corresponding to $x_{\mathrm{RR}}(n)$=0.9 has less weight in the OLS minimization when N increases.

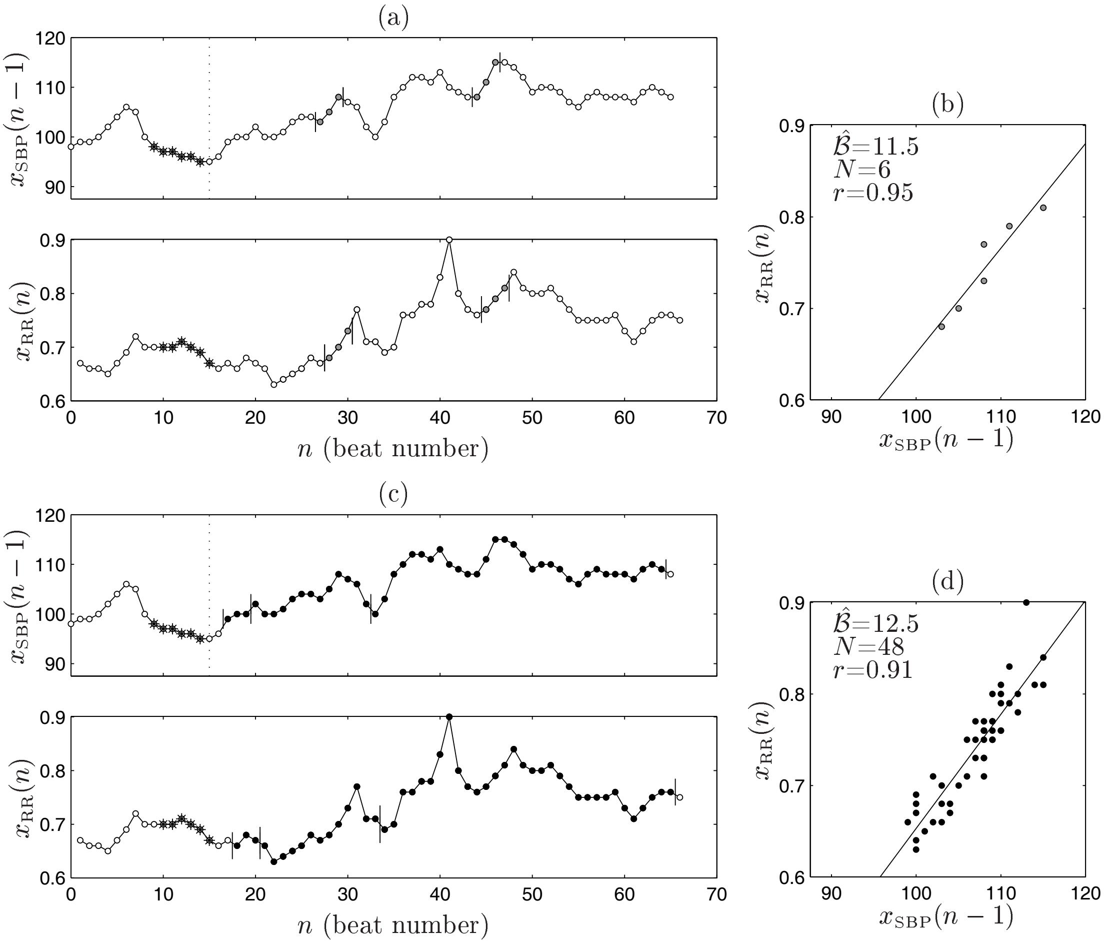

Figure 4.3: Plot of identified (a) BSs and (c) BEs after the bolus, with respective dispersion diagrams (b,d). The solid line is the global regression line with slope $\hat{\mathcal{B}}$.

After the drug-stimulation of the BRS, it is expected that the beat-to-beat SBP changes are greater and sustained for longer time. For normal baroreflex cases, it is also expected a higher and longer sustained SBP and RR coupling in spontaneous condition, to be translated in longer segments of high correlation. As a matter of fact, as illustrated in Fig. 4.4, it is possible to identify baroreflex segments before the beginning of the bolus. The BS identified before the drug injection has the same length as the BSs identified afterwards, whereas the two BEs identified before are shorter than the following BEs.

The spontaneous BRS methods based on global slope estimators rely on local mean detrended data. In spontaneous condition, the local mean detrend enhances the global SBP and RR correlation (Sec. 3.3.2.2) and it is based on the assumption that the BRS is stationary on the time window chosen for BRS analysis. On the other hand, the use of local mean detrend in invasive data implicitly assumes that the operating point of each identified segment lies in the approximately linear range of the SBP and RR sigmoidal relationship. A potential disadvantage of local mean detrending invasive data is that the wide range in $x_{\mathrm{SBP}}(n)$ and

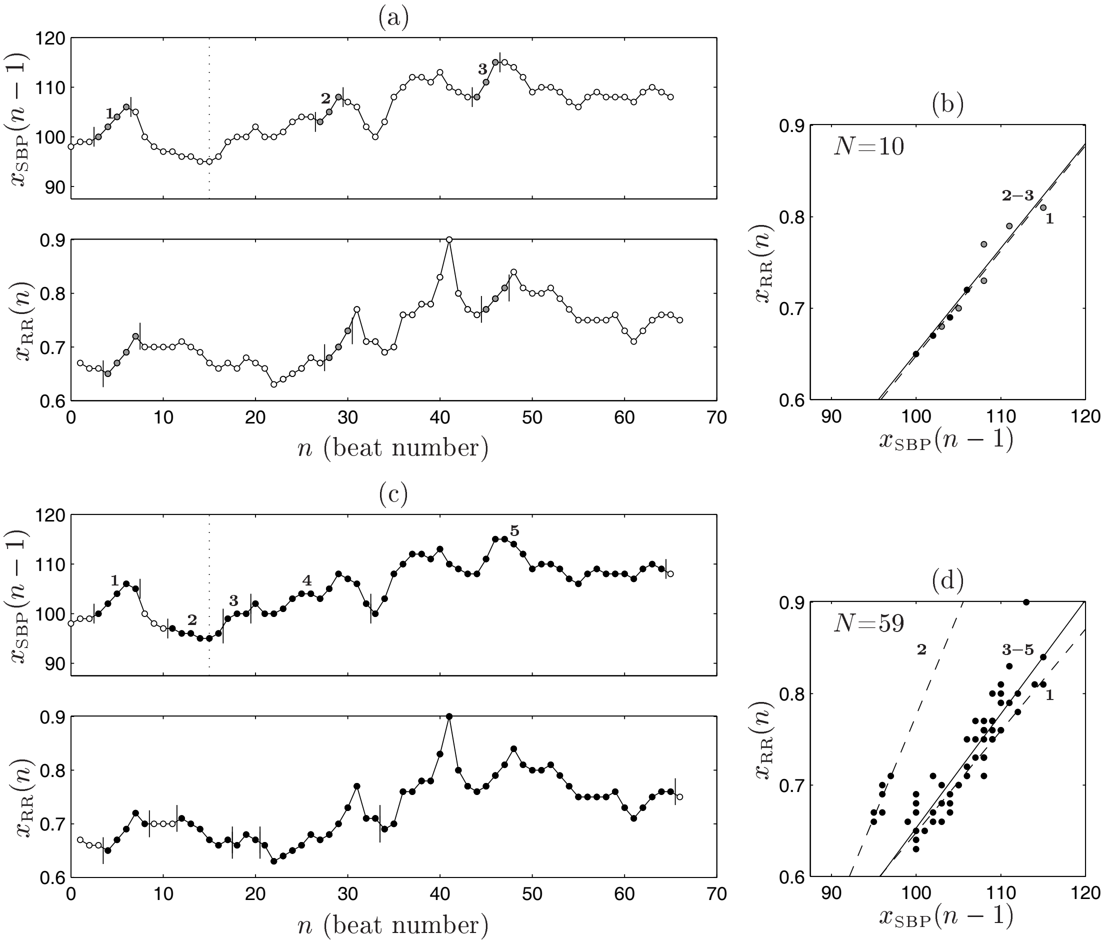

Figure 4.4: Plot of identified (a) BSs and (c) BEs for the entire recording, with respective dispersion diagrams (b,d). The solid/dashed lines are the global regression lines obtained from the beats identified after/before the bolus.

$x_{\text{RR}}(n)$ values might decrease (in particular, if several segments are identified), with possible decrease in the $x_{\text{SBP}}(n)$ and $x_{\text{RR}}(n)$ correlation. However, if r_{min} is apriori set as 0.8 and stationarity is satisfied the correlation between the local mean detrended values $\mathbf{d}_{\text{SBP}}$ and $\mathbf{d}_{\text{RR}}$ is still close to 0.8, and so the linear regression analysis is suitable to use in the data.

Figure 4.5 represents the local mean detrended data, distinguishing the BSs and BEs identified before and after the bolus injection. The effect of local mean detrend the data can be depicted from the comparison between Figs. 4.5(b,d) and Figs 4.3(b,d), respectively for BSs and BEs: the $\hat{\mathcal{B}}$ obtained after the bolus injection is lower when the local mean detrend of the data is carried out. Nevertheless, the estimated BRS slopes vary more with the SBP–RR segmentation procedure (Figs. 4.1(b), 4.2(b), 4.3(b)), rather than with introducing a local mean detrending step in the BRS analysis. Finally, it can be observed that the smaller differences between spontaneous and invasive BRS estimates are obtained for the BRS estimation from BEs, rather than from BSs.

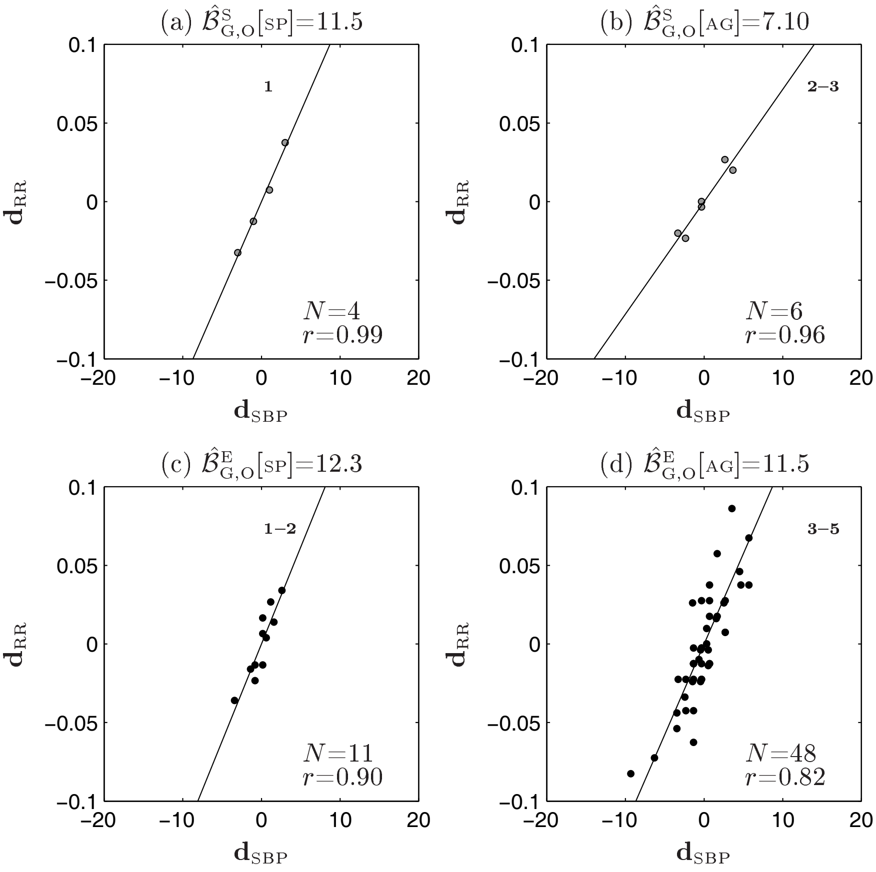

Figure 4.5: Dispersion diagrams for (a–b) BSs and (c–d) BEs after local mean detrend, distinguishing the segments identified before (SP) and after the bolus (AG). The solid line is the global regression line with slope $\hat{\mathcal{B}}_{\mathrm{G,O}}$. Same data as in Fig. 4.4.

4.3 Methodologies for BRS analysis in Drug-induced data

In this section, the methodological aspects involved in the BRS analysis from drug-induced data are presented. In particular, in Sec. 4.3.1 the Modified Oxford protocol (OX) is described and the experimental data analyzed in this work is presented. Next, the invasive BRS estimator used to quantify the BRS from the OX data is described in Sec. 4.3.2. For a more detailed BRS analysis in the invasive setting, the data obtained for each subject has to be split into smaller intervals, according to the different BRS conditions occurring during the OX protocol. In Sec. 4.3.3.1 the procedure used in this work to divide the OX data is presented and illustrated with a different graphical display of the data, enhancing the time intervals of the OX protocol corresponding to sympathetic ANS activation and deactivation. Finally, the obtained BRS estimates were validated with respect to the expected relationship between the BRS values and the mean RR interval, described in Sec. 4.3.3.2.

4.3.1 Experimental protocol and data: the SP/NT/PH dataset

The SP/NT/PH dataset consists of 30 sets of ECG, ABP, RESP and MSNA signals collected from 15 healthy male subjects (20–36 years) in supine rest condition (Gujic *et al.*, 2007). Each subject was monitored 5 minutes in spontaneous (SP) condition and during 3 min in the Modified Oxford protocol (OX). The OX protocol described in Rudas *et al.* (1999) consists of a 3 minutes recording in supine position: after 1 minute of acquisition, a bolus injection of 150 μg sodium nitroprusside (NT) is administrated followed, one minute after, by a bolus of 150 μg phenylephrine hydrochloride (PH). Figure 4.6 presents the data from one subject, illustrating that the NT (vasodilator) bolus acutely decrease x_{SBP} and produce a baroreflex mediated shortening of the x_{RR} interval. On the contrary, the PH (vasoconstrictor) bolus acutely increase x_{SBP} and lengths the x_{RR} interval.

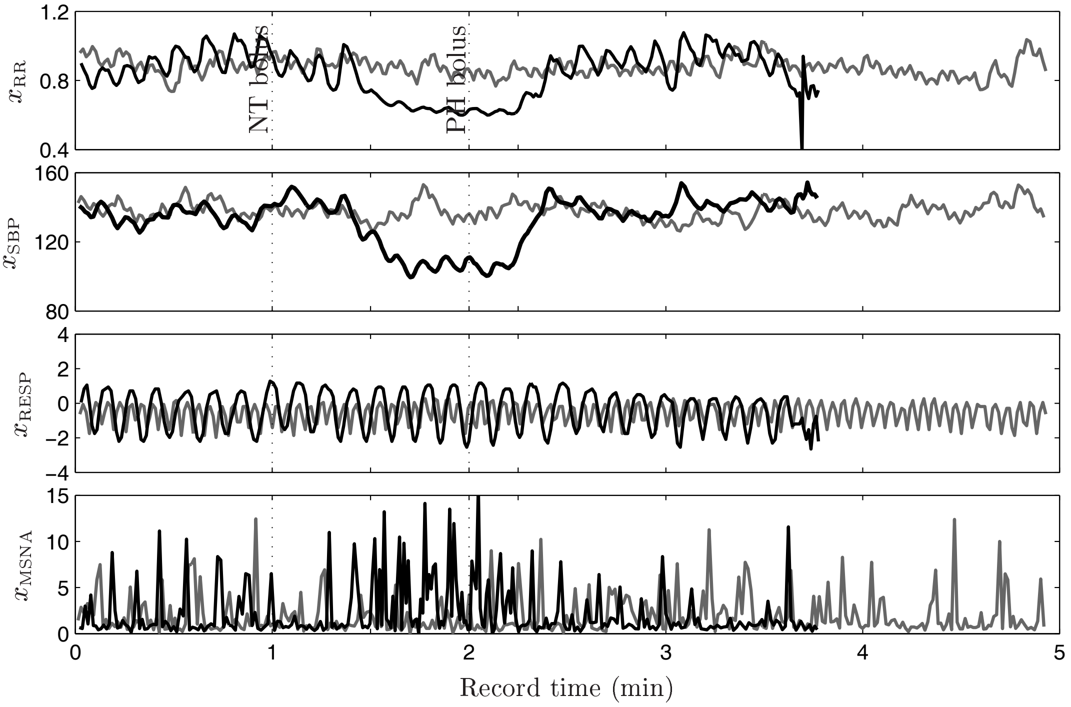

Figure 4.6: Plot of x_ϑ with $\vartheta = \{\mathrm{RR,SBP,RESP,MSNA}\}$ from one representative subject in SP condition (grey) and during the OX protocol (black), to facilitate the comparison. The dotted lines identify the timing of NT and PH bolus during the OX protocol. Same data as in Fig. 1.5.

The expected response to an acute ABP drop was a marked increased MSNA activity, reflected by the larger, wider and more frequent x_{MSNA} bursts after the NT bolus. As a response to the PH bolus, it is observed a x_{SBP} increase towards the baseline level and expected sympathetic inhibition. Regarding x_{RESP}, no changes were observed before, during and after the drug administrations, in terms of mean, variance and frequency. Yet, there are perceptible differences in x_{RESP} from SP to OX condition that were found in this subject and not for all patients of the dataset. For this subject, during the OX protocol, the x_{RESP} presents lower frequency which is accompanied with an expected higher variance. This observation is in accordance with the fact that respiratory variance increases with decreasing respiratory frequency (Brown *et al.*, 1993).

Figure 4.6 also illustrates the short time gap between the successive NT and PH injections, with the PH being administrated still under the NT effect, leading to a mixture of effects. Therefore, this experimental setting allows to increase the range of SBP changes observed in SP acquisition, but only by lowering the x_{SBP} and x_{RR} values with respect to the baseline.

Differences between OX protocols described in the literature

The Modified Oxford protocol (OX) is generally described in the literature as the administration of successive injections of NT and PH (or vice versa). However, the experimental protocol followed in Parlow *et al.* (1995) has important differences to the OX protocol used in this work (Gujic *et al.*, 2007) and, therefore, the invasive data obtained by these two protocols do not have the same characteristics.

In the work of Parlow *et al.* (1995), at least 5 minutes were allowed between the administrations allowing the SBP and RR values to return fully to their baseline values. This longer time gap between the successive NT and PH injections in comparison with the OX protocol, indicates that the PH administration was performed from the baseline of the subject and not in a time when the subject was still under the effect of the NT administration. Therefore, unlike the OX protocol, the protocol followed by Parlow *et al.* (1995) allowed to increase the range of SBP changes observed in SP condition, by both lowering and raising the x_{SBP} and x_{RR} values with respect to the baseline. In this way, the entire sigmoidal function that characterizes the BRS function could be obtained while, for the OX protocol, only the downpart of that curve can be drawn.

4.3.2 Invasive BRS estimator

The previous comparison between the spontaneous and invasive BRS estimates have shown that they are correlated and exhibit no statistically significant differences (Parlow *et al.*, 1995). In that work, the SBP and RR values obtained from the OX protocol were used to estimate the sigmoidal function that characterizes the BRS function (Fig. 1.7) and the invasive BRS estimate was computed as the tangent slope to the sigmoid at the point corresponding to the mean pre-injection SBP value.

In this work, the sigmoidal tangent slope described in Parlow *et al.* (1995) was also considered to obtain an invasive BRS estimate. However, because the OX protocol used in this work differs from the one described in Parlow *et al.* (1995), adjustments in the estimation of the sigmoidal model had to be introduced. The methods used in this work to obtain an invasive BRS estimate are illustrated in Figs. 4.7 and 4.8.

Figure 4.7(a) shows the same data as in Fig. 4.6, represented in the dispersion diagram of the $x_{\text{SBP}}(n-1)$ versus the $x_{\text{RR}}(n)$ values. The high dispersion of the data, in particular around the operating point of the subject, can lead to difficulties in a model estimation. This difficulty was overcome in two ways. First, only the data in the time window from the NT bolus to the maximal effect of the bolus, i.e., the minimum $x_{\text{SBP}}(n-1)$ value was considered (Fig. 4.7(b)). Second, as proposed in Ebert and Cowley Jr (1992), by averaging the $x_{\text{SBP}}(n-1)$ and $x_{\text{RR}}(n)$ values across bins of 2 mmHg increments in the $x_{\text{SBP}}(n-1)$ values (Fig. 4.7(c)). The averaged $\bar{\mathbf{x}}_{\text{SBP}}$ and $\bar{\mathbf{x}}_{\text{RR}}$ values were then used for the estimation of the sigmoidal model.

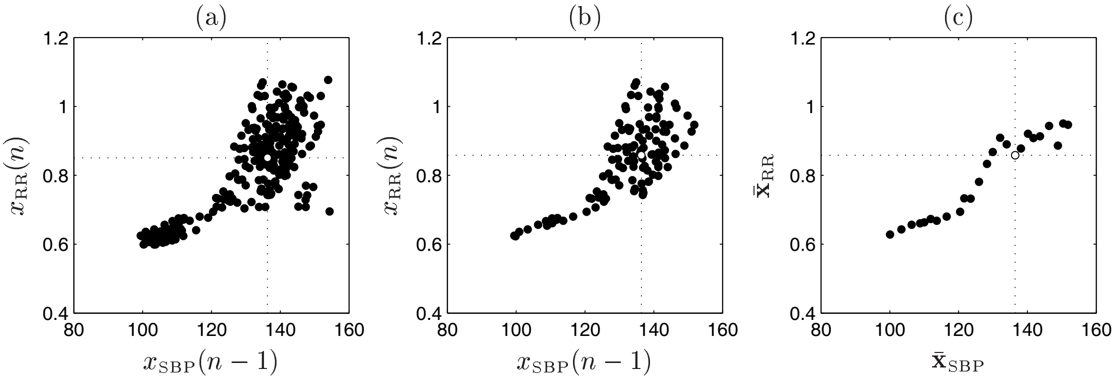

Figure 4.7: Plot of $x_{\text{SBP}}(n-1)$ versus $x_{\text{RR}}(n)$ obtained from (a) the entire OX protocol and in (b) the time window between the NT bolus and the minimum $x_{\text{SBP}}(n-1)$ value. Figure (c) represents the data in (b), after data averaging across $x_{\text{SBP}}(n)$ bins of 2 mmHg width. The white dot localizes the operating point of the subject ($\bar{x}_{\text{SBP}}[\text{BAS}]$,$\bar{x}_{\text{RR}}[\text{BAS}]$). Same data as in Fig. 4.6.

As illustrated in Fig. 4.7(c), the relation between the mean $\bar{\mathbf{x}}_{\text{SBP}}$ and $\bar{\mathbf{x}}_{\text{RR}}$ values can be adequately described by the lower arch of a sigmoidal function. As presented in Fig. 4.8(a), only the $\bar{\mathbf{x}}_{\text{SBP}}$ and $\bar{\mathbf{x}}_{\text{RR}}$ below the corresponding coordinates of the operating point of the subject were considered for the estimation of the sigmoidal parameters. The BRS estimate was then taken as the slope of the tangent line to the curve at the operating point of the subject (Fig. 4.8(b)).

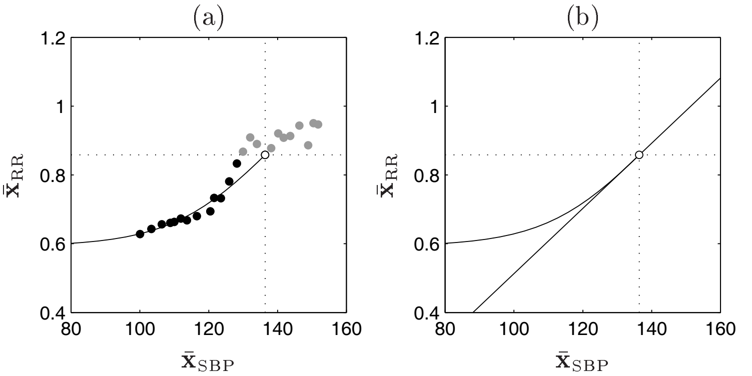

Figure 4.8: Plot of $\bar{\mathbf{x}}_{\text{SBP}}$ and $\bar{\mathbf{x}}_{\text{RR}}$, superimposing (a) the estimated sigmoidal function and (b) the tangent line to the curve at the operating point of the subject (white circle). The black circles identify the points used for the estimation of the sigmoidal parameters. Same data as in Fig. 4.6.

The operating point of each subject corresponds to pair of values baseline mean SBP and mean RR values, respectively $\bar{x}_{\text{SBP}}[\text{BAS}]$ and $\bar{x}_{\text{RR}}[\text{BAS}]$ and, in accordance with Ebert and Cowley Jr (1992); Parlow *et al.* (1995), it was estimated from the SBP and RR values in the first minute of the OX protocol, just before the NT bolus (see Fig. 4.6).

Due to the differences between the experimental protocol used in this work (Sec. 4.3.1) and the one described in Parlow *et al.* (1995), here the parameters of the sigmoidal function have to be estimated with the use of data localized in the lower arch of that sigmoidal function. Therefore, in this work, the sigmoidal parameters were estimated assuming that the inflection point of the sigmoidal function is the operating point of the subject. Hunt and Farquhar (2005) reported that humans do not exhibit systematic asymmetries in the BRS sigmoid, so supporting the use of a symmetric sigmoidal function for BRS assessment. However, their approach did not make any assumption regarding the inflection point of the curve. Nevertheless, in that study the operating points for young healthy subjects (22–38 years) were found to be evenly distributed around the midpoint of the sigmoidal and localized in the approximately linear portion of the sigmoidal (defined by the SBP range in between the zeros in the third derivative of the sigmoidal function).

Estimation of the sigmoidal model

The sigmoidal function is defined by

$$f(x) = \frac{b}{1 + e^{-a(x-c)}} + m, \tag{4.1}$$

where a, b, c and m are the constants defining the $f(x)$ shape. As illustrated in Fig. 4.9, the sigmoidal curve has an S-shape with either a non-negative ($a > 0$) or non-positive first derivative ($a < 0$) and exactly one inflection point. The function has two asymptotes for $x \to \pm\infty$, with m and $m + b$ corresponding to the bottom and upper plateau values of $f(x)$. The variable a describes the steepness of the curve, with $f(x)$ tending to the Heaviside step function as $a \to \pm\infty$.

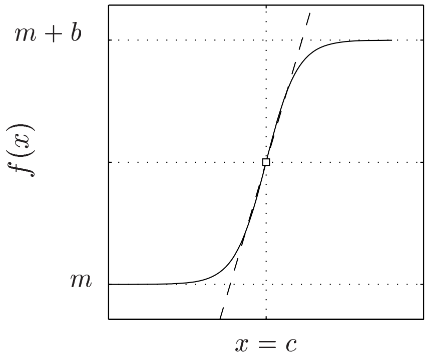

Figure 4.9: Plot of the sigmoid function $f(x)$ as a function of x. The dashed line corresponds to the tangent line to the sigmoidal curve at the inflection point of the function.

For each subject, the parameters of the model were obtained by OLS minimization, using the Levenberg-Marquardt method for nonlinear least-squares optimization (Nocedal and Wright, 1999). The estimation of the parameters of the sigmoidal function was carried out with the "lsqcurvefit.m" function, from the Optimization Toolbox v.3.0.4 Matlab (R2006a). With the constraint that the inflection point of the sigmoidal is the pair $(\bar{x}_{\text{SBP}}[\text{BAS}], \bar{x}_{\text{RR}}[\text{BAS}])$ then

$$c = \bar{x}_{\text{SBP}}[\text{BAS}] \text{ and } m + \frac{b}{2} = \bar{x}_{\text{RR}}[\text{BAS}] \Leftrightarrow m = \bar{x}_{\text{RR}}[\text{BAS}] - \frac{b}{2}. \tag{4.2}$$

Therefore, the replacement of c and m in Eq. 4.1 by the previous expression implies that only a and b need to be estimated. Analogously to Parlow *et al.* (1995), the invasive BRS estimator $\mathcal{B}^{\text{I}}$ is taken as the slope of the tangent line to the sigmoidal curve evaluated at $\bar{x}_{\text{SBP}}[\text{BAS}]$, i.e.,

$$\mathcal{B}^{\text{I}} = \left(\frac{b\ a\ e^{-a(x-c)}}{(1+e^{-a(x-c)})^2} \right)_{x=\bar{x}_{\text{SBP}}[\text{BAS}]} = \frac{b\ a}{4}. \tag{4.3}$$

4.3.3 Validation of the estimated BRS values

For a more detailed BRS analysis in the invasive setting, the data obtained for each subject has to be split into smaller intervals, according to the different BRS conditions occurring during the OX protocol (NT and PH effect).

The BRS estimators based on BEs and BSs were then compared in these smaller time intervals and in SP condition. The BRS estimates obtained in SP, NT and PH conditions were also validated with respect to the expected relationship between the BRS values and the mean RR interval. Finally, the BRS estimates obtained in NT condition were associated with the amount of sympathetic activation produced by the administration of the nitroprusside bolus. The amount of sympathetic activation was quantified from the methods described in Sec. 2.3.2.

4.3.3.1 Data partition according to the BRS condition

Figure 4.10 represents the function f_ϑ with $\vartheta = \{\text{RR,SBP,RESP,MSNA}\}$, defined as the cumulative sum of the corresponding ϑ mean detrended series in Fig. 4.6, i.e.,

$$f_\vartheta(n) = \sum_{i=1}^{n} \left(x_\vartheta(n) - \bar{x}_\vartheta \right), \tag{4.4}$$

with $\bar{x}_\vartheta$ denoting the mean of x_ϑ series and $\vartheta = \{\text{RR,SBP,RESP,MSNA}\}$. This representation allows a clearer visualization of small deviations from the mean and facilitates the comparison between the data obtained by the spontaneous and the invasive protocol.

Figure 4.10 also illustrates the latency between the drug administration and the expected changes in x_{SBP}, x_{MSNA} and x_{RR} series. In this work, the BRS analysis under NT and PH effect was computed from the time intervals delimitated in Fig. 4.10 with the dashed lines. The analysis windows are consecutive 45 sec segments starting 30 sec after the NT bolus. The 30 sec lag assures that the NT effect is present (Brunton *et al.*, 2007), whereas 45 sec is the time interval between the beginning of NT and PH effects.

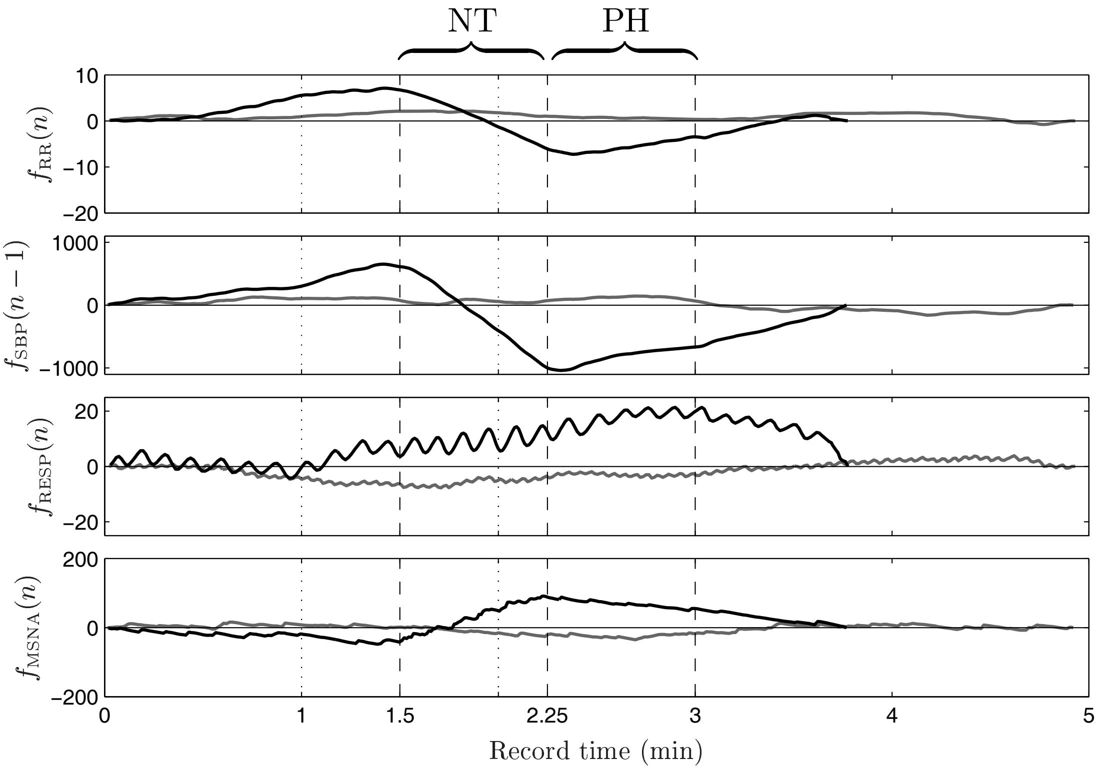

Figure 4.10: Plot of $f_\vartheta(n) = \sum_{i=1}^{n}(x_\vartheta(n) - \bar{x}_\vartheta)$ with $\bar{x}_\vartheta$ denoting the mean of the $x_\vartheta(n)$ values, $\vartheta = \{\text{RR,SBP,RESP,MSNA}\}$. The dashed lines delimitate the time intervals for BRS analysis in NT and PH conditions. Same data and caption as in Fig. 4.6.

Figure 4.11 shows $f_\vartheta(n)$ superimposing all subjects of the dataset, illustrating the wide range of inter-subject responses obtained under the same stimulation. Several reasons can explain such inter-subject differences. As an example, the amount of x_{SBP} reduction after a bolus of nitroprusside has been reported to be inversely related with the subject age (Rudas *et al.*, 1999). Also, other factors, e.g. the weight of the subject, might be of importance to explain the variability in the inter-subject responses. To overcome the difficulty of not having homogeneous responses, the administration of different doses to different subjects might be considered, e.g., consecutive small doses instead of one single bolus to provoke a predetermined amount of SBP increase or decrease (Matsukawa *et al.*, 1996).

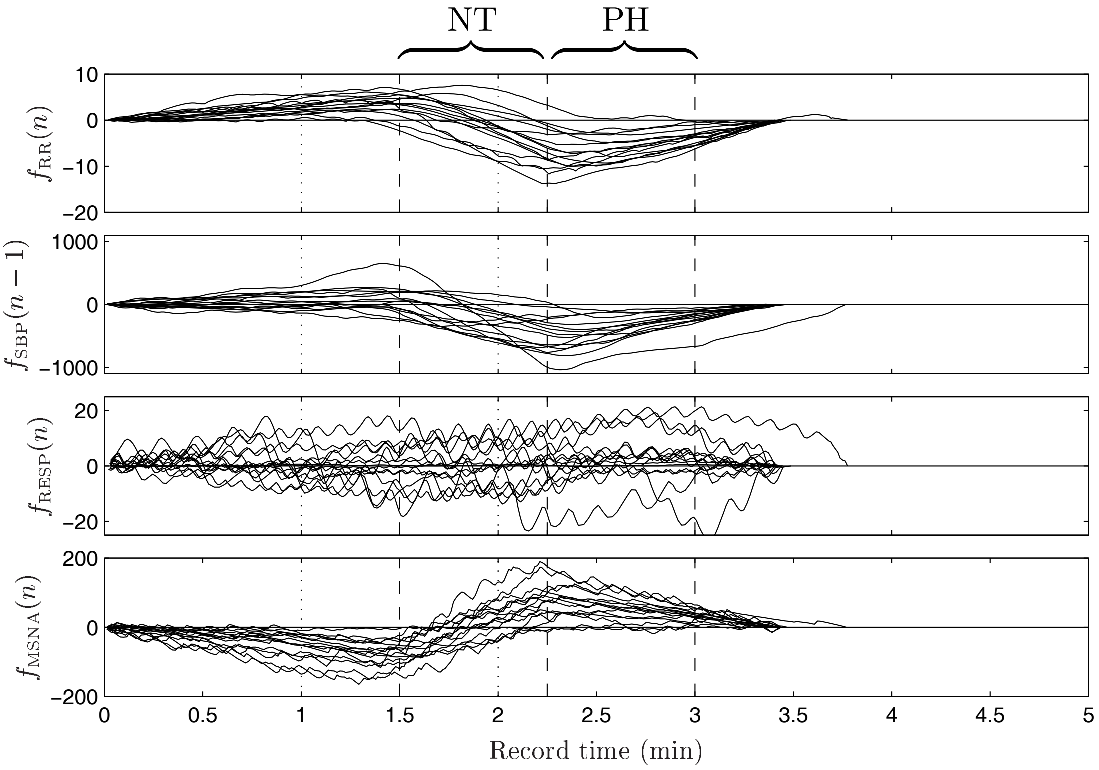

Figure 4.11: Plot of f_ϑ during the OX protocol, superimposing the data obtained from the 15 subjects of the dataset. Same caption as in Fig. 4.10.

4.3.3.2 BRS estimates and mean RR interval

In the pioneer study of phenylephrine-induced BRS estimation (Smyth *et al.*, 1969), it was observed that the BRS estimate is directly related to the baseline mean RR interval. Generally, the BRS has been shown to increase with increasing mean RR interval (Smyth *et al.*, 1969; Mancia and Mark, 1983; Bertineri *et al.*, 1988). The direct relationship between $\hat{\mathcal{B}}$ and $\bar{x}_{\mathrm{RR}}$ might be at some extent due to the choice of x_{RR} to compute the BRS estimate (Mancia and Mark, 1983). However, there are physiological aspects that suggest that changes in BRS triggered by SBP changes are the primarily cause of alterations in the mean RR interval (Mancia and Mark, 1983), apart of others, e.g. respiration.

The indicative relationship between the $\hat{\mathcal{B}}$ and the corresponding $\bar{x}_{\mathrm{RR}}$ values was inferred from the study of Abrahamsson *et al.* (2003). In that study, the relationship between HR and the $\hat{\mathcal{B}}$ obtained by the sequences technique has already been investigated for normal subjects, using an exercise protocol. In an exercise protocol, like in the OX protocol, it is expected that the HR is increased in comparison to the HR in SP condition. Therefore, the results from the work of Abrahamsson *et al.* (2003) are convenient for a comparison with the results obtained from the BRS analysis in the drug-induced protocol.

The work of Abrahamsson *et al.* (2003) evidences that the BRS estimates and HR follow the exponential model

$$\hat{\mathcal{B}}(\text{HR}) = a\ e^{-\lambda\ \text{HR}}, \tag{4.5}$$

with the parameters a and λ. In that work, the authors proposed to normalize the BRS estimate of one subject to the fixed HR of 60 bmp, by regressing the $\hat{\mathcal{B}}$ natural logarithm on HR and predicting $\hat{\mathcal{B}}(60)$. The authors justify the need of such normalization with the fact that the HR differences from different BRS studies imply that the results from these studies may not be comparable. For the purpose of this work, the indicative relationship between HR and $\hat{\mathcal{B}}$ reproduced from Abrahamsson *et al.* (2003) will be used. As illustrated in Fig. 4.12, the $\hat{\mathcal{B}}$ value decreases exponentially with the HR increases (Fig. 4.12(a)) and the relationship appears to be linear if a logarithmic scale is used in the $\hat{\mathcal{B}}$ axis (Fig. 4.12(b)).

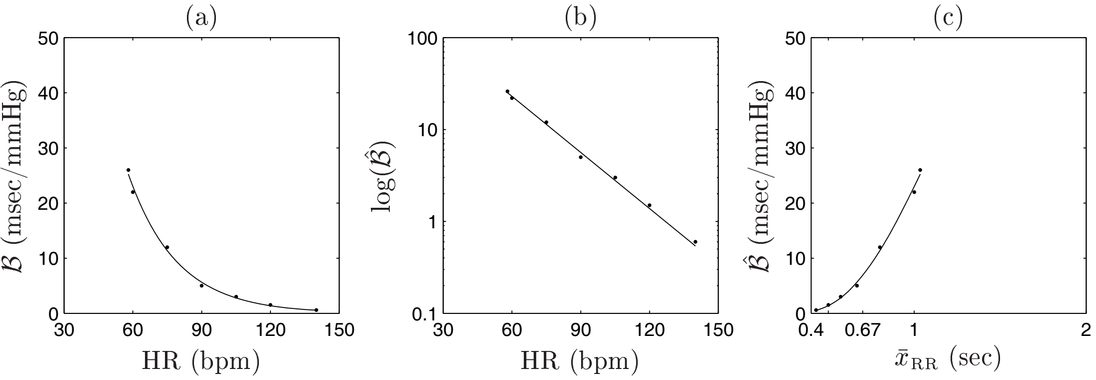

Figure 4.12: Dispersion diagrams illustrating the relationship between $\hat{\mathcal{B}}$ and HR, in (a) linear and (b) log scale. Figure (c) represents the data in (a) with the conversion $\bar{x}_{\text{RR}} = 60/\text{HR}$ in the horizontal axis. Reproduced from Abrahamsson *et al.* (2003).

Figure 4.12(c) represents the same as in Fig. 4.12(a), with the horizontal axis HR converted in $\bar{x}_{\text{RR}}$ by the transformation $\bar{x}_{\text{RR}} = 60/\text{HR}$. Figure 4.12(c) illustrates that the relationship between $\hat{\mathcal{B}}$ and $\bar{x}_{\text{RR}}$, observed in Abrahamsson *et al.* (2003) for an exercise protocol, corroborates the previous findings of higher BRS values being associated with higher $\bar{x}_{\text{RR}}$ for drug-induced experiments (Smyth *et al.*, 1969). The function represented in Fig. 4.12(c) will be used as the indicative relationship between the $\hat{\mathcal{B}}$ and the corresponding $\bar{x}_{\text{RR}}$ values, to validate the obtained BRS estimates.

The parameters of the model in Eq. (4.5) were estimated as $\hat{a} = 383.273$ and $\hat{\lambda} = 0.047$, using the data $\{(58, 26)(60, 22), (75, 12), (90, 5), (105, 3), (120, 1.5), (140, 0.6)\}$ that was retrieved from Figs. 1(c) and 1(d) of Abrahamsson *et al.* (2003). The model estimates were obtained by unconstrained nonlinear minimization, using the Nelder-Mead simplex method (Walsh, 1975), implemented in the "fminsearch.m" function from the Optimization Toolbox v.3.0.4 Matlab (R2006a).

4.4 Results

The methods were compared with respect to the variables given in Table 3.2, evaluated for BSs and BEs and, as before, the upper index S or E was added to each variable according to its evaluation in BSs or BEs.

The methods were additionally compared in the different conditions: 5 min spontaneous (SP), 3 min Modified Oxford protocol (OX) and the 45 sec length data segments under nitroprusside (NT) and phenylephrine (PH) effects. Therefore, a right index was added to each variable according to its evaluation in each condition, e.g., $N^{\mathrm{E}}[\textsc{sp}]$ and $N^{\mathrm{E}}[\textsc{nt}]$ indicate the number of beats available for BRS analysis using BEs in SP and NT conditions.

With respect to the display of results, in a dispersion diagram representing x versus y e.g., Fig. 4.13, the percentage $\mathcal{C}$ defined as the ratio $\#(x > y)/\#x$ where $\#$ indicates the counting numbers, is indicated at the lower right corner of the figure. If justified, the correlation between the x and y values (r) is also presented at the top of each dispersion diagram, as well as the number of values (n). The level of statistical significance was fixed at $p < 0.05$, and indicated with the symbol *.

As previously referred, it is possible that the reported differences between spontaneous and invasive BRS estimates are due to physiological and methodological differences between the methods. Therefore, the BRS estimates were compared from the evaluation of the different BRS estimators in the same data or the same BRS estimator evaluated in different data (Sec. 4.4.1). Next, the BRS estimates evaluated in BSs and BEs were compared in the different BRS conditions occurring during the OX protocol (Sec. 4.4.2). Additionally, the BRS estimates are compared with respect to the expected relation between the BRS estimates and the mean RR interval (Sec. 4.4.3) and with respect to the amount of sympathetic activation produced by the administration of the nitroprusside bolus (Sec. 4.4.4). Finally, the trade-off between N and r is studied in terms of variance in BRS analysis carried out from NT, PH and SP conditions (Sec. 4.4.5).

4.4.1 Invasive and Spontaneous BRS estimates

Figure 4.13 shows the comparison between $\hat{\mathcal{B}}^{\mathrm{I}}$ and the spontaneous BRS estimates, evaluated from BSs and BEs. As indicated in Fig. 4.13(a), in 1 out of the 15 subjects it was not possible to obtain a $\hat{\mathcal{B}}^{\mathrm{S}}_{\mathrm{G,O}}[\textsc{sp}]$ value, because BSs were not identified ($\hat{\mathcal{B}}^{\mathrm{S}}_{\mathrm{G,O}}[\textsc{sp}] = 0$). The overall results indicate that the invasive and spontaneous estimates are correlated and exhibit no statistically significant differences ($p = 0.56$, $n = 14$ for BSs and $p = 0.5$, $n = 15$ for BEs). Figure 4.13(b) also shows that 5 out of the 15 subjects exhibit the largest $\hat{\mathcal{B}}^{\mathrm{I}} - \hat{\mathcal{B}}^{\mathrm{E}}_{\mathrm{G,O}}[\textsc{sp}]$ values. Not considering these 5 subjects, the invasive and spontaneous BRS estimates are more correlated ($r = 0.84^*$, $n = 10$ for BSs and $r = 0.97^*$, $n = 10$ for BEs).

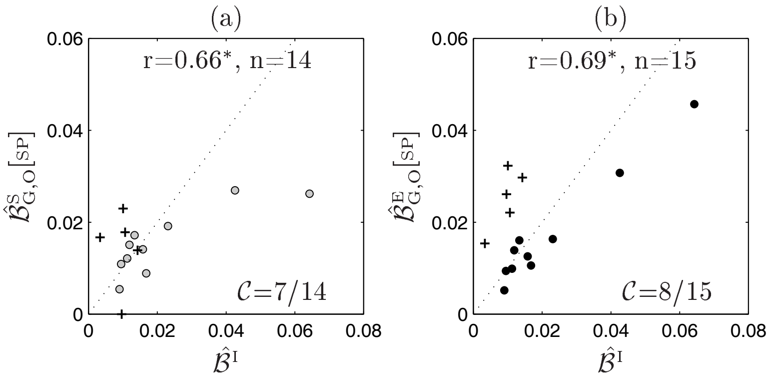

Figure 4.13: Dispersion diagrams comparing $\hat{\mathcal{B}}^{\mathrm{I}}$ with $\hat{\mathcal{B}}^{\mathrm{S}}_{\mathrm{G,O}}[\textsc{sp}]$ and $\hat{\mathcal{B}}^{\mathrm{E}}_{\mathrm{G,O}}[\textsc{sp}]$. The crosses indicate the subjects with the larger $\hat{\mathcal{B}}^{\mathrm{I}} - \hat{\mathcal{B}}^{\mathrm{E}}_{\mathrm{G,O}}[\textsc{sp}]$ values.

The larger $\hat{\mathcal{B}}^{\mathrm{I}} - \hat{\mathcal{B}}^{\mathrm{E}}_{\mathrm{G,O}}[\textsc{sp}]$ values observed in 5 of the 15 subjects can be due to dissimilarities found in the invasive and spontaneous data. As a matter of fact, the baseline mean SBP value $\bar{x}_{\textsc{sbp}}[\textsc{bas}]$ (i.e., the SBP operating value of $\hat{\mathcal{B}}^{\mathrm{I}}$) and the spontaneous mean SBP value $\bar{x}_{\textsc{sbp}}[\textsc{sp}]$ show statistically significant differences (p = 0.004, Fig. 4.14(a)), whereas $\bar{x}_{\textsc{rr}}[\textsc{bas}]$ and $\bar{x}_{\textsc{rr}}[\textsc{sp}]$ do not (p = 0.68, Fig. 4.14(d)).

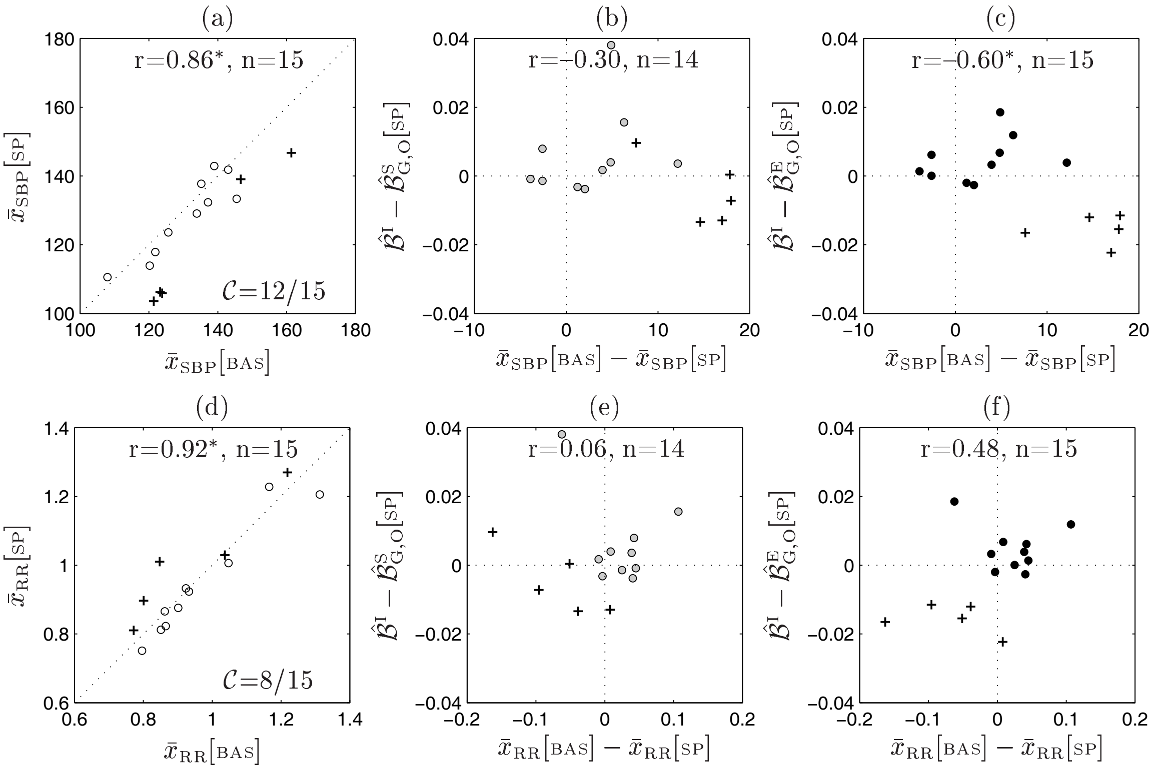

Figure 4.14: Dispersion diagrams comparing $\bar{x}[\textsc{bas}]$ and $\bar{x}[\textsc{sp}]$, and comparing $\hat{\mathcal{B}}^{\mathrm{I}} - \hat{\mathcal{B}}_{\mathrm{G,O}}[\textsc{sp}]$ as a function of $\bar{x}[\textsc{bas}] - \bar{x}[\textsc{sp}]$. The crosses localize the subjects with the larger $\hat{\mathcal{B}}^{\mathrm{I}} - \hat{\mathcal{B}}^{\mathrm{E}}_{\mathrm{G,O}}[\textsc{sp}]$ values.

Regarding the BRS estimates, as is illustrated in Figs. 4.14(b–c), the subjects exhibiting the lowest $\hat{\mathcal{B}}^{\mathrm{I}} - \hat{\mathcal{B}}^{\mathrm{E}}_{\mathrm{G,O}}[\textsc{sp}]$ values present the largest $\bar{x}_{\mathrm{SBP}}[\textsc{ox}] - \bar{x}_{\mathrm{SBP}}[\textsc{sp}]$ values, with $\hat{\mathcal{B}}^{\mathrm{I}} - \hat{\mathcal{B}}^{\mathrm{E}}_{\mathrm{G,O}}[\textsc{sp}]$ showing significant correlation with $\bar{x}_{\mathrm{SBP}}[\textsc{bas}] - \bar{x}_{\mathrm{SBP}}[\textsc{sp}]$. Finally, as presented in Figs. 4.14(e–f), there is a tendency for the lowest $\hat{\mathcal{B}}^{\mathrm{I}} - \hat{\mathcal{B}}_{\mathrm{G,O}}[\textsc{sp}]$ values to be associated with the lowest $\bar{x}_{\mathrm{RR}}[\textsc{bas}] - \bar{x}_{\mathrm{RR}}[\textsc{sp}]$ values, although not exhibiting a significant correlation.

The results point out that the differences between the invasive and spontaneous BRS estimates are associated with the differences found in the OX and SP operating points. However, the obtained low pairwise correlations indicate that other factors, besides dissimilarities in the data, might explain the differences between these estimates. To further evaluate these differences, the BRS estimates were compared from the evaluation of the different BRS estimators in the same data and the same BRS estimator evaluated in different data.

Evaluation of the different BRS estimators in OX condition

Figure 4.15 shows the comparison between the different $\hat{\mathcal{B}}$ values evaluated in OX condition. As presented in Fig. 4.15(a), the $\hat{\mathcal{B}}^{\mathrm{S}}_{\mathrm{G,O}}[\textsc{ox}]$ and $\hat{\mathcal{B}}^{\mathrm{E}}_{\mathrm{G,O}}[\textsc{ox}]$ values are highly correlated and show the relationship $\hat{\mathcal{B}}^{\mathrm{S}}_{\mathrm{G,O}}[\textsc{ox}] > \hat{\mathcal{B}}^{\mathrm{E}}_{\mathrm{G,O}}[\textsc{ox}]$ for most of the files. As illustrated in Figs. 4.15(b–c), the $\hat{\mathcal{B}}^{\mathrm{I}}$ values are correlated with $\hat{\mathcal{B}}^{\mathrm{S}}_{\mathrm{G,O}}[\textsc{ox}]$ and $\hat{\mathcal{B}}^{\mathrm{E}}_{\mathrm{G,O}}[\textsc{ox}]$, showing no statistically significant differences ($p = 0.82$, $n = 14$ for BSs and $p = 0.40$, $n = 15$ for BEs).

As before, if the 5 out of the 15 subjects exhibiting the largest $\hat{\mathcal{B}}^{\mathrm{I}} - \hat{\mathcal{B}}^{\mathrm{E}}_{\mathrm{G,O}}[\textsc{ox}]$ values would not be considered in the analysis, the pairwise correlation between estimates would be higher ($r{=}0.87^{*}$, $n{=}10$ for BSs and $r = 0.97^{*}$, $n{=}10$ for BEs). Also, the $\hat{\mathcal{B}}^{\mathrm{I}}$ would still show significant differences with $\hat{\mathcal{B}}^{\mathrm{S}}_{\mathrm{G,O}}[\textsc{ox}]$ ($p = 0.29$, $n = 10$), whereas the differences between $\hat{\mathcal{B}}^{\mathrm{I}}$ and $\hat{\mathcal{B}}^{\mathrm{E}}_{\mathrm{G,O}}[\textsc{ox}]$ would be non significant ($p = 0.04$, $n = 10$).

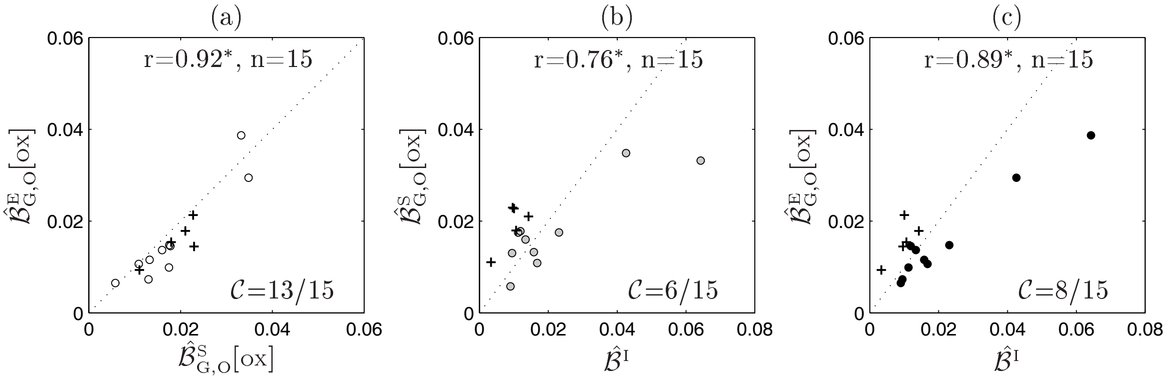

Figure 4.15: Dispersion diagrams comparing $\hat{\mathcal{B}}^{\mathrm{I}}$ with $\hat{\mathcal{B}}^{\mathrm{S}}_{\mathrm{G,O}}$ and $\hat{\mathcal{B}}^{\mathrm{E}}_{\mathrm{G,O}}$ evaluated in OX condition. The crosses localize the subjects with the largest $\hat{\mathcal{B}}^{\mathrm{I}} - \hat{\mathcal{B}}^{\mathrm{E}}_{\mathrm{G,O}}[\textsc{sp}]$ values.

Because the pairwise correlation between $\hat{\mathcal{B}}^{\mathrm{I}}$ and the $\hat{\mathcal{B}}_{\mathrm{G,O}}[\textsc{ox}]$ estimates is higher than the pairwise correlation between $\hat{\mathcal{B}}^{\mathrm{I}}$ and the $\hat{\mathcal{B}}_{\mathrm{G,O}}[\textsc{sp}]$ estimates (Fig. 4.13), it is possible to conclude that some of the dissimilarities between the invasive and the spontaneous BRS estimates are due to methodological differences between the corresponding BRS estimators.

Evaluation of the same BRS estimator in OX and SP conditions

The spontaneous BRS estimators from BSs and BEs were also compared in OX and SP conditions. The $\mathcal{B}^{\mathrm{I}}$ estimator was not evaluated in SP condition, because $\mathcal{B}^{\mathrm{I}}$ assumes that the data follows a sigmoidal model, which is not a valid assumption for data in SP condition.

Figure 4.16(a) illustrates that again the relation $\hat{\mathcal{B}}^{\mathrm{S}}_{\mathrm{G,O}}[\textsc{sp}] > \hat{\mathcal{B}}^{\mathrm{E}}_{\mathrm{G,O}}[\textsc{sp}]$ was found for most of the files, corroborating the results obtained in OX condition in Fig. 4.15(a). As presented in Figs. 4.16(b–c), $\hat{\mathcal{B}}[\textsc{ox}]$ and $\hat{\mathcal{B}}[\textsc{sp}]$ values are correlated, with the highest correlation between OX and SP estimates being obtained for $\hat{\mathcal{B}}^{\mathrm{E}}_{\mathrm{G,O}}$. The differences between BRS estimates are not statistically significant for $\hat{\mathcal{B}}^{\mathrm{S}}_{\mathrm{G,O}}[\textsc{sp}]$ ($p = 0.11$, $n = 14$), and statistically significant for $\hat{\mathcal{B}}^{\mathrm{E}}_{\mathrm{G,O}}[\textsc{sp}]$ ($p = 0.0004$, $n = 15$). Nevertheless, without considering the 5/15 subjects exhibiting the largest $\hat{\mathcal{B}}^{\mathrm{I}} - \hat{\mathcal{B}}^{\mathrm{E}}_{\mathrm{G,O}}[\textsc{sp}]$ values, the pairwise correlation between estimates would be higher ($r = 0.94^{*}$, $n = 10$ for BSs and $r = 0.99^{*}$, $n = 10$ for BEs), and the estimates would show no statistically significant differences either for BSs and BEs ($p = 0.06$, $n = 10$ for BSs and $p = 0.1$, $n = 10$ for BEs).

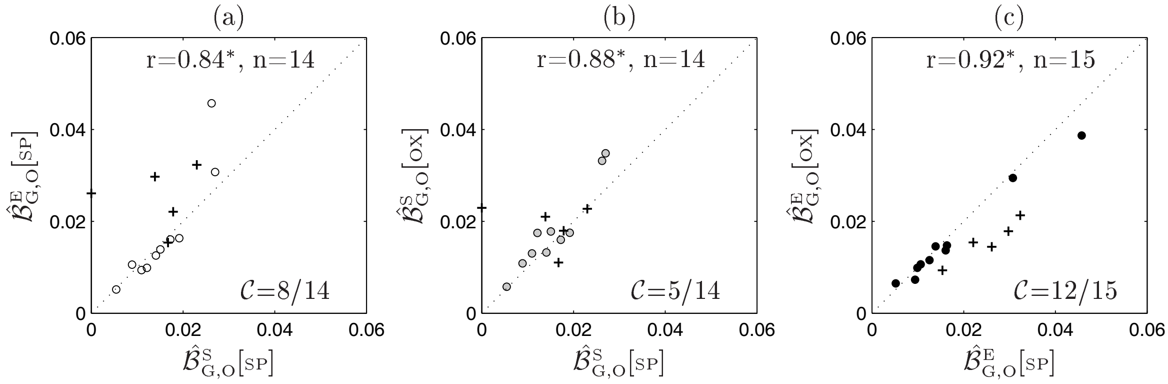

Figure 4.16: Dispersion diagrams comparing $\hat{\mathcal{B}}^{\mathrm{S}}_{\mathrm{G,O}}$ and $\hat{\mathcal{B}}^{\mathrm{E}}_{\mathrm{G,O}}$ evaluated in OX and SP condition. The crosses localize the subjects with larger $\hat{\mathcal{B}}^{\mathrm{I}} - \hat{\mathcal{B}}^{\mathrm{E}}_{\mathrm{G,O}}[\textsc{sp}]$ values.

In conclusion, BRS estimates from BEs are more correlated with $\hat{\mathcal{B}}^{\mathrm{I}}$. Also, the BRS analysis from BEs achieves the highest reproducibility in different data, because the correlation between $\hat{\mathcal{B}}_{\mathrm{G,O}}[\textsc{ox}]$ and $\hat{\mathcal{B}}_{\mathrm{G,O}}[\textsc{sp}]$ is higher for the BRS estimates evaluated from BEs against BSs. Therefore, if the BRS analysis from BEs is able to provide a value that reflects the physiology of the baroreflex, the BRS analysis from BEs is preferable, even to compute a BRS estimate with data following the OX protocol.

4.4.2 Discrimination between NT, PH and SP conditions

Figures 4.16(b–c) show that 5 out of the 14 subjects of the dataset exhibit $\hat{\mathcal{B}}^{\mathrm{S}}_{\mathrm{G,O}}[\textsc{sp}] > \hat{\mathcal{B}}^{\mathrm{S}}_{\mathrm{G,O}}[\textsc{ox}]$, whereas 12 out of the 15 files present $\hat{\mathcal{B}}^{\mathrm{E}}_{\mathrm{G,O}}[\textsc{sp}] > \hat{\mathcal{B}}^{\mathrm{E}}_{\mathrm{G,O}}[\textsc{ox}]$. Because there seems to be no well-established relationship between the BRS estimates obtained from the OX protocol and the BRS estimates evaluated in SP condition, this contradictory result motivated an additional comparison between the $\hat{\mathcal{B}}^{\mathrm{S}}_{\mathrm{G,O}}$ and $\hat{\mathcal{B}}^{\mathrm{E}}_{\mathrm{G,O}}$ values. Therefore, the methods were further compared with the additional evaluation of the BRS estimators in data representative of the NT and PH effect, obtained from the data partition of the OX data, as described in Sec. 4.3.3.1.

In general, it is expected that the RR response to a falling SBP to be lower than of that to a rising SBP (Pickering *et al.*, 1972). The study of Rudas *et al.* (1999) reports the relationship between BRS estimates obtained during the OX protocol and SP condition for healthy subjects: $\hat{\mathcal{B}}[\textsc{nt}]$ are lower than $\hat{\mathcal{B}}[\textsc{ph}]$, $\hat{\mathcal{B}}[\textsc{nt}]$ are lower than $\hat{\mathcal{B}}[\textsc{sp}]$ and $\hat{\mathcal{B}}[\textsc{ph}]$ show no statistically significant differences from $\hat{\mathcal{B}}[\textsc{sp}]$, because the PH is administrated still under the NT effect. If the PH injection would have been administrated after NT recovery to baseline, it would have been expected that $\hat{\mathcal{B}}[\textsc{nt}]<\hat{\mathcal{B}}[\textsc{sp}]<\hat{\mathcal{B}}[\textsc{ph}]$ (Pickering *et al.*, 1972).

Figure 4.17 shows the comparison of the BRS estimates evaluated from BSs and BEs in NT, PH and SP conditions, corroborating that $\hat{\mathcal{B}}[\textsc{nt}]<\hat{\mathcal{B}}[\textsc{sp}]\approx\hat{\mathcal{B}}[\textsc{ph}]$ (Rudas *et al.*, 1999). Also, the comparison between the results obtained for $\hat{\mathcal{B}}^{\mathrm{S}}$ and $\hat{\mathcal{B}}^{\mathrm{E}}$ indicates that the $\hat{\mathcal{B}}^{\mathrm{E}}_{\mathrm{G,O}}$ values are more in accordance to what was expected, with the different BRS conditions being discriminated for more subjects of the dataset. The $\hat{\mathcal{B}}^{\mathrm{E}}_{\mathrm{G,O}}$ values also discriminate the different conditions for the subjects exhibiting the highest $\hat{\mathcal{B}}^{\mathrm{E}}_{\mathrm{G,O}}[\textsc{sp}]$, whereas the $\hat{\mathcal{B}}^{\mathrm{S}}_{\mathrm{G,O}}$ values cannot.

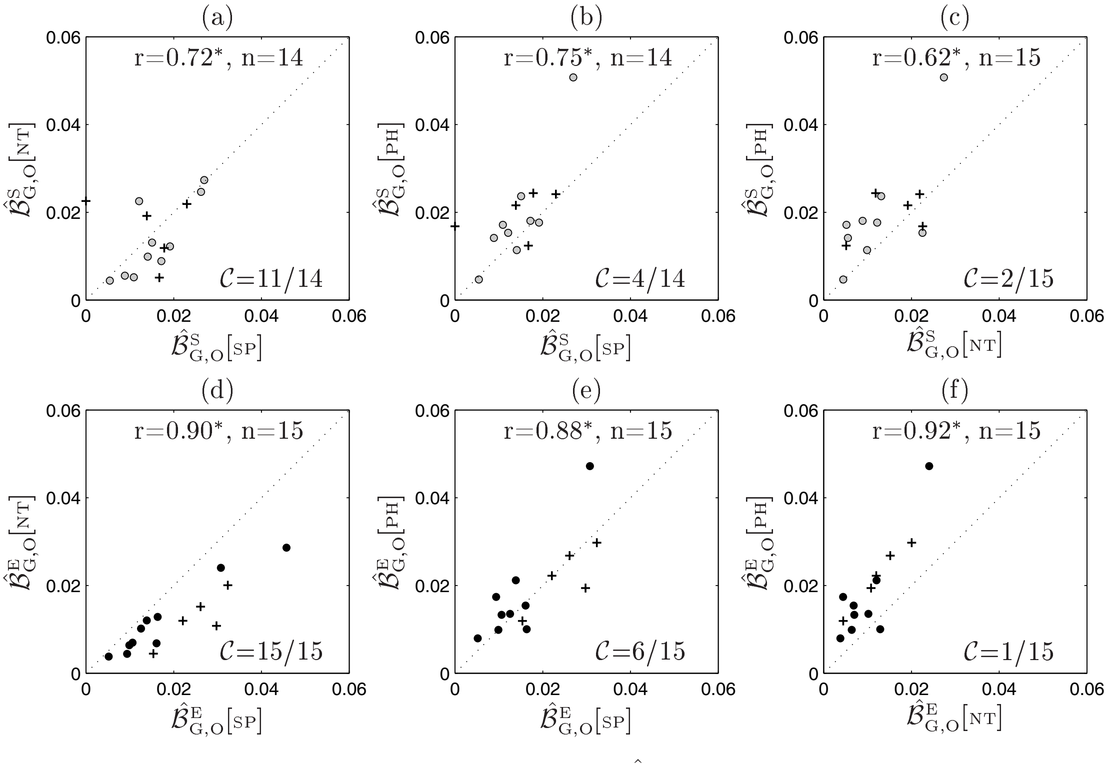

Figure 4.17: Dispersion diagrams comparing different $\hat{\mathcal{B}}$ evaluated for BSs and BEs in SP, NT and PH conditions.

Considering all subjects of the dataset, the BRS analysis from BEs indicated that the mean paired differences $\hat{\mathcal{B}}^{\mathrm{E}}_{\mathrm{G,O}}[\textsc{sp}] - \hat{\mathcal{B}}^{\mathrm{E}}_{\mathrm{G,O}}[\textsc{nt}]$ and $\hat{\mathcal{B}}^{\mathrm{E}}_{\mathrm{G,O}}[\textsc{ph}] - \hat{\mathcal{B}}^{\mathrm{E}}_{\mathrm{G,O}}[\textsc{nt}]$ both differ from zero ($p < 0.001$), whereas $\hat{\mathcal{B}}^{\mathrm{E}}_{\mathrm{SP}} - \hat{\mathcal{B}}^{\mathrm{E}}_{\mathrm{PH}}$ do not ($p = 0.28$), in accordance with the results in the study of Rudas *et al.* (1999). Finally, the pairwise correlation between BRS estimates in SP, NT and PH conditions is higher for the $\hat{\mathcal{B}}^{\mathrm{E}}_{\mathrm{G,O}}$ values.

4.4.3 BRS estimates and mean RR interval

Figure 4.18 shows the $\hat{\mathcal{B}}_{\mathrm{G,O}}$ values evaluated in SP, NT and PH conditions superimposed with the function plotted in Fig. 4.12(c), included for comparison purposes. For all conditions, the $\hat{\mathcal{B}}_{\mathrm{G,O}}$ values typically follow the relation depicted from Abrahamsson *et al.* (2003). In SP condition, with $\bar{x}_{\mathrm{RR}}[\textsc{sp}]$ between 0.75 and 1.25 sec, the $\hat{\mathcal{B}}_{\mathrm{G,O}}[\textsc{sp}]$ and $\bar{x}_{\mathrm{RR}}[\textsc{sp}]$ relationship is approximately linear. The $\hat{\mathcal{B}}_{\mathrm{G,O}}[\textsc{nt}]$ and $\bar{x}_{\mathrm{RR}}[\textsc{nt}]$ are lower than when evaluated in SP condition, and also follow the indicative relation retrieved from Abrahamsson *et al.* (2003). In PH condition, the $\hat{\mathcal{B}}_{\mathrm{G,O}}[\textsc{ph}]$ and $\bar{x}_{\mathrm{RR}}[\textsc{ph}]$ values are similar to the ones in SP condition. However, the $\hat{\mathcal{B}}_{\mathrm{G,O}}[\textsc{ph}]$ and $\bar{x}_{\mathrm{RR}}[\textsc{ph}]$ relationship is less evident than that evaluated in SP condition, probably due to the presence of the NT effect when the PH injection is administrated.

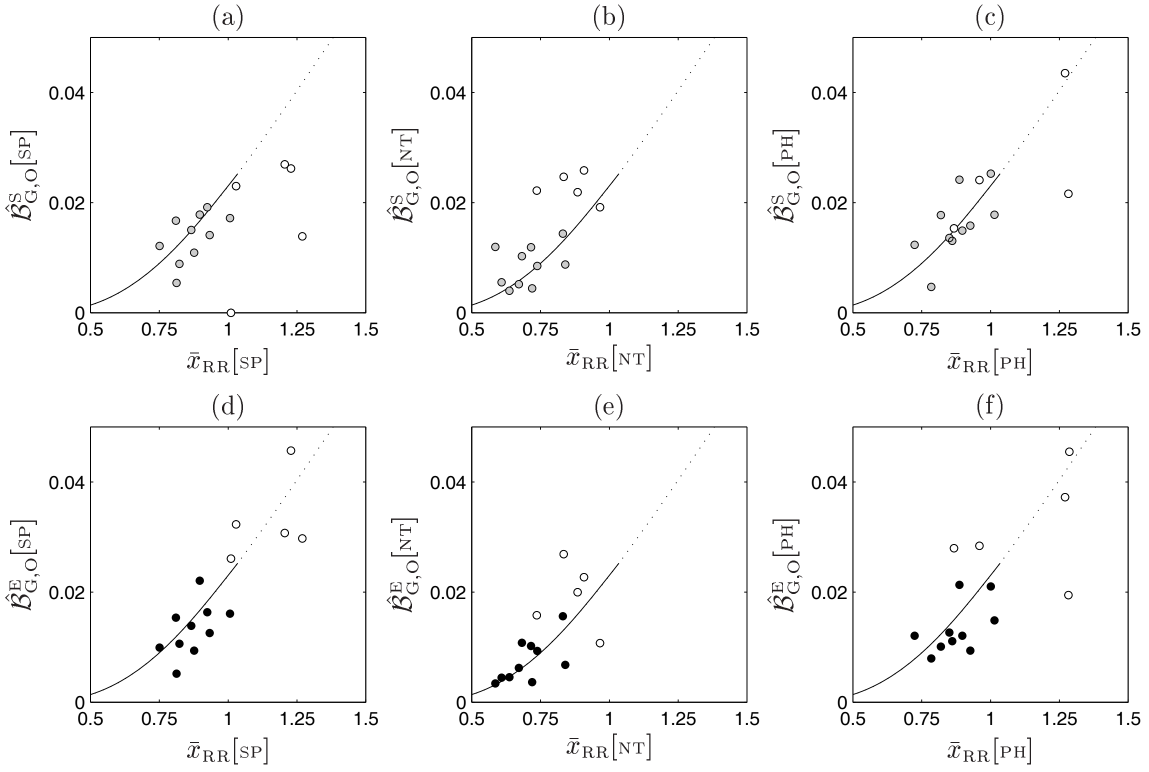

Figure 4.18: Dispersion diagrams showing the relationship between $\bar{x}_{\mathrm{RR}}$ and $\hat{\mathcal{B}}_{\mathrm{G,O}}$, evaluated from BEs and BSs in SP, NT and PH conditions. The solid line corresponds to the indicative relationship for $\bar{x}_{\mathrm{RR}}$ between 0.4 and 1 sec (Fig. 4.12), while the dotted line represents the same function for $\bar{x}_{\mathrm{RR}} > 1$. The white circles identify the subjects with highest $\hat{\mathcal{B}}^{\mathrm{E}}_{\mathrm{G,O}}[\textsc{sp}]$ values.

The SP recordings of the SP/NT/PH dataset have 5 min of duration and therefore, a subject with a higher $\bar{x}_{\text{RR}}[\text{SP}]$ exhibits a lower $N[\text{SP}]$ for slope estimation with repercussions on the BRS variance, in particular if the BRS is estimated from BSs (see results in Sec. 3.5.4). Regarding the comparison between the BRS analysis from BSs and from BEs, the relationship between $\hat{\mathcal{B}}_{\text{G,O}}$ and $\bar{x}_{\text{RR}}$ is more evident for the BRS analysis from BEs, and the $\hat{\mathcal{B}}^{\text{E}}_{\text{G,O}}$ values for the subjects exhibiting the highest $\bar{x}_{\text{RR}}[\text{SP}]$ values follow better the indicative relationship in comparison with the $\hat{\mathcal{B}}^{\text{S}}_{\text{G,O}}$.

The results presented in Fig. 4.18 suggest that the observed inter condition changes in the $\hat{\mathcal{B}}$ values, can also be associated with changes in $\bar{x}_{\text{RR}}$ values. Figure 4.19 shows the dispersion diagrams of the ratios R and differences D between the $\hat{\mathcal{B}}_{\text{G,O}}$ and the $\bar{x}_{\text{RR}}$ values evaluated considering the paired conditions NT and SP, PH and SP, and PH and NT.

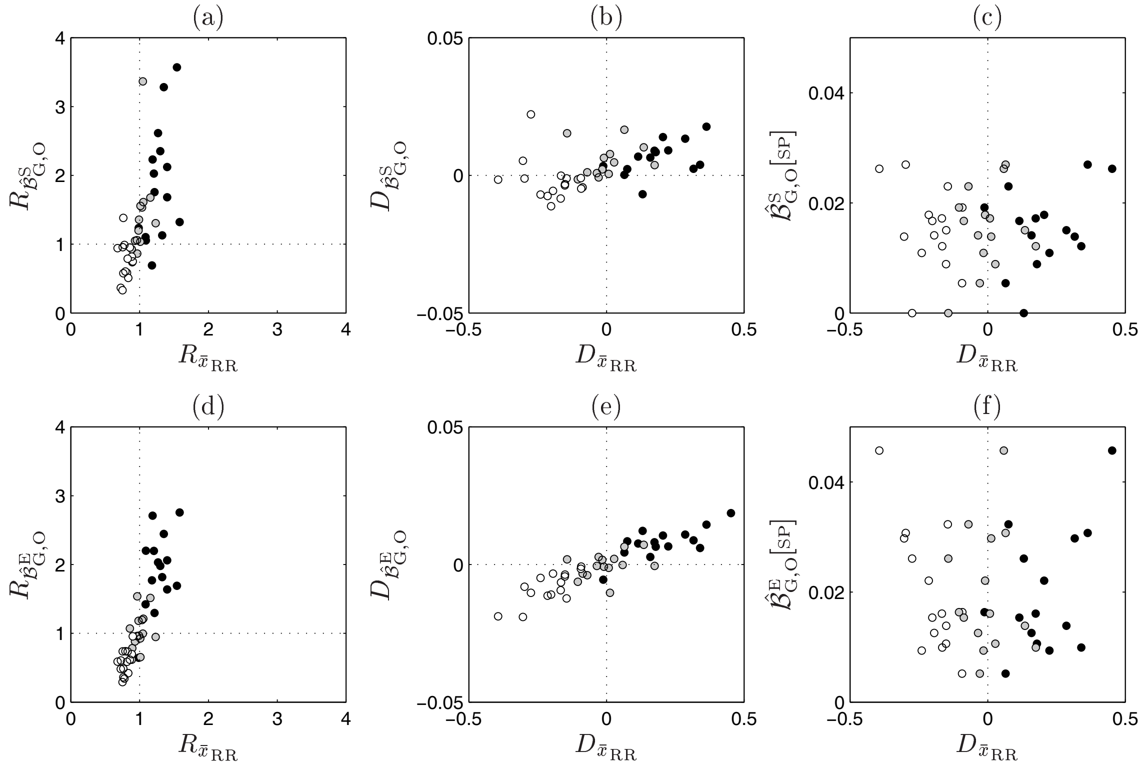

Figure 4.19: Dispersion diagrams comparing the changes in $\hat{\mathcal{B}}^{\text{S}}_{\text{G,O}}$ (a–b) and $\hat{\mathcal{B}}^{\text{E}}_{\text{G,O}}$ (c–d) with the changes in $\bar{x}_{\text{RR}}$. The changes were quantified from the ratios (R) and the differences (D) between pairs of conditions, being NT to SP (white), PH to SP (grey) and PH to NT (black).

The inter condition changes in $\hat{\mathcal{B}}_{\text{G,O}}$ are linearly associated with the $\bar{x}_{\text{RR}}$ changes. From SP to NT condition, the $\bar{x}_{\text{RR}}$ and $\hat{\mathcal{B}}_{\text{G,O}}$ values decrease, so that $R_{\text{G,O}}$ is smaller than 1 and $D_{\hat{\mathcal{B}}_{\text{G,O}}}$ is smaller than 0. From NT to PH condition, the $\bar{x}_{\text{RR}}$ and $\hat{\mathcal{B}}_{\text{G,O}}$ values increase again, so that $R_{\hat{\mathcal{B}}_{\text{G,O}}}$ is above 1 and $D_{\hat{\mathcal{B}}_{\text{G,O}}}$ is above 0. From SP to PH condition, the $R_{\text{G,O}}$ can be above or below 1, what emphasizes the similarity between the BRS analysis obtained from SP and from PH after NT. Also, the PH to SP ratios present a higher inter subject variability in comparison to the PH to NT ratios, stressing out the intra subject variability in the responses to the consecutive NT and PH boluses. The results in Fig. 4.19 also indicate that the association between the changes in $\hat{\mathcal{B}}_{\mathrm{G,O}}$ and in $\bar{x}_{\mathrm{RR}}$ is more evident for $\hat{\mathcal{B}}^{\mathrm{E}}_{\mathrm{G,O}}$. In particular, the subjects exhibiting the largest $\bar{x}_{\mathrm{RR}}$ changes present $\hat{\mathcal{B}}^{\mathrm{E}}_{\mathrm{G,O}}$ changes more aligned with those observed for the remaining subjects (both for ratios and differences). The subjects exhibiting the largest $|D_{\bar{x}_{\mathrm{RR}}}|$ also exhibit the highest $\hat{\mathcal{B}}^{\mathrm{E}}_{\mathrm{G,O}}$, being in a trend more in accordance with the $\hat{\mathcal{B}}^{\mathrm{E}}_{\mathrm{G,O}}$ of the remaining subjects (Figs. 4.19(c,f)).

4.4.4 BRS estimates and sympathetic activity

As illustrated in Fig. 4.6, the sympathetic activity in NT condition is higher than in SP and in PH conditions, with the sympathetic activity in SP and PH being comparable.

Figures 4.20(a–b) show the relationship between the changes in BRS estimates and the changes in $\mathcal{A}_{\mathrm{T}}$ values (MSNA burst intensity per min, see Sec. 2.3.2), from one condition to another. It can be observed that, in a condition of clear sympathetic activation (NT to SP ratio corresponding to the white circles in the figure), the changes in $\hat{\mathcal{B}}^{\mathrm{E}}_{\mathrm{G,O}}$ from NT to SP conditions are more associated with the changes in $\mathcal{A}_{\mathrm{T}}$ from NT to SP conditions, than that evaluated for $\hat{\mathcal{B}}^{\mathrm{S}}_{\mathrm{G,O}}$. As a matter of fact, the $R_{\hat{\mathcal{B}}^{\mathrm{E}}_{\mathrm{G,O}}}$ and the $R_{\mathcal{A}_{\mathrm{T}}}$ values exhibit significant correlation ($\mathrm{r} = -0.55$, $\mathrm{p} = 0.03$, $\mathrm{n} = 15$), whereas that correlation evaluated for $R_{\hat{\mathcal{B}}^{\mathrm{S}}_{\mathrm{G,O}}}$ is not statistically significant ($\mathrm{r} = -0.08$, $\mathrm{p} = 0.76$, $\mathrm{n} = 14$). The sensitivity of the obtained r value was studied with respect to γ, i.e., the constant threshold value used for the selection of significant MSNA bursts (see Sec. 2.3.2). As it is possible to observe in Fig. 4.20(c), there is a relatively wide interval around γ=3 (the threshold value chosen) for which the correlation between $R_{\hat{\mathcal{B}}^{\mathrm{E}}_{\mathrm{G,O}}}$ and $R_{\mathcal{A}_{\mathrm{T}}}$ remains significant.

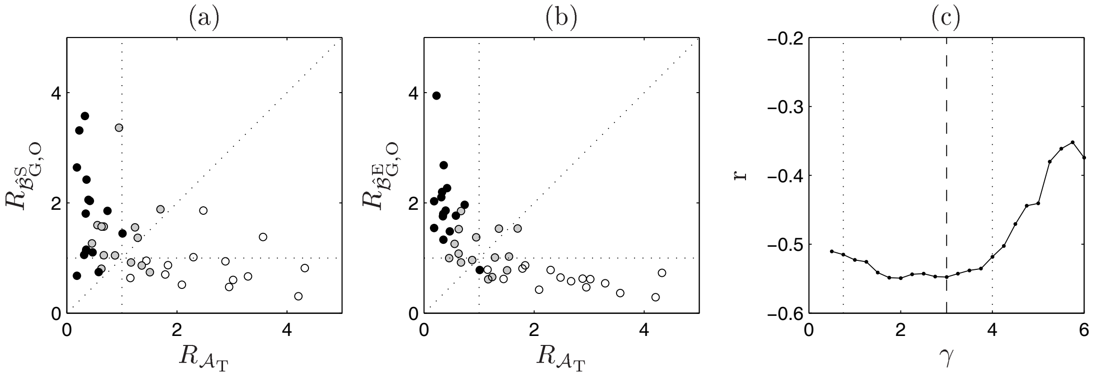

Figure 4.20: (a–b) Dispersion diagrams comparing changes in the BRS estimates with changes in $\mathcal{A}_{\mathrm{T}}$, quantified by the ratios of each variable R between pairs of conditions, being NT to SP (white), PH to SP (grey) and PH to NT (black). (c) Correlation between $R_{\mathcal{A}_{\mathrm{T}}}$ and $R_{\hat{\mathcal{B}}^{\mathrm{E}}_{\mathrm{G,O}}}$ evaluated for NT to SP conditions (white dots), as a function of γ.

The results obtained point out that, in a condition of a clear sympathetic activation, the BRS estimates from BEs are able to capture better changes in the sympathetic activity of the subject in comparison with the BRS estimates from BSs. Also, the changes observed in the BRS estimates from BEs are significantly correlated with the changes observed in sympathetic activity.

4.4.5 Dispersion in invasive BRS estimation

In recordings of the same time length, the higher BRS values are estimated from a smaller number of beats. As a matter of fact, from Fig. 4.18, the higher BRS estimates are associated with the higher $\bar{x}_{\mathrm{RR}}$ values.

Figure 4.21 illustrates that the $\hat{\mathcal{B}}^{\mathrm{E}}_{\mathrm{G,O}}[\textsc{sp}]$ values decay with increasing $N^{\mathrm{E}}[\textsc{sp}]$ and $r^{\mathrm{E}}[\textsc{sp}]$ values remaining close to 0.8. This relation is not so evident for the variables evaluated from BSs. As the SP condition files have the same time length (5 min), but not the same number of beats, Figs. 4.21(b) and 4.21(e) additionally present the dispersion diagram of $\hat{\mathcal{B}}_{\mathrm{G,O}}[\textsc{sp}]$ with $N[\textsc{sp}]$ in % units. The results indicate that subject with higher $\hat{\mathcal{B}}_{\mathrm{G,O}}$ are associated with lower percentage of points in BEs.

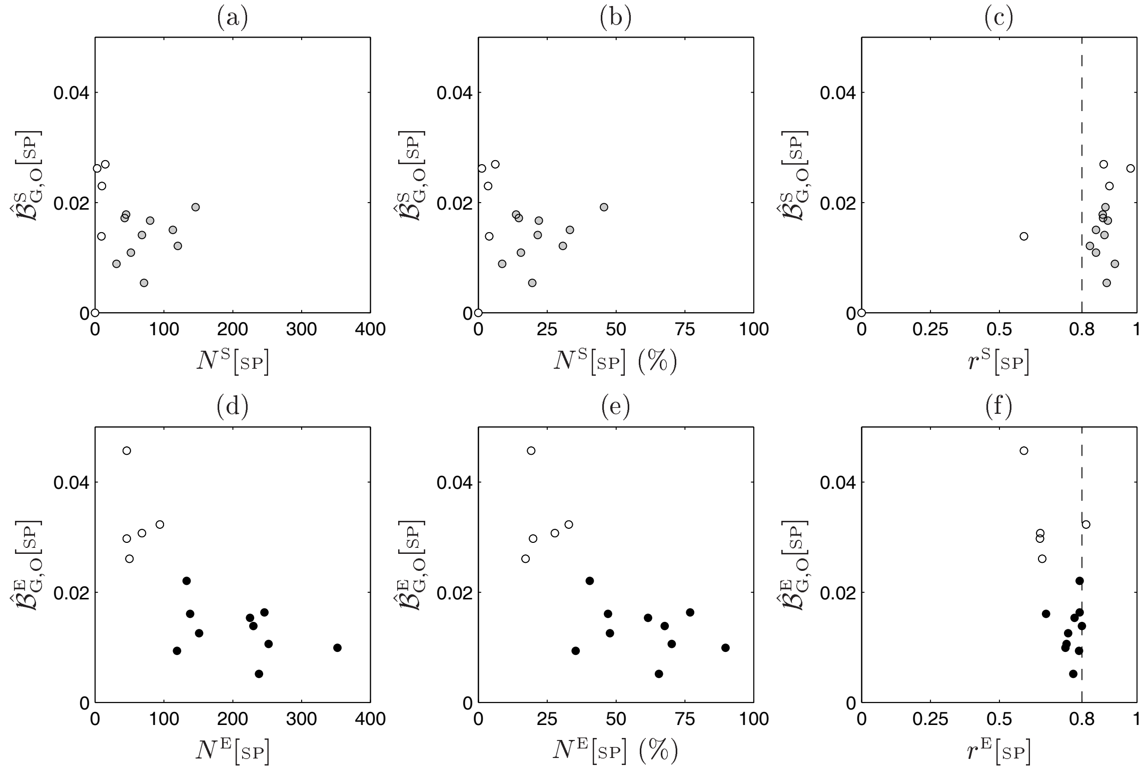

Figure 4.21: Plot of $\hat{\mathcal{B}}_{\mathrm{G,O}}$ as a function of N and r, evaluated for BSs (grey) and BEs (black) in SP condition. The white circles identify the subjects with highest $\hat{\mathcal{B}}^{\mathrm{E}}_{\mathrm{G,O}}[\textsc{sp}]$ values. The $N[\textsc{sp}]$ in % is obtained dividing $N[\textsc{sp}]$ in beats by the recording beats length.

There is one subject (out of the 15) in which no BSs were identified in SP condition and, therefore, no $\hat{\mathcal{B}}^{\mathrm{S}}_{\mathrm{G,O}}[\textsc{sp}]$ was obtained for that subject. All subjects presented BEs and the BRS analysis from BEs was carried out for all subjects. In particular, there are 5 subjects (out of the 15) presenting a noticeable higher $\hat{\mathcal{B}}^{\mathrm{E}}_{\mathrm{G,O}}[\textsc{sp}]$ values in comparison with that of the remaining subjects. These evaluations exhibit the lowest N^{E} and the most extreme r^{E} values in comparison with the remaining evaluations.

Figure 4.22 shows the distribution of N and r evaluated in NT and PH conditions. The $N^{\mathrm{S}}[\textsc{nt}]$ and $N^{\mathrm{S}}[\textsc{ph}]$ values show no statistically significant differences (p = 0.19, n = 14), whereas $N^{\mathrm{E}}[\textsc{nt}]$ are higher than $N^{\mathrm{E}}[\textsc{ph}]$ (p = 0.002, n = 15). The $r[\textsc{nt}]$ values are similar to those evaluated in PH condition (p = 0.80 for BSs and p = 0.69 for BEs). In comparison with SP condition, $N[\textsc{nt}]$ and $N[\textsc{ph}]$ are much decreased, at the trade-off of increased $r[\textsc{nt}]$ and $r[\textsc{ph}]$ values (with values typically higher than 0.8).

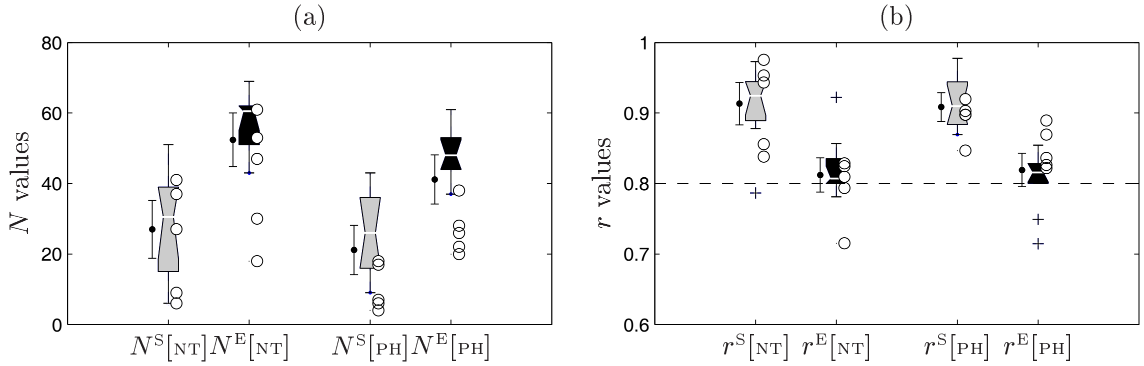

Figure 4.22: Distribution of N and r, evaluated for BSs (grey) and BEs (black) in NT and PH conditions. The white circles identify the subjects with highest $\hat{\mathcal{B}}^{\mathrm{E}}_{\mathrm{G,O}}[\textsc{sp}]$ values.

Regarding the BRS dispersion in SP condition, the BRS analysis from BEs provided a larger N^{E}, obtained at the expense of a lower r^{E}, in comparison with that evaluated from BSs, leading to a decrease in the dispersion of the BRS estimator based on BEs (see Fig. 3.25). The results presented in Fig. 4.22 point out that, in drug-induced data, N is diminished with respect to the SP condition, whereas r is increased due to the drug effect. The BRS dispersion in SP, NT and PH conditions was quantified through the computation of the standard deviation of the slope $\mathcal{B}_{\mathrm{G,O}}$, using the Bootstrap-based methodology described in Sec. 3.5.4. Similarly, the dispersion in BRS estimation was quantified by δ as the estimated $\hat{\mathcal{B}}$ standard deviation divided by $\hat{\mathcal{B}}$ and multiplied by 100 (Eq. 3.9).

Figure 4.23 shows the $\delta_{\mathrm{G,O}}$ values as a function of N and r. The results for the SP condition corroborate the results obtained for the EuroBaVar files (Fig. 3.27): $\delta[\textsc{sp}]$ value decays with increasing $N[\textsc{sp}]$ and $r[\textsc{sp}]$ remains close to 0.8, being higher than 0.8 for BSs and lower than 0.8 for BEs (Figs. 4.23(a,d)). The subjects exhibiting the highest $\hat{\mathcal{B}}^{\mathrm{E}}_{\mathrm{G,O}}[\textsc{sp}]$ values also exhibit the lowest $N^{\mathrm{E}}[\textsc{sp}]$ and lowest $r^{\mathrm{E}}[\textsc{sp}]$ values (Fig. 4.21). Consequently, these subjects also exhibit the highest $\delta^{\mathrm{E}}_{\mathrm{G,O}}[\textsc{sp}]$ values of the dataset. Regarding the drug-induced conditions,

$N[\mathrm{NT}]$ and $N[\mathrm{PH}]$ are lower than $N[\mathrm{SP}]$, and $r[\mathrm{NT}]$ and $r[\mathrm{PH}]$ are higher than $r[\mathrm{SP}]$ (Figs. 4.23(b–c) and 4.23(e–f)), so that $\delta_{\mathrm{G,O}}[\mathrm{NT}]$ and $\delta_{\mathrm{G,O}}[\mathrm{PH}]$ are in the same range of values than $\delta_{\mathrm{G,O}}[\mathrm{SP}]$.

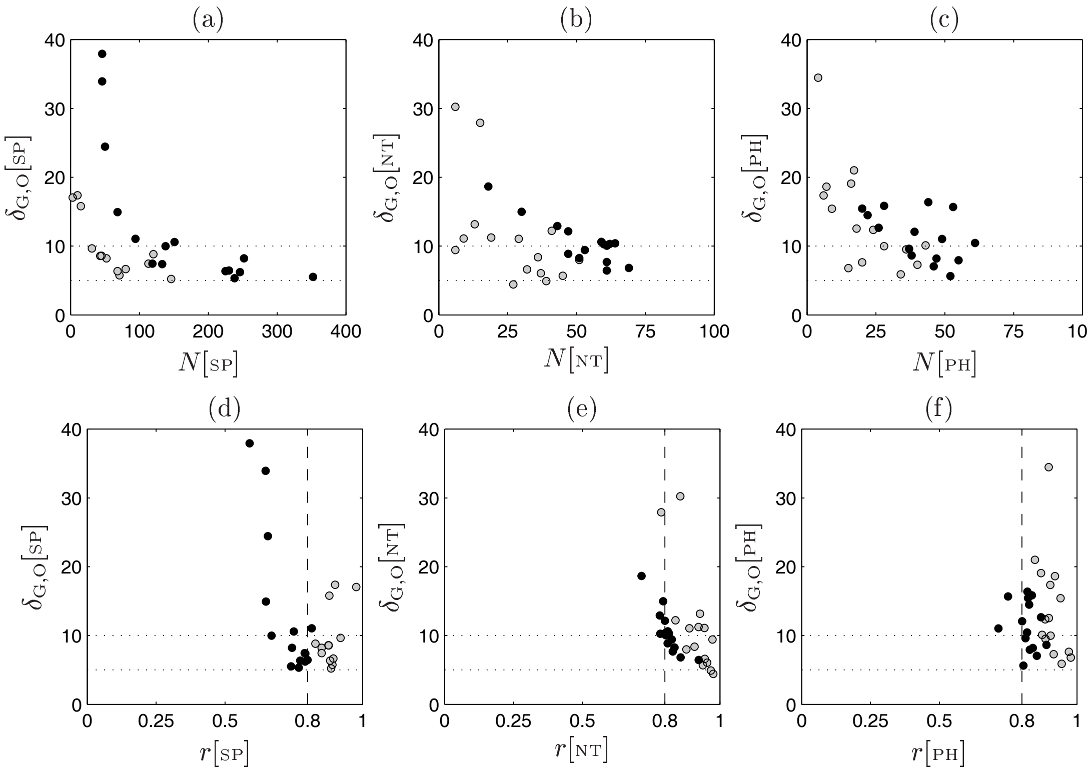

Figure 4.23: Plot of $\delta_{\mathrm{G,O}}$ versus N and r for $\hat{\mathcal{B}}^{\mathrm{S}}$ (grey) and $\hat{\mathcal{B}}^{\mathrm{E}}$ (black) in SP, NT and PH conditions.

For the illustration of the overall results, Fig. 4.24 presents the distribution of $\delta_{\mathrm{G,O}}$ evaluated for BSs and BEs in SP, NT and PH conditions. The results point out that around 50% of the files present $\delta_{\mathrm{G,O}}[\mathrm{NT}]$ and $\delta_{\mathrm{G,O}}[\mathrm{PH}]$ below 10%, while that percentage increases for $\delta_{\mathrm{G,O}}[\mathrm{SP}]$. As a matter of fact, the distribution of the $\delta_{\mathrm{G,O}}[\mathrm{SP}]$ is below 10%, if excluding the subjects that exhibit the lowest N^{E} of the dataset.

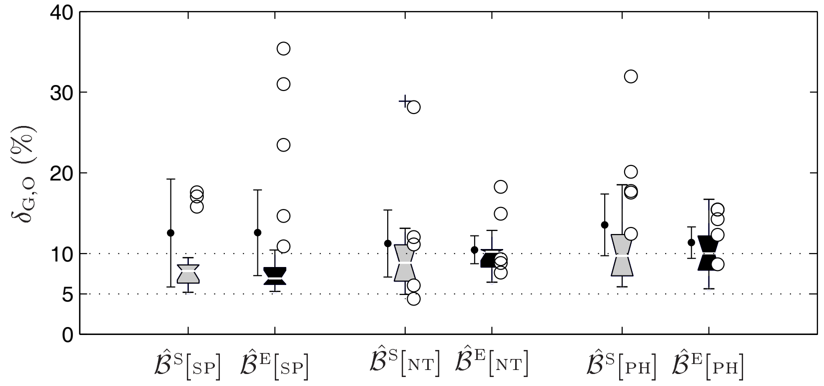

Figure 4.24: Boxplots of $\delta_{\mathrm{G,O}}$ evaluated for BSs (grey) and BEs (black) in SP, NT and PH conditions. Median and mean 95% confidence intervals represented by the notch and by the interval displayed at the left of each boxplot. The white circles identify the subjects with highest $\hat{\mathcal{B}}^{\mathrm{E}}_{\mathrm{G,O}}[\mathrm{SP}]$ values.

The dispersion limits for the $\mathcal{B}_{\text{G,O}}$ estimator evaluated in SP, NT and PH conditions was also quantified from the percentiles of the δ empirical distribution, provided in Table 4.1. The $\hat{\mathcal{B}}^{\text{E}}_{\text{G,O}}[\text{SP}]$ estimates provided the lowest median and lowest P_{75} of the δ values, indicating that 50% of the files present a $\delta[\text{SP}]$ value below 7.8% and 75% of the files exhibit a $\delta[\text{SP}]$ value below 11.1%. Attending the entire distribution of the δ values, the lowest δ values where obtained from $\hat{\mathcal{B}}^{\text{E}}_{\text{G,O}}[\text{PH}]$, with 95% of the files exhibiting a $\delta[\text{PH}]$ value below 16.4%.

Table 4.1: Dispersion limits for the BRS estimators in spontaneous and invasive conditions, quantified from δ. The variable P_k, $k = \{50, 75, 95\}$ is the value below which k% of the observations fall, and n indicates the # of files from which the statistics were computed.

	$\delta_{\text{G,O}}$ (%)			
	P_{50}	P_{75}	P_{95}	n
$\hat{\mathcal{B}}^{\text{S}}[\text{SP}]$	8.6	15.8	56.8	14
$\hat{\mathcal{B}}^{\text{E}}[\text{SP}]$	7.8	11.1	37.9	15
$\hat{\mathcal{B}}^{\text{S}}[\text{NT}]$	10.3	12.2	30.2	15
$\hat{\mathcal{B}}^{\text{E}}[\text{NT}]$	10.3	12.2	18.7	15
$\hat{\mathcal{B}}^{\text{S}}[\text{PH}]$	11.2	17.4	34.5	15
$\hat{\mathcal{B}}^{\text{E}}[\text{PH}]$	11.6	15.5	16.4	15

Finally, Fig. 4.25 presents the comparison of the $\delta_{\text{G,O}}$ evaluated in SP, NT and PH conditions. The results indicate that no precision improvement is achieved with the BRS analysis from the drug-induced data, in comparison with the BRS analysis from SP condition: for BEs, 8 out of the 15 files exhibit $\delta[\text{NT}] < \delta[\text{SP}]$ and 4 out of the 15 files present $\delta[\text{PH}] < \delta[\text{SP}]$. From the comparison between SP and NT condition, the lower $N[\text{NT}]$ is balanced by the increased $r[\text{NT}]$ in comparison with the SP condition, and the number of files presenting either $\delta[\text{NT}] < \delta[\text{SP}]$ or $\delta[\text{NT}] > \delta[\text{SP}]$ is similar (Figs. 4.25(a) and 4.25(d)). The comparison between SP and PH conditions, indicates that $\delta[\text{SP}]$ is lower than $\delta[\text{PH}]$ for more than half of the files (Figs. 4.25(b) and 4.25(e)), which is likely due to the variable response of the subjects to the cumulative effect of the NT and PH boluses. Finally, the $\delta[\text{PH}]$ are typically higher than the $\delta[\text{NT}]$ probably because $N[\text{NT}]$ had the tendency to be higher than $N[\text{PH}]$ (Fig. 4.22).

4.5 Discussion

The comparison between the invasive BRS estimates ($\hat{\mathcal{B}}^{\text{I}}$) and spontaneous BRS estimates ($\hat{\mathcal{B}}_{\text{G,O}}[\text{SP}]$) corroborates the previous findings that these estimates are correlated (Parlow *et al.*, 1995). However, the study of Parlow *et al.* (1995) also indicated that there were no statistical significant differences between invasive and spontaneous estimates and, in this study, the $\hat{\mathcal{B}}^{\text{I}}$

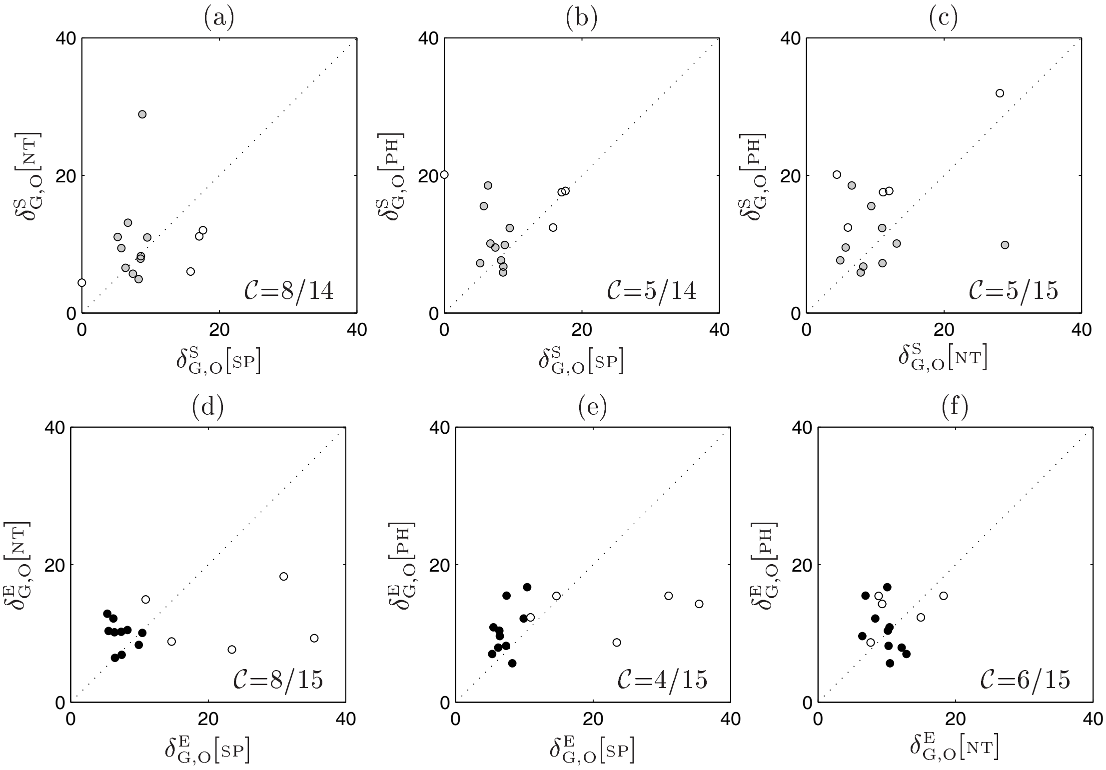

Figure 4.25: Comparison between the $\delta_{\mathrm{G,O}}$ obtained for $\hat{\mathcal{B}}^{\mathrm{S}}$ (grey) and $\hat{\mathcal{B}}^{\mathrm{E}}$ (black) in SP, NT and PH conditions. The white circles identify the subjects with highest $\hat{\mathcal{B}}^{\mathrm{E}}_{\mathrm{G,O}}[\mathrm{SP}]$ values.

tend to be higher than spontaneous BRS estimates. The differences between invasive and spontaneous BRS estimates were found to be significantly correlated with the differences between the mean SBP values evaluated in the invasive and spontaneous recordings. However, as this correlation was found to be moderated, other reasons to explain the differences between the estimates were explored.

The differences between the invasive and spontaneous BRS estimates can possibly be due to the methodological differences between the BRS estimators or due to the differences in the physiological information that the invasive and spontaneous data carry. The effect of using different data was removed by evaluating the different estimators in invasive data. The results pointed out that the correlation between $\hat{\mathcal{B}}^{\mathrm{I}}$ and $\hat{\mathcal{B}}_{\mathrm{G,O}}[\mathrm{OX}]$ is higher than that evaluated from $\hat{\mathcal{B}}^{\mathrm{I}}$ and $\hat{\mathcal{B}}_{\mathrm{G,O}}[\mathrm{SP}]$, showing significant differences for BRS estimates evaluated from BEs. The effect of using different estimators was removed by evaluating the same estimators in invasive and SP condition. The results pointed out that the BRS analysis from BEs achieves the highest reproducibility in different data, because the correlation between $\hat{\mathcal{B}}_{\mathrm{G,O}}[\mathrm{OX}]$ and $\hat{\mathcal{B}}_{\mathrm{G,O}}[\mathrm{SP}]$ is higher for the BRS estimates evaluated from BEs against BSs. Therefore, if the BRS analysis from BEs is able to provide a value that reflects the physiology of the baroreflex, the BRS analysis from BEs is preferable, even to compute a BRS estimate with data following the OX protocol.

Validation of the BRS estimates obtained from BEs

The BRS estimates obtained from BSs and from BEs were further compared in drug-induced data, in order to validate the obtained BRS values. The results obtained provided indirect evidences that the BRS estimates from BEs are more suitable than the BRS estimates from BSs to represent the BRS physiology. First, the BRS analysis from BEs offers an increased ability to discriminate SP, NT and PH conditions (Fig. 4.17). Second, those estimates are in accordance with the expected relationship between BRS estimates and mean RR interval (Fig. 4.18). Finally, the inter condition changes in the $\hat{\mathcal{B}}^{\mathrm{E}}_{\mathrm{G,O}}$ values are more correlated with the changes in $\bar{x}_{\mathrm{RR}}$, in comparison with the $\hat{\mathcal{B}}^{\mathrm{S}}_{\mathrm{G,O}}$ (Fig. 4.19).

From the 15 subjects of the dataset, 5 exhibited the highest $\hat{\mathcal{B}}^{\mathrm{E}}_{\mathrm{G,O}}[\textsc{sp}]$ values in the dataset, and were found to be associated with the highest $\bar{x}_{\mathrm{RR}}$ values (i.e., the recordings of smaller beat length) and the lowest $N^{\mathrm{E}}[\textsc{sp}]$ values. In one of these files, it was not possible to identify BSs in SP condition and, therefore, a $\hat{\mathcal{B}}^{\mathrm{S}}_{\mathrm{G,O}}[\textsc{sp}]$ for that subject could not be obtained. The remaining 4 files were associated with the highest differences between the $\hat{\mathcal{B}}^{\mathrm{E}}_{\mathrm{G,O}}[\textsc{sp}]$ and $\hat{\mathcal{B}}^{\mathrm{S}}_{\mathrm{G,O}}[\textsc{sp}]$ values. This result indicates that nonexistent BSs in a recording is not necessarily associated to BRS failure, because the analysed data is from normal subjects. Instead, this result is a clear sign that for the lower HR cases, 5 minutes length recordings in SP condition are not suffice to obtain a BRS estimate from BSs. Moreover, it was found that the BRS estimates obtained for the files exhibiting the lowest $N^{\mathrm{S}}[\textsc{sp}]$ values did not discriminate SP, NT and PH conditions and did not follow the expected relationship between the BRS estimates and the mean RR interval. On the other hand, the BRS analysis from BEs provides a larger $N^{\mathrm{E}}[\textsc{sp}]$ and, therefore, it holds an increased likelihood of providing a BRS estimate for all files. Moreover, for the cases exhibiting the lowest $N^{\mathrm{E}}[\textsc{sp}]$ values, the BRS estimates from BEs discriminated SP, NT and PH conditions and followed the expected relationship between the BRS estimates and the mean RR interval. Therefore, the BRS analysis from BEs provide suitable BRS estimates, even for the subjects exhibiting the lowest $N^{\mathrm{E}}[\textsc{sp}]$ values.

Dispersion in spontaneous and invasive BRS analysis

The BRS analysis from BEs provides a larger $N^{\mathrm{E}}[\textsc{sp}]$ value obtained at the expense of a lower $r^{\mathrm{E}}[\textsc{sp}]$ value in comparison with that evaluated from BSs, leading to a decrease in the dispersion if the BRS is estimated from BEs (see Fig. 3.25). In drug-induced data, N is diminished and r is increased with respect to that evaluated for SP condition. The comparison between the BRS analysis from SP recordings of 5 minutes length and from invasive recordings of 45 seconds length indicated that no precision improvement is achieved if the BRS is estimated from drug induced data. In SP condition, there is no time span constrain as in drug-induced experiments (in particular if using a bolus instead of a continuous infusion). Therefore, the possibility of increase N in SP condition is an advantage in terms of dispersion over increase r with a drug-induced protocol, because higher $N[\textsc{sp}]$ simply requires longer recordings, whereas higher r requires higher $x_{\mathrm{SBP}}(n)$ and $x_{\mathrm{RR}}(n)$ correlation (only obtained with BRS stimulation). Thus, if the SP stationary conditions are satisfied (i.e.,

$r^{\text{E}}[\textsc{sp}]$ close to 0.8) in recordings longer than 5 minutes, it is expected that spontaneous BRS estimates will achieve an even lower dispersion.

4.6 Conclusions

In this chapter, the BRS analysis from baroreflex events (BEs) and baroreflex sequences (BSs) were further compared with spontaneous and drug induced data.

The results in the SP/NT/PH dataset corroborate that BRS estimates obtained from spontaneous and drug induced data are correlated. In particular, if BRS analysis is carried out from BEs, the correlation between invasive and spontaneous BRS estimates is higher and their differences are smaller.

The BRS analysis from BEs is also able to provide BRS values that reflect better the physiology of the baroreflex, against the BRS analysis from BSs. First, the BRS estimates from BEs discriminate between spontaneous, nitroprusside and phenylephrine conditions for more subjects of the dataset. Second, the BRS estimates from BEs are more in accordance with the expected relationship between the BRS estimates and the mean RR interval. Finally, the BRS estimates from BEs are more correlated with the amount of sympathetic activity in a condition of sympathetic activation. Therefore, BRS analysis from BEs is advantageous in comparison with BRS analysis from BSs, being also suitable to compute a BRS estimate with data following the Modified Oxford protocol.

With respect to the dispersion in BRS analysis, no decrease in the BRS dispersion is achieved if the BRS is estimated from drug induced data, thus, pointing out other advantages of spontaneous BRS analysis over invasive BRS analysis.

Chapter 5

BRS Estimation from Short and Long Events

The results in previous chapters evidence that baroreflex changes, associated with posture changes and drug induced BRS stimulation, can be adequately detected using the BRS estimates from the events technique. Nevertheless, time domain BRS estimates are overall estimates that account for both parasympathetic and sympathetic ANS modulations. On the other hand, frequency domain BRS estimates provide separate BRS estimates for low frequency (LF) and high frequency (HF) bands, more associated to sympathetic and to parasympathetic ANS modulations, respectively (Pagani *et al.*, 1986). Because the sequences technique provides a slope based on short segments of data, it is accepted that BRS estimates based on BSs essentially reflect the parasympathetic activity (Persson *et al.*, 2001).

The sympathetic ANS branch presents oscillations with lower frequency than the parasympathetic branch (Pagani *et al.*, 1997), and longer SBP and RR data segments are needed to detect and quantify this modulation. As the events technique is able to provide longer BEs, besides the BEs of the same length as BSs, BEs are more likely to also capture the sympathetic modulation than BSs. **In this chapter**, the BRS analysis from BEs is further compared with the frequency domain BRS estimates, more conventionally accepted to distinguish the sympathetic/parasympathetic effects. Furthermore, the BRS analysis from short and long BEs is associated with the respiratory activity. The study focuses on data acquired in spontaneous condition, with the objective to evidence the value of including the long SBP and RR segments provided by the events technique, besides the short SBP and RR segments of data already provided by the sequences technique.

5.1 Time and frequency domain BRS estimation

Frequency domain analysis of the cardiovascular series has been used to analyse the SBP and RR variabilities and to quantify the power of the series at specific frequency bands (Task Force of ESC & NASPE, 1996). In the same way, frequency domain BRS analysis, based on cross spectral analysis of the SBP and RR series, is able to provide BRS estimates in different frequency bands, typically more associated to the sympathetic or to the parasympathetic ANS modulations (Robbe *et al.*, 1987; Pagani *et al.*, 1988). Time domain BRS estimates, by their turn, are overall estimates that account for both sympathetic and parasympathetic ANS influences.

In power spectral analysis of short-term SBP and RR variabilities, three main frequency bands can be distinguished: very low frequency (VLF), low frequency (LF) and high frequency (HF) bands. Traditionally, the VLF band is defined in the 0–0.04Hz range, the LF band is defined in the 0.04–0.15Hz range and HF is defined in the 0.15–0.4Hz range (Task Force of ESC & NASPE, 1996). These frequency bands are associated with the physiological regulation of the cardiovascular function related to thermoregulation, baroreflex and respiration. While there is general agreement that the HF component is mostly derived by vagal activity, the mechanisms inherent to the LF component are less consensual. The HF band reflects predominantly oscillations related to respiration, which are partly mediated by parasympathetic modulation, but also reflects mechanical influences. On one hand, the HF power in the RR series becomes unnoticeable in apnoea condition (van de Borne *et al.*, 2001) and, on the other hand, there is still a reduced RR power in the HF band after pharmacological parasympathetic blockade (Challapalli *et al.*, 2007). Disagreement exists regarding the origins of the LF power in the cardiovascular series. Some authors suggest that the LF component is an expression of both sympathetic and vagal activity (Task Force of ESC & NASPE, 1996). Regarding the sympathetic modulation, previous studies reported that during pharmacological sympathetic activation (by a continuous infusion of nitroprusside) the LF powers of the SBP, RR and MSNA series are increased in comparison with a baseline spontaneous condition, whereas during sympathetic inhibition (by a continuous infusion of phenylephrine) the LF powers are decreased and HF power is predominant (Pagani *et al.*, 1997). Nevertheless, other factors, such as thermoregulation and paced breathing, have also been reported to be associated with the SBP and RR oscillations in the LF band (Parati *et al.*, 1995). With the evidence that LF and HF power components of RR spectral analysis are more associated with sympathetic and vagal ANS activity, respectively, their ratio (LF/HF) has been suggested as an index of sympatho-vagal balance (Pagani *et al.*, 1986; Malliani *et al.*, 1998).

The effect of respiration on the SBP and RR relation is a frequency-dependent phenomenon that is independent of the sympathetic drive (Pitzalis *et al.*, 1998*b*). Different respiratory frequencies and depths have major effects on SBP and RR oscillations and on their relationship (i.e., on baroreflex sensitivity). As a matter of fact, with increasing respiratory frequency, SBP and RR powers tend to decrease in the entire frequency range, and SBP and RR powers at a fixed respiratory frequency are increased for larger tidal volumes (Brown *et al.*, 1993). This is explained by the fact that a subject breathing slowly tends to perform deep breathing as well (increase the range of lung volume variations), and the SBP and RR modulations due to respiration are more perceptible: typically, there is an increase of the series variance with deep breathing.

Due to the respiratory influence on SBP and RR, a BRS estimate obtained at different frequency bands depends on the respiratory frequency and depth. As a matter of fact, it has been shown that the BRS estimates increase in patients with Chronic Heart Failure (CHF), if the respiration is paced at the LF band (Bernardi *et al.*, 2002). Therefore, in a clear case of baroreflex dysfunction, the BRS value can be *overestimated*, simply if the respiration is paced at the same frequency as the baroreflex modulation. In this case, the BRS mechanisms related and unrelated with respiration are more difficult to distinguish and the BRS analysis should include the respiratory information to distinguish such effects (Tiinanen *et al.*, 2008).

The use of deep breathing protocols can be an advantage for BRS estimation, if there is no interest in distinguishing the BRS mechanisms related and unrelated with respiration. As a matter of fact, deep breathing protocols have been proposed to enhance the BRS estimation evaluated from frequency domain methods (Davies *et al.*, 1999) and from the sequences technique (Oka *et al.*, 2003). With frequency domain BRS analysis, deep breathing protocols have been shown to provide more reproducible BRS estimates and lowest failure rate in controls and in CHF patients (Davies *et al.*, 1999). With time domain BRS analysis, deep breathing protocols have been shown to increase the probability of the sequences technique to provide a BRS estimate (Oka *et al.*, 2003). Also, the higher variance of the SBP and RR series observed in deep breathing data is an advantage in the slope computation, because BSs with wider SBP and RR ranges will be identified. As the SBP and RR ranges are increased, it likely that the spontaneous slope estimated in deep breathing data is more similar to an invasive slope obtained from sigmoidal function (Fig. 1.7), rather than a spontaneous slope derived from shallow breathing data.

Previous comparisons between time and frequency domain methods for BRS estimation have shown that time and frequency BRS estimates are correlated and able to provide comparable information on BRS changes over time (Persson *et al.*, 2001). The concordance between time and frequency BRS estimates in the LF band has been shown to depend on the threshold values apriori set for BSs identification (Davies *et al.*, 2001). In healthy controls, the correlation between the sequences technique estimates and the frequency domain estimates increased with increasing threshold value for SBP beat-to-beat changes $\Delta_{min}^{\text{SBP}}$, regardless of the threshold for the RR beat-to-beat changes (Δ_{min}^{RR}). Therefore, that concordance could be optimized by increasing $\Delta_{min}^{\text{SBP}}$ above the standard value of 1 mmHg. Nevertheless, increase the $\Delta_{min}^{\text{SBP}}$ value would result in decrease the number of identified BSs, because higher range SBP ramps are more unlikely to occur for subjects with attenuated BRS in comparison with subjects with normal BRS.

Regarding the sequences technique, there has been debate about the meaning of BSs and the reasons why the SBP–RR analysis based on BSs reflects the BRS function (Bertineri *et al.*, 1988; Parlow *et al.*, 1995). It is reported that the parasympathetic modulation may be already active on the same RR interval or on the one immediately following a blood pressure change, while sympathetic modulation usually becomes apparent after 5–6 beats (Bertineri *et al.*, 1988; Parlow *et al.*, 1995). As illustrated in Fig. 3.17 for the EuroBaVar dataset, BSs are typically of 3-beat length, 12/46 of the records have 6-beat BSs and none present BSs longer than 8 beats. Therefore, BRS analysis from BSs mostly reflects the autonomic control of the heart through parasympathetic neural afferents (Parlow *et al.*, 1995). A previous comparisons between time and frequency BRS estimates indicated that the BRS estimates from the sequences technique are more correlated with the frequency estimates derived from HF rather than with the frequency estimates derived from LF band (Watkins *et al.*, 1996), strengthening the hypothesis that the BRS estimates derived from the sequences technique mostly reflect parasympathetic activity.

The sympathetic branch of the ANS presents oscillations of lower frequency than the parasympathetic (Pagani *et al.*, 1997) and, therefore, longer SBP and RR data segments are needed to detect and quantify this modulation. The events technique is able to provide long data segments, besides the short segments already identified by the sequences technique. Therefore, BEs are more likely to also capture the sympathetic modulation than BSs. **In this chapter**, the BRS analysis from BEs is further compared with the frequency domain BRS estimates, with the goal of evidencing the value of including the long SBP and RR segments provided by the events technique in time domain BRS estimation.

5.2 Methods for frequency domain analysis

Figure 5.1 shows the SBP, RR, MSNA and RESP series for one representative subject in SP condition, from the SP/NT/PH dataset (described in Sec. 4.3.1). As it can be observed, the series of beat-to-beat variability exhibit rhythmical oscillations that can be described as the sum of elementary oscillatory components, defined by their frequency and amplitude. This information can be represented with the power spectral density (PSD) function or *spectrum*, describing how the power of a time series is distributed over frequency. Similarly, the joint analysis of two distinct series allows the identification of common oscillations, and the corresponding information can be represented with the *cross-spectrum*.

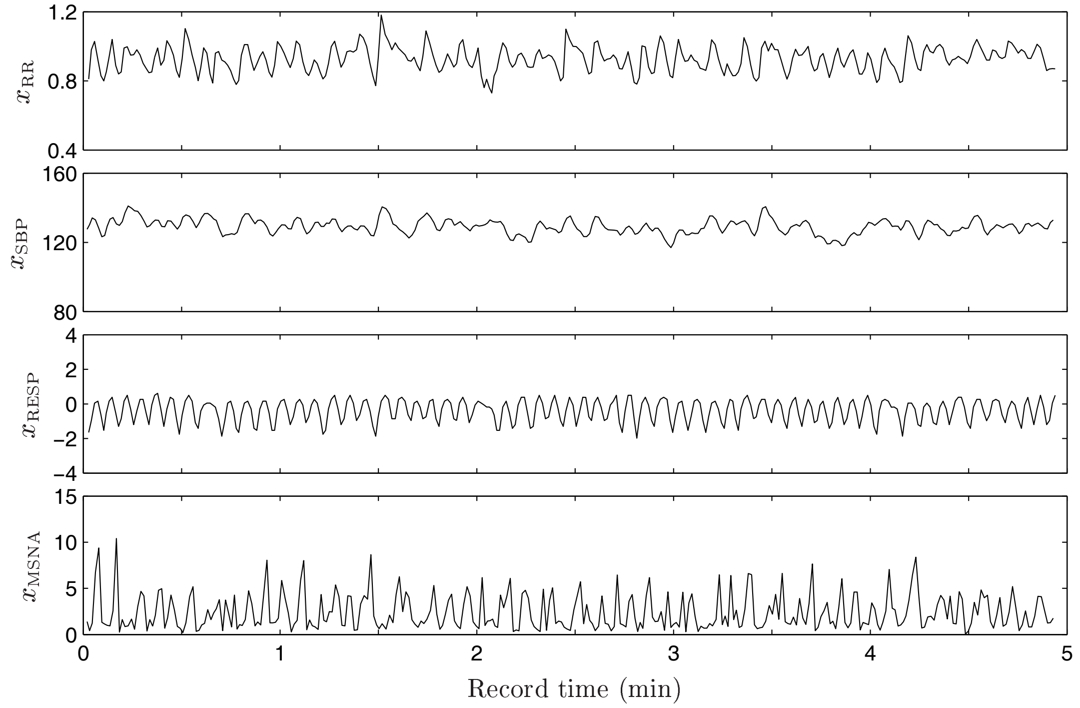

Figure 5.1: Plot of x_ϑ with $\vartheta = \{\mathrm{RR,SBP,RESP,MSNA}\}$ from one representative subject in SP condition from the SP/NT/PH dataset. The 5 min recording corresponds to 320 heartbeats.

The methods here described are based in the notation considered by Manolakis *et al.* (2000), and the definitions in this thesis follow the usual notation in signal processing theory, which differs from time series analysis.

The PSD function of a wide-sense stationary time series $x(n)$ with zero mean, is defined as the Fourier transform of its auto-correlation function $r_{xx}(k)$, i.e.,

$$S_{xx}(e^{j\omega}) = \sum_{k=-\infty}^{+\infty} r_{xx}(k)e^{-j\omega k}, \quad -\pi < \omega \leq \pi \tag{5.1}$$

where $r_{xx}(k)$ is defined as

$$r_{xx}(k) = E\left[x(n+k)x(n)\right] \tag{5.2}$$

represents a measure of linear dependence between $x(n+k)$ and $x(n)$.

Similarly, the *cross-power spectrum* can be used to investigate if the oscillations of two distinct series $x(n)$ and $y(n)$ are linearly related. Considering $x(n)$ as the input and $y(n)$ the output of the system, both jointly wide-sense stationary, their *cross-spectrum* is the Fourier transform of the cross-correlation function $r_{xy}(k)$, i.e.,

$$S_{xy}(e^{j\omega}) = \sum_{k=-\infty}^{+\infty} r_{xy}(k) e^{-j\omega k}, \tag{5.3}$$

where $r_{xy}(k)$ is defined as

$$r_{xy}(k) = E\left[x(n+k)y(n)\right]. \tag{5.4}$$

The amount of linear coupling between $x(n)$ and $y(n)$ in the frequency domain can be expressed by means of the normalized cross-spectrum, also called *complex coherence function*

$$\mathcal{K}(e^{j\omega}) = \frac{S_{xy}(e^{j\omega})}{\sqrt{S_{yy}(e^{j\omega})\; S_{xx}(e^{j\omega})}}. \tag{5.5}$$

The coherence is usually represented by its squared magnitude $|\mathcal{K}(e^{j\omega})|^2$, which exhibits the property $0 \leq |\mathcal{K}(e^{j\omega})|^2 \leq 1$. This function is comparable to the coefficient of determination in regression analysis (i.e., squared correlation coefficient, r^2), with zero indicating no linear relation between the series at a given frequency, and one indicating that the series exhibit a *perfect* linear relation at a given frequency within some fixed phase relationship (Challis and Kitney, 1991). Therefore, this function reflects the degree of linear relation between the two series as a function of frequency.

The relation between the output $y(n)$ and input $x(n)$ of a linear and time-invariant system can be expressed from the *transfer function* defined as

$$\mathcal{H}(e^{j\omega}) = \frac{S_{yx}(e^{j\omega})}{S_{xx}(e^{j\omega})}. \tag{5.6}$$

Alternatively, using the input–output relation

$$S_{yy}(e^{j\omega}) = |\mathcal{H}(e^{j\omega})|^2\; S_{xx}(e^{j\omega}), \tag{5.7}$$

the gain of the transfer function $|\mathcal{H}(e^{j\omega})|$ can be obtained as

$$|\mathcal{H}(e^{j\omega})| = \sqrt{\frac{S_{yy}(e^{j\omega})}{S_{xx}(e^{j\omega})}}. \tag{5.8}$$

From the use of Eq. (5.8) only $|\mathcal{H}(e^{j\omega})|$ can be determined, while the use of the Eq. (5.6) allows to determine both the gain and the phase of $\mathcal{H}(e^{j\omega})$, as $S_{yx}(e^{j\omega})$ is a complex function.

There are different methods for PSD estimation, which can be classified into two nonparametric and parametric (model based) methods (Manolakis *et al.*, 2000). In nonparametric methods, a usual estimator for PSD function is the Welch periodogram (Welch, 1967). The Welch method consists of dividing $x(n)$ into (possibly overlapping) windowed segments, computing a periodogram for each one and then averaging the estimates. If the original data is divided into K segments with $L-D$ points of overlap, then each segment can be defined as $x_i(n) = x(n+iD)$ with $0 \le i \le K-1$ and $0 \le n \le L-1$. The Welch estimate is

$$\widehat{S}_{xx}(e^{j\omega}) = \frac{1}{KLU} \sum_{i=0}^{K-1} \left| \sum_{n=0}^{L-1} x_i(n) w(n) e^{-jn\omega} \right|^2 , \tag{5.9}$$

where U is a normalization factor related to the window $w(n)$ characteristics

$$U = \frac{1}{L} \sum_{i=0}^{L-1} w^2(n). \tag{5.10}$$

Similarly, the cross-spectra $S_{xy}(e^{j\omega})$ can be estimated using the Welch method (Manolakis *et al.*, 2000). The $x(n)$ and $y(n)$ series are both divided into overlapping windowed segments and the Welch estimate is given by

$$\widehat{S}_{xy}(e^{j\omega}) = \frac{1}{KLU} \sum_{i=0}^{K-1} \left(\sum_{n=0}^{L-1} x_i(n) w(n) e^{-jn\omega} \right) \left(\sum_{n=0}^{L-1} y_i(n) w(n) e^{-jn\omega} \right)^* . \tag{5.11}$$

Averaging of the periodograms leads to a consistent and asymptotically unbiased PSD estimator. Although overlap between segments tends to introduce some dependency in segments, this effect can be diminished by the use of nonrectangular windows, which reduce the importance or weight given to the samples that overlap in consecutive segments. Thus, the overlapping between segments and the adequate window are two variables of the method that can be balanced in order to achieve a reduction in the PSD estimator variance and an increase in spectral resolution (Manolakis *et al.*, 2000).

5.2.1 Spectral analysis of series of beat-to-beat variability

In many conditions, the SBP, RR, MSNA and RESP series are typically non stationary, due to the physiological adaptation processes to external stimulations. However, if the ECG and ABP acquisition is carried out in a stationary condition of the subject (e.g., lying and minimizing any external perturbation) the series can be considered wide-sense stationary, and the methods described in the previous section can be used.

Discrete signals are, by definition, recorded at discrete time points. Consequently, the oscillations of a signal occurring faster than the time interval between two consecutive samples cannot be detected. The maximum frequency possible to analyse relates to the sampling theorem and it corresponds to the Nyquist frequency, i.e., half of the sampling frequency F_s of the signal (Manolakis *et al.*, 2000). In order to introduce the time information in the frequency analysis, the frequency axis ω is normalized by F_s as

$$f = \frac{\omega}{2\pi} F_s. \tag{5.12}$$

Cardiovascular series exhibit non uniform sampling and are indexed to the occurrence of each heartbeat. However, as the PSD estimation method assumes that the discrete series are wide-sense stationary, the frequency axis in the spectra can be normalized assuming a uniform sampling period equal to the mean RR interval, i.e., the mean distance between two consecutive samples. In this case, the frequency axis ω is normalized as

$$f = \frac{\omega}{2\pi} \frac{1}{\bar{x}_{\mathrm{RR}}}. \tag{5.13}$$

The approximation $F_s \approx 1/\bar{x}_{\mathrm{RR}}$ has been shown to be acceptable for low frequencies far from the Nyquist frequency (Mateo and Laguna, 2000). Furthermore, with this normalization, the respiratory frequency obtained from the respiratory signal is correctly reflected in the spectra of the RESP series. Alternatives to this approximation can also be considered, e.g., interpolation/resampling of the series before spectral analysis or the use of Lomb method for direct PSD estimation of the unevenly series (Sörnmo and Laguna, 2005).

Figure 5.2 shows the power spectra of the SBP, RR, MSNA and RESP series using the Welch method. As illustrated in Fig. 5.2(a), three main spectral components can be distinguished in the RR spectrum, located at very low frequency (VLF: 0–0.04 Hz), low frequency (LF: 0.04–0.15 Hz), and high frequency (HF: 0.15–0.4 Hz) bands. The MSNA spectral analysis (Fig. 5.2(d)) evidenced the presence of two major components, one in LF and the other in HF component, around the respiratory frequency of that subject (Fig. 5.2(c)). Due to the sympathetic and respiratory influences in the RR oscillations, two similar components were observed in the RR and SBP spectra (Fig. 5.2(a–b)).

The MSNA signal has been used to directly investigate sympathetic modulation to better understand the SBP and RR oscillations. Therefore, the observation that the MSNA exhibits power in both LF and HF frequency bands has been an issue of debate (Montano *et al.*, 2009). The RR oscillations around the respiratory frequency (RSA) are primarily mediated by the parasympathetic ANS activity and, therefore, increased RSA indicates increased parasympathetic activity. Because respiration also induces mechanical effects on SBP, the HF oscillations in MSNA can be due to the respiratory modulation in the SBP values and, by this reason, due to increased parasympathetic activity (Fig. 1.4). Previous studies corroborate this hypothesis: it was reported that under a sympathetic inhibition (by continuous administration of phenylephrine) the MSNA power in the LF frequency band decreases and the MSNA power in the HF frequency band dominates over that evaluated for LF band (Pagani *et al.*, 1997). Therefore, these authors suggested that MSNA powers in LF and HF bands are related with sympathetic neural excitation and inhibition, respectively.

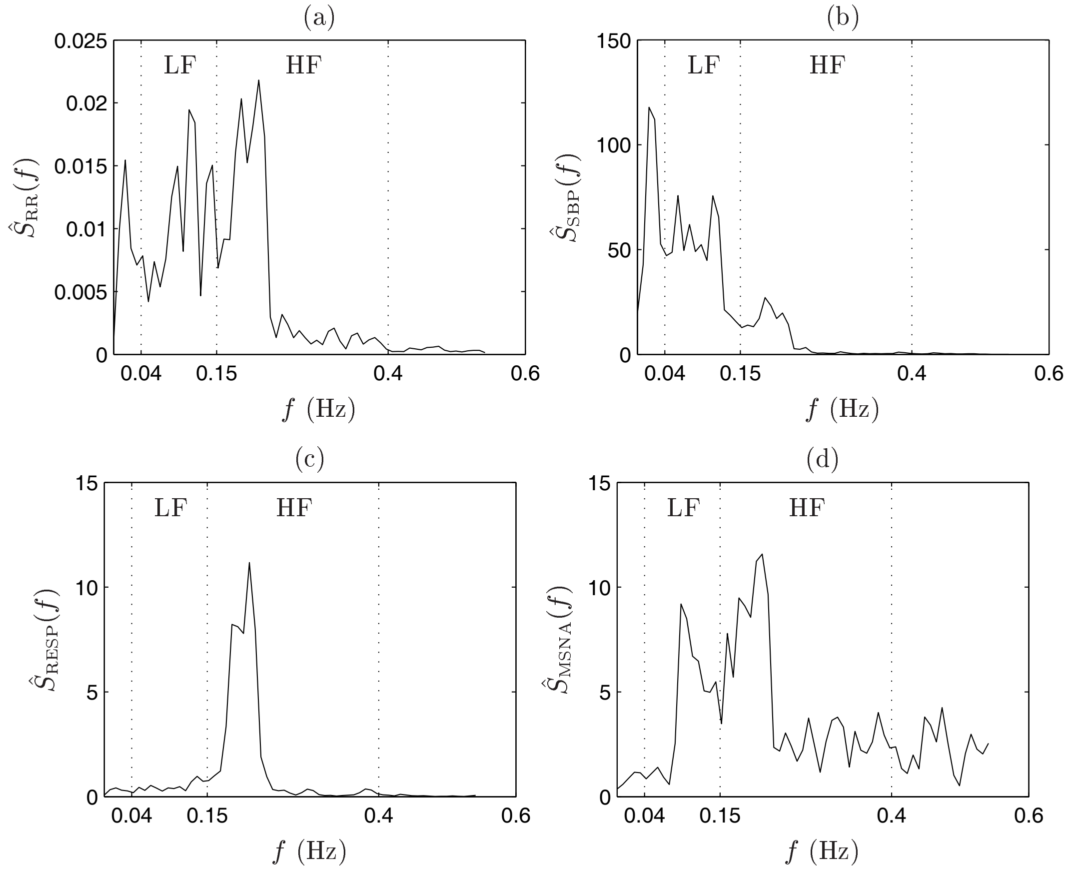

Figure 5.2: Power spectra of RR, SBP, MSNA and RESP time series computed with the Welch method (Hanning window, 62,5% overlap, 128 FFT points, 5 segments). Frequency axis normalized by RR mean. Same data as in Fig. 5.1.

The typical variables extracted from nonparametric spectral analysis are related with the distribution of the power in VLF, LF and HF bands (Task Force of ESC & NASPE, 1996), because power distribution has been shown to change in accordance to changes in autonomic RR modulations (Pagani *et al.*, 1986). With non parametric methods, the VLF component requires longer data series ($>$ 5 min) to be accurately estimated (Leite *et al.*, 2007) and it was not considered in the analysis. The power of each series in each frequency band $\mathrm{B} = \{\mathrm{LF},\mathrm{HF}\}$

was computed from the PSD area in the frequency band B, i.e.,

$$\mathcal{P}^{\mathrm{B}} = \int_{f \in \mathrm{B}} \hat{S}_{xx}(f) df, \tag{5.14}$$

and expressed in squared units of each series $x = \{\mathrm{RR,SBP,RESP,MSNA}\}$. The LF and HF power components can also be measured in normalized units (nu), obtained by dividing the power of each component $\mathrm{B} = \{\mathrm{LF,HF}\}$ by the total power subtracted by the VLF power and multiplying by 100, i.e.,

$$\mathcal{P}^{\mathrm{B},nu} = \frac{\mathcal{P}^{\mathrm{B}}}{\mathcal{P}^{\mathrm{TF}} - \mathcal{P}^{\mathrm{VLF}}} \times 100. \tag{5.15}$$

This normalization emphasizes the balance between the two branches of the ANS, with the LF band being more associated to sympathetic activity and HF band being more associated with parasympathetic activity (Task Force of ESC & NASPE, 1996). Also, this normalization reduces the limitation that the acquired RESP and MSNA signals are not calibrated.

5.2.2 Frequency domain BRS estimators

The methods proposed for the estimation of a frequency domain BRS value (α) were already overviewed in Sec. 1.3.3. In this section, the Transfer Function Method (Robbe *et al.*, 1987) and the Alpha Technique (Pagani *et al.*, 1988) will be detailed. These frequency domain BRS methods assume an open-loop relation between SBP and RR (being SBP the input and RR the output of the system), similarly to the time domain BRS methods. Both types of methods cannot distinguish between negative and positive feedback components, neither can account for the influence of respiration in the SBP and RR coupling (see Fig. 1.4).

5.2.2.1 BRS estimate from the Transfer Function Method

The BRS estimate obtained by the transfer function method was first described as the average of the $|\mathcal{H}(f)|$ values, at the frequency values exhibiting a minimum degree of linear coupling (Robbe *et al.*, 1987), i.e.,

$$\hat{\alpha} = \overline{|\mathcal{H}(f)|}, \quad f: \; |\mathcal{K}(f)|^2 \geq \kappa. \tag{5.16}$$

To guarantee a relevant coupling between SBP and RR series, and consequently a meaningful BRS value, a threshold level κ in the coherence function is usually considered. In this work, $\kappa = 0.5$ was considered, following previous frequency BRS studies (Robbe *et al.*, 1987).

As illustrated in Fig. 5.3, the SBP and RR series show a high correlation typically around 0.1 Hz (LF band) and around the respiratory frequency of that subject (see Fig. 5.2(c)).

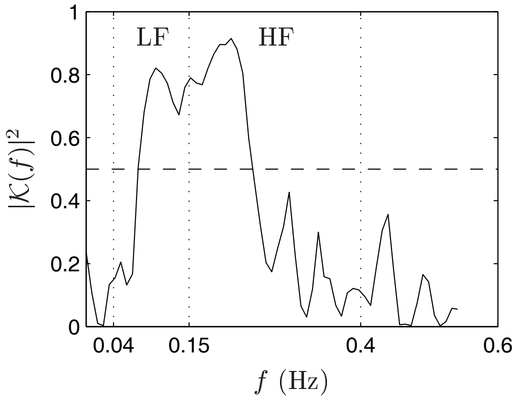

Figure 5.3: Squared Coherence magnitude ($|\mathcal{K}(f)|^2$) between SBP and RR, based on Welch method. The dashed line identifies the threshold level for a significant coherence. Same data as in Fig. 5.1.

The magnitude and phase of $\mathcal{H}(f)$ is presented in Fig. 5.4. It can be observed that the $\mathcal{H}(f)$ phase is more stable for the frequencies exhibiting very high $|\mathcal{K}(f)|^2$ values. The phase function indicates if the changes in the two series can be considered synchronous in each frequency band. Also, it allows to access the lag for which their coupling is higher. Within the LF band, a negative phase is observed, which can be interpreted as a baroreflex effect, once SBP changes induce RR changes with a determined time delay. The approximately zero phase at the HF band expresses a zero time lag between the two series, indicating that their changes in this frequency band are synchronous.

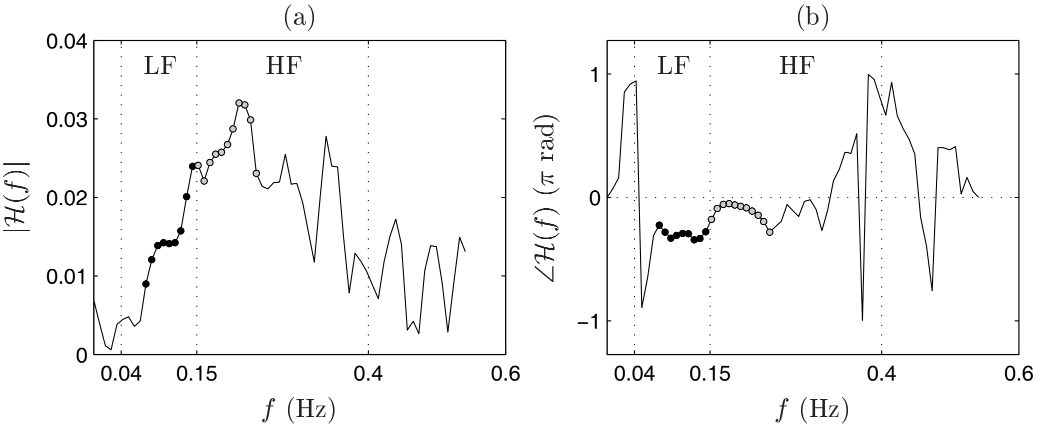

Figure 5.4: Transfer Function magnitude (a) and phase (b) between SBP and RR, based on Welch method. The black and grey circles identify the frequencies with $|\mathcal{K}(f)|^2 \geq 0.5$ in LF and HF bands, respectively. Same data as in Fig. 5.3.

In order to distinguish the SBP and RR interactions due to the baroreflex and the respiratory activity, the BRS estimate from the transfer function method is computed in the frequency bands B = {LF,HF}. In experimental data with HF respiration, the α^{LF} can be considered as a BRS measure avoiding the respiratory influence, while the α^{HF} evaluate the BRS response to SBP oscillations specifically associated to respiration.

Overall frequency BRS estimates have also been proposed to quantify the BRS function across the entire frequency range, e.g., the average of the $\hat{\alpha}^{\mathrm{LF}}$ and $\hat{\alpha}^{\mathrm{HF}}$ values (Pitzalis *et al.*, 1998*a*). In this work, a frequency BRS estimate computed in the total frequency (TF) range was also considered: the $\hat{\alpha}^{\mathrm{TF}}$ is estimated in the same way as $\hat{\alpha}^{\mathrm{LF}}$ and $\hat{\alpha}^{\mathrm{HF}}$, but considering the entire frequency range instead of B = {LF,HF} bands.

5.2.2.2 BRS estimate from the Alpha Technique

A simplified approach to compute a frequency BRS value has been proposed by the Alpha technique (Pagani *et al.*, 1988). The BRS estimate is obtained as the square root of the ratio between the RR and SBP spectral powers, i.e.,

$$\hat{\alpha}^{\mathrm{B}} = \sqrt{\frac{\mathcal{P}^{\mathrm{B}}_{\mathrm{RR}}}{\mathcal{P}^{\mathrm{B}}_{\mathrm{SBP}}}} \tag{5.17}$$

with B = {LF,HF} and considering the frequency values in which the coherence is above 0.5. Figure 5.5 shows the RR and SBP spectra highlighting the areas used for the computation of α by the Alpha technique.

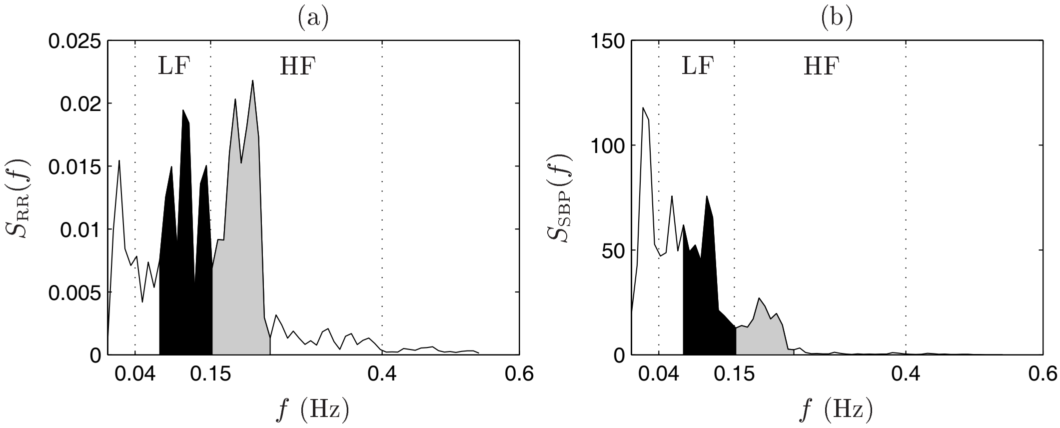

Figure 5.5: Spectra of RR and SBP series based on Welch method. The black and grey areas indicate the frequencies with $|\mathcal{K}(f)|^2 \geq 0.5$ in LF and HF bands, respectively. Same data as in Fig. 5.1.

Previous comparisons between frequency BRS methods have pointed out that the Transfer Function method provides lower BRS estimates in comparison with the Alpha Technique, and the BRS estimates obtained by the two methods exhibit more differences when computed for frequencies presenting lower levels of coherence (Barbieri and Saul, 1999). Nevertheless, because both methods provide correlated BRS estimates, only one of them was used in this thesis to compute a frequency BRS estimate. The choice was naturally for the Transfer Function method, because a transfer function is basically a (linear) way of describing a relationship between an system input and output and, therefore, the mean of the transfer function amplitudes (Eq. 5.16) holds more methodological similarities with the slope in regression analysis than the BRS estimate obtained from the Alpha technique (Eq. 5.17).

5.3 Results

The experimental data consists of the spontaneous recordings from the SP/NT/PH dataset, described in Sec. 4.3.1, and spontaneous recordings from the EuroBaVar dataset, described in Sec. 3.2. The SP/NT/PH recordings were used to compare the frequency BRS estimates from the LF and HF bands with the time BRS estimates from BSs and BEs. These recordings were also used to estimate the indicative cutoff value to define short and long BEs, by maximizing the correlations between time domain BRS estimates with MSNA measures. The EuroBaVar recordings were used to further explore the ability of the time and frequency BRS methods to discriminate Lying from Standing positions, including the time domain BRS estimates from short and long BEs.

As previously, in a dispersion diagram representing x versus y, the percentage $\mathcal{C}$ defined as the ratio $\#(x > y)/\#x$ where $\#$ indicates the counting numbers, is indicated at the lower right corner of the figure. If justified, the correlation between the x and y values (r) is also presented at the top of each dispersion diagram, as well as the number of values (n). The cases of statistical significance level (fixed for $p < 0.05$) are indicated with the symbol *.

5.3.1 Frequency and time domain BRS estimates

Figure 5.6(a) presents the dispersion diagram of $\hat{\alpha}^{\mathrm{LF}}$ and $\hat{\alpha}^{\mathrm{HF}}$ values, showing that there are subjects exhibiting similar $\hat{\alpha}^{\mathrm{LF}}$ and $\hat{\alpha}^{\mathrm{HF}}$ values, and subjects exhibiting $\hat{\alpha}^{\mathrm{HF}}/\hat{\alpha}^{\mathrm{LF}} > 1.5$. As illustrated in Fig. 5.6(b), the subjects with the highest differences between $\hat{\alpha}^{\mathrm{LF}}$ and $\hat{\alpha}^{\mathrm{HF}}$ also present the highest differences between $\hat{\mathcal{B}}^{\mathrm{E}}_{\mathrm{G,O}}$ and $\hat{\mathcal{B}}^{\mathrm{S}}_{\mathrm{G,O}}$. This result indicates that $\hat{\mathcal{B}}^{\mathrm{E}}_{\mathrm{G,O}}$ and $\hat{\mathcal{B}}^{\mathrm{S}}_{\mathrm{G,O}}$ can be measuring different aspects of the BRS function, such as the $\hat{\alpha}^{\mathrm{LF}}$ and $\hat{\alpha}^{\mathrm{HF}}$ values.

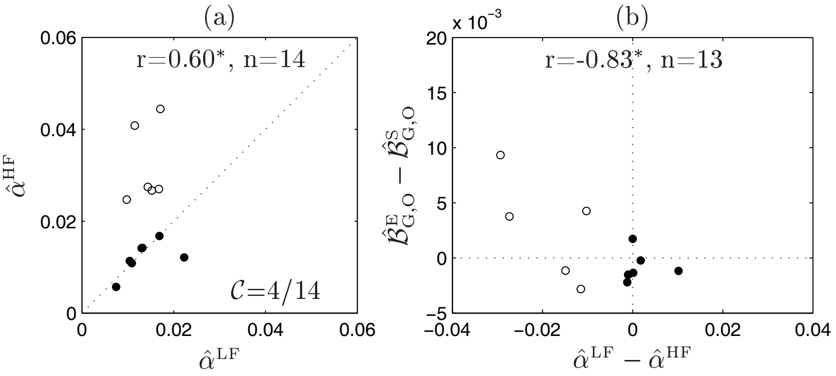

Figure 5.6: Dispersion diagrams comparing (a) $\hat{\alpha}^{\mathrm{LF}}$ with $\hat{\alpha}^{\mathrm{HF}}$ and comparing (b) their differences with the differences between $\hat{\mathcal{B}}^{\mathrm{E}}_{\mathrm{G,O}}$ and $\hat{\mathcal{B}}^{\mathrm{S}}_{\mathrm{G,O}}$. Results for the SP/PH/NT recordings.

Figure 5.7 shows the comparison between time and frequency domain BRS estimates. As illustrated in Figs. 5.7(a,d), the $\hat{\alpha}^{\mathrm{TF}}$ values are more correlated with the $\hat{\mathcal{B}}^{\mathrm{E}}_{\mathrm{G,O}}$ values than with the $\hat{\mathcal{B}}^{\mathrm{S}}_{\mathrm{G,O}}$ values. The results obtained for BSs (Figs. 5.7(b,c)) corroborate that the $\hat{\mathcal{B}}^{\mathrm{S}}_{\mathrm{G,O}}$ values are more correlated with the $\hat{\alpha}^{\mathrm{HF}}$ values rather than with $\hat{\alpha}^{\mathrm{LF}}$ (Watkins *et al.*, 1996; Persson *et al.*, 2001). Similarly, the results obtained for BEs (Figs. 5.7(e,f)) indicate that the $\hat{\mathcal{B}}^{\mathrm{E}}_{\mathrm{G,O}}$ values are more correlated with $\hat{\alpha}^{\mathrm{HF}}$ than with $\hat{\alpha}^{\mathrm{LF}}$. Finally, the BRS estimates from BEs are more correlated with the spectral estimates (regardless of the frequency band they are computed from), in comparison with the BRS estimates from BSs.

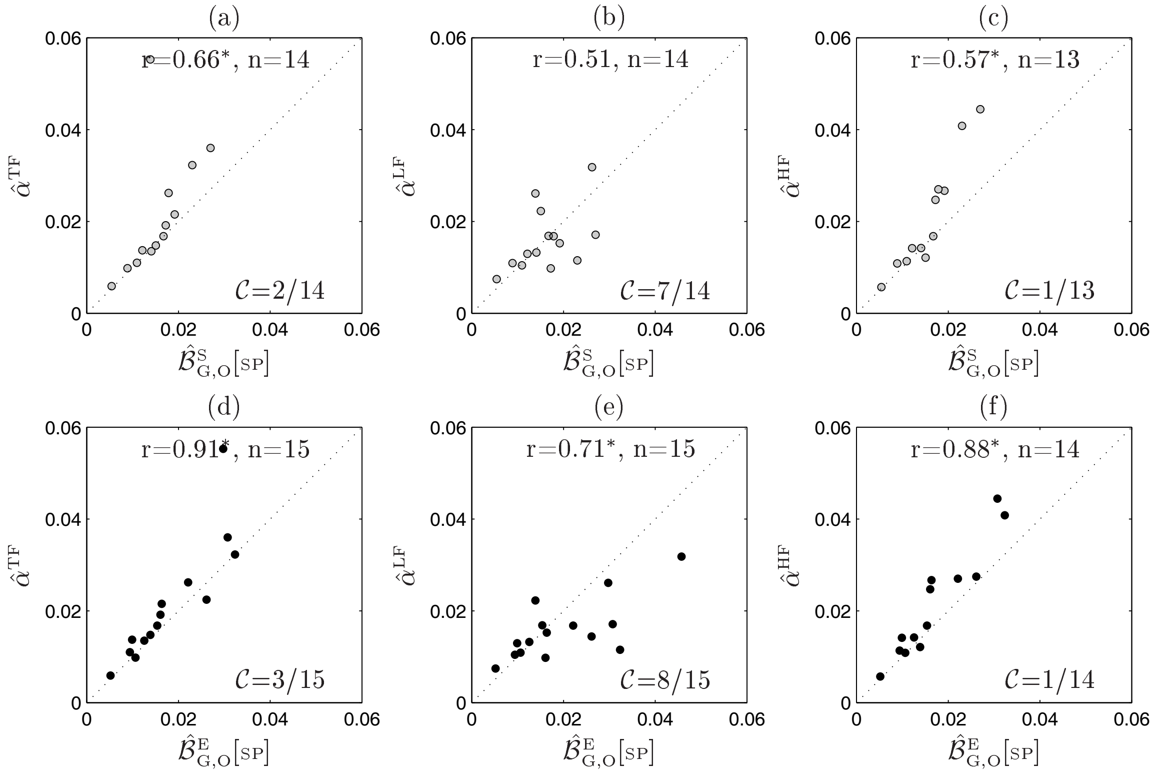

Figure 5.7: Dispersion diagrams comparing $\hat{\mathcal{B}}_{\mathrm{G,O}}$ evaluated from BSs and from BEs, and $\hat{\alpha}$ evaluated in TF, LF and HF bands. Results for the SP/PH/NT recordings.

Figure 5.7 also shows that the subjects with low $\hat{\mathcal{B}}^{\mathrm{E}}_{\mathrm{G,O}}$ values have similar $\hat{\alpha}^{\mathrm{LF}}$ and $\hat{\alpha}^{\mathrm{HF}}$ values, while the subjects with high $\hat{\mathcal{B}}^{\mathrm{E}}_{\mathrm{G,O}}$ values exhibit the highest differences between the $\hat{\alpha}^{\mathrm{LF}}$ and $\hat{\alpha}^{\mathrm{HF}}$ values. As a matter of fact, for the 7/15 files exhibiting $\hat{\alpha}^{\mathrm{HF}}/\hat{\alpha}^{\mathrm{LF}} > 1.5$, 7 out of the 7 subjects presented $\hat{\alpha}^{\mathrm{LF}} < \hat{\mathcal{B}}^{\mathrm{E}}_{\mathrm{G,O}} < \hat{\alpha}^{\mathrm{HF}}$. On one hand, $\hat{\alpha}^{\mathrm{HF}}/\hat{\alpha}^{\mathrm{LF}} > 1.5$ indicates that the parasympathetic and sympathetic contributions to the BRS response in those subjects are not similar and, on the other hand, $\hat{\alpha}^{\mathrm{LF}} < \hat{\mathcal{B}}^{\mathrm{E}}_{\mathrm{G,O}} < \hat{\alpha}^{\mathrm{HF}}$ indicates that $\hat{\mathcal{B}}^{\mathrm{E}}_{\mathrm{G,O}}$ is a measure that accounts for both ANS contributions.

Table 5.1 resumes the measures obtained from the analysis of the RR, SBP, MSNA and RESP series, for all subjects of the dataset and distinguishing the subjects exhibiting $\hat{\alpha}^{\mathrm{LF}} \approx \hat{\alpha}^{\mathrm{HF}}$ (group gA) from the subjects presenting $\hat{\alpha}^{\mathrm{HF}}/\hat{\alpha}^{\mathrm{HF}} > 1.5$ (group gB).

Group gB exhibit higher $\bar{x}_{\mathrm{RR}}(n)$ mean values, together with lower $\mathcal{P}^{\mathrm{LF}}_{\mathrm{RR}}$ and higher $\mathcal{P}^{\mathrm{HF}}_{\mathrm{RR}}$ mean values in comparison with group gA. The differences in the RR power distribution over frequency bands is enhanced for the normalized variables $\mathcal{P}^{\mathrm{LF},nu}_{\mathrm{RR}}$ and $\mathcal{P}^{\mathrm{HF},nu}_{\mathrm{RR}}$: in mean, 61,6% and 35,3% of the RR power is respectively distributed over the LF and HF bands, for the group gA, whereas for the group gB the average percentages are 36,9% and 60,8%. The SBP power distribution over frequency bands indicates that the SBP power is mainly on the LF band, for both groups. Nevertheless, group gB have the tendency to present higher $\mathcal{P}^{\mathrm{LF},nu}_{\mathrm{SBP}}$ and lower $\mathcal{P}^{\mathrm{HF},nu}_{\mathrm{SBP}}$ mean values in comparison with the group gA. Finally, all subjects exhibit more MSNA and RESP power in the HF rather than in the LF band, with group gB having the tendency to exhibit higher $\mathcal{P}^{\mathrm{HF},nu}_{\mathrm{MSNA}}$ and $\mathcal{P}^{\mathrm{HF},nu}_{\mathrm{RESP}}$ mean values in comparison with group gA.

Regarding the BRS estimates, $\hat{\alpha}^{\mathrm{TF}}$ is increased for group gB, mainly due to the increased $\hat{\alpha}^{\mathrm{HF}}$ values in comparison with that for group gA. The time domain BRS estimates $\hat{\mathcal{B}}_{\mathrm{G,O}}$ have the same tendency as the $\hat{\alpha}^{\mathrm{TF}}$ values between groups. Group gB exhibits lower N and K mean values in comparison with group gA, because gB recordings present shorter length in beats. Also, shorter BEs were identified for the subjects in group gB.

In summary, the results presented in Table 5.1 show that the different subjects evaluated in spontaneous condition exhibit different patterns. In particular, the higher $\mathcal{P}^{\mathrm{HF},nu}_{\mathrm{RR}}$ and the lower $\mathcal{P}^{\mathrm{HF},nu}_{\mathrm{SBP}}$ mean values are associated with higher $\bar{x}_{\mathrm{RR}}(n)$ mean values (group gB). Also, gB group presents higher $\hat{\alpha}^{\mathrm{HF}}$ and $\hat{\mathcal{B}}_{\mathrm{G,O}}$ mean values, pointing out increased parasympathetic activity for these subjects.

Different patterns can also be observed regarding the length of the identified BEs. As shown in Table 5.1, group gB exhibits BEs with shorter length in comparison with BEs identified for group gA, evidencing that the identification of shorter BEs can be related with increased parasympathetic activity.

Table 5.1: Variables extracted from spectral analysis of the RR, SBP, RESP and MSNA series and from BRS analysis. Mean±Std values for all subjects of the dataset (n=15) and distinguishing the subjects exhibiting $\hat{\alpha}^{\mathrm{LF}} \approx \hat{\alpha}^{\mathrm{HF}}$ (group gA, n=8) and $\hat{\alpha}^{\mathrm{HF}}/\hat{\alpha}^{\mathrm{HF}} > 1.5$ (group gB, n=7). The $\mathcal{P}_{\mathrm{RR}}$ values are presented in $10^3 sec^2$ units.

	All subjects	Group gA	Group gB
$\bar{x}_{\mathrm{RR}}$	0.96±0.16	0.89±0.15	1.05±0.14
$\mathcal{P}_{\mathrm{RR}}^{\mathrm{TF}}$	3.42±2.49	3.30±3.27	3.56±1.39
$\mathcal{P}_{\mathrm{RR}}^{\mathrm{VLF}}$	0.79±0.41	0.71±0.33	0.89±0.49
$\mathcal{P}_{\mathrm{RR}}^{\mathrm{LF}}$	1.16±1.04	1.33±1.34	0.96±0.59
$\mathcal{P}_{\mathrm{RR}}^{\mathrm{HF}}$	1.41±1.57	1.18±2.04	1.67±0.88
$\mathcal{P}_{\mathrm{RR}}^{\mathrm{LF},nu}$	50.1±19.8	61.6±17.9	36.9±12.6
$\mathcal{P}_{\mathrm{RR}}^{\mathrm{HF},nu}$	47.2±19.8	35.3±17.1	60.8±13.1
$\bar{x}_{\mathrm{SBP}}$	125.6±14.9	132.9±12.7	117.3±13.6
$\mathcal{P}_{\mathrm{SBP}}^{\mathrm{TF}}$	17.7±7.9	15.2±6.6	20.6±8.8
$\mathcal{P}_{\mathrm{SBP}}^{\mathrm{VLF}}$	9.6±6.0	7.4±4.7	12.0±6.7
$\mathcal{P}_{\mathrm{SBP}}^{\mathrm{LF}}$	6.3±3.5	5.4±2.3	7.4±4.5
$\mathcal{P}_{\mathrm{SBP}}^{\mathrm{HF}}$	1.6±1.6	2.1±2.0	1.1±0.8
$\mathcal{P}_{\mathrm{SBP}}^{\mathrm{LF},nu}$	78.4±13.9	71.3±15.3	86.4±6.1
$\mathcal{P}_{\mathrm{SBP}}^{\mathrm{HF},nu}$	19.6±12.1	25.2±13.6	13.2±5.9
$\mathcal{P}_{\mathrm{MSNA}}^{\mathrm{LF},nu}$	28.0±7.1	25.9±8.4	30.5±4.7
$\mathcal{P}_{\mathrm{MSNA}}^{\mathrm{HF},nu}$	53.1±10.1	48.8±9.6	58.0±8.9
$\mathcal{P}_{\mathrm{RESP}}^{\mathrm{LF},nu}$	14.1±11.2	17.4±12.4	10.4±9.3
$\mathcal{P}_{\mathrm{RESP}}^{\mathrm{HF},nu}$	80.4±12.8	73.9±12.5	87.9±8.8
$\hat{\alpha}^{\mathrm{TF}}$	25.9±21.7	21.9±27.7	30.4±12.5
$\hat{\alpha}^{\mathrm{LF}}$	15.8±6.6	15.7±7.9	15.8±5.3
$\hat{\alpha}^{\mathrm{HF}}$	24.5±16.7	12.2±3.5	36.9±15.4
$\hat{\mathcal{B}}_{\mathrm{G,O}}^{\mathrm{S}}$	16.2±6.20	13.7±6.2	19.7±4.6
r^{S}	0.86±0.09	0.89±0.05	0.83±0.12
N^{S}	57.6±44.8	67.3±39.1	44.7±52.2
K^{S}	17.8±13.3	20.8±11.8	13.8±15.3
$N^{\mathrm{S}}/K^{\mathrm{S}}$	3.18±0.17	3.21 ±0.17	3.13±0.18
$\hat{\mathcal{B}}_{\mathrm{G,O}}^{\mathrm{E}}$	19.7±11.1	15.3±12.7	24.8± 6.7
r^{E}	0.73±0.07	0.74±0.07	0.72±0.08
N^{E}	159.2±93.3	201.6±93.7	110.7±70.1
K^{E}	33.8±12.9	37.9±13.0	29.1±12.0
$N^{\mathrm{E}}/K^{\mathrm{E}}$	4.48±1.80	5.25±2.07	3.60±0.95

Figure 5.8 presents the distribution of the BSs and BEs number, as a function of the segment length. Subjects gA present more BEs than subjects gB and the groups exhibit differences in the BEs number distribution. As illustrated in Fig. 5.8(b), subjects from group gB exhibit more BEs in the class between 2.5 and 3.5 seconds in comparison with subjects from group gA. Also, subjects from group gA exhibit higher dispersion in the BEs length, with all gA

subjects exhibiting at least one BEs in all classes. As a matter of fact, the $\bar{x}_{\mathrm{RR}}(n)$ values were found to be correlated with the standard deviation of the BEs length (r = −0.66, p = 0.007, n = 15), indicating that the subjects with higher $\bar{x}_{\mathrm{RR}}(n)$, i.e. the subjects from group gB, tend to have lower standard deviation of the BEs length.

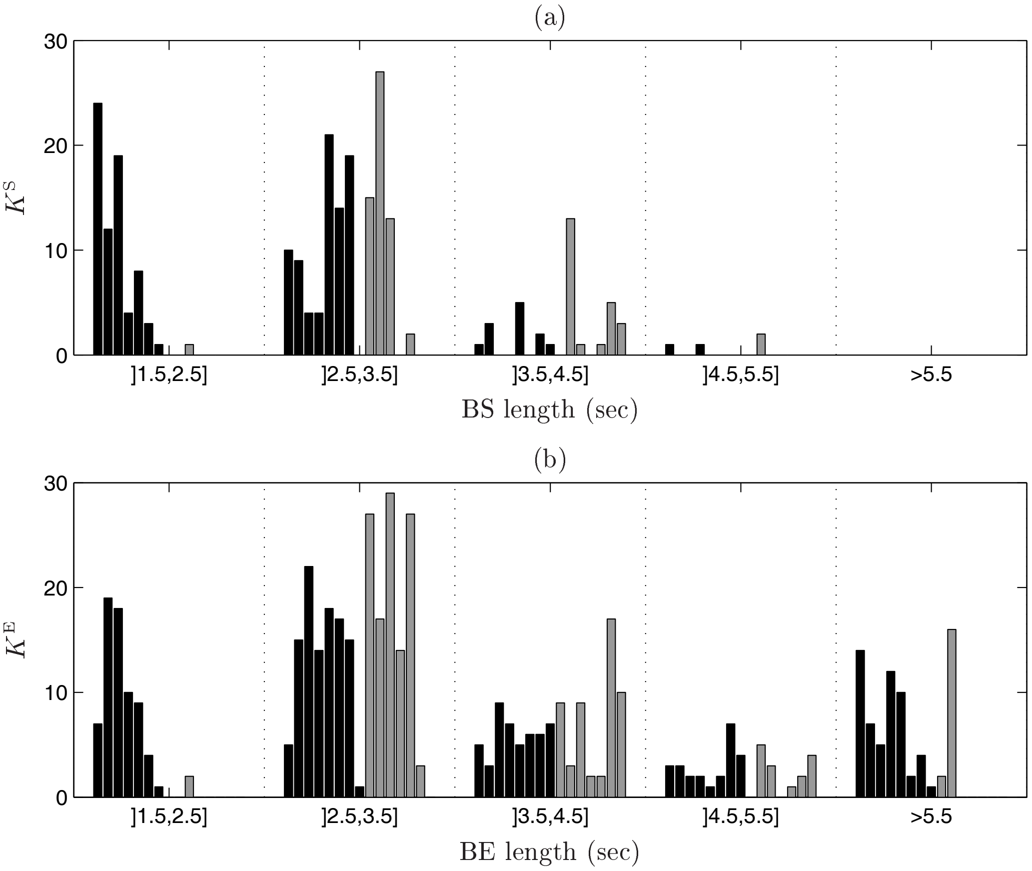

Figure 5.8: Barplot of the BSs and BEs number (K) per segment length (dividing the scale in classes of 1 sec). Each bar corresponds to one SP/PH/NT subject, distinguishing subjects from groups gA and gB (black/grey). The subjects are sorted by increasing $\bar{x}_{\mathrm{RR}}(n)$ value.

The results displayed in Fig. 5.8 are in accordance with the fact that the subjects from group gB exhibit an increased parasympathetic activity and a higher BRS estimate in the HF band in comparison with the subjects with group gA (Table 5.1). The vagal activity influences the RR in a faster way than the sympathetic activity and, therefore, short BEs are expected to reflect predominantly parasympathetic activity. As the subjects from group gA also exhibit long BEs (longer than those of the subjects from group gB) and, therefore, long BEs may reflect the sympathetic activity of the subject. In order to further investigate the ability of short and long BEs to capture parasympathetic and sympathetic activities, respectively, indicative cutoff values to define short and long BEs have to be estimated.

5.3.2 Cutoff to define short and long baroreflex events

To determine an indicative cutoff value to define short and long BEs, the time and frequency BRS estimates were first compared with the amount of sympathetic activity, measured from the MSNA series.

Figure 5.9 shows the dispersion diagrams between the BRS estimates and the MSNA power in each frequency band. As presented in Fig. 5.9(a–c), the $\hat{\alpha}^{\mathrm{LF}}$, $\hat{\mathcal{B}}^{\mathrm{S}}_{\mathrm{G,O}}$ and $\hat{\mathcal{B}}^{\mathrm{E}}_{\mathrm{G,O}}$ values are not significantly correlated with the $\mathcal{P}^{\mathrm{LF},nu}_{\mathrm{MSNA}}$ values. On the contrary, as presented in Fig. 5.9(d–f), the $\hat{\alpha}^{\mathrm{HF}}$, $\hat{\mathcal{B}}^{\mathrm{S}}_{\mathrm{G,O}}$ and $\hat{\mathcal{B}}^{\mathrm{E}}_{\mathrm{G,O}}$ values are significantly correlated with the $\mathcal{P}^{\mathrm{HF},nu}_{\mathrm{MSNA}}$ values. Regarding the frequency BRS estimates, the $\hat{\alpha}^{\mathrm{LF}}$ values were not significantly correlated with the $\mathcal{P}^{\mathrm{LF},nu}_{\mathrm{MSNA}}$ values ($\mathrm{r} = 0.46$, $\mathrm{p} = 0.09$, $\mathrm{n} = 15$). However, the $\hat{\alpha}^{\mathrm{LF}}$ values were found to be correlated with $\mathcal{P}^{\mathrm{LF}}_{\mathrm{RR}}$ ($\mathrm{r} = 0.55$, $\mathrm{p} = 0.03$, $\mathrm{n} = 15$) and with the $\mathcal{P}^{\mathrm{HF}}_{\mathrm{RR}}$ values ($\mathrm{r} = 0.81$, $\mathrm{p} = 0.0002$, $\mathrm{n} = 15$). Furthermore, the $\mathcal{P}^{\mathrm{LF}}_{\mathrm{RR}}$ and $\mathcal{P}^{\mathrm{HF}}_{\mathrm{RR}}$ values were not correlated ($\mathrm{r} = 0.42$, $\mathrm{p} = 0.12$, $\mathrm{n} = 15$). The results obtained support that $\hat{\alpha}^{\mathrm{LF}}$ is a measure considering both sympathetic and parasympathetic ANS contributions (Task Force of ESC & NASPE, 1996). Finally, the $\hat{\alpha}^{\mathrm{HF}}$ values were found to be significantly correlated with $\mathcal{P}^{\mathrm{HF}}_{\mathrm{RR}}$ ($\mathrm{r} = 0.81$, $\mathrm{p} = 0.0005$, $\mathrm{n} = 14$) and not significantly correlated with $\mathcal{P}^{\mathrm{LF}}_{\mathrm{RR}}$ ($\mathrm{r} = -0.09$, $\mathrm{p} = 0.73$, $\mathrm{n} = 14$), providing evidence that $\hat{\alpha}^{\mathrm{HF}}$ is a measure related with parasympathetic modulation and not with sympathetic modulation.

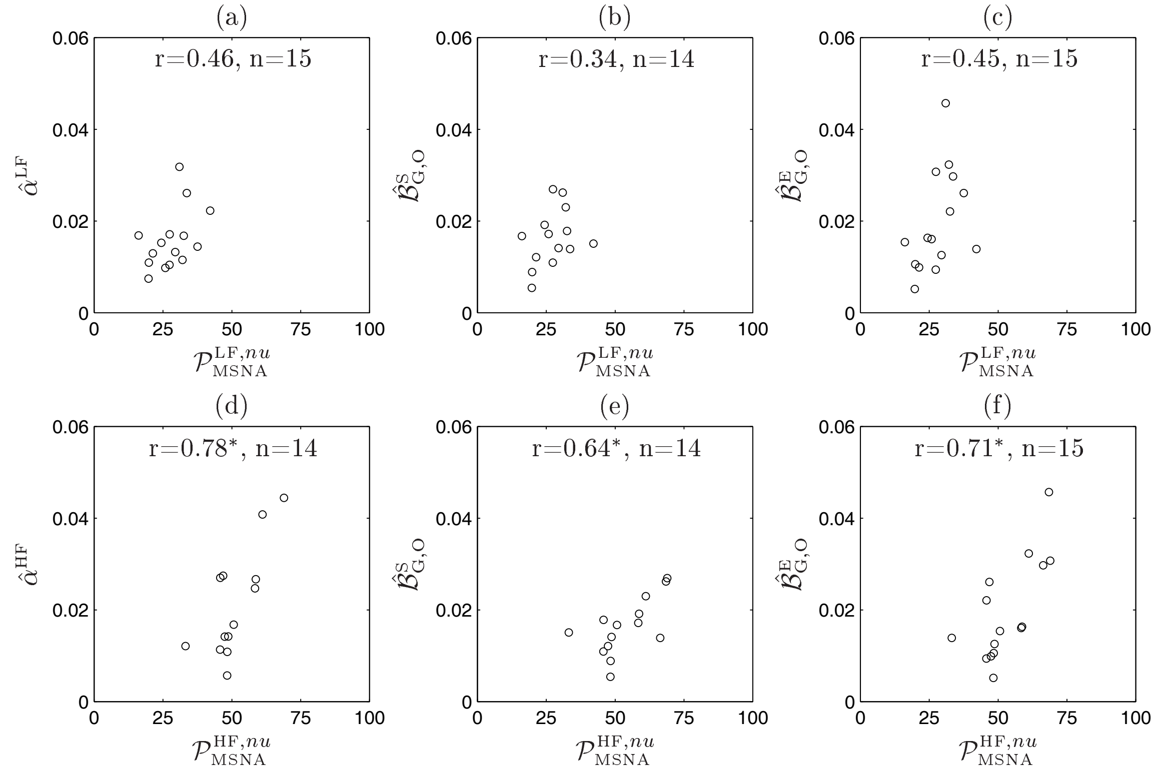

Figure 5.9: Dispersion diagrams between BRS estimates and sympathetic activity, quantified from the normalized MSNA power distribution in $\mathrm{B} = \{\mathrm{LF},\mathrm{HF}\}$ bands ($\mathcal{P}^{\mathrm{B},nu}_{\mathrm{MSNA}}$).

Figure 5.9 also shows that time domain BRS estimates are correlated with $\mathcal{P}^{\mathrm{HF},nu}_{\mathrm{MSNA}}$ and not with $\mathcal{P}^{\mathrm{LF},nu}_{\mathrm{MSNA}}$. This result indicates that time domain BRS estimates are measures predominantly of parasympathetic activity and is in accordance with the fact that time domain BRS estimates are more correlated with $\hat{\alpha}^{\mathrm{HF}}$ rather than with $\hat{\alpha}^{\mathrm{LF}}$ (Fig. 5.7).

Indicative cutoff to define short and long BEs: adjusted to each subject

The BRS analysis from BEs can be advantageous in comparison with the BRS analysis from BSs, because BEs are in larger number and some of the BEs are longer than BSs (Fig. 5.8). Therefore, BRS analysis from BEs is more likely to also capture the sympathetic modulation than BSs.

In order to perform the BRS analysis from short and long segments, the cutoff length c to define a *short* and a *long* BE must be estimated. Then, two distinct BRS estimates can be obtained: a $\hat{\mathcal{B}}^{\mathrm{E},\leq c}_{\mathrm{G,O}}$ value estimated from BEs with length shorter than c and a $\hat{\mathcal{B}}^{\mathrm{E},>c}_{\mathrm{G,O}}$ value estimated from BEs with length longer than c.

The c value is expected to change for different subjects and conditions, because the sympathetic and parasympathetic modulations are known to be different for different subjects (Table 5.1) and for different conditions (e.g., Lying from Standing positions). Therefore, an optimal cutoff adjusted for each subject was considered. Intuitively, the cutoff was first considered as a function of the BSs length in each recording, with a BE shorter than the BSs identified in a recording being considered as *short*, and a BE longer than the BSs considered as *long*. However, it is known that the BSs length is directly related with the length of the inspirations and expiration phases in the respiratory cycle, with typical duration of 3 to 6 cardiac beats (Rothlisberger *et al.*, 2003). Therefore, the length of a breathing cycle can be used as a majorant for the BSs length and it can be estimated from the respiratory frequency f_r of the subject, as $1/f_r$. In this work, the f_r value for each subject was estimated from the RESP series with the methods described in Sec. 2.3.1. Briefly, f_r was taken as the central frequency of the spectral component with highest variance from the RESP parametric spectrum.

Figure 5.10 shows the distribution of the BSs and BEs number, distinguishing the segments shorter and longer than a respiratory cycle. As illustrated in Fig. 5.10(a), BSs are segments typically shorter than one respiratory cycle. Because BEs are identified without being restricted to be SBP and RR ramps over time, these segments can be longer than the length of a respiratory cycle. Figure 5.10(b) illustrates that there are BEs of the same length of BSs. Additionally, there BEs longer than BSs, with duration longer than one respiratory cycle. Therefore, because BSs are shorter than one respiratory cycle and BEs can be either shorter or longer than one respiratory cycle, the length of the respiratory cycle can be used as an indicative cutoff value to define short and long BEs.

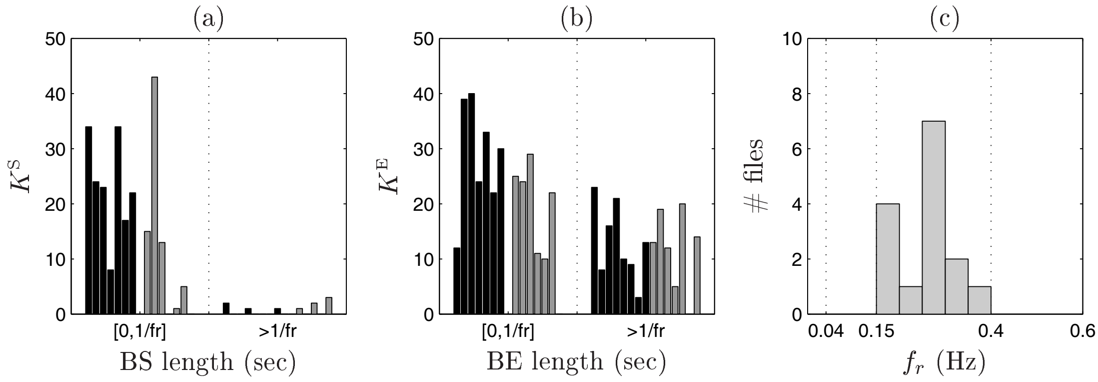

Figure 5.10: Barplot of the BSs and BEs number (K) per segment length (segments shorter and longer than f_r). Each bar corresponds to one SP/PH/NT subject, distinguishing subjects from groups gA and gB (black/grey). The subjects are sorted by increasing $\bar{x}_{\mathrm{RR}}(n)$ value.

Figure 5.11 presents the dispersion diagrams between the MSNA powers per frequency band and the BRS estimates from short and long BEs, defined from the indicative cutoff of $1/f_r$ sec adjusted to each subject. It can be observed that, on one hand, the $\hat{\mathcal{B}}_{\mathrm{G,O}}^{\mathrm{E},>1/f_r}$ values are significantly correlated with the $\mathcal{P}_{\mathrm{MSNA}}^{\mathrm{LF},n}$ and not significantly correlated with the $\mathcal{P}_{\mathrm{MSNA}}^{\mathrm{HF},n}$. On the other hand, the $\hat{\mathcal{B}}_{\mathrm{G,O}}^{\mathrm{E},\leq 1/f_r}$ values are significantly correlated with the $\mathcal{P}_{\mathrm{MSNA}}^{\mathrm{HF},n}$ values, but not significantly correlated with the $\mathcal{P}_{\mathrm{MSNA}}^{\mathrm{LF},n}$ values.

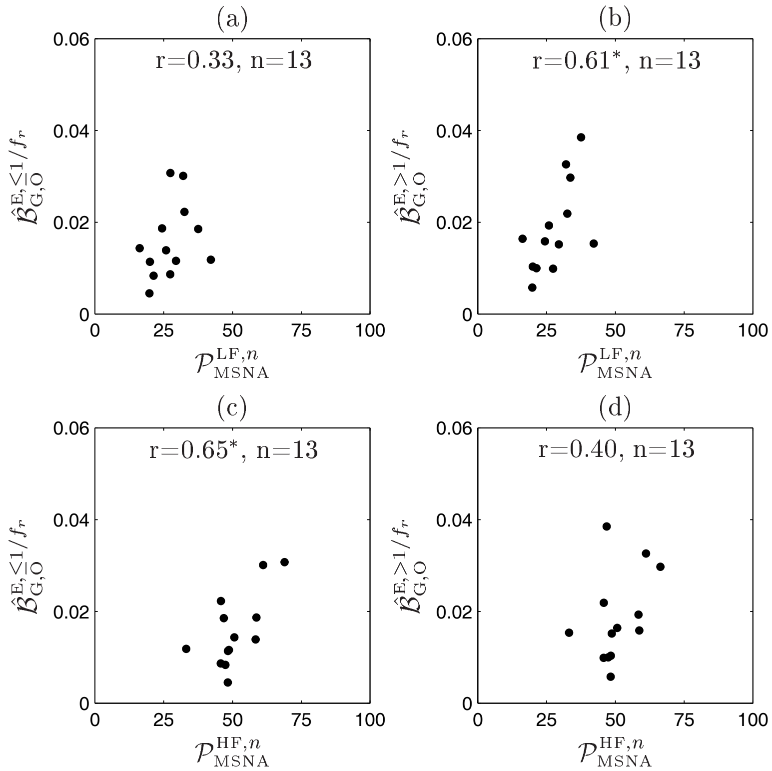

Figure 5.11: Dispersion diagrams between the MSNA powers per frequency band and the BRS estimates obtained from BEs shorter and longer than $1/f_r$ sec, with f_r indicating the respiratory frequency estimated for each subject.

Indicative cutoff to define short and long BEs: adjusted to a dataset

The use of f_r to estimate a cutoff value to define short and long BEs, demands for the acquisition of the respiratory signal or, at least, the use of signal processing techniques to derive the respiratory frequency from the ECG (Bailón *et al.*, 2006). Nevertheless, the BRS estimation, using the time and frequency domain methods explored in this thesis, implicitly assume that the SBP and RR series are acquired in stationary recording conditions. Consequently, it is also expected that the reference respiratory frequency f_r does not change significantly along the short recording. Moreover, in short recordings, it is not expected that many segments of several lengths would be identified, such that the BRS estimate would change significantly. Therefore, a constant cutoff value for all subjects was considered as an alternative to $1/f_r$ sec, with f_r being estimated for each subject.

In the SP/NT/PH dataset, a c value can be estimated to maximize the correlation between the $\hat{\alpha}^{\mathrm{LF}}$ and the $\hat{\mathcal{B}}^{\mathrm{E},>c}_{\mathrm{G,O}}$ values, or as to maximize the correlation between the $\hat{\alpha}^{\mathrm{HF}}$ and the $\hat{\mathcal{B}}^{\mathrm{E},\leq c}_{\mathrm{G,O}}$ values. An optimum c value could also be set as a trade-off between both correlations. However, because $\hat{\alpha}^{\mathrm{LF}}$ and $\mathcal{P}^{\mathrm{LF},nu}_{\mathrm{MSNA}}$ were not significantly correlated (Fig. 5.9(a)), the frequency BRS estimates were not considered to estimate an optimal c value for all subjects.

Alternatively, the c value was estimated from the correlations between the BRS estimates from short and long BEs with the MSNA powers computed at each frequency band. Specifically, the correlation between the $\hat{\mathcal{B}}^{\mathrm{E},>c}_{\mathrm{G,O}}$ and $\mathcal{P}^{\mathrm{LF},nu}_{\mathrm{MSNA}}$ values, and the correlation between the $\hat{\mathcal{B}}^{\mathrm{E},\leq c}_{\mathrm{G,O}}$ and $\mathcal{P}^{\mathrm{HF},nu}_{\mathrm{MSNA}}$ values should be maximized. Figure 5.12 shows these correlations as a function of c ($2 \leq c \leq 15$ sec). As illustrated in Fig. 5.12(a), the number of subjects exhibiting BEs shorter than c sec increase for increasing values of c, while the number of subjects exhibiting BEs longer than c sec decrease. Figure 5.12(b) shows the correlation between the $\hat{\mathcal{B}}^{\mathrm{E},>c}_{\mathrm{G,O}}$ and the $\mathcal{P}^{\mathrm{LF},nu}_{\mathrm{MSNA}}$ values, and the correlation between the $\hat{\mathcal{B}}^{\mathrm{E},\leq c}_{\mathrm{G,O}}$ and the $\mathcal{P}^{\mathrm{HF},nu}_{\mathrm{MSNA}}$ values. The optimal cutoff c should be taken as to maximize simultaneously the correlation between the $\hat{\mathcal{B}}^{\mathrm{E},>c}_{\mathrm{G,O}}$ and the $\mathcal{P}^{\mathrm{LF},nu}_{\mathrm{MSNA}}$ values, and the correlation between the $\hat{\mathcal{B}}^{\mathrm{E},>c}_{\mathrm{G,O}}$ and the $\mathcal{P}^{\mathrm{LF},nu}_{\mathrm{MSNA}}$ values. The optimum c value was estimated as the maximum of the product between these two correlations and it was estimated to be $c = 3.5$ sec, in the SP/NT/PH dataset.

In the SP/NT/PH dataset, the results obtained for the constant cutoff value of 3.5 sec are similar to those obtained for $1/f_r$ (and presented in Fig. 5.11). By one hand, the $\hat{\mathcal{B}}^{\mathrm{E},>3.5}_{\mathrm{G,O}}$ values are significantly correlated with the $\mathcal{P}^{\mathrm{LF},n}_{\mathrm{MSNA}}$ values (r = 0.55, p = 0.04, n = 14) and not significantly correlated with the $\mathcal{P}^{\mathrm{HF},n}_{\mathrm{MSNA}}$ values (r = 0.49, p = 0.08, n = 14). On the contrary, the $\hat{\mathcal{B}}^{\mathrm{E},\leq 3.5}_{\mathrm{G,O}}$ values are significantly correlated with the $\mathcal{P}^{\mathrm{HF},n}_{\mathrm{MSNA}}$ values (r = 0.66, p = 0.01, n = 13), but not significantly correlated with the $\mathcal{P}^{\mathrm{LF},n}_{\mathrm{MSNA}}$ values (r = 0.11, p = 0.72, n = 13).

The similarity of the results obtained for $1/f_r$ (adjusted to each subject) and 3.5 sec (constant for all subjects), evidences that 3.5 sec can be used as an indicative cutoff value to define short and long BEs, if there is no information about the respiratory information of the subject, e.g., the recordings of the EuroBaVar dataset.

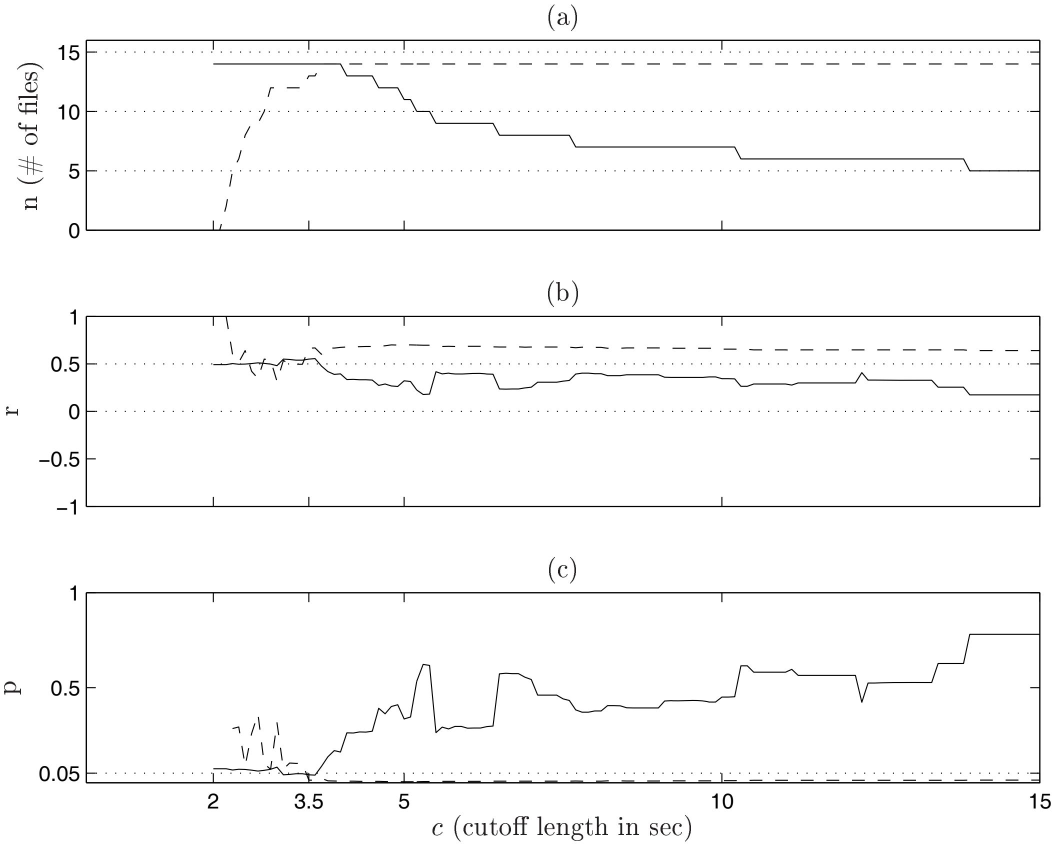

Figure 5.12: (a) Number of subjects with long/short BEs (solid/dashed), as a function of c. (b) Correlation between $\hat{\mathcal{B}}^{\mathrm{E},>c}_{\mathrm{G,O}}$ and $\mathcal{P}^{\mathrm{LF},nu}_{\mathrm{MSNA}}$ (solid), and between $\hat{\mathcal{B}}^{\mathrm{E},\leq c}_{\mathrm{G,O}}$ and $\mathcal{P}^{\mathrm{HF},nu}_{\mathrm{MSNA}}$ (dashed). (c) Corresponding p-values for the hypothesis of no correlation. Results from SP/NT/PH dataset.

5.3.3 BRS estimates from short/long BEs and L from S discrimination

The time and frequency BRS estimates were also compared with respect to the discrimination between Lying and Standing positions. This comparison was carried out with the EuroBaVar dataset files (paired Lying/Standing evaluations from 23 subjects), described in Sec. 3.2.

As previously remarked, the L to S ratio of $\bar{x}_{\mathrm{RR}}(n)$ is able to identify the posture changes in 22 out of the 23 subjects. This result indicates that the $\bar{x}_{\mathrm{RR}}(n)$ not only changes from subject to subject, but also changes when a specific subject is evaluated in different positions: $\bar{x}_{\mathrm{RR}}(n)$ for one subject is typically higher in Lying than in Standing position. Other variables also differ: from Lying to Standing position, $\mathcal{P}^{\mathrm{LF},n}_{\mathrm{RR}}$ increased and $\mathcal{P}^{\mathrm{HF},n}_{\mathrm{RR}}$ decreased ($p < 0.005$, $n = 23$), while $\mathcal{P}^{\mathrm{LF},n}_{\mathrm{SBP}}$ and $\mathcal{P}^{\mathrm{HF},n}_{\mathrm{SBP}}$ did not changed significantly ($p = 0.13$ and $p = 0.10$, respectively, $n = 23$). The results indicate that sympathetic modulation increases and parasympathetic modulation decreases, from Lying to Standing position.

As the EuroBaVar dataset do not include respiratory signals, it was not possible to estimate the respiratory frequency from the RESP series. Therefore, 3.5 sec was used as the indicative cutoff to define short and long BEs. Figure 5.13 illustrates that BSs are segments typically shorter than 3.5 sec, while there are BEs shorter and longer than 3.5 sec. Also, differences between the number of segments in Lying and Standing positions are not perceptible.

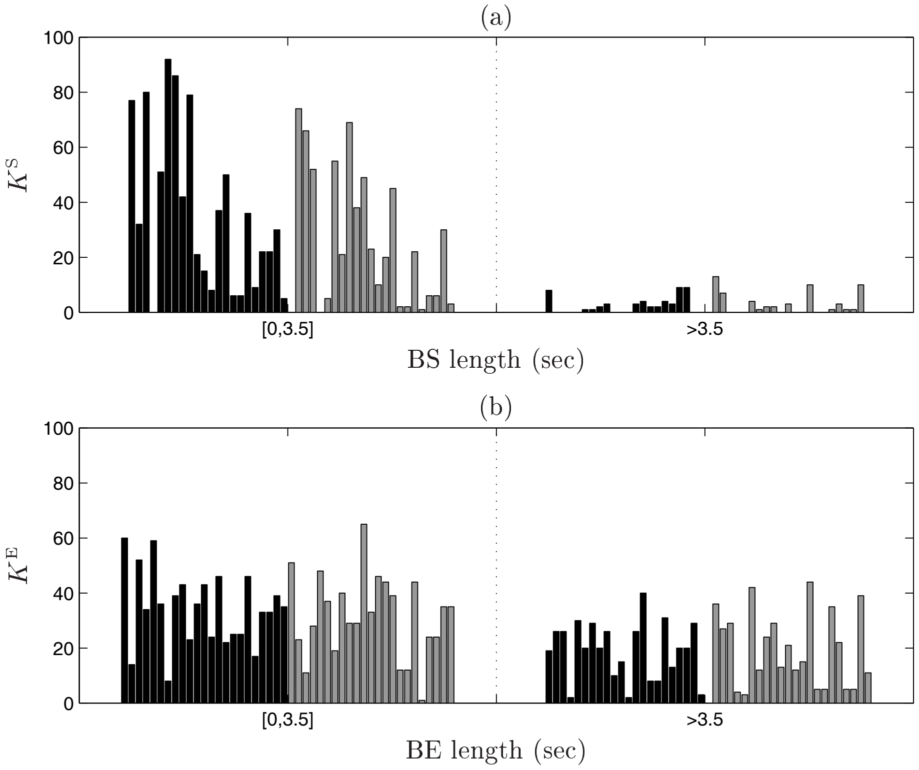

Figure 5.13: Barplot of the BSs and BEs number (K) distinguishing the recordings in Standing and Lying positions (black/grey). Each bar corresponds to one subject of the EuroBaVar dataset.

Regarding the BRS estimates, it was possible to obtain a $\hat{\alpha}^{\mathrm{TF}}$ for the 46 files of the EuroBaVar dataset. Only in 34/46 recordings it was possible to obtain simultaneously a $\hat{\alpha}^{\mathrm{LF}}$ and $\hat{\alpha}^{\mathrm{HF}}$ value. All subjects presented BEs and all subjects presented short and long BEs, using the indicative cutoff of 3.5 sec. As illustrated in Fig. 5.14(a), all estimates were found to be comparable, with the confidence intervals over the mean and median BRS estimates indicating no statistical differences among the BRS values. As illustrated in Fig. 5.14(b), the L to S ratio of the BRS estimates ($\hat{R}_{LS}$) was above 1 for all estimates, indicating that the BRS values typically increased in Lying position (Laude *et al.*, 2004). Of the 23 pairs of records, the $\hat{R}_{LS}$ obtained from $\hat{\alpha}^{\mathrm{TF}}$ is above 1 in 23/23 pairs. From the 34 recordings with $\hat{\alpha}^{\mathrm{LF}}$ and $\hat{\alpha}^{\mathrm{HF}}$ values, 17 paired L and S evaluations were obtained. Of those, 15/17 and 17/17 were found to exhibit $\hat{R}_{LS}$ above 1, respectively, for $\hat{\alpha}^{\mathrm{LF}}$ and $\hat{\alpha}^{\mathrm{HF}}$. Also, the $\hat{\alpha}^{\mathrm{HF}}$ increase more from Standing to Lying position than $\hat{\alpha}^{\mathrm{LF}}$, i.e., $\hat{R}_{LS}$ is higher for $\hat{\alpha}^{\mathrm{HF}}$ than for $\hat{\alpha}^{\mathrm{LF}}$ in 15 out of 17 cases. Regarding the time domain BRS analysis, the $\hat{R}_{LS}$ obtained from $\hat{\mathcal{B}}^{\mathrm{E}}_{\mathrm{G,O}}$ is above 1 in 23 of the 23 pairs. All recordings present short and long BEs, and the corresponding $\hat{R}_{LS}$ is above 1 in 21 of the 23 pairs. In 19 out of the 23 cases, $\hat{R}_{LS}$ from $\hat{\mathcal{B}}^{\mathrm{E},\leq 3.5}_{\mathrm{G,O}}$ was found to be lower than the $\hat{R}_{LS}$ from $\hat{\mathcal{B}}^{\mathrm{E},>3.5}_{\mathrm{G,O}}$.

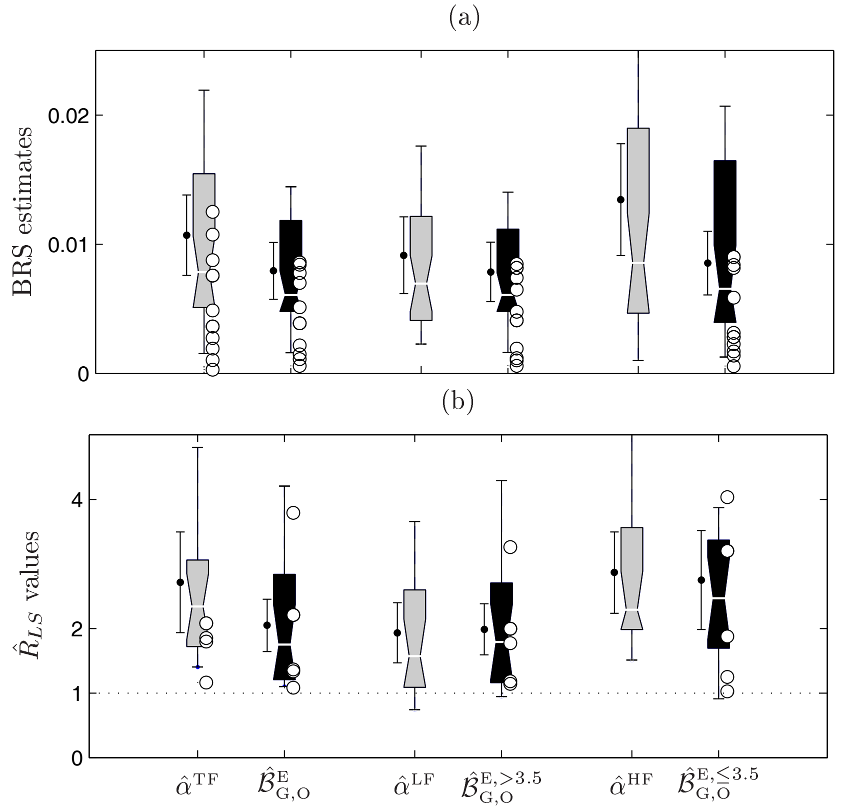

Figure 5.14: Boxplots of (a) $\hat{\mathcal{B}}$ and (b) L to S ratio of $\hat{\mathcal{B}}$ ($\hat{R}_{LS}$). Median and mean 95% confidence intervals represented by the notch and by the interval displayed at the left of each boxplot. The circles localize the files without $\hat{\alpha}^{\text{LF}}$ or $\hat{\alpha}^{\text{HF}}$ values for the EuroBaVar recordings.

5.4 Discussion

Time domain BRS estimates are overall estimates that account for both sympathetic and parasympathetic influences. In this work, they were found to be highly correlated with $\hat{\alpha}^{\text{TF}}$, a frequency BRS estimate obtained considering the entire frequency range. In particular, BRS estimates from BEs were found to be more correlated with $\hat{\alpha}^{\text{TF}}$ than BRS estimates from BSs.

Frequency domain analysis is able to provide BRS estimates from the LF and HF components, respectively, more associated to the sympathetic and the parasympathetic contributions (Pagani *et al.*, 1997). Distinguishing the two frequency bands, previous comparisons between BRS estimates from the sequences technique and from the transfer function method indicate that $\hat{\mathcal{B}}^{\text{S}}_{\text{L,O}}$ values are more correlated with $\hat{\alpha}^{\text{HF}}$ values than with $\hat{\alpha}^{\text{LF}}$ (Watkins *et al.*, 1996). The observation that $\hat{\alpha}^{\text{HF}}$ and $\hat{\mathcal{B}}^{\text{S}}_{\text{L,O}}$ values are both related with fast SBP and RR simultaneous changes (fast oscillations in frequency domain and short segments in time domain) and that the BRS estimates based on such changes are correlated, supports the validation of the sequences technique to provide a measure more related with parasympathetic activity

(Persson *et al.*, 2001). In this work, the $\hat{\mathcal{B}}^{\mathrm{S}}_{\mathrm{G,O}}$ and $\hat{\mathcal{B}}^{\mathrm{E}}_{\mathrm{G,O}}$ values were also found to be more correlated with $\hat{\alpha}^{\mathrm{HF}}$ rather than with $\hat{\alpha}^{\mathrm{LF}}$, corroborating the previous studies (Watkins *et al.*, 1996; Persson *et al.*, 2001). However, the files exhibiting $\hat{\alpha}^{\mathrm{HF}}/\hat{\alpha}^{\mathrm{LF}} > 1.5$ also presented $\hat{\alpha}^{\mathrm{LF}} < \hat{\mathcal{B}}^{\mathrm{E}}_{\mathrm{G,O}} < \hat{\alpha}^{\mathrm{HF}}$, indicating that $\hat{\mathcal{B}}^{\mathrm{E}}_{\mathrm{G,O}}$ is a BRS measure that accounts for both sympathetic and parasympathetic ANS contributions.

Time domain BRS estimates and ability to discriminate different BRS conditions
Even if not distinguishing sympathetic and parasympathetic influences, time domain BRS analysis is able to identify changes in BRS function. The results in spontaneous data indicate that the BRS estimation from BEs is able to capture changes in the BRS function due to parasympathetic withdraw, including for the subjects with BRS dysfunction (Fig. 3.19). The results in drug-induced data indicate that the BRS estimation from BEs is able to capture BRS changes in conditions of a clear sympathetic or parasympathetic activation (Fig. 4.17). Finally, the events technique has been shown to be able to capture changes in the BRS function that are not due to changes in sympathetic activity (Beloka *et al.*, 2009). In that parallel study, the effect of prolonged oral beta blockade with bisoprolol was studied in normal subjects[1]. Bisoprolol was found to increase the mean RR interval and the MSNA burst incidence (# bursts/100 HB). Time domain BRS analysis indicated that bisoprolol significantly increased the sequences/events BRS estimates, with the events technique providing more statistical evidence of such change. Regarding the frequency BRS estimates, there was no statistically significant change in BRS estimates computed either in LF or in HF bands (with the Transfer Function method), from placebo to bisoprolol conditions. Unchanged SBP, RR, MSNA and RESP powers in LF and HF frequency bands from placebo to bisoprolol condition suggested that the larger burst incidence and increased BRS is not due to sympathetic activation.

Time domain BRS estimation from short/long BEs and sympathetic activity
The events technique is able to identify short and long BEs. The causes to the occurrence of a BE still remain to determine, as well as the physiological sources that trigger their length. However, the results in this study bring evidence that short and long BEs carry different information on the ANS modulations. As a matter of fact, BRS estimates from short BEs were found to be significantly correlated with the MSNA powers in HF, while not being significantly correlated with the MSNA powers in LF band. Additionally, BRS estimates from long BEs were significantly correlated with the MSNA powers in LF, while not being significantly correlated with the MSNA power in HF band. Nevertheless, the

---

[1] Beta blockers are frequently used for the treatment of cardiovascular diseases, e.g., hypertension (Burns *et al.*, 2004). They are also administered to normotensive patients to prevent migraine (Stark *et al.*, 2007) and to relief essential tremor, e.g., in Parkinson's disease (Uitti, 1998). However, the effects of prolonged beta blockade in normotensive individuals were unknown, in particular, with respect to the cardiovascular variables and the BRS function. This motivated the study of Beloka *et al.* (2009), a parallel study in the scope of the thesis objectives.

obtained correlations were found to be moderate (i.e., $r < 0.7$).

The moderate level of correlation point out for other possible sources that determine a BRS response, besides sympathetic/parasympathetic balance (Lanfranchi and Somers, 2002). Also, it should be considered that the distinction between sympathetic and parasympathetic influences might be impossible to achieve, simply because these activities are complementary and not mutually exclusive (Falcão de Freitas, 1999). Therefore, it is possible that any cutoff length to define short and long BEs will not distinguish completely the parasympathetic and sympathetic influences on the BRS response. It is expected that longer segments are able to capture the slower frequency responses as well as the faster ones, and any cutoff will distinguish both responses. Consequently, the BRS analysis from short BEs is expected to reflect exclusively the faster responses, while the BRS from long BEs is expected to reflect a mixture of both fast and slow responses. Finally, the moderate level of correlations found can be a consequence of the definition of the LF and HF frequency bands. As a matter of fact, more expressive correlations between MSNA and RR powers evaluated in LF and HF bands were referred to be obtained with the use of parametric spectral analysis methods and the use of a *restricted* definition of the LF and HF bands (Pagani *et al.*, 1997). In that study, the MSNA and RR powers were estimated as the variance associated to the parametric spectral component with central frequency within LF: 0.10 ± 0.01 Hz and HF: 0.23 ± 0.01 Hz.

Regarding the discrimination between Lying from Standing position in the EuroBaVar dataset, the ratio $\hat{R}_{LS}$ obtained from the overall estimates $\hat{\alpha}^{\mathrm{TF}}$ and $\hat{\mathcal{B}}^{\mathrm{E}}_{\mathrm{G,O}}$ allows the discrimination for all subjects. Only 17 of the 23 pairs of L and S recordings presented simultaneously $\hat{\alpha}^{\mathrm{LF}}$ and $\hat{\alpha}^{\mathrm{HF}}$ values. From those 17 pairs, $\hat{R}_{LS} > 1$ in 15/17 and 17/17 of the cases, respectively for $\hat{\alpha}^{\mathrm{LF}}$ and $\hat{\alpha}^{\mathrm{HF}}$. It was possible to identify short and long BEs in all 23 pairs and, both $\hat{\mathcal{B}}^{\mathrm{E},\leq 3.5}_{\mathrm{G,O}}$ and $\hat{\mathcal{B}}^{\mathrm{E},>3.5}_{\mathrm{G,O}}$ values are able to distinguish Lying from Standing position in 21 out of 23 of the cases. Finally, in accordance with a parasympathetic inhibition in Lying position (Mancia and Mark, 1983), the $\hat{\alpha}^{\mathrm{HF}}$ were found to be typically higher than the $\hat{\alpha}^{\mathrm{LF}}$ in that condition. Similarly, the $\hat{\mathcal{B}}^{\mathrm{E},\leq 3.5}_{\mathrm{G,O}}$ values were found to be higher than the $\hat{\mathcal{B}}^{\mathrm{E},>3.5}_{\mathrm{G,O}}$ values in Lying position.

The evidence that BRS estimates from long and short BEs capture sympathetic and parasympathetic effects explain the results obtained from the comparison between the different spontaneous BRS estimates (Fig. 3.18). Spontaneous BRS estimates based on BSs measure typically parasympathetic modulations (Parlow *et al.*, 1995). For the $\hat{\mathcal{B}}^{\mathrm{E}}_{\mathrm{G,O}}$ computation, all identified BEs are considered, both short and long. It was found that $\hat{\mathcal{B}}^{\mathrm{E}}_{\mathrm{G,O}}$ and $\hat{\mathcal{B}}^{\mathrm{S}}_{\mathrm{L,O}}$ are correlated, although exhibiting statistically significant differences (Fig. 3.18(c)). The observed difference is due to the use of different slope approaches ($\hat{\mathcal{B}}^{\mathrm{S}}_{\mathrm{G,O}}$ and $\hat{\mathcal{B}}^{\mathrm{S}}_{\mathrm{L,O}}$ also show differences, Fig. 3.18(a)), but also due to the use of BEs in the BRS estimation instead of BSs. The latter point out that BEs and BSs carry different physiological information. As a matter of fact, the $\hat{\mathcal{B}}^{\mathrm{E}}_{\mathrm{G,O}}$ values discriminate better L and S positions in comparison with $\hat{\mathcal{B}}^{\mathrm{S}}_{\mathrm{L,O}}$ and $\hat{\mathcal{B}}^{\mathrm{S}}_{\mathrm{G,O}}$ (Fig. 3.19(b)). Distinguishing the short and long BEs, $\hat{\mathcal{B}}^{\mathrm{E}}_{\mathrm{G,O}}$ estimated from the short and long BEs was found to discriminate L and S positions similarly to the frequency BRS estimates computed in HF and LF bands, respectively (Fig. 5.14). Regarding the robust global approach, the $\hat{\mathcal{B}}^{\mathrm{E}}_{\mathrm{G,T}}$ value is computed with an outlier rejection rule that keeps the segments with similar slope (Fig. 3.8). As short BEs are in a larger number than long BEs (Fig. 3.17), the $\hat{\mathcal{B}}^{\mathrm{E}}_{\mathrm{G,T}}$ value is evaluated predominantly with shorter BEs and points out this BRS estimate as mostly reflecting the parasympathetic effect on the cardiovascular variables. This is also corroborated by the fact that $\hat{\mathcal{B}}^{\mathrm{S}}_{\mathrm{L,O}}$ is a measure of the BRS associated with parasympathetic activity (Parlow *et al.*, 1995) and that $\hat{\mathcal{B}}^{\mathrm{S}}_{\mathrm{L,O}}$, $\hat{\mathcal{B}}^{\mathrm{S}}_{\mathrm{G,T}}$ and $\hat{\mathcal{B}}^{\mathrm{E}}_{\mathrm{G,T}}$ values do not exhibit statistically significant pairwise differences (Fig. 3.18(d–e)).

Indicative cutoff to define short/long BEs and respiration

The indicative cutoff to define short and long BEs was first considered as function of the breathing frequency (f_r). The use of f_r demands for the acquisition of the respiratory signal or, at least, the use of signal processing techniques to derive the respiratory frequency from the ECG, but this strategy also presents some shortcomings. The estimation of f_r from the RR spectra is based on the fact that respiration influences the RR variability (RSA), and when that influence is diminished (e.g., in standing position) an inaccurate estimate can be obtained (Leanderson *et al.*, 2003). Also, it is worthwhile to mention that as an EDR method based on 3 ECG orthogonal leads improves significantly the accuracy in the f_r estimation when compared with a 2 ECG lead based method (Bailón *et al.*, 2006), it is likely that the use of only one ECG lead could not provide an accurate f_r value. Therefore, in the impossibility to record the respiratory signal, a viable alternative to perform the time domain BRS analysis based on short and long BEs is to acquire more than one ECG lead (preferably, orthogonal ECG leads) to obtain more accurate f_r value.

In this work, it was found that the replacement of the individually adjusted cutoff $1/f_r$ by a constant cutoff did not change the results significantly. As a matter of fact, the cutoff of 3.5 sec estimated in the SP/NT/PH dataset is a value comparable to the typical length of a breathing cycle (12 cycles per minute), considering a normal and spontaneous breathing condition[2]. Also, in short recordings, it is not expected that many segments of several length would be identified, such that the BRS estimate would change significantly, by considering 3.5 sec instead of $1/f_r$ sec.

Further studies are now needed to validate the indicative cutoff provided in this work. These studies should include experimental SBP, RR and RESP data (and preferably also MSNA data) following a suitable protocol, e.g., invasive protocol involving continuous injections

---

[2] In healthy adults and spontaneous breathing condition, the average respiratory rate is typically of 12 breaths per minute (Guyton and Hall, 2000), being able to change within the range of 12 to 20 breaths per minute. Therefore, the typical length of the respiratory cycle ($1/f_r$) in spontaneous condition is within the range from 3 to 5 sec.

of nitroprusside or phenylephrine (Pagani *et al.*, 1997) or spontaneous protocol involving controlled breathing at different breathing frequencies (Pitzalis *et al.*, 1998*b*). As an example, in LF controlled breathing, the BEs are expected to be longer because this condition increases the power of the SBP and RR series in the LF band, while abruptly diminishes their power in HF band[3].

Thresholds and threshold values used in frequency domain BRS methods
In this work, the frequency BRS estimates were computed considering the coherence threshold value $\kappa = 0.5$. The choice of this threshold becomes particularly important for BRS dysfunction cases, in which the coupling between the SBP and RR series is expected to be lower than for normal BRS cases. If restrictive κ values are considered the method loses the ability to provide a BRS estimate, while if κ is set *too* low the transfer function estimate is more *unreliable*. An alternative to avoid the choice of a value for κ is to estimate the significance of the coherence function (as a function of frequency) from surrogate data analysis, e.g. Faes *et al.* (2004). In that study, surrogate series were generated preserving the modulus of the Fourier Transform of the original series, while randomizing the phase. The threshold for "zero" coherence was then derived from confidence intervals of the distribution of surrogated coherence functions. However, this approach is dependent on that experimental dataset and, therefore, provides a coherence threshold tuned for a BRS condition.
Also, Pinna *et al.* (2002) has suggested to disregard that threshold, always obtaining a BRS estimate, with similar limits of a agreement to the invasive BRS estimates. Furthermore, disregarding that threshold was reported to increase the bias and dispersion in BRS estimation to values still suitable for clinical practice (Pinna and Maestri, 2002). However, disregarding the coherence threshold can lead to important methodological issues. In fact, the model underlying the estimation of the BRS through the transfer function method assumes that the baroreflex response is linear and, therefore, this assumption should be at least verified. Additionally, the inclusion of "unreliable" values in the average of few values (Eq. 5.16) can lead to excessive increases in BRS dispersion.

The drawbacks of the use of the transfer function method are avoided by the use of the events technique (choosing threshold values to verify linearity). The events technique is based on a slope computation and, therefore, also assumes that the baroreflex response is linear. The BEs used to compute the slope are identified as exhibiting high SBP and RR correlation and, consequently, the linear BRS assumption is implicitly satisfied. Also, under stationary acquisition conditions, the SBP and RR correlation in all identified BEs still exhibit high

---

[3] In LF controlled breathing, the baroreflex and respiratory contributions to the cardiovascular oscillations are mixed around the 0.1 Hz frequency. Lower frequency breathing is accompanied by deeper breathing (Brown *et al.*, 1993) and, therefore, an increased range of the SBP and RR amplitudes is observed. Consequently, the correlation between the SBP and RR values tends to be higher, what is translated in longer length segments of correlation 0.8, in the same way that lower SBP and RR correlation expected in BRS dysfunction cases is translated into shorter segments of correlation 0.8, see Fig. 3.11.

correlation, which is convenient for the computation of a global slope. If future results corroborate that short and long BEs are more related, respectively, to the parasympathetic and sympathetic ANS modulations in cardiovascular oscillations, time domain BRS methods can be preferable to frequency domain methods also because the only threshold used for BEs identification is set regardless of the BRS condition ($r_{min} = 0.8$, see Fig. 3.11).

5.5 Conclusions

In this chapter, time domain BRS analysis was associated with ANS sympathetic activity and respiration. The results in this study bring evidence that short and long BEs carry different information on the ANS modulations.

In the SP/NT/PH dataset, the BRS estimates from short BEs were significantly correlated with the MSNA powers in HF and not significantly correlated with the MSNA powers in LF band. Additionally, the BRS estimates from long BEs were significantly correlated with the MSNA powers in LF, while not being significantly correlated with the MSNA power in HF band. In the EuroBaVar dataset, the BRS estimation from short and long BEs was found to distinguish Lying from Standing positions in 21 out of the 23 cases. Additionally, frequency BRS estimates from HF band were found to be higher than those evaluated in LF band in 15 out of the 17 pairs. Following the same trend, time BRS estimates from short BEs were found to be higher than that evaluated from long BEs in 19 out of 23 cases.

In this work, indicative cutoffs to define short and long BEs are provided. In the SP/NT/PH dataset, the individually adjusted cutoff $1/f_r$ (with f_r being the respiratory frequency of the subject) and the optimal dataset cutoff of 3.5 sec did not change the results significantly. This result can be explained by the fact that 3.5 sec is a value comparable to the typical length of a breathing cycle (12 cycles per minute), considering a normal and spontaneous breathing condition. Further studies are now needed to validate the indicative cutoff values, considering different experimental protocols.

Chapter 6

Concluding Remarks

The main goal of this work is the study and the improvement of time domain methods for spontaneous BRS assessment, as well as to contribute to their validation as reliable methods to assess the autonomic reflex function.

The first part of this work consisted of the development of BRS methods offering a higher ability to provide a BRS estimate in ANS dysfunction cases as reliable as the BRS estimates provided for the ANS normal function cases. Other aspects considered in this study are the ability of the methods to discriminate conditions in which the BRS is expected to be modified, as well as reproducibility and dispersion in BRS estimation.

The second part of this work consisted of the validation of the improved BRS methods, and to further explore the BRS function with respect to respiration, sympathetic and parasympathetic ANS modulations. The validation is carried out from the comparison of the improved estimators with time domain BRS estimators proposed for the analysis of drug-induced data (Parlow *et al.*, 1995) and frequency domain BRS estimators developed for the analysis of spontaneous data (Robbe *et al.*, 1987), both conventionally accepted to distinguish the sympathetic and parasympathetic ANS effects (La Rovere *et al.*, 2008).

Multimodal system to extract beat-to-beat variability from the acquired signals The joint analysis of the beat-to-beat series of SBP values and RR intervals allows the BRS assessment (La Rovere *et al.*, 2008). Therefore, to carry out the BRS estimation, the beat-to-beat series have to be extracted from the acquired ABP and ECG signals. In this work, a multimodal system to detect the reference points in the cardiovascular signals is presented. This system is based on independent ABP and ECG beat detections with following fusion of the results, making use of the robust ECG beat detector previously evaluated by the group (Martínez *et al.*, 2004). Additionally, to explore the BRS dependencies with respiration and sympathetic activity, methods for automatic extraction of RESP and MSNA features are presented. The performance of the methods is illustrated with experimental data.

Improvement of time domain BRS estimation in spontaneous data

The **sequences technique** is a frequently used time domain method for spontaneous BRS estimation. This method is based on the identification of baroreflex sequences (BSs) and linear regression over the corresponding SBP and RR values. An overall estimate is obtained by averaging the slope estimates from all BSs identified in a record. In spite of its clinical usefulness (Di Rienzo *et al.*, 2001), experimental literature studies argue that changes should be made to the sequences technique. On one hand, reference threshold values for the identification of BSs should be established to optimize its validity in humans, particularly when applied to patients with attenuated BRS (Davies *et al.*, 2001). On the other hand, reference BRS values should be established to allow the diagnosis of an impaired baroreflex function in individual patients (Tank *et al.*, 2000).

The study on the effect of changing the threshold values currently used for BS identification points out that the thresholds are redundant and that its simultaneous use reduce the ability of providing a BRS estimate. The results also indicate that the SBP and RR segments of high correlation, defined here as baroreflex events (BEs), are a reliable alternative to the traditional BSs. To additionally increase robustness and decrease the variance in BRS estimation, global/total slope estimators are proposed to replace the average slope estimator. The combined use of BEs and global/total estimators constitutes the **events technique**, proposed in this work to enhance spontaneous BRS estimation.

The performance of the BEs based BRS methods is evaluated in the spontaneous EuroBaVar dataset (Laude *et al.*, 2004). With the use of BEs instead of BSs, the BRS analysis benefits from more and longer segments of data, leading to a higher number of beats available for the slope estimation. Therefore, there is a higher likelihood of obtaining a BRS estimate from BEs than from BSs: if BSs are identified, BRS estimates from BEs and BSs are highly correlated; for the cases of BSs absence, BRS estimates based on BEs are lowest. The fact that BRS estimates from BSs and BEs are correlated, though in the latter case obtained from a higher number of beats, indicates that both are measuring the same phenomenon but with a more visible expression in BEs. The absence of BSs in a record, and the impossibility to assess the BRS, is not synonymous of an absent BRS function, but rather a shortcoming of the sequences technique to provide a BRS estimate. The results also point out that the events technique provides a higher BRS estimates inter-subject variability, allowing a better discrimination between conditions in which it is expected the BRS to be modified (Lying versus Standing). Finally, the BRS estimation from the events technique achieves a higher reproducibility and a lower dispersion, with the files not presenting BSs (and presenting BEs) exhibiting similar values to those of the remaining files.

Validation of the events technique with drug-induced data

Drug-induced protocols are considered as a *gold standard* for BRS quantification because they allow to characterize the BRS function over its entire sigmoidal range (Fig. 1.7). Therefore, the novel BRS methods were further compared with data following the “Modified Oxford” protocol, involving drug-stimulation of the sympathetic and parasympathetic activity of the ANS with Nitroprusside and Phenylephrine boluses (Ebert and Cowley Jr, 1992). The results corroborate that spontaneous and drug induced estimates are different although correlated (Parlow *et al.*, 1995). The differences between the invasive and spontaneous BRS estimates were found to be due to the differences in the physiological information that the invasive and spontaneous data carry, and also due to the methodological dissimilarities between the invasive and spontaneous BRS estimators. The BRS analysis from BEs was found to provide values that reflect better the physiology of the baroreflex, against the BRS analysis from BSs: BRS estimates from BEs discriminate better SP, NT and PH conditions, they are in accordance with the expected relationship between the BRS estimates and the mean RR interval and, finally, they are more correlated with the amount of sympathetic activity in a condition of sympathetic activation. Therefore, the BRS analysis from BEs is preferable, even to compute a BRS estimate with data following the “Modified Oxford” protocol. Finally, the results indicate that no decrease in the BRS variability is achieved with drug induced data, pointing out that the possibility of increase the number of beats in spontaneous experiments is clearly an advantage over increasing the SBP–RR correlation in drug experiments, as a higher number of beats for slope estimation in spontaneous recordings requires only longer stationary recordings.

Time domain BRS estimation from short and long baroreflex events

Time domain BRS estimates are overall estimates that do not traditionally distinguish parasympathetic and sympathetic ANS modulations. Nevertheless, they are able to identify changes in the BRS function. The results in spontaneous data indicate that the BRS estimation from BEs is able to capture changes in the BRS function due to parasympathetic withdraw, including for the subjects with BRS dysfunction (Fig. 3.19). The results in drug-induced data indicate that the BRS estimation from BEs is able to capture BRS changes in conditions of a clear sympathetic or parasympathetic activation (Fig. 4.17). Finally, the events technique has been shown to be able to capture changes in the BRS function that are not due to changes in sympathetic activity (Beloka *et al.*, 2009).

In conditions of drug-induced sympathetic activation, the changes in BRS estimates from BEs are correlated with the changes in sympathetic activity (Fig. 4.20). In spontaneous condition, the sympathetic activity is more reduced and the ability of the BRS estimation from BEs to capture the sympathetic activity in such condition was studied. The sympathetic branch of the ANS presents typically oscillations of lower frequency than the parasympathetic (Parlow *et al.*, 1995) and, therefore, longer SBP–RR data segments are needed to detect and quantify this modulation. Because BSs are short segments of data, the BRS analysis from BSs mostly reflects the parasympathetic ANS control of the heart (Parlow *et al.*, 1995). As the events technique is able to provide long BEs besides short BEs (of the same length as BSs), BEs are more likely to additionally capture the sympathetic modulation than BSs.

The results obtained in this thesis evidence that short and long BEs carry different information on the ANS modulations (Fig. 5.11). On one hand, the BRS estimates from short BEs are significantly correlated with the MSNA powers in HF, while not being significantly correlated with the MSNA powers in LF band. On the other hand, the BRS estimates from long BEs are significantly correlated with the MSNA powers in LF, while not being significantly correlated with the MSNA power in HF band. The evidence that BRS estimates from long and short BEs are more associated with sympathetic and parasympathetic effects, respectively, explain the relation between the different spontaneous BRS estimates (Fig. 3.18). BRS estimates based on BSs measure typically parasympathetic modulations (Parlow *et al.*, 1995). The events technique estimate (global approach and BEs) is computed considering all identified BEs, both short and long. The global BRS estimates based on BEs hold differences to the BRS estimates based on BSs, what is indicative that BEs (short and long) and BSs carry different physiological information. As a matter of fact, this is corroborated by the fact that total BRS estimates from BEs do not exhibit differences with BRS estimates based on BSs. The events technique estimate (total approach and BEs) is computed with an outlier rejection rule that predominantly keeps the short segments. Therefore, total BRS estimates from BEs mostly reflect the parasympathetic effect on the cardiovascular variables.

In conclusion, this work indicates that the use of the events technique, which can be considered as a simplification of the sequences technique, brings advantage in BRS estimation. The events technique makes use of less thresholds to identify a baroreflex related segment and only one slope obtained for all identified segments (instead of the average of the slopes obtained for each identified segment). The events technique is set with a single threshold for the BEs identification (minimum beat to beat SBP and RR correlation, r_{min}) with reference value suitable for the identification of BEs both for normal and for dysfunction BRS cases ($r_{min} = 0.8$). The results obtained for the EuroBaVar files without BSs are promising and should now be corroborated with the comparison of a normal BRS group against a group of attenuated BRS.

As a final remark, it is worthwhile to refer that there is a significant correlation among the BRS estimates provided by the various methods (time and frequency) and experimental protocols (spontaneous and invasive). Therefore, if the aim is merely to derive an index that quantifies the BRS of an individual subject, it is not important which method is used for BRS assessment. However, if the goal is to further understand the human physiology, most of the literature results on BRS are not comparable and it is essential to establish reference experimental protocols, methods and thresholds for BRS assessment.

Chapter 7

Scientific Contributions

The main framework of this PhD thesis is related with the analysis of short-term SBP and RR series, as a tool for a non invasive study of the Autonomic Nervous System. The scientific contributions directly related with the work described in the thesis are resumed in the following lists.

International Journals

- S Gouveia, AP Rocha, P Laguna and P Lago, "Time Domain Baroreflex Sensitivity Assessment by Joint Analysis of Spontaneous SBP and RR", *Biomedical Signal Processing and Control* 4: 254–261, 2009. DOI:10.1016/j.bspc.2009.03.003.

- SP Beloka, S Gouveia, M Gujic, R Naeije, AP Rocha and P van de Borne, "Differential Effects of Oral Beta Blockade on Cardiovascular and Sympathetic Regulation in Normal Subjects", Accepted in *Journal of Cardiovascular Pharmacology and Therapeutics.* 2009

Proceedings of Scientific Meetings with Referees (* indicates the presenter)

- S Gouveia*, AP Rocha, P Van de Borne and P Lago, "Assessing Baroreflex Sensitivity in the Sequences Technique: Local versus Global Approach", *Comput Cardiol* 32: 279–282, 2005.

- S Gouveia*, AP Rocha, P Laguna, P Van de Borne and P Lago, "Improved BRS Assessment Using the Global Approach in the Sequences Technique", *Comput Cardiol* 33: 641–644, 2006.

- S Gouveia*, AP Rocha, P Laguna and P Lago, "Improved Time Domain BRS Assessment with the Use of Baroreflex Events", *Comput Cardiol* 34: 813–816, 2007.

- S Gouveia*, AP Rocha, P Laguna and P Lago, “Threshold Sensitivity in Time Domain BRS Estimation: Minimum Beat-to-Beat Changes and Minimum Correlation”, *Comput Cardiol* 34: 557–560, 2007.
- SP Beloka*, M Gujic, S Gouveia, AP Rocha and P van de Borne, “Differential Effects of Oral Beta Blockade on Cardiovascular and Sympathetic Regulation During Normoxia and Hypoxia”, *Acta Cardiologica* 63(4): 525–534, 2008. DOI:10.2143/AC.63.4.2033055.
- S Gouveia*, AP Rocha, P Laguna and P Lago, “Methodological Insights on Time Domain Baroreflex Sensitivity Analysis Illustrated with the EuroBaVar Data”, *Acta Cardiologica* 63(5): 669, 2008. DOI: 10.2143/AC.63.5.2033239.
- SP Beloka*, M Gujic, S Gouveia, AP Rocha and P Van de Borne, “Effects of Beta Blockade on Hemodynamics and Muscle Sympathetic Activity”, *J Hypertens* 26(s1): 479, 2008.
- S Gouveia*, AP Rocha, P Laguna, M Gujic, SP Beloka, P Van de Borne and P Lago, “BRS Analysis from Baroreflex Sequences and Baroreflex Events Compared Using Spontaneous and Drug Induced Data”, *Comput Cardiol* 35: 737–740, 2008.

Presentations, besides the included in Scientific Meetings with Referees (* indicates the presenter)

- S Gouveia*, AP Rocha, P Laguna and P Lago, “Thresholds Tuning in Time Domain Methods for BRS Estimation”,
  Poster presentation in *6th EMB-IEEE International Summer School on Biomedical Signal Processing* 2007, Certosa di Pontignano, Siena, Italy.
- S Gouveia*, AP Rocha, P Laguna and P Lago, “Improved Time Domain BRS Assessment with the use of Baroreflex Events”,
  Oral presentation in *8th STAFF Studies Symposium* 2007, Shell Island, USA.
- S Gouveia*, AP Rocha, P Laguna, M Gujic, SP Beloka, P Van de Borne and P Lago, “BRS Analysis from Baroreflex Sequences and Baroreflex Events Compared Using Spontaneous and Drug Induced Data”,
  Oral presentation in *9th STAFF Studies Symposium* 2008, Bertinoro, Italy.
- SP Beloka*, S Gouveia, M Gujic, AP Rocha and P Van de Borne, “Differential Effects of Oral Beta Blockade on Cardiovascular and Sympathetic Regulation”,
  Oral presentation in *BHC/CBH Scientific Meeting of the Belgian Hypertension Committee* 2008, Gent, Belgium.

During the PhD period (2005–2009), there was also collaboration in other projects in the scope of the main PhD framework. These projects were related with the study of the interactions between cardiovascular parameters extracted from the ECG (RR and QT interval variability), related with the study of ambulatory long term HRV recordings and related with the study of the parameters extracted from the RR and/or SBP series in the characterization of different conditions: Diabetes Mellitus pathology, Pediatric coma and Sleep disorders. The scientific material that resulted from these collaborations is resumed in the following list.

Other Publications/Presentations during the PhD period (* indicates the presenter)

- R Almeida, S Gouveia, AP Rocha, E Pueyo, JP Martínez and P Laguna, "QT variability and HRV interactions in ECG: Quantification and Reliability", *IEEE Trans Biomed Eng* 53(7): 1317–1329, 2006.
- A Leite, AP Rocha*, ME Silva, S Gouveia, J Carvalho and O Costa, "Long-Range Dependence in Heart Rate Variability Data: ARFIMA Modelling vs DFA Analysis", *Comput Cardiol* 34: 21–24, 2007.
- A Leite*, AP Rocha, S Gouveia, ME Silva, O Costa and J Winck, "Modelação ARFIMA-GARCH na Variabilidade da Frequência Cardíaca",
  Oral presentation in *SPE'08 - Congresso Anual da Sociedade Portuguesa de Estatística* 2008, Vila Real, Portugal.
- AP Rocha, S Gouveia, JP Fernandes, MJ Carvalho, P Lago and AF Freitas, "Caracterização da Variabilidade dos Sinais Cardiovasculares na Diabetes Mellitus",
  Poster presentation of the research work developed in the project "Diabetes Mellitus: Indícios na fase pré-sintomática da disfunção autonómica", program *Investigação Científica na Pré-graduação 2004/2005*, promoted by UPorto, in partnership with Fundação Ilídio Pinho. Project awarded in the area of Exact and Natural Sciences, after jury evaluation.
- AP Rocha, R Almeida, S Gouveia, P Lago, J Aparício, O Costa, P Costa, LA Santos, L Barros, L Lacerda, A Vela, A Castro, T Ventura, A Almeida, J Carvalho, L Ribeiro and J Sousa, "Heart Rate Variability in Critical Illness: Follow-up from Admission to Outcome",
  Poster presentation of the research work developed in the project "Análise da variabilidade cardiovascular em doença crítica: seguimento e prognóstico", program *Projectos pluridisciplinares Investigação Científica na Pré-Graduação 2006/2007*, promoted by UPorto and Caixa Geral de Depósitos.
- JC Winck*, M Sequeiros, M Drummond, J Pipa, S Magalhães, P Simões, S Gouveia and AP Rocha, "Blood Pressure Levels during Sleep – a pilot study",

Oral presentation in *XXIV Congresso de Pneumologia da Sociedade Portuguesa de Pneumologia* 2008, Porto, Portugal.

- AP Rocha, S Gouveia, H Araújo, B Ferreira, P Miranda, J Carvalho, J Aparício, A Ribeiro, MJ Silva, R Almeida, A Leite, P Caldas and O Costa, “Cardiovascular Variability Monitoring in Pediatric Coma”,
  Poster presentation in *II Encontro de Jovens Investigadores da UPorto 2009*, Porto, Portugal.
  Research work developed in the project “Multimodal analysis in pediatric coma”, program *Projectos pluridisciplinares Investigação Científica na Pré-Graduação 2007/2008*, promoted by UPorto and Caixa Geral de Depósitos.

- JC Winck, S Magalhães, P Simões, S Gouveia, AP Rocha, M Sequeiros, J Pipa, M Drummond, O Costa and C Rocha, “Cardio-respiratory Interactions during Sleep in Snorers and Patients with Obstructive Sleep Apnoea Syndrome”,
  Poster presentation in *II Encontro de Jovens Investigadores da UPorto* 2009, Porto, Portugal.
  Research work developed in the project “Arterial Blood Pressure responses and Heart rate Variability: role in the diagnosis and prognosis of Sleep Disordered Breathing”, program *Projectos pluridisciplinares Investigação Científica na Pré-Graduação 2007/2008*, promoted by UPorto and Caixa Geral de Depósitos.

References

Aboy, M, J McNames, T Thong, D Tsunami, MS Ellenby and B Goldstein (2005). An automatic beat detection algorithm for pressure signals. *IEEE Trans Biomed Eng* **52**(10), 1662–1670.

Abrahamsson, C, C Ahlund, M Nordlander and L Lind (2003). A method for heart rate-corrected estimation of baroreflex sensitivity. *J Hypertens* **21**(11), 2133–2140.

Akaike, H (1974). A new look at the statistical model identification. *IEEE Trans Autom Contr* **19**, 716–723.

Akselrod, S, D Gordon, FA Ubel, DC Shannon, AC Berger and RJ Cohen (1981). Power spectrum analysis of heart rate fluctuation: a quantitative probe of beat-to-beat cardiovascular control. *Science* **213**, 220–222.

Allen, J (2007). Photoplethysmography and its application in clinical physiological measurement. *Physiol Meas* **28**, R1–R39.

Almeida, R, S Gouveia, AP Rocha, E Pueyo, JP Martínez and P Laguna (2006). QT variability and HRV interactions in ECG: quantification and reliability. *IEEE Trans Biomed Eng* **53**(7), 1317–1329.

Antonelli, L, R Khamlach and W Ohley (1994*a*). Wavelet transform of the arterial pressure waveform. *Proc of the IEEE-SP International Symposium on Time-Frequency and Time-Scale* pp. 568–571.

Antonelli, L, W Ohley and R Khamlach (1994*b*). Dicrotic notch detection using wavelet transform analysis. *Proc 16th Annual International IEEE–EMBS Conf* pp. 1216–1217.

Bailón, R, L Sörnmo and P Laguna (2006). ECG-derived respiratory frequency estimation. In: *Advanced methods and tools for ECG data analysis* (GD Clifford, F Azuaje and PE McSharry, Eds.). Chap. 8, pp. 215–243. Artech House.

Barbieri, R, A Bianchi, J Triedman, L Mainardi, S Cerruti and J Saul (1997). Model dependency of multivariate autoregressive spectral analysis. *IEEE Eng Med Biol Mag* **16**(5), 74–85.

Barbieri, R and J Saul (1999). Autoregressive modeling for assessing closed-loop feedback and feedforward in arterial baroreflex. In: *Methodology and clinical applications of blood pressure and heart rate* (M Di Rienzo, G Mancia, G Parati, A Pedotti and A Zanchetti, Eds.). Vol. 60 of *Studies in Health Technology and Informatics*. pp. 21–34. IOS Press.

Baselli, G, S Cerutti, S Civardi, A Malliani and M Pagani (1988). Cardiovascular variability signals: Towards the identification of a closed-loop model of the neural control mechanisms. *IEEE Trans Biomed Eng* **35**(12), 1033–1046.

Beloka, SP, S Gouveia, M Gujic, R Naeije, AP Rocha and P van de Borne (2009). Differential effects of oral beta blockade on cardiovascular and sympathetic regulation in normal subjects. *Accepted in Journal of Cardiovascular Pharmacology and Therapeutics.*

Bernardi, L, C Porta, L Spicuzza, J Bellwon, G Spadacini, AW Frey, LYC Yeung, JE Sanderson, R Pedretti and R Tramarin (2002). Slow breathing increases arterial baroreflex sensitivity in patients with chronic heart failure. *Circulation* **105**, 143–145.

Bertineri, G, M Di Rienzo and A Cavallazzi (1988). Evaluation of baroreceptor reflex by blood pressure monitoring in unanesthetized cats. *Am J Physiol* **254**, H377–H383.

Bristow, JD, AJ Honour, GW Pickering, P Sleight and HS Smyth HS (1969). Diminished baroreflex sensitivity in high blood pressure. *Circulation* **39**, 48–54.

Brown, TE, LA Beightol, J Koh and DL Eckberg (1993). Important influence of respiration on human R–R interval power spectra is largely ignored. *J Appl Physiol* **75**(5), 2310–2317.

Brunton, L, D Blumenthal and I Buxton (2007). *Goodman and Gilman Manual of Pharmacology and Therapeutics*. McGraw-Hill.

Burns, J, DA Mary, AF Mackintosh, SG Ball and JP Greenwood (2004). Arterial pressure lowering effect of chronic atenolol therapy in hypertension and vasoconstrictor sympathetic drive. *Hypertens* **44**, 454–458.

Cerutti, C, M Ducher, P Lantelme, MP Gustin and CZ Paultre (1995). Assessment of spontaneous baroreflex sensitivity in rats a new method using the concept of statistical dependence. *Am J Physiol Regul Integr Comp Physiol* **268**, R382–R388.

Challapalli, S, AH Kadish and G Horvath JJ Goldberger (2007). Differential effects of parasympathetic blockade and parasympathetic withdrawal on heart rate variability. *J Cardiovasc Electrophysiol* **10**(9), 1192–1199.

Challis, R and R Kitney (1991). Biomedical signal processing (in four parts). Part 3. The power spectrum and coherence function. *Med Biol Eng Comput* **29**(3), 225–241.

Chen, RY, FC Fan, GB Schuessler and S Chien (1982). Baroreflex control of heart rate in humans during nitroprusside-induced hypotension. *Am J Physiol* **243**, R18–R24.

Davies, L, D Francis, A Scott, P Ponikowskic, M Piepolia and A Coats (2001). Effect of altering conditions of the sequence method on baroreflex sensitivity. *J Hypertens* **19**(7), 1279–1287.

Davies, L, D Francis, P Jurák, T Kára, M Piepoli and A Coats (1999). Reproducibility of methods for assessing baroreflex sensitivity in normal controls and in patients with chronic heart failure. *Clinical Science* **97**, 515–522.

De Ferrari, GM, A Sanzo, A Bertoletti, G Specchia, E Vanoli and PJ Schwartz (2007). Baroreflex sensitivity predicts long-term cardiovascular mortality after myocardial infarction even in patients with preserved left ventricular function. *J Am Coll Cardiol* **50**(24), 2285–2290.

De Ferrari, GM, M Landolina, M Mantica, R Manfredini, PJ Schwartz and A Lotto (1995). Baroreflex sensitivity, but not heart rate variability, is reduced in patients with life-threatening ventricular arrhythmias long after myocardial infarction. *Am Heart J* **130**(3 Pt 1), 473–480.

deBoer, RW, JM Karemaker and J Strackee (1987). Hemodynamic fluctuations and baroreflex sensitivity in humans: a beat-to-beat model. *Am J Physiol* **253**, 680–689.

Di Rienzo, M, G Bertinieri, G Mancia and A Pedotti (1985). A new method for evaluating the baroreflex role by a joint pattern. Analysis of pulse interval and systolic blood pressure series. *Med Biol Eng Comput* **23**(Suppl 1), 313–314.

Di Rienzo, M, G Parati, A Radaelli and P Castiglioni (2009). Baroreflex contribution to blood pressure and heart rate oscillations: time scales, time-variant characteristics and nonlinearities. *Phil Trans R Soc A* **367**, 1301–1318.

Di Rienzo, M, P Castiglioni, G Mancia, A Pedotti and G Parati (2001). Advancements in estimating baroreflex function: Exploring different aspects of autonomic control of the heart through the sequence technique. *IEEE Eng Med Biol Mag* **20**, 25–32.

Ducher, M, C Cerutti, MP Gustin and CZ Paultre (1994). Statistical relationships between systolic blood pressure and heart rate and their functional significance in conscious rats. *Med Biol Eng Comput* **32**(6), 649–655.

Ebert, TJ (1990). Differential effects of nitrous oxide on baroreflex control of heart rate and peripheral sympathetic nerve activity in humans. *Anesthesiology* **72**, 16–22.

Ebert, TJ and AW Cowley Jr (1992). Baroreflex modulation of sympathetic outflow during physiological increases of vasopressin in humans. *Am J Physiol Heart Circ Physiol* **262**, H1372–H1378.

Ebert, TJ, JJ Hayes, J Ceschi, KJ Kotrly, J van Brederode and JJ Smith (1984). Repetitive ramped neck suction: a quantitative test of human baroreceptor function. *Am J Physiol Heart Circ Physiol* **247**, H1013–H1017.

Efron, B and RJ Tibshirani (1993). *An introduction to the Bootstrap.* Chapman & Hall.

EHN, European Heart Network (2008). European cardiovascular disease statistics. Available online at http://www.ehnheart.org/files/statistics%202008%20web-161229A.pdf (accessed in May 2009).

Ernsting, J and DJ Parry (1957). Some observations on the effects of stimulating the stretch receptors in the carotid artery in man. *J Physiol* **137**, 44–46.

Faes, L, G Pinna, A Porta, R Maestri and G Nollo (2004). Surrogate data analysis for assessing the significance of the coherence function. *IEEE Trans Biomed Eng* **51**(7), 1156–1166.

Falcão de Freitas, A (1999). Sistema Nervoso Autónomo e Aparelho Cardiovascular: Um paradigma de auto-organização, complexidade e caos. *Colóquio/Ciências – Fundação Calouste Gulbenkian* **23**, 60–74.

Farrell, TG, V Paul, TR Cripps, M Malik, ED Bennett, D Ward and AJ Camm (1991). Baroreflex sensitivity and electrophysiological correlates in patients after acute myocardial infarction. *Circulation* **83**, 945–952.

Folke, M, L Cernerud, M Ekström and B Hök (2003). Critical review of non-invasive respiratory monitoring in medical care. *Med Biol Eng Comput* **41**(4), 377–383.

Foo, JYA and CS Lim (2006). Pulse Transit Time as an indirect marker for variations in cardiovascular related reactivity. *Technol Health Care* **14**(2), 97–108.

Frattola, A, G Parati, P Gamba, F Paleari, G Mauri, M Di Rienzo, P Castiglioni and G Mancia (1997). Time and frequency domain estimates of spontaneous baroreflex sensitivity provide early detection of autonomic dysfunction in diabetes mellitus. *Diabetologia* **40**(12), 1470–1475.

Fritsch, JM, DL Eckberg, LD Graves and GB Wallin (1986). Arterial pressure ramps provoke linear increases of heart period in humans. *Am J Physiol* **251**(6 Pt 2), R1086–R1090.

Goldberger, JJ, ME Cain, SH Hohnloser, AH Kadish, BP Knight, MS Lauer, BJ Maron, RL Page, RS Passman, D Siscovick, WG Stevenson and DP Zipes (2008). American Heart Association/American College of Cardiology Foundation/Heart Rhythm Society Scientific statement on noninvasive risk stratification techniques for identifying patients at risk for sudden cardiac death. *J Am Coll Cardiol* **52**, 1179–1199.

Gouveia, S, AP Rocha, A Leite, P Lago, O Costa and AF Freitas (2001). Matlab implementation of a method for the estimation of the respiratory signal in 24-hour holter recordings. *Proc BioEng'01, 6th Portuguese Conf on Biomedical Signal Processing.*

Gouveia, S, AP Rocha, P Lago, O Costa and A Falcão de Freitas (2000). Matlab implementation of a system for the detection and delineation of QRS-T complexes in 24h-holter recordings. *Proc BioEng'00, 5th Portuguese Conf on Biomedical Signal Processing.*

Gouveia, S, AP Rocha, P Laguna and P Lago (2007). Thresholds sensitivity in time domain BRS estimation: minimum beat-to-beat changes and minimum correlation. *Comput Cardiol* **34**, 557–560.

Gouveia, S, AP Rocha, P Laguna and P Lago (2009). Time domain baroreflex sensitivity assessment by joint analysis of spontaneous SBP and RR series. *Biomed Signal Process Control* **4**(3), 254–261.

Gouveia, S, AP Rocha, P Laguna, P van de Borne and P Lago (2006). Improved BRS assessment using the global approach in the sequences technique. *Comput Cardiol* **33**, 641–644.

Gouveia, S, AP Rocha, P van de Borne and P Lago (2005). Assessing baroreflex sensitivity in the sequences technique: local versus global approach. *Comput Cardiol* **32**, 279–282.

Gribbin, B, TG Pickering, P Sleight and R Peto (1971). Effect of age and high blood pressure on baroreflex sensitivity in man. *Circ Res* **29**, 424–431.

Guelen, L, BE Westerhof, GL Van Der Sar, GA van Montfrans, F Kiemeneij, KH Wesseling and WJW Bos (2003). Finometer, finger pressure measurements with the possibility to reconstruct brachial pressure. *Blood Pressure Monit* **8**(1), 27–30.

Guelen, L, BE Westerhof, GL Van Der Sar, GA van Montfrans, F Kiemeneij, KH Wesseling and WJW Bos (2008). Validation of brachial artery pressure reconstruction from finger arterial pressure. *J Hypertens* **26**(7), 1321–1327.

Gujic, M, D Laude, A Houssière, S Beloka, JF Argacha, D Adamopoulos, O Xhaët, JL Elghozi and P van de Borne (2007). Differential aspects of metaboreceptor and chemoreceptor activation on sympathetic and cardiac baroreflex control following exercise in hypoxia in human. *J Physiol* **585**(1), 165–174.

Guyton, AC and JE Hall (2000). *Textbook of Medical Physiology.* 10th ed.. WB Saunders. Philadelphia.

Halliwill, JR (2000). Segregated signal averaging of sympathetic baroreflex responses in humans. *J Appl Physiol* **88**, 767–773.

Hamilton, P and W Tompkins (1986). Quantitative investigation of QRS detection rules using the MIT/BIH database. *IEEE Trans Biomed Eng* **33**(12), 1157–1164.

Hamner, JW and JA Taylor (2001). Automated quantification of sympathetic beat-by-beat activity, independent of signal quality. *J Appl Physiol* **91**, 1199–1206.

Hartikaninen, JEK, KUO Tahvanainen, MJ Mäntysaari, PE Tikkanen, EA Länsimies and KEJ Airaksinen (1995). Simultaneous invasive and noninvasive evaluations of baroreflex sensitivity with bolus phenylephrine technique. *Am Heart J* **130**(2), 296–301.

He, T, G Clifford and L Tarassenko (2006). Application of independent component analysis in removing artefacts from the electrocardiogram. *Neural Comput & Applic* **15**(2), 105–116.

Hirsch, JA and B Bishop (1981). Respiratory sinus arrhythmia in humans: how breathing pattern modulates heart rate. *Am J Physiol Heart Circ Physiol* **241**(4), H620–H629.

Hunt, BE and WB Farquhar (2005). Nonlinearities and asymmetries of the human cardiovagal baroreflex. *Am J Physiol Regulatory Integrative Comp Physiol* **288**(5), R1339–R1346.

Jones, NB and P Lago (1982). Spectral analysis and the interference EMG. *IEE Proc* **129**(9), 673–678.

Karamanoglu, M (1997). A system for analysis of arterial blood pressure waveforms in humans. *Comput Biomed Res* **30**(3), 244–255.

Keselbrener, L and S Akselrod (1995). Artefacts in standard and time-dependent spectral analysis of arterial blood pressure signals obtained by Finapres: Importance and correction. *Clin Autonom Res* **5**(5), 295–301.

Köhler, BU, C Hennig and R Orglmeister (2002). The principles of software QRS detection. *IEEE Eng Med Biol Mag* **21**(1), 42–57.

Kim, SY and DE Euler (1997). Baroreflex sensitivity assessed by complex demodulation of cardiovascular variability. *Hypertens* **29**(5), 1119–1125.

Kinias, PF, HA Fozzard and MJ Norusis (1981). A real time pressure algorithm. *Comput Biol Med* **11**(4), 211–220.

Klingenheben, T, P Ptaszynski and SH Hohnloser (2008). Heart rate turbulence and other autonomic risk markers for arrhythmia risk stratification in dilated cardiomyopathy. *J Electrocardiol* **41**, 306–311.

Korhonen, I, R Takalo and V Turjanmaa (1996). Multivariate autoregressive model with immediate transfer paths for assessment of interactions between cardiopulmonary variability signals. *Med Biol Eng Comput* **34**, 199–206.

Korner, PI, MJ West, J Shaw and JB Uther (1974). ‘Steady-state’ properties of the baroreceptor-heart rate reflex in essential hypertension in man. *Clin Exp Pharm Physiol* **1**(1), 65–76.

La Rovere, MT, GD Pinna and G Raczak (2008). Baroreflex sensitivity: Measurement and clinical implications. *Ann Noninvasive Electrocardiol* **13**(2), 191–207.

La Rovere, MT, JT Bigger Jr, FI Marcus and A Mortara (1998). Baroreflex sensitivity and heart-rate variability in prediction of total cardiac mortality after myocardial infarction. ATRAMI Investigators. *Lancet* **351**, 478–84.

Laguna, P, NV Thakor, P Caminal, R Jané, HR Yoon, A Bayés de Luna, V Marti and J Guindo (1990). New algorithm for QT interval analysis in 24-hour holter ECG: performance and applications. *Med Biol Eng Comput* **28**(1), 67–73.

Lanfranchi, PA and VK Somers (2002). Arterial baroreflex function and cardiovascular variability: interactions and implications. *Am J Physiol Regulatory Integrative Comp Physiol* **283**(4), R815–R826.

Langewouters, GJ, JJ Settels, R Roelandt and KH Wesseling (1998). Why use Finapres or Portapres rather than intra-arterial or intermittent non-invasive techniques of blood pressure measurement?. *J Med Eng Technol* **22**, 37–43.

Laude, D, JL Elghizi, A Girard, E Bellard, M Bouhaddi, P Castiglioni, C Cerutti, A Cividjan, M Di Rienzo, JO Fortrat, B Janssen, JM Karemaker, G Leftheriotis, G Parati, PB Persson, A Porta, L Quintin, J Regnerd, H Rüdiger and HM Stauss (2004). Comparison of various techniques used to estimate spontaneous baroreflex sensitivity. (the EuroBaVar study). *Am J Physiol Regul Integr Comp Physiol* **286**(1), R226–R231.

Leanderson, S, P Laguna and L Sörnmo (2003). Estimation of the respiratory frequency using spatial information in the VCG. *Med Eng & Phys* **25**(6), 501–507.

Lee, CT and LY Wei (1983). Spectrum analysis of human pulse. *IEEE Trans Biomed Eng* **30**(6), 348–352.

Leite, A, AP Rocha, ME Silva, S Gouveia, J Carvalho and O Costa (2007). Long-range dependence in Heart Rate Variability data: ARFIMA modelling vs Detrended Fluctuation Analysis. *Comput Cardiol* **34**, 21–24.

Li, C, C Zheng and C Tai (1995). Detection of ECG characteristic points using wavelet transforms. *IEEE Trans Biomed Eng* **42**(1), 21–28.

Li, Q, RG Mark and GD Clifford (2008). Robust heart rate estimation from multiple asynchronous noisy sources using signal quality indices and a Kalman filter. *Physiol Meas* **29**, 15–32.

Liang, H, Z Lin and F Yin (2005). Removal of ECG contamination from diaphragmatic EMG by nonlinear filtering. *Nonlinear Analysis* **63**(5–7), 745–753.

Lipman, RD, JK Salisbury and JA Taylor (2003). Spontaneous indices are inconsistent with arterial baroreflex gain. *Hypertens* **42**, 481–487.

Lénárd, Z, P Studinger, B Mersich, G Pavlik and M Kollai (2005). Cardiovagal autonomic function in sedentary and trained offspring of hypertensive parents. *J Physiol* **565**, 1031–1038.

Macedo, A, A Santos, E Rocha and C Perdigão (2008). Self-reported cerebrovascular and heart diseases and cardiovascular risk factors in portugal: the AMALIA study. *Rev Port Cardiol* **27**(5), 569–580.

Malberg, H, N Wessel, A Hasart, K Osterziel and A Voss (2002). Advanced analysis of spontaneous baroreflex sensitivity, blood pressure and heart rate variability in patients with dilated cardiomyopathy. *Clinical Science* **102**, 465–473.

Mallat, S (1999). *A Wavelet Tour of Signal Processing.* Academic Press.

Mallat, S and S Zhong (1992). Characterization of signals from multiscale edges. *IEEE Transactions on Pattern Analysis and Machine Intelligence* **14**(7), 710–732.

Malliani, A and N Montano (2004). Gold standard in assessing baroreceptive function. *Hypertens* **43**, e24.

Malliani, A, M Pagani, N Montano and GS Mela (1998). Sympathovagal balance: A reappraisal. *Circulation* **98**, 2640–2643.

Malmivuo, J and R Plonsey (1995). *Bioelectromagnetism - Principles and Applications of Bioelectric and Biomagnetic Fields.* Oxford University Press. Available online at http://www.bem.fi/book/ (accessed in May 2009).

Mancia, G and AL Mark (1983). Arterial baroreflexes in humans. In: *Handbook of Physiology. The Cardiovascular System.* (MD Bethesda, Ed.). Vol. 3. Chap. 20, pp. 755–793. Am Physiol Soc.

Mancia, G, G Parati, P Castiglioni and M Di Rienzo (1999). Effect of sinoaortic denervation on frequency-domain estimates of baroreflex sensitivity in conscious cats. *Am J Physiol Heart Circ Physiol* **276**, H1987–H1993.

Manolakis, D, V Ingle and S Kogon (2000). *Statistical and Adaptive Signal Processing: Spectral Estimation, Signal Modeling, Adaptive Filtering and Array Processing.* McGraw-Hill Education.

Marple, L (1987). *Digital spectral analysis with applications.* Prentice Hall.

Martínez, JP, R Almeida, S Olmos, AP Rocha and P Laguna (2004). Wavelet-based ECG delineator: evaluation on standard databases. *IEEE Trans Biomed Eng* **51**(4), 570–581.

Mateo, J and P Laguna (2000). Improved heart rate variability signal analysis from the beat occurrence times according to the IPFM model heart timing signal. *IEEE Trans Biomed Eng* **47**(8), 985–996.

Matsukawa, T, Y Sugiyama and T Mano (1996). Age related changes in baroreflex control of heart rate and sympathetic nerve activity in healthy humans. *J Auton Nerv Syst* **60**(3), 209–212.

Moffitt, JA, AJ Grippo and AK Johnson (2005). Baroreceptor reflex control of heart rate in rats studied by induced and autogenic changes in arterial pressure. *Am J Physiol Heart Circ Physiol* **288**, 2422–2430.

Montano, N, R Furlan, S Guzzetti, RM McAllen and C Julien (2009). Analysis of sympathetic neural discharge in rats and humans. *Phil Trans R Soc A* **367**, 1265–1282.

Moody, GB and RG Mark (1996). A database to support development and evaluation of intelligent intensive care monitoring. *Comput Cardiol* **42**, 657–660.

Mortara, A, MT La Rovere, GD Pinna, P Parziale, R Maestri, S Capomolla, C Opasich, F Cobelli and L Tavazzi (1997). Depressed arterial baroreflex sensitivity and not reduced heart rate variability identifies patients with chronic heart failure and nonsustained ventricular tachycardia. *Am Heart J* **134**(5 Pt 1), 879–888.

Navakatikyan, MA, CJ Barrett, GA Head, JH Ricketts and SC Malpas (2002). A real-time algorithm for the quantification of blood pressure waveforms. *IEEE Trans Biomed Eng* **49**(7), 662–670.

Nocedal, J and S Wright (1999). *Numerical Optimization*. Springer Series in Operations Research and Financial Engineering. Springer.

Nollo, G, A Porta, L Faes, M Del Greco, M Disertori and F Ravelli (2001). Causal linear parametric model for baroreflex gain assessment in patients with recent myocardial infarction. *Am J Physiol Heart Circ Physiol* **280**(4), H1830–H1839.

Nollo, G, L Faes, R Antolini and A Porta (2009). Assessing causality in normal and impaired short-term cardiovascular regulation via nonlinear prediction methods. *Phil Trans R Soc A* **367**, 1423–1440.

Nygårds, ME and L Sörnmo (1983). Delineation of the QRS complex using the envelope of the e.c.g. *Med Biol Eng Comput* **21**, 289–297.

Oka, H, S Mochio, M Yoshioka, M Morita and K Inoue (2003). Evaluation of baroreflex sensitivity by the sequence method using blood pressure oscillations and RR interval changes during deep respiration. *Eur Neurol* **50**, 230–243.

O'Rourke, MF (2009). Time domain analysis of the arterial pulse in clinical medicine. *Med Biol Eng Comput* **47**, 119–129.

O'Rourke, MF and DE Gallagher (1996). Pulse wave analysis. *J Hypertens* **14**(5), S147–157.

Orr, WC and HJ Hoffman (1974). A 90-min cardiac biorhythm: methodology and data analysis using modified periodograms and complex demodulation. *IEEE Trans Biomed Eng* **21**(2), 130–143.

Pagani, M, F Lombardi, S Guzzetti, O Rimoldi, R Furlan, P Pizzinelli, G Sandrone, G Malfatto, S Dell'Orto, E Piccaluga, M Turiel, G Baselli, S Cerutti and A Malliani (1986). Power spectral analysis of heart rate and arterial pressure variabilities as a marker of sympatho-vagal interaction in man and conscious dog. *Circ Res* **59**, 178–193.

Pagani, M, N Montano, A Porta, A Malliani, F Abboud, C Birkett and V Somers (1997). Relationship between spectral components of cardiovascular variabilities and direct measures of muscle sympathetic nerve activity in humans. *Circulation* **95**, 1441–1448.

Pagani, M, V Somers, R Furlan, S Dell'Orto, J Conway, G Baselli, S Cerutti, P Sleight and A Malliani (1988). Changes in autonomic regulation induced by physical training in mild hypertension. *Hypertens* **12**(6), 600–610.

Pahlm, O and L Sörnmo (1984). Software QRS detection in ambulatory monitoring – a review. *Med Biol Eng Comput* **22**, 289–297.

Pan, J and W Tompkins (1985). A real–time QRS detection algorithm. *IEEE Trans Biomed Eng* **32**(3), 230–236.

Parati, G, JP Saul and P Castiglioni (2004). Assessing arterial baroreflex control of heart rate: new perspectives. *J Hypertens* **22**(7), 1259–63.

Parati, G, JP Saul, M Di Rienzo and G Mancia (1995). Spectral analysis of blood pressure and heart rate variability in evaluating cardiovascular regulation: a critical appraisal. *Hypertens* **25**, 1276–1286.

Parati, G, M Di Rienzo and G Mancia (2000). How to measure baroreflex sensitivity: from the cardiovascular laboratory to daily life. *J Hypertens* **18**(1), 7–19.

Parati, G, R Casadei, A Groppelli and M Di Rienzo (1989). Comparison of finger and intra-arterial blood pressure monitoring at rest and during laboratory testing. *Hypertens* **13**, 647–655.

Parlow, J, JP Viale, G Annat, R Hughson and L Quintin (1995). Spontaneous cardiac baroreflex in humans: comparison with drug-induced responses. *Hypertens* **25**, 1058–1068.

Persson, P, M Di Rienzo, P Castiglioni, M Pagani, N Honzikova, A Akselrod and G Parati (2001). Time versus frequency domain techniques for assessing baroreflex sensitivity. *J Hypertens* **19**(10), 1699–1705.

Peñáz, J (1973). Photoelectric measurements of blood pressure, volume and flow in the finger. *Digest 10th Int Conf Med Biol Eng* p. 104.

Pickering, TG, B Gribbin and P Sleight (1972). Comparison of the reflex heart rate response to rising and falling arterial pressure in man. *Cardiovasc Res* **6**(3), 277–283.

Pinna, GD and R Maestri (2002). New criteria for estimating baroreflex sensitivity using the transfer function method. *Med Biol Eng Comput* **40**(1), 79–84.

Pinna, GD, MT La Rovere, R Maestri, A Mortara, JT Bigger Jr and PJ Schwartz (2000). Comparison between invasive and non-invasive measurements of baroreflex sensitivity. *Eur Heart J* **21**, 1522–1529.

Pinna, GD, R Maestri, G Raczak and MT La Rovere (2002). Measuring baroreflex sensitivity from the gain function between arterial pressure and heart period. *Clinical Science* **103**, 81–88.

Pitzalis, M, F Mastropasqua, A Passantino, F Massari, L Ligurgo, C Forleo, C Balducci, F Lombardi and P Rizzon (1998*a*). Comparison between noninvasive indices of baroreceptor sensitivity and the phenylephrine method in post–myocardial infarction patients. *Circulation* **97**, 1362–1367.

Pitzalis, M, F Mastropasqua, F Massari, A Passantino, R Colombo, A Mannarini, C Forleo and P Rizzon (1998*b*). Effect of respiratory rate on the relationships between RR interval and systolic blood pressure fluctuations: a frequency-dependent phenomenon. *Cardiovasc Res* **38**, 332–339.

Porta, A, F Aletti, F Vallais and G Baselli (2009). Multimodal signal processing for the analysis of cardiovascular variability. *Phil Trans R Soc A* **367**, 391–409.

Porta, A, G Baselli, O Rimoldi, A Malliani and M Pagani (2000). Assessing baroreflex gain from spontaneous variability in conscious dogs: role of causality and respiration. *Am J Physiol Heart Circ Physiol* **279**, H2558–H2567.

Rathmann, W, D Ziegler, M Jahnke, B Haastert and FA Gries (1993). Mortality in diabetic patients with cardiovascular autonomic neuropathy. *Diabetic Med* **10**, 820–824.

Rüdiger, H, L Klinghammer and K Scheuch (1999). The trigonometric regressive spectral analysis – a method for mapping of beat-to-beat recorded cardiovascular parameters on to frequency domain in comparison with Fourier transformation. *Comput Methods Programs Biomed* **58**, 1–15.

Robbe, H, L Mulder, H Ruddel, W Langewitz, J Veldman and G Mulder (1987). Assessment of baroreceptor reflex sensitivity by means of spectral analysis. *Hypertens* **10**(5), 538–43.

Robertson, D, P Low and R Polinsky (1996). *Primer on the Autonomic Nervous System.* Academic Press.

Rocha, AP, S Gouveia, A Leite, P Lago, O Costa, AF Freitas and M Carvalho (2002). A study on the estimation of the respiratory signal in 12-lead Holter recordings. *Proc EMBEC'02, 2nd IFMBE Med Biol Eng Conf* pp. 508–509.

Rothlisberger, BW, LJ Badra, JB Hoag, WH Cooke, TA Kuusela, KUO Tahvanainen and DL Eckberg (2003). Spontaneous 'baroreflex sequences' occur as deterministic functions of breathing phase. *Clin Physiol Funct Imaging* **23**(4), 307–313.

Rudas, L, AA Crossman, CA Morillo, J Halliwill, KUO Tahvanainen, TA Kuusela and DL Eckberg (1999). Human sympathetic and vagal baroreflex responses to sequential nitroprusside and phenylephrine. *Am J Physiol Heart Circ Physiol* **276**, 1691–1698.

Saul, J, R Berger, P Albrecht, S Stein, M Chen and R Cohen (1991). Transfer function analysis of the circulation: unique insights into cardiovascular regulation. *Am J Physiol* **261**, H1231–1245.

Sleight, P (2007). New methods for risk stratification in patients after myocardial infarction: Autonomic control and substrate sensitivity. *J Am Coll Cardiol* **50**, 2291–2293.

Smith, RP, J Argod, JL Pépin and PA Lévya (1999). Pulse Transit Time: an appraisal of potential clinical applications. *Thorax* **54**, 452–457.

Smyth, H, P Sleight and G Pickering (1969). Reflex regulation of arterial pressure during sleep in man: A quantitative method of assessing baroreflex sensitivity. *Circ Res* **24**, 109–121.

Sörnmo, L and P Laguna (2005). *Bioelectrical Signal Processing In Cardiac And Neurological Applications*. Academic Press.

Stark, RJ, L Valenti and GC Miller (2007). Management of migraine in australian general practice. *Med J Aust* **187**, 142–146.

Stauss, HM, JA Moffitt, MW Chapleau, FM Abboud and AK Johnson (2006). Baroreceptor reflex sensitivity estimated by the sequence technique is reliable in rats. *Am J Physiol Heart Circ Physiol* **291**, 482–483.

Sundlöf, G and BG Wallin (1978). Human muscle nerve sympathetic activity at rest. Relationship to blood pressure and age. *J Physiol* **274**, 621–637.

Takeshita, A, S Tanaka, A Kuroiwa and M Nakamura (1975). Reduced baroreceptor sensitivity in borderline hypertension. *Circulation* **51**, 738–742.

Tank, J, RM Baesvski, A Fender, AR Baevski, KF Graves, K Ploewka and M Weck (2000). Reference values of indices of spontaneous baroreceptor reflex sensitivity. *Am J Hypertens* **13**(3), 268–275.

Task Force of ESC & NASPE (1996). Heart rate variability. standards of measurement, physiological interpretation, and clinical use. *Eur Heart J* **17**, 354–381.

Thakor, NV, JG Webster and WJ Tompkins (1983). Optimal QRS detector. *Med Biol Eng Comput* **21**(5), 343–350.

Tiinanen, S, M Tulppo and T Seppänen (2008). Reducing the effect of respiration in baroreflex sensitivity estimation with adaptive filtering. *IEEE Trans Biomed Eng* **55**(1), 51–59.

Uitti, RJ (1998). Tremor: how to determine if the patient has parkinson's disease. *Geriatrics* **53**, 30–36.

van de Borne, P, B Zimmerman, N Montano, M Pagani and VK Somers (1997). Relationship between repeated measures of hemodynamics, muscle sympathetic nerve activity, and their spectral oscillations. *Circulation* **96**, 4326–4332.

van de Borne, P, N Montano, K Narkiewicz, JP Degaute, A Malliani, M Pagani and VK Somers (2001). Importance of ventilation in modulating interaction between sympathetic drive and cardiovascular variability. *Am J Physiol Heart Circ Physiol* **280**, H722–H729.

van Huffel, S and Joos Vandewalle (1991). *The Total Least Squares Problem: Computational Aspects and Analysis.* SIAM. Philadelphia.

Wallin, BG (2007). Interindividual differences in muscule sympathetic nerve activity: a key to new insight into cardiovascular regulation. *Acta Physiol* **190**, 265–275.

Wallin, BG and N Charkoudian (2007). Sympathetic neural control of integrated cardiovascular function: Insights from measurement of human sympathetic nerve activity. *Muscle Nerve* **36**, 595–614.

Walsh, GR (1975). *Methods of Optimization.* John Wiley & Sons.

Watkins, L, P Grossman and A Sherwood (1996). Noninvasive assessment of baroreflex control in borderline hypertension: comparison with the phenylephrine method. *Hypertens* **28**, 238–243.

Welch, PD (1967). The use of fast Fourier transform for the estimation of power spectra: a method based on time averaging over short modified peridiograms. *IEEE Trans Audio and Electroacoust* **15**, 70–73.

Wesseling, KH, B de Wit, GMA van der Hoeven, J van Goudoever and JJ Settels (1995). Physiocal, calibrating finger vascular physiology for Finapres. *Homeostasis* **36**, 67–82.

Westerhof, BE, J Gisolf, WJ Stok, KH Wesseling and JM Karemaker (2004). Time-domain cross-correlation baroreflex sensitivity: performance on the EUROBAVAR data set. *J Hypertens* **22**(7), 1371–80.

Wilcox, R (2001). *Fundamentals of modern statistical methods: substantially improving power and accuracy*. Springer-Verlag. New York.

Wilcox, R (2005). *Introduction to robust estimation and hypothesis testing*. 2nd ed.. Elsevier Academic Press.

Zetterberg, L (1969). Estimation parameter of a linear difference equation with application to eeg analysis. *Math Biosci* **5**, 227–275.

Ziegler, D, D Laude, F Akila and JL Elghozi (2001). Time- and frequency-domain estimation of early diabetic cardiovascular autonomic neuropathy. *Clin Auton Res* **11**(6), 369–376.

Zong, W, GB Moody and D Jiang (2003*a*). A robust open-source algorithm to detect onset and duration of QRS complexes. *Comput Cardiol* **30**, 737–740.

Zong, W, GB Moody and RG Mark (2004). Reduction of false arterial blood pressure alarms using signal quality assessment and relationships between the electrocardiogram and arterial blood pressure. *Med Biol Eng Comput* **42**(5), 698–706.

Zong, W, T Heldt, GB Moody and RG Mark (2003*b*). An open-source algorithm to detect onset of Arterial Blood Pressure pulses. *Comput Cardiol* **30**, 259–262.

Zoubir, AM and B Boashash (1998). The bootstrap and its application in signal processing. *IEEE Signal Processing Magazine* **15**(1), 56–76.

List of Tables

List of Figures